



Marinero III, Ralph Michael (2024) *Performance and commissioning of the BigBite Timing Hodoscope for nucleon form factor measurements at Jefferson Lab*. PhD thesis.

<https://theses.gla.ac.uk/84182/>

Copyright and moral rights for this work are retained by the author

A copy can be downloaded for personal non-commercial research or study, without prior permission or charge

This work cannot be reproduced or quoted extensively from without first obtaining permission from the author

The content must not be changed in any way or sold commercially in any format or medium without the formal permission of the author

When referring to this work, full bibliographic details including the author, title, awarding institution and date of the thesis must be given

Enlighten: Theses

<https://theses.gla.ac.uk/>
research-enlighten@glasgow.ac.uk

Performance and Commissioning of the BigBite Timing Hodoscope for Nucleon Form Factor Measurements at Jefferson Lab

Ralph Michael Marinaro III

Presented as a Thesis for the degree of
Doctor of Philosophy



School of Physics and Astronomy
College of Science and Engineering
University of Glasgow
July 2023

© R. M. Marinaro 2023

Acknowledgements

To my supervisors, Dr. David J. Hamilton and Dr. Rachel A. Montgomery, it is an absolute pleasure to work with you both. I have learned so much from our regular meetings and those conversations will last a lifetime. The University of Glasgow administration, the School of Physics and Astronomy staff, and every member of the Nuclear Physics group must be recognized as well because without them there would be no structure or support for their students. I would have never made it this far without the mentoring of Dr. Peter Monaghan, and Dr. Edward Brash both of whom first introduced me to nuclear physics research at Jefferson Lab, and helped secure my acceptance to the University of Glasgow, among countless other opportunities. The Physics, Computer Science, and Engineering Department and its faculty, specifically Dr. David Gore, Dr. David Heddle, Dr. Anna DeJong, Dr. Robert Fersch, Dr. Anton Riedl, and Clare Maliniak, at Christopher Newport University must also be recognized for the formative years that defined my time as an undergraduate student. Now I must recognize the Super BigBite Collaboration members, and Jefferson Lab staff who made this research possible. In particular I would like to thank Dr. Mark Jones, Dr. Alexandre Camsonne, Dr. Arun Tadepalli, Dr. Andrew Puckett, all of the then Hall A SBS postdocs, and graduate students, and all those whom I worked along side countless hours installing detector hardware, laying cables, and troubleshooting data acquisition electronics. Now, I must thank my peers over the years, past and current, but particularly those at Glasgow who were always inviting, friendly, welcoming, and willing to listen to my ramblings, or share a laugh. It is thanks to the University of Glasgow Science and Engineering College Scholarship award that provided the funding which allowed me to embark on this opportunity. I have taken great care to detail all the help, support, and advice I have received over the years from countless people, but none of it compares to that which I have received from my dear parents, Ralph and Bernadette, including their love, respect, and admiration, all of which has never been less than mutual. Thank you to my sister, Fiona, an ideal friend, and sibling. Also, I must include a special recognition for my grandparents, Ralph and Italia, and James and Mary, and all the sacrifices they made for their children and grandchildren.

Declaration

The work in this thesis is based on research carried out within the Nuclear Physics Experimental Group, School of Physics and Astronomy, College of Science and Engineering, University of Glasgow, Scotland and with a collaboration of Thomas Jefferson National Accelerator Facility, U.S. Department of Energy, Virginia, United States. The information describing Jefferson Lab, the Super BigBite Spectrometer, and the Timing Hodoscope from Chapters 1-3 is provided based on my own knowledge, and in collaboration with colleagues and peers of Jefferson Lab and University of Glasgow. The setup of the data acquisition system detailed in Chapter 3, and the construction, installation, and commissioning analysis of the Timing Hodoscope provided in Chapter 4 is all work for which I had direct participation, and with the help of colleagues and peers of Jefferson Lab and University of Glasgow. Lastly, the calibration and performance analyses detailed in Chapters 4 and 5 is research for which I had direct participation, and in collaboration with colleagues and peers from the Nuclear Physics Experimental Group, University of Glasgow. No part of this thesis has been submitted elsewhere at any institution for any other degree or qualification and it is all my own work unless referenced to the contrary in the text.

Ralph Michael Marinaro III

July 2023

Abstract

The BigBite Timing Hodoscope detector is the primary subject of this thesis. The Super BigBite Spectrometer is a Jefferson Lab Hall A Collaboration project that has and will continue to measure nucleon electromagnetic form factors. This spectrometer includes the Timing Hodoscope which provides high resolution particle timing data for scattered electrons in the electron arm of BigBite. The Timing Hodoscope utilizes 90, $25 \times 25 \times 600 \text{ mm}^3$ scintillator bars stacked on top of each other to form a single detector plane, and these bars are connected to 180 photo-multiplier tubes via light guides. Particles collide with the scintillating material creating a shower of optical photons and these particle events in the bars are collected to generate signals that are readout by the data acquisition (DAQ) electronics. NINO ASIC amplifier-discriminator cards output signals from the photo-multiplier tubes into analogue and logic signals, which are sent to analogue-to-digital (ADC) and time-to-digital (TDC) converter data acquisition readout modules. This data is then used for analysis of the detector.

The focus of this thesis is the construction, commissioning, calibration, and performance of the BigBite Timing Hodoscope before and during the first of five nucleon electromagnetic form factor experiments at Jefferson Lab Hall A. Before the neutron magnetic form factor, G_M^n , experiment, cosmic ray data was collected during commissioning to confirm proper operation of the Timing Hodoscope electronics by observing the ADC and TDC data. Commissioning studies for charge normalization, gain matching, and other ADC and TDC detector data variables were performed before moving the detector into Hall A. Following installation in Hall A, several calibration studies were implemented to fine-tune the detector in preparation for use in the experiment. The calibration studies included analysis of timing cuts, TDC alignment, the time-walk effect, time difference offsets, and scintillator velocity corrections. Once the Timing Hodoscope was well-calibrated, data-taking during the experiment commenced and the beam-on-target data was used to characterize the Timing Hodoscope performance during the G_M^n experiment run-time. The performance analysis included studies observing energy deposit, cluster size, rates, accidentals, pile-up, tracking efficiency, position resolution, and time resolution. After application of physics cuts to ensure a data set comprised of particle tracks corresponding to elastic electrons, which is the main data of interest for measurement of G_M^n , the Timing Hodoscope is shown on average across all kinematic settings to have a $>98\%$ tracking efficiency, a position resolution of 4-6 cm in the non-dispersive plane and 1.5-2 cm in the dispersive plane, and a time resolution of 500-750 ps. These performance results are compared to a GEANT4 based performance simulation of the BigBite Timing Hodoscope for reference, showing to what degree the measured performance values match those taken from the simulation.

List of Figures

1.1	A representative picture of quarks and gluons (yellow) within the nucleon. Blue, red, and green arrows indicate the spins of the quarks, white arrows indicate orbital angular momentum of the quarks and gluons, and the grey arrow represents the spin of the nucleon. Image from [5].	3
1.2	A combination of world data for both the magnetic (top and bottom left) and electric (top right) form factors of the neutron, the electromagnetic form factor ratio of the neutron (bottom right), the magnetic form factor of the proton (middle left), and the electromagnetic form factor ratio of the proton (middle right). These plots show that most data points are on the lower end of each plotted Q^2 range respectively. The trend lines and markers are consistent across all above plots. Plots from [8].	4
1.3	A Feynman diagram of an incident electron scattering off of a neutron using the one-photon exchange process. The generalized spin polarizabilities of the neutron can be measured when both incident electron and neutron are polarized. Here $Q^2 = -q^2$. Image from [10].	5
1.4	An aerial view photo of the CEBAF accelerator site with red dashed lines for racetrack-shaped design, with two linear accelerator (linac) sections in the straight-line portions of the racetrack, and red circles to indicated the three experimental Halls A, B, and C where beam is delivered. Not shown is the more recently built Hall D. Image from [15].	8
1.5	A layout diagram of CEBAF before the 12 GeV upgrade. The electron beam is generated with the injector which uses illumination on a photocathode. The beam is next accelerated in both superconducting linacs, which can recirculate the beam. The beam is then extracted to each of the experimental halls. Image from [17].	10
1.6	The essential diagram for the 12 GeV upgrade. With the upgrade of the accelerator system to deliver 12 GeV beam, the experimental technologies are improved to allow complete advantage to be made of the higher energy beam, including new detection systems and new Hall D. The setup for Hall A involved upgrades such as the installation of SBS. Image from [21].	11
1.7	A schematic of the one-photon exchange mechanism is depicted for elastic electron-nucleon scattering showing resultant e' trajectory.	16

2.1	Two plots for world data on the neutron magnetic form factor GMn (top) and the neutron electromagnetic form factor ratio (bottom) with projected SBS statistical precision for the SBS GMn and GEn experiments. Trend lines and data marker are specific to each plot separately. Data markers for Hall A and C data are placeholders because these values have not yet been calculated, and are currently in the post-experiment analysis stage. Plots by A. Puckett [8].	27
2.2	A layout diagram of SBS hadron (below electron beam) and electron (above electron beam) arms, including detectors: Timing Hodoscope (light blue), Pre-shower and Shower (light blue), GRINCH (green), GEMs (pink), Magnets (light purple), and Hadron Calorimeter (dark blue). The kinematic setting of SBS varies throughout the experiment run time. Image from [13].	30
2.3	Several diagrams of the GEMs with a single GEM (top left) dimensions, a GEM chamber layer frame of three GEMs, stack of single GEM chamber components (top right), GEM layers with readout boards (ROB) using the U/V and X/Y strips design (bottom left), particle cascade in the three-layer GEM foils filled with gas (bottom right), and readout board layout (bottom). Diagrams from [42].	34
2.4	Calorimeter block arrays with numbering and Pb glass block positions for the PS (left) and SH (right) detectors which comprise BBCal showing the direction of the incident scattered electron coming out of the page. Therefore, this perspective is from the back of the two BBCal detectors relative to the target. Diagrams by P. Datta.	35
2.5	A layout diagram of the BigBite electron arm showing the component detector subsystems, including the BigBite magnet, GRINCH, GEM layers, TH detector, and the BigBite calorimeter comprised of the shower and pre-shower. The LD2 target chamber in the diagram can be interchanged with the LH2 target chamber. The dashed black line shows the scattered electron trajectory with the BigBite magnet off while the dashed blue line shows the scattered electron trajectory with the BigBite magnet turned on. Diagram from [2].	36
2.6	A diagram of a single HCal block, with all measurements in mm, pointing left toward the target. These blocks are arrayed in an 11 x 22 matrix to make HCal. Diagram from [42].	38
2.7	Two diagrams of the SBS electron (left) and hadron (right) arms with target and detector frames installed in Hall A. These images include both SBS arms with the electron arm left of the beam-line and the hadron arm to the right, showing the setup for the GMn, nTPE, and GEn experiments, which exclude the SBS hadron arm polarimeter and coordinate detector. Images courtesy of the SBS Collaboration at JLab.	39
2.8	An image showing just the SBS hadron arm, excluding the polarimeter and coordinate detector. The HCal is represented by the stack of orange colored blocks. The 48D48 dipole magnet is shown in green, positioned close to the target. Image courtesy of the SBS Collaboration at JLab.	39

3.1	A 3D diagram of the TH detector showing central plane made of stacked scintillator bars, which are attached to light guides and PMTs. The PMTs are inside individual housing assemblies, which are made light-tight. In the BigBite frame, the TH detector is installed between the PS and SH detectors of the BBCal. Diagram courtesy of the SBS Collaboration.	41
3.2	A plot of the Eljen EJ-200 scintillator bar emission spectrum with measured wavelength versus amplitude. This plot shows the peak wavelength occurring at 425 nm. Plot from [47].	43
3.3	A plot showing how the TH detector scintillator bars respond to the energy of the particles detected given by the number of scintillation photons produced. This plot shows electrons outputting more photons per MeV thus making this specific scintillating material optimal for use in the BigBite electron arm of SBS. Plot from [47].	44
3.4	This diagram shows the internal construction of a general photo-multiplier tube design with light incident on the PMT face plate and photo-cathode turned into electrons which are multiplied by the dynodes and output as a signal pulse. Image from [50].	45
3.5	The left diagram shows the physical measurements in mm of the ET-9142 PMTs used for the TH detector and the right diagram is a schematic of the internal circuitry showing all 10 dynodes, anode, and resistors. Diagrams from [51] (left) and by J. Annand and P. S. Lumden [52] (right).	46
3.6	A schematic of the ET-9142 PMT installed inside a unit of the PMT housing assembly with measurements showing depth of light guide (light blue) within the housing. Image by J. Annand and A. Shahinyan.	46
3.7	A block diagram of the NINO ASIC showing the logic behind the information flow for a single channel in the electronic chip. Diagram from [53].	47
3.8	A schematic of the NINO ASIC amplifier-discriminator chip input stage showing signal input and output, current source, and common gate. Diagram from [53].	48
3.9	A photo of the specific 16 coaxial input connector NINO ASIC amplifier-discriminator card version. This version is particular to the TH as NINO card designs can vary as needed to accommodate different input signal cable connectors. Photo by R. Marinaro.	49
3.10	A photo of the KEYSIGHT LV power supply unit mounted in an electronics rack in the bunker used to power the NINO cards. The power supply on top is used for the TH detector, the other is for the GRINCH. Photo by R. Marinaro.	51
3.11	A diagram of the TH detector frame LV distribution box which splits the power from the KEYSIGHT power supply unit to the individual NINO cards. Diagram from [52].	51
3.12	Front and back photos of the HV mainframe, which was installed in the electronic racks in the Hall A SBS bunker, used for the TH detector to power the 180 PMTs. Photos by R. Marinaro.	52
3.13	The ADC slot number refers to the position of each FADC readout module in the DAQ crate. The same crate houses the TDC v1190 readout modules.	54

3.14	Color coded maps of the TDC labelling used from the TH detector frame patch panel to the TDC v1190 readout modules in the DAQ crates. The readout inputs A, B, C, and D correspond to the physical position of the connection points to the v1190s further discussed in the next section.	55
3.15	Two photos with labels showing where the NINOs, and distribution boxes are located on the TH detector frame. The NINOs are mounted to the frame with metal screws that provide grounding to the frame which has a common ground for all electronics attached to the BigBite frame. Photos by R. Marinaro, and labels by R. Montgomery.	56
3.16	Three photos showing the TH detector HV distribution boxes H-HV-PP-L0 (left), H-HV-PP-L1 (middle), and H-HV-PP-R0 and -R1 (right). Photos by R. Marinaro.	56
3.17	A photo of two NINOs mounted to the detector frame with ADC and TDC ribbon cables installed (top left), the LV distribution box (top right), and the TDC and ADC patch panels at the TH detector frame (bottom). Photos by R. Marinaro.	57
3.18	Two photos of the level translator repeater (left) and the TDC patch panel (right) both located in the electronics bunker racks. Photos by R. Marinaro.	58
3.19	A flow chart diagram of the DAQ system going from scintillator bars to DAQ crate, and including the HV (red) and LV (pink) power supply systems for the PMTs and NINOs respectively. The path for ADC and TDC signals are in green and blue respectively. . . .	60
3.20	A flow chart diagram of the analysis software process going from the TDC and FADC readout modules to sbs-replay using sbs-offline, and final analysis. This diagram includes the simulation software repositories as well.	62
4.1	Laser tests in light-tight black box: resting no laser (1), no light guide (2), smooth light guide (3), two smooth light guides (4), two smooth light guides glued together (5), light guide roughened one side (6), two light guides roughened one side (7), two light guides roughened one side glued together (8).	66
4.2	Diagram of stress test setup using clamp bolted to a table. Smooth-surface light guides would break with only a moderate touch, but after roughening, the glue joint became significantly stronger.	67
4.3	Diagram of the precision alignment apparatus used during the gluing of the roughened light guides to the roughened scintillator bars. Only a drop of optical glue 5 mm wide and 1 mm high was needed to cover the whole contact surface between the light guide and the scintillator bar. Optical glue was stored in a sealed container to prevent drying. .	68
4.4	Diagrams of the wrapping procedure for both straight and curved light guides, and scintillator bars with dimensions. The final wrapping thickness leaves only a <0.5 mm gap between the stacked scintillator bars. The light guide is shown in blue, the yellow is the mylar wrap, grey is the industrial wrapping paper, and black is electrical tape.	69
4.5	A diagram of the PMT inside the housing and attachment to light guides using a brace and screws which were tightened once the PMT and light guide were inserted in the housing.	70

4.6	A diagram of the final light-tight scintillator bar, light guides, and PMT housing assemblies with added support bars to further prevent roughened glue joint from breaking. . . .	70
4.7	Two images of the fully stacked and assembled TH detector. The left image shows what the detector looks like without the detector frame to hold it up. The right image shows a portion of the red detector frame and the angled brackets which the TH scintillator bars are attached. This allows for the bars to be stacked without falling over. The angle brackets also help alleviate some of the weight pressing down on the scintillator bars at the bottom of the stack. The right image is what the target would see if it had a direct line-of-sight to the TH and no other detectors were blocking the TH from the target. . . .	72
4.8	The HV distribution boxes (light grey) are attached to the frame (dark red) and are labeled L0, L1, R0, and R1 corresponding to the right and left side and bottom (0) 48 channels or the top (1) 42 channels. Individual PMT HV cables (bright red) go from the PMTs to the HV distribution boxes. The individual signal cables (blue) go from the PMTs to the NINOs (light green) labeled 1-12. NINO 1 corresponds to bottom left 16 PMTs, 6 to top left, 7 to bottom right, and 12 to top right. The individual LV NINO power supply cables (orange) go from the LV distribution (dark grey) to the NINOs. ADC ribbon cables (purple) and TDC ribbon cables (yellow) connect the NINO analogue and logical output to the ADC and TDC patch panels (dark green). Cable lengths are provided in Appendix D.	74
4.9	The cable path for the HV, LV, ADC coax, and TDC ribbon cables are show by red arrows. The total laid cable length from BigBite to the bunker is 90 ft with an additional few feet of laid cable at BigBite for slack and inside the bunker to reach the electronics. Additional cable length was coiled and stored in the bunker. The TDC ribbon cables were run through a flexible rubber conduit for protection. Image courtesy of the SBS Collaboration at JLab.	75
4.10	A photo of the left half of the electronics racks (left) housing the TH detector TDC and ADC bunker patch panels, the DAQ crate, the LV power supply, and HV power supply, and the right half of the electronics racks (right) housing the LTR and other BigBite detector DAQ modules. Photos by R. Marinaro.	76
4.11	A side profile photo of the BigBite electron arm as it is currently, fully installed in Experimental Hall A. Photo by R. Marinaro.	77
4.12	A photo of the back-view for the BigBite electron arm looking in the direction of the detector stack towards the target hidden on the other side of BigBite. Platforms on either side allow for access to the PMTs, and NINOs during experiment down time where troubleshooting takes place for any malfunctions of the TH detector of which there were next to none. Photo by R. Marinaro.	77

4.13	A plot of 16 good ADC distributions with pedestal and ADC signal peaks cleanly separated using minimal ADC cuts on the ADC signals from adjacent scintillator bar ADC channels, which ensures that only particle tracks from events that pass all or mostly through the scintillator are being plotted. These plots were generated using cosmic data before installation in Hall A using a large external trigger scintillator positioned on top of the detector frame.	79
4.14	A plot of the ADC distribution for channel 48 left (48L) showing the Gaussian fit to the pedestal. Once the mean is subtracted the whole distribution shifts down by an amount equal to the mean of the fit. This was repeated for all ADC channels left and right.	80
4.15	A plot of the pedestal Gaussian fit mean values for the set of 64 middle, bars 33-64 left and right, channels of the TH detector using cosmic ray data with the v792s and large external scintillator trigger. Similar plots were generated for every ADC channel to confirm an initial uniformity of the pedestal means across the whole TH detector.	80
4.16	The left set of 16 plots (in a 4x4 array) in this figure show the Landau fit for a set of 16 ADC distributions with pedestals subtracted and removed. These plots are far less uniform than the set of 16 plots on the right which were generated after adjusting the HV settings for a successful optimized charge normalization.	81
4.17	Four plots from Bars 11, 13, 27, and 29 showing the ADC distributions left and right for each bar plotted against each other after charge normalization. These plots show a strong correlation and uniformity by their tight cone shape, which further underscores the success of the ADC distribution charge normalization process. The only cuts applied here are ADC neighbor cuts to ensure cosmic tracks that pass all the way through the scintillator bar.	82
4.18	Six plots of ADC Means or MPVs from the Landau fits on the ADC distributions. The first column of plots shows charge normalization for the lower third of the detector progressing from the initial ADC MPV values at the top to their final values at the bottom. The second column shows, similarly, charge normalization for the middle third of the detector. This process was repeated for the upper third with similar behavior and results as in the plots shown above. These plots were generated using cosmic ray data with the ADC v792 readout modules and a larger external scintillator trigger.	83
4.19	A plot of ADC multiplicity where on the y-axis 0-31 corresponds to bars 33-64L and 32-63 to bars 33-64R. These bars are the middle third of the TH detector. This plot was generated with beam-on-target data and using the BigBite calorimeter trigger and FADC readout modules.	84
4.20	Two plots for PMTs left and right attached to bar 36 showing the relative gain curves fitted to FADC amplitude most-probable-values (MPVs) extracted from landau fits to the mV distribution from each PMT. This process was completed for all TH detector PMTs and the parameters of their relative gain curve power-law fits were recorded.	85

4.21	An example plot of a corrected, not calibrated TDC distribution from after Hall A installation during the SBS-4 kinematic setting of the GMn experiment. This plot was generated with cosmic ray data using the BBCal trigger after alignment. Here the peak represents the center of the scintillator bar.	86
4.22	Two plots showing the TDC distributions for every channel plotted against their PMT number for the left and right side of the TH detector. Monitoring plots like these are used during the experiment run time for quick checks as time passes and more data runs are taken to confirm there are no missing or noisy TDC channels. These plots were generated with cosmic ray data after installation in Experimental Hall A using the BigBite calorimeter trigger before alignment.	87
4.23	An example plot of the TDC mean time leading edge distributions versus bar number using SBS-4 kinematic production data and the BBCal trigger.	88
4.24	An example plot of the TDC leading edge time difference distributions versus bar number using SBS-4 kinematic production data, an LH2 target, and the BBCal trigger.	89
4.25	An example plot of a time over threshold distribution versus ADC distribution for a single channel using cosmic ray data with the FADC readout modules and the BigBite calorimeter trigger after Hall A installation. The fit used is an exponential function.	90
4.26	An example plot of a time over threshold distribution versus TDC distribution for a single channel using cosmic ray data and the BigBite calorimeter trigger after Hall A installation.	90
4.27	An example monitoring plot of the time over threshold distributions versus PMT number using cosmic ray data and the BigBite calorimeter trigger after Hall A installation. This plot is useful during experiment run time to monitor all TDC channels and their time over threshold distributions making missing or noisy channels easy to identify.	91
4.28	A plot of TDC multiplicity for all 180 channels of the TH detector. This plot was generated with cosmic ray data and using the BigBite calorimeter trigger and FADC readout modules after Hall A installation.	92
4.29	Two plots of TDC leading edge time versus PMT number left and right after TDC alignment. This data was taken from an SBS-4 cosmic data run in Hall A using the BBCal trigger.	95
4.30	The difference in time for the leading edge of the blue versus the purple pulse is the result of the time-walk effect which causes the time over threshold (TOT) to be shorter for smaller signals and longer for larger signals. Image from [63].	95
4.31	Four plots including TDC leading edge versus TOT (top left) for PMT 42, left side. The other three plots are the mean (top right), maximum (bottom left), and sigma (bottom right) parameters taken from Gaussian fits applied to the TDC distributions for one bin segments of the TOT.	96

4.32	Four plots including TDC leading edge versus TOT (top left) for PMT 42, right side. The other three plots are the mean (top right), maximum (bottom left), and sigma (bottom right) parameters taken from Gaussian fits applied to the TDC distributions for one bin segments of the TOT.	97
4.33	Two plots of TDC time difference versus transport coordinate y-position for bars 9 (left) and 45 (right). This data was collected using a run from SBS-4 with an LH2 target and a beam of 3.5 uA. The BBcal trigger was used. Cuts correspond to cluster number, size, and width, and for ensuring only elastic electrons were applied.	99
4.34	A plot of scintillator velocity correction values from the slope of the fit to the TDC time difference versus transport coordinate y-position. These calibration values are plotted versus bar number.	100
5.1	Two plots showing before (left) and after (right) applying energy-momentum ratio cuts for both PS and SH detectors to ensure only electron tracks, thus cutting out lower energy pions.	103
5.2	Two plots (top) showing all-tracks (blue) and elastics (red) with HCal position difference cuts applied, and plots of all tracks (bottom left), and elastics (bottom right).	105
5.3	Two plots of all-tracks momentum difference distribution (blue) and elastics (red). The data shown is from SBS-4 kinematic setting runs 11547 and 11548 using an LH2 target with 3.5 uA beam. These plots were generated for all six of the SBS kinematic settings to optimize the physics cuts, so each could be specifically tailored to the data set being analyzed.	106
5.4	Several plots comparing all-tracks (blue) and elastics (red) distributions for track momentum, y-position at the target, and the angles θ_{tgt} and ϕ_{tgt} measured at the target, which were generated using the BBCal trigger and a 3.5 uA beam on an LH2 target from SBS-4 runs 11547 and 11548.	107
5.5	Two images comparing visually the showering of particles created by the interaction of a 1 GeV (top) and a 3 GeV (bottom) electron in the PS and how that shower looks when passing through the TH detector. The spread of the particle shower is much larger and creates a greater number of shower particles at 3 GeV than at 1 GeV for the incident electron. This larger particle shower at the 3 GeV setting will degrade the timing resolution of the TH detector compared to a smaller shower produced by an electron energy of 1 GeV.	109
5.6	A plot showing the position distribution in both the horizontal (y) and vertical (x) directions for fifty-thousand 1 GeV incident electrons at a very small angle, and with a cut to remove photons. This plot corresponds to the analyzed, not the Monte Carlo generated, events from the simulation.	110

5.7	Two plots of projections of the y (left) and x (right) distributions center at (0,0) in a transport coordinate system. These plots were generated using fifty-thousand 1 GeV incident electrons and are one dimensional projections of the 2D plot from Figure 5.6. These distributions are a result of multiple scattering which is Lorentzian in shape, but close to the center the distribution can be fitted with a Gaussian function if the tails on either side are excluded.	110
5.8	Two plots of horizontal position distribution 1-sigma values and combined time resolutions over a range of GeV for the incident electron particle track using fifty-thousand events. The data in black is from the stimulation only, and the other data points are from measured data collected during the running of the GMn experiment.	111
5.9	A plot of mean energy deposit for particle showers created by an incident electron over a range of GeV particle track values from 1-3.5 GeV with 0.25 incremental steps. The black data points are only simulated data, and the other data points are from real data taken during the GMn experiment.	112
5.10	A plot showing means for left PMTs (0-31), and right PMTs (32-63) for the 32 middle scintillator bars of the TH detector. The average of these means for SBS-4 is 48.88 ± 0.2 mV. The FADC data used was taken from cosmic data run 11610 at the SBS-4 kinematic setting.	114
5.11	A plot of the MeV conversion factors for each of the 64 PMTs in the middle third of the TH detector. In this plot left PMTs are represented by PMT number 0-31 and right PMTs correspond to PMT number 32-63.	115
5.12	An example plot for PMT 7, corresponding to PMT number 39L, of an FADC MeV corrected amplitude distribution. This histogram has three layers: a distribution with just the ADC cuts, and TDC multiplicity cuts (black), another distribution with added TDC window cuts (blue), and a third distribution with added time over threshold cuts (red).	116
5.13	A plot of the means for each addition of cuts to the FADC MeV corrected amplitude distributions. Plotted are means, all of which include the TDC multiplicity cut, TDC good timing, and the ADC cuts (black), added TDC window cuts (blue), and added time over threshold cuts (red). The average MeV FADC amplitude mean for SBS-4 with all cuts is 4.31 MeV.	118
5.14	A plot showing Means for left PMTs (0-31), and right PMTs (32-63) for the 32 middles scintillator bars of the TH detector. The average of these means for SBS-9 is 37.33 ± 0.2 mV. The FADC data used was taken from cosmic data run 13701 at the SBS-9 kinematic setting.	119

5.15	A plot of the means for each addition of cuts to the FADC MeV corrected amplitude distributions. Plotted are means, all of which include the TDC multiplicity cut, TDC good timing, and the ADC cuts (black), added TDC window cuts (blue), and added time over threshold (TOT) cuts (red). The average MeV FADC amplitude mean for SBS-9 with all cuts is 3.32 MeV.	120
5.16	Two plots of the FADC mV (left) and MeV corrected (right) amplitude distribution minimum thresholds for each PMT connected to ADC channels from SBS-4 cosmic run 11610. These plots provide a basis for deciding where to set the minimum ionizing energy threshold for the TH detector.	121
5.17	Two plots of the FADC mV (left) and MeV corrected (right) amplitude distribution minimum thresholds for each PMT connected to ADC channels from SBS-9 cosmic run 13701. These plots provide a basis for deciding where to set the minimum ionizing energy threshold for the TH detector.	121
5.18	A plot of average mean FADC amplitude in MeV across all 64 PMTs connected to the FADC modules for each kinematic setting and with different layers of physics cuts. . . .	122
5.19	A plot of average cluster size across all TH detector PMTs connected to the TDC v1190 readout modules for each kinematic setting and with different layers of physics cuts. . . .	123
5.20	Six plots of the average cluster size distributions for SBS-4 (top left), SBS-7 (top middle), SBS-11 (top right), SBS-14 (bottom left), SBS-8 (bottom middle), and SBS-9 (bottom right).	124
5.21	A plot of occupancy versus bar number using data from an 11 uA beam on an LD2 target from SBS-11 run 12946 with the BBCal trigger for 500K events. The black line is coincidence events between left and right PMTs for each bar within a narrowed TDC window.	125
5.22	Six plots of scintillator bar rates versus luminosity for each of the SBS kinematic settings. These plots are arranged in timeline order, going from top left to bottom right. The target type and beam current are labeled next to their corresponding data points for each run used in the rates analysis. The highest rates recorded from SBS-4 and SBS-11 come close to exceeded the recommended 2.5 MHz upper limit, while SBS-8 surpasses this value by roughly a few hundred MHz. The symbol eN represents electron neutron scattering luminosity with units of $\text{cm}^{-2}\text{s}^{-1}$	127
5.23	Two plots of the average hit rate versus kinematic setting with relatively constant luminosity at both low (left) and high (right) values within a narrow range. SBS-8 holds the highest rates for both data sets because it has the smallest BigBite angle relative to the beam-line. This shows that a significantly greater numbers of particle tracks originating from the beam-line and not the target are interacting with the TH detector at this kinematic setting, causing the rates to increase drastically.	128

5.24	A combined plot of all rates for each of the six SBS kinematic settings during the G_M^n experiment in timeline order from left to right, segmented by run group with luminosity increasing from left to right for each group of runs, which go left to right on the plot in the same order from top to bottom of Table 5.1. SBS kinematic settings 4, 11, and 8 boasted the highest rate values which pushed the TH detector right up and slightly past its limit in terms of its performance relative to the recommended range of operation. Leading and trailing data points overlap.	129
5.25	An example plot of the accidentals ratio calculation for scintillator bar 40. This same plot was generated and used for the calculation of the ratio for each of the same five data runs of the six kinematic settings used in the rates analysis. The red straight line is an average of the background hits without the peak included.	130
5.26	Six plots of scintillator bar accidental ratios versus luminosity for each of the SBS kinematic settings. These plots are arranged in timeline order, going from top left to bottom right. The target type and beam current are the same for each data point as those used in the rates analysis. The highest ratios recorded from SBS-4, SBS-7, SBS-11, and SBS-14 come close to a value of 0.4, while SBS-8 reaches slightly above a ratio value of 0.2. The symbol eN represents electron neutron scattering luminosity with units of $\text{cm}^{-2}\text{s}^{-1}$	132
5.27	Two plots of the accidental ratios versus kinematic setting with relatively constant luminosity at both low (left) and high (right) values within a narrow range. SBS-8 shows a more constant ratio value when comparing both data sets. This shows that a significantly greater amount of background originating from the beam-line and not the target is interacting with the TH detector at this kinematic setting causing the ratio to be comparatively less affected by changes in the target luminosity. The left plot is from low luminosity runs and the right is from high luminosity runs.	133
5.28	A combined plot of all accidental ratios for each of the six SBS kinematic settings during the G_M^n experiment in timeline order from left to right, separated by run group with luminosity increasing from left to right for each group of runs, which go left to right on the plot in the same order from top to bottom of Table 5.1. SBS kinematic settings 4, 7, 11, 14, and 9 show similar behavior in there upward trend such that the ratio increases with luminosity. SBS-8 shows an upward trend as well, but at a slightly lower slope caused by proximity to the beam-line.	133
5.29	Two example plots of the FADC pedestal spectra for left (left) and right (right) PMTs versus PMT number. These plots were generated from data taken during the SBS-4 kinematic setting using an LH2 target and the BBCal trigger.	134
5.30	Two plots of left PMT pedestal means and rms values versus PMT number. For the PMT numbering, 0-31 on the plots corresponds to the left PMTs that were connected to the FADC readout modules during the experiment.	135

5.31	Two plots of right PMT pedestal means and rms values versus PMT number. For the PMT numbering, 0-31 on the plots corresponds to the right PMTs that were connected to the FADC readout modules during the experiment.	136
5.32	Two plots showing the comparison of particle track locations in the TH compared to where the GEMs predict the tracks should pass. These plots were generated using LH2 data and a 3.5 uA beam from the SBS-4 kinematic setting with cuts applied for only elastic electrons.	138
5.33	An example plot of the track matching efficiency versus bar number for data taken from the SBS-4 kinematic setting using an LH2 target, 3.5 uA beam, and the BBCal trigger. The mean is calculated by excluding a couple bars on the extremes of the TH detector at the top and bottom with efficiency values and statistics that do not allow for reliable data points.	139
5.34	A plot of the mean track matching efficiency across all scintillator bars for the six kinematic settings with cuts applied for all-tracks, electrons, and elastics. This data was collected across several runs from each kinematic setting using an LH2 target and the BBCal trigger.	140
5.35	Example plots of the position difference spectra in both the x-direction and y-direction transport coordinate system focal planes versus scintillator bar number. These plots were generated with data from the SBS-4 kinematic setting with cuts applied for only elastic electrons using an LH2 target and the BBCal trigger. The same plots were generated for all six kinematic settings.	141
5.36	Two plots of the position resolution in both the vertical and horizontal versus bar number with a linear fit for the mean. This data was generated from the SBS-4 kinematic setting using only elastics data with an LH2 target and the BBCal trigger.	142
5.37	A plot of the vertical position resolution versus kinematic setting for each layer of physics cuts applied to the data using an LH2 target and BBCal trigger.	143
5.38	A plot of the horizontal position resolution versus kinematic setting for each layer of physics cuts applied to the data using an LH2 target and BBCal trigger.	143
5.39	A plot of the time resolution versus scintillator bar number using a time difference and cluster-based analysis. This plot was generated using only elastics data from the SBS-4 kinematic setting with an LH2 target and the BBCal trigger.	144
5.40	A plot of the mean time resolution versus kinematic setting for each layer of physics cuts applied to the data using an LH2 target and BBCal trigger. The cosmics data was also taken in Hall A during the GMn experiment using the BBCal trigger.	145
B.1	Schematics of the circuit diagrams for two slightly different versions of the NINO ASIC chip used for the TH detector. Diagram by J. Annand.	162
B.2	A circuit diagram of the front end from input to output for the NINO amplifier-discriminator cards of which there are 12 used for the TH detector. Diagram by J. Annand.	163

B.3	A circuit diagram of a single NINO input channel with two outputs to analogue signal and LVDS which are the ADC and TDC signals respectively. It is important for the NINO logic output TDC signal to be LVDS compatible since the readout electronics require an LVDS to ECL converter which makes the signals readable for the TH detector data acquisition system. Diagram by J. Annand.	163
F.1	Caen v1190 TDC diagrams from manual. Inputs A, B, C, and D for the v1190 (a) are labelled under their respective locations. The diagram of the input connector (b) for the v1190 shows the locations of the pin assignments. Images from [68].	182
F.2	Input Connector (Mod. A967 Cable Adapter) takes in two TDC ribbon cables (two sets of 16 channels each) and delivers their signals to the v1190s. Image from [52].	183
F.3	Front view of the CAEN v792 ADC readout module. These were replaced by the FADCs and were mostly used initially simply to confirm all ADC data coming from the PMT signals through the NINO analogue output looked as expected. Image from [69].	183
F.4	Front view of the FADC readout modules. Four FADCs were installed to replace the two v792s. Their channels are labelled 1 to 16 from bottom to top. This picture shows four FADCs together as they are in slots 14-17 of the DAQ crate. The two FADCs on the left read in 32 channels from the left side of 32 scintillator bar PMT assemblies in the TH detector, and the same corresponding scintillator bar PMT assemblies channels for the two FADCs on the right to the right side of the TH detector. Image from [70].	184

List of Tables

3.1	NINO serial numbers corresponding to the NINO card labels.	53
4.1	List of values for the measured currents and transparency of the different light guide configurations for the laser test.	67
4.2	List of six SBS kinematic settings in run-time order from top to bottom, and their corresponding kinematic values. Additional comments on added shielding and HV changes are in Table 5.1.	93
5.1	List of six SBS kinematic settings and comments on adjustments made regarding shielding added between the beam-line and BigBite magnet, and changes to the TH HV value settings.	102
5.2	FADC mean amplitudes measured in mV and their corresponding PMT number and MeV conversion factors. These values were calculated using cosmic data of more than 350K events total for all 64 PMTS connected to the FADC readout modules from run 11610 of the G_M^n experiment at the SBS-4 kinematic setting using only particle tracks that pass fully through the scintillator bars. The average error for conversion factors is ± 0.6 and ± 0.8 for the means.	113
5.3	FADC mean amplitudes measured in MeV and their corresponding PMT number. These values were calculated using cosmic data of more than 350K events from runs 11610 for SBS-4 and 13701 for SBS-9 of the G_M^n experiment. This list of MeV mean values is taken from the distributions which include all three layers of TOT, TDC window, and ADC and TDC timing cuts. The average error for the means is ± 0.1 MeV for SBS-4 and ± 0.05 MeV for SBS-9.	117
6.1	A table for all of the six SBS kinematic settings and their corresponding performance values for all-tracks data.	147
6.2	A table for all of the six SBS kinematic settings and their corresponding performance values for only electrons data.	147
6.3	A table for all of the six SBS kinematic settings and their corresponding performance values for only elastic electrons data.	147

A.1	A list of abbreviations used throughout this thesis with their corresponding definitions, and the page numbers of their first use.	159
C.1	Table of the mapping for the labelling scheme used corresponding between the front-end NINO ASIC amplifier-discriminator cards and the LV power cables to the TH detector frame at the LV distribution box.	164
C.2	Mapping of the labels for the entire TH detector HV system from the PMT bases to HV patch panels on the TH frame to the HV channel names for the HV mainframe. During the experiment run time, this mainframe is controlled remotely from outside Experimental Hall A.	165
E.1	Map for the labelling of components from the scintillator bars to the NINO card inputs.	176
E.2	Table of mapping for the labelling scheme used for the TH detector frame TDC patch panel (TH LOGIC) and ADC patch panel (TH ANALOG).	180
E.3	Table of mapping for the labelling scheme corresponding between the components going from the front-end NINO ASIC amplifier-discriminator cards on the TH detector frame to the FADC readout modules in the DAQ crate located inside the Hall A SBS electronics bunker.	180
E.4	The TDC slot labels are slightly different from the ADC as they have an additional letter. This letter corresponds with which set of pins (L-left, R-right) the Nugent cables connectors attach to on the TDC v1190 readout modules. The TDC slot number corresponds to the v1190's position in the DAQ crate, same as the FADCs.	181
G.1	List of HV value settings from the ADC charge normalization study which were used for the G_M^n Experiment. These values are from after the 50V drop across all channels which occurred before the SBS-9 kinematic setting run period.	185
H.1	List of FADC mV values for each HV setting, from 700V to 100V in one hundred volt increments, used during the study of PMT relative gain for the TH detector. The mV values listed below were generated in Hall A using cosmic ray data with the BBCal trigger. The average error across all PMTs for mV values at 700, 800, 900, and 1000 V are ± 0.3 , ± 0.5 , ± 0.7 , and ± 2.1 mV, respectively.	188
I.1	A table of calibration values for every scintillator bar in the TH detector: bar number, TDC alignment offset (TAO) in nanoseconds (ns), Time-walk slope (TWS), Time-walk intercept (TWI) in ns, TDC time difference offset (TDO) in ns, and scintillation velocity correction (SVC).	190

Contents

1	Introduction	2
1.1	Thomas Jefferson National Accelerator Facility	7
1.1.1	12 GeV Upgrade	10
1.2	Nucleon Structure and Electron Scattering Formalism	12
1.2.1	Nucleon Structure	12
1.2.2	Rutherford and the Coulomb Interaction	13
1.2.3	Electron Scattering	15
2	Super BigBite Spectrometer	19
2.1	SBS Physics Overview	19
2.1.1	Electromagnetic Form Factors	20
2.1.2	Born Approximation	22
2.1.3	Ratio Method	24
2.2	SBS Hall A Physics Program	25
2.2.1	Neutron FF Experiments	25
2.2.2	Proton FF Experiments	28
2.3	SBS Design and Detectors	29
2.3.1	Targets and Magnets	30
2.3.2	Electron Arm	32
2.3.3	Hadron Arm	37
3	TH Detector Design and Major Components	40
3.1	BigBite TH Detector Design	40
3.1.1	Scintillating Material	42
3.1.2	Photo-multiplier Tubes	45
3.1.3	NINO ASIC Amplifier-Discriminator Cards	47
3.1.4	High and Low Voltage	50
3.2	Data Acquisition	53
3.2.1	Readout Modules and Trigger	58
3.2.2	Software and Analysis Structure	60

4	TH Construction, Installation, Commissioning, and Calibration	63
4.1	SBS TH Detector Requirements	64
4.1.1	Repairs Procedure	65
4.1.2	Experimental Hall A Installation	73
4.2	TH Commissioning Studies	78
4.2.1	ADC Testing and Analysis	78
4.2.2	TDC Testing and Analysis	86
4.3	TH Calibration Studies	92
4.3.1	Timing Cuts	93
4.3.2	TDC Alignment	94
4.3.3	Time-walk Correction	95
4.3.4	Time Difference Offset	97
4.3.5	Scintillation Velocity Correction	99
5	TH Performance Studies for G_M^n Experiment	101
5.1	Definition of Physics Cuts	102
5.2	Simulation for Detector Performance	107
5.3	Energy Deposit	112
5.4	Average Cluster Size	123
5.5	Occupancy and Rates	125
5.6	Accidentals and Pile-up	130
5.7	Track Matching Efficiency	137
5.8	Position Resolution	140
5.9	Time Resolution	144
6	Conclusion	146
	Appendices	158
A	List of Abbreviations	159
B	NINO ASIC Amplifier-Discriminator Card Circuit Diagrams	162
C	High and Low Voltage Mapping Tables	164
D	List of Cables and Electronics Hardware	172
E	DAQ Mapping Tables	176
F	Readout Module Diagrams	182
G	Table of Charge Normalization HV Values	185

H	Table of Relative Gain FADC Values	188
I	Table of Calibration Values	190

Chapter 1

Introduction

One of the most important objectives in nuclear physics is furthering scientific knowledge on the structure of nucleons and the characterization of quark confinement to better understand how mass is created in the nucleus. Quantum Chromodynamics (QCD), the field theory which attempts to explain the strong force and the gluon-quark interaction, is prohibitive when trying to be solved by perturbative methods at the approximately femtometer (fm) scale characteristic of hadrons. Understanding non-perturbative QCD continues to be a crucial problem facing theoretical physics [1]. The availability of high precision electron scattering results over a wide spectrum of squared four-momentum transfer (Q^2), especially at higher momentum transfer, remains a central factor demanding advances in understanding nucleon structure. Particularly for the neutron, the higher Q^2 range is comparatively lacking in reliable results, and therefore has a vast potential to differentiate among various nucleon structure models to better understand how matter is generated. At smaller transverse distance scales, the measurement of the electromagnetic form factors, precise quantities encoding the electromagnetic distributions in nucleons, continues to play a major role in the accumulation of information pertaining to quark distributions [2]. The diagram shown in Figure 1.1 shows the spin structure from inside the nucleon. The simplified structure of the nucleon from fifty years ago is shown on the left dating from before the gluon was fully incorporated into the structural understanding of the nucleon, with the first proof for discovering the gluon surfacing in 1979 [3]. The image on the right from Figure 1.1 is a diagram of nucleon structure with gluons incorporated to show their purpose as carriers of the strong force, which glues quarks together to form nucleons. Each of these nucleons have spin and the nucleon magnetic and electrical characteristics depend on the direction and intensity of its spin, which affects the structure of the nucleon as its spin changes [4].

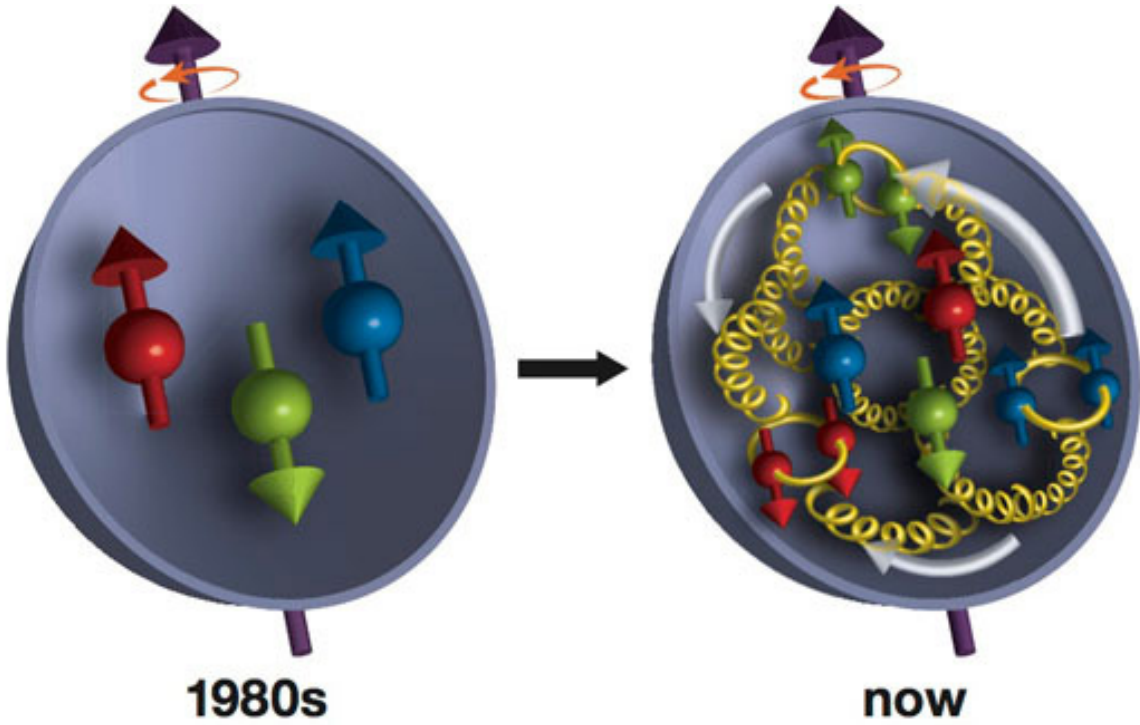


Figure 1.1: A representative picture of quarks and gluons (yellow) within the nucleon. Blue, red, and green arrows indicate the spins of the quarks, white arrows indicate orbital angular momentum of the quarks and gluons, and the grey arrow represents the spin of the nucleon. Image from [5].

For the dependence of G_E^n/G_M^n , the ratio of the Sachs electromagnetic form factors for the neutron, on Q^2 there is substantial expectation, due to the lack of data at high Q^2 , in relation to new results that drive both G_E^p/G_M^p , the ratio of the Sachs electromagnetic form factors for the proton, and G_E^n/G_M^n to larger values of Q^2 . The capacity to measure the electromagnetic form factor (EMFF) with an acceptable accuracy and breadth in the higher Q^2 domain will allow for some of the most essential and pertinent questions in hadronic physics to be answered. The high-precision measurement of G_E^n/G_M^n over a range of Q^2 , through the quasi-elastic interaction ${}^2H(e, e'n)$, using the Super BigBite Spectrometer (SBS), poses an opportunity to perform an analysis of the performance for the latest assembly of detector systems and channels for measurements at the highest Q^2 ever achieved [6]. Plots of the Sachs form factors (FF), and their ratio for the neutron, and the magnetic form factor, and electromagnetic form factor ratio of the proton from Figure 1.2 provide a set of world data points. This data provides a historical reference for the range of Q^2 used to measure the neutron and proton EMFFs and their ratios. It is clear to see that most data points from past experiments are limited to the Q^2 range below 3-4 GeV. The 21st century has seen the construction and upgrade of several accelerators and colliders for probing higher Q^2 regions [7].

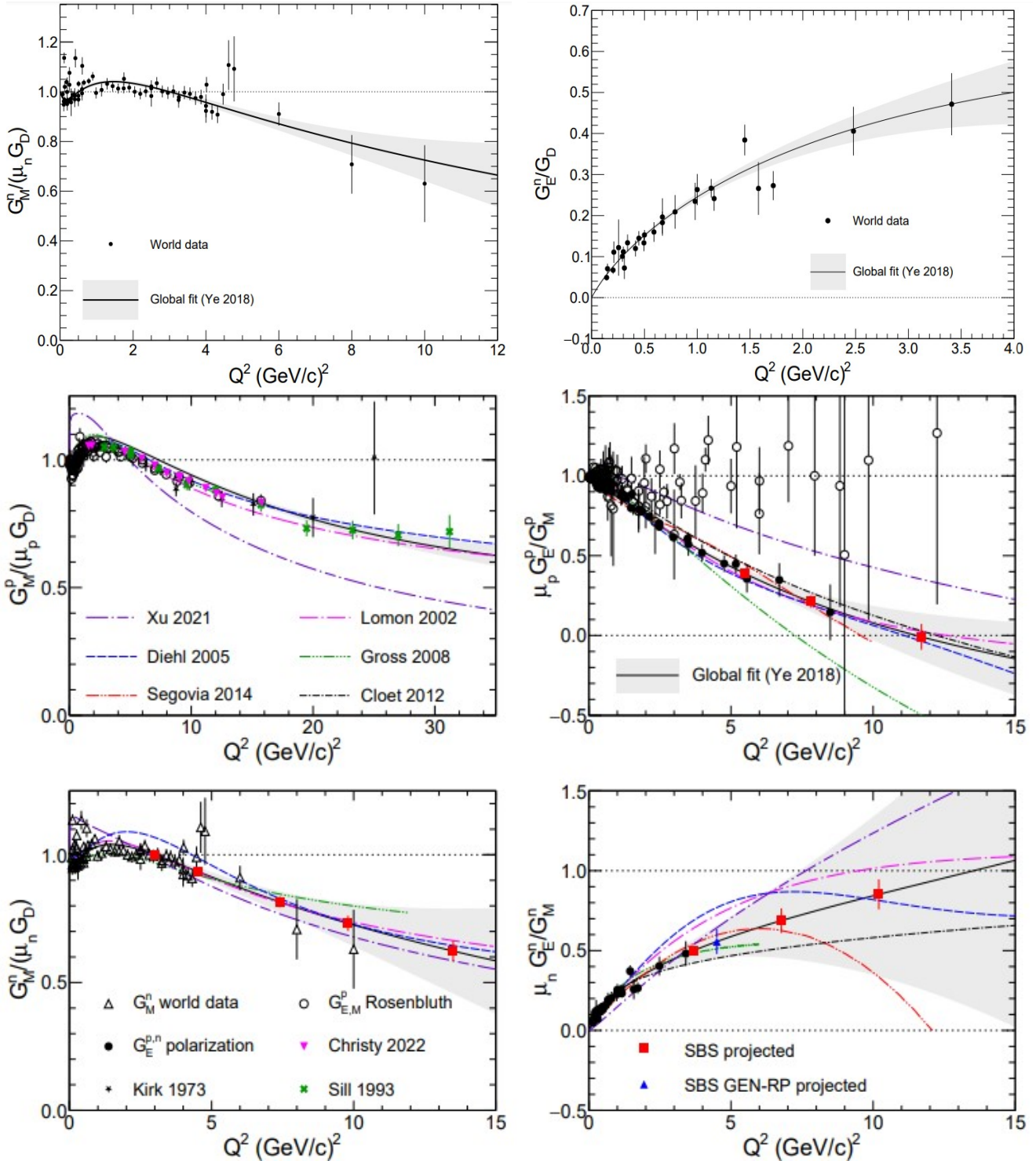


Figure 1.2: A combination of world data for both the magnetic (top and bottom left) and electric (top right) form factors of the neutron, the electromagnetic form factor ratio of the neutron (bottom right), the magnetic form factor of the proton (middle left), and the electromagnetic form factor ratio of the proton (middle right). These plots show that most data points are on the lower end of each plotted Q^2 range respectively. The trend lines and markers are consistent across all above plots. Plots from [8].

As stated, advancements in nucleon structure and quark confinement behavior are of the highest significance in nuclear physics due to the lack of data at high momentum transfer. This lack of data is because the cross sections at Q^2 are so small therefore requiring higher luminosity and detectors able to handle higher background. Because cross sections are small, the number of events decreases, causing larger uncertainties. The creation of mass inside the nucleon mostly solves one of the biggest issues challenging scientist when determining the origin of mass. Though the Higgs mechanism is often cited in reaction to that problem it is widely considered that the majority of the proton and neutron mass arises from the massless gluons and the essentially massless quarks, and their kinetic and potential energy, held within the nucleon. Neutron structure can be probed using the reaction mechanism shown in Figure 1.3 which provides a Feynman diagram of electron scattering off a neutron using the one-photon exchange process. In this case, the neutron, or target, and the incident electron, or beam, are both polarized. Again, it is widely considered that the understanding of the non-perturbative area of QCD remains one of the most important outstanding questions in theoretical physics. Those who study nuclear physics consider hydrogen structure was to atomic physics, in the 20th century, what nucleon structure is to nuclear physics, during the 21st century in terms of the possible scientific advancements that can be made [9].

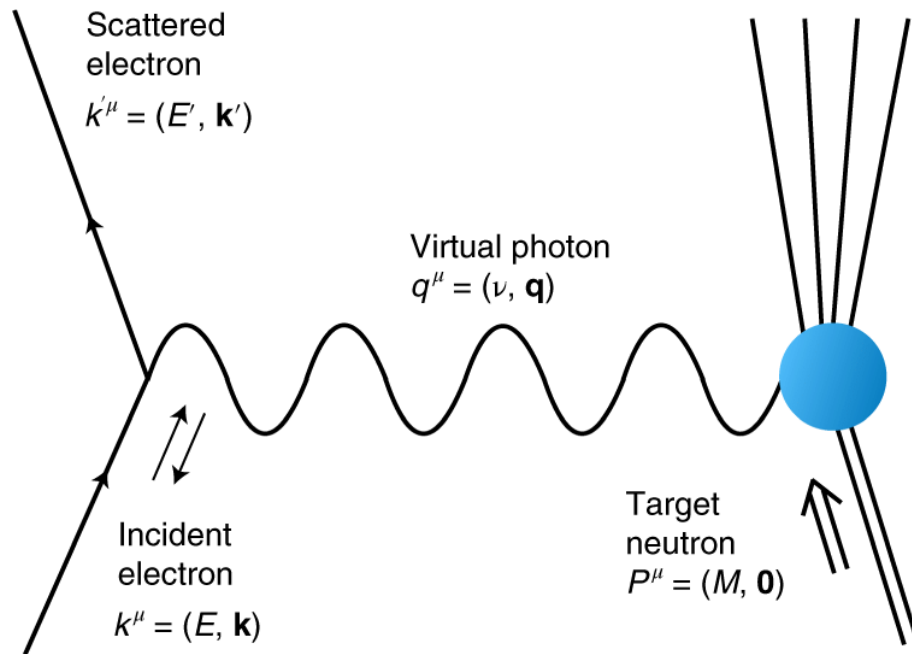


Figure 1.3: A Feynman diagram of an incident electron scattering off of a neutron using the one-photon exchange process. The generalized spin polarizabilities of the neutron can be measured when both incident electron and neutron are polarized. Here $Q^2 = -q^2$. Image from [10].

Even though a genuine answer to QCD for the non-perturbative regime continues to be obscure, substantial improvements have been completed. Modern theoretical models have aided in clarifying the pertinent degrees of freedom inside the nucleon. A few of these models come enticingly close to a method akin to an analytic approach. Perturbative QCD (pQCD), although it cannot be utilized to determine fundamental measurements such as form factors or structure functions, is able to calculate how likely these measurements change with Q^2 . Theoretical inventions like the creation of Generalized Parton Distributions (GPDs) have also permitted us to incorporate form factors and structure functions using a specific uniting framework. Additionally, lattice QCD, which might eventually deliver subjectively exact mathematical explanations to potentially any problem presented, continues to make spectacular improvement. Some of the key reasons pushing growth in knowledge of nucleon structure is the accessibility of accurate experimental findings at the highest achievable Q^2 . Several of the current theoretical methodologies to understand nucleon structure analysis is centered around GPDs and lattice computations, necessitating values and constraints provided by measurements of form-factors. Low Q^2 measurements allow for measurement of nucleon size, but at high Q^2 the structure of the nucleon is more complex in terms of scattering. Thus, complexity evolves with increased Q^2 and the validity of theory models defining nucleon structure over a range of Q^2 can be tested experimentally.

Measurements of the electric and magnetic form factors for both the proton and neutron are planned for the Super BigBite Spectrometer (SBS), which is a multipurpose spectrometer for hadron structure experiments at Jefferson Lab (JLab). Currently, the SBS measurements for G_M^n and G_E^n are almost complete. These experiments combined will deliver exact values of all four nucleon form factors, reaching unparalleled Q^2 . Together, allowing for low expected systematic errors, the Super Bigbite Spectrometer will offer exceptional precision at the highest achieved Q^2 regime with extraordinary breakthrough capability [11].

The Continuous Electron Beam Accelerator Facility (CEBAF) is housed at Jefferson Lab (Virginia, USA), which originally operated a 6 GeV electron beam. The upgrade of the CEBAF beam to 12 GeV warranted the installation of the Super BigBite Spectrometer to achieve better precision measurement capability at higher Q^2 . The challenge at higher Q^2 is that spectrometer time and position resolution worsens with an increase in GeV^2 , due to increased background rates. The SBS addresses this challenge by utilizing the latest detector technology, improving upon previous spectrometers. The Timing Hodoscope

(TH) detector is one sub-system of the SBS that will provide improved particle time-stamping compared to past form factor experiments [12]. The G_M^n experiment, or "GMn" utilized electron-nucleon scattering with polarized beams over a series of kinematic settings. For completion of the SBS physics program, accurate particle timing and position tracking over the entire planned kinematic range is important.

In order to accomplish this, the construction, installation, commissioning, calibration, and performance analysis of the Timing Hodoscope detector for the BigBite electron arm of SBS was required. The main expectation proving the usefulness of the TH detector will be its ability to provide a time stamp for scattered electrons with high timing resolution. The research covered in this thesis illustrates various comprehensive analyses which have contributed substantially to the successful operation and performance of the TH detector during the running of the G_M^n experiment.

The thesis starts with an introduction to Jefferson Lab (JLab) and an overview of the physics studied there. Next, an overview is given of SBS and its sub-detectors, their purpose and relevant SBS physics background. A summary of the TH detector follows, providing information on the major components, technologies, and design as well as TH detector construction, installation, commissioning, and calibration. The result of that work is a working TH detector, and therefore, the final chapter is devoted to the TH detector performance during the G_M^n experiment run-time. The analysis studies comprise a comprehensive overview of the TH detector commissioning, calibration, and performance across several kinematic settings including plots describing the detector performance simulation, energy deposit, average cluster sizes, rates, occupancies, efficiencies, and resolutions. This thesis, based upon the results of the detector studies, confirm the usefulness of the TH detector as a vital subsystem to the electron arm of the Super BigBite Spectrometer.

1.1 Thomas Jefferson National Accelerator Facility

The objective of the Continuous Electron Beam Accelerator Facility (CEBAF) at Jefferson Lab (JLab) is to explore nucleon structure, hadrons, and the fundamental interactions in the zone beneath the high-energy asymptotically-free regime of QCD. The abilities of existing models are constrained, like how deuteron structure is not completely known at sizes less than 1.5 fm. Mesonic degrees of freedom are established as essential in the electromagnetic interaction, however pionic degrees of freedom are lacking

from current dynamics. As well, the influence of quark degrees of freedom in nuclei continues to be a mystery. Nucleon structure is plagued with abstract obstacles when linking constituent quark models to the primary QCD Lagrangian, established as doing well at the perturbative high-energy QCD regime [13]. CEBAF's high luminosity continuous-wave electron beam is the perfect means for studying the strong QCD zone since the electromagnetic interaction is clearly known, and the electron wavelength at that energy is only a small percentage of the nucleon size. The advantages of polarized electron beams include the capacity of the lab to involve both parity-violation experiments and spin-dependent interactions probing, respectively, the weak and the spin structures within the system. CEBAF was initially intended to send electrons up to 6 GeV via passing the beam up to five times along two superconducting linear accelerators (linacs) both generating an energy gain of 600 MeV per pass. Magnets bend the beam around the curved sections of the accelerator [14]. Figure 1.4 provides a visual description of CEBAF.



Figure 1.4: An aerial view photo of the CEBAF accelerator site with red dashed lines for racetrack-shaped design, with two linear accelerator (linac) sections in the straight-line portions of the racetrack, and red circles to indicated the three experimental Halls A, B, and C where beam is delivered. Not shown is the more recently built Hall D. Image from [15].

Electrons are injected to the accelerator using a polarized gun. For the polarized gun a strained Ga-As cathode is illuminated using a gain-switched diode laser. Beam polarization is evaluated at the injector with a Mott polarimeter, and a Wien filter can orientate the polarization vector. The current delivered to the three experimental halls may be regulated individually. Both linacs house 25 cryo-modules which are positioned in a series, one after the other. The beam has the ability to be divided indiscriminately among four interspersed bunch trains that can peel off following each linac pass into either of Halls A, B, C, and D utilizing RF filters and septa [16].

The essential arrangement of Hall A before SBS installation included two main features which were two High Resolution Spectrometers (HRS), both of which offer high momentum resolution as the name implies and horizontal angular resolution less than 2 mrad. The original baseline equipment in Hall A has been applied with much success in experiments at high resolution and high luminosity. The Hall A left (LHRS) and right (RHRS) spectrometers were intended for comprehensive analysis of nucleon structure with $(e, e'p)$ scattering. Their dimensions expand the scope of internal nucleon momenta and momentum transfer examined past the hitherto investigated zone. These measures can uncover constraints to the standard nuclear structure built on nucleon interaction via meson exchange, sufficient to illustrating the low momentum-transfer region. For few-body systems precise results may be ascertained for nucleon interactions and these experiments might exhibit a full summary meson-exchange. More sensibly, the research seeks to determine that quark models can present more efficient explanation of experimental data. Spectrometers need high resolution to separate various reactions such that a clear comparison to theory may be realized. High definite precision is essential to distinguish the different forms of electromagnetic currents contributory to nuclei interactions [17].

Experiments of the electromagnetic and weak neutral current nucleon structure are likewise a key element of Hall A studies. The HRS detector systems have been employed to determine the charge and magnetic form factors for nucleons at high-level accuracy. An all-encompassing plan has been established to examine neutron spin structure utilizing a polarized ^3He target. The strange-quark impacts for the charge and magnetization nucleon distributions have been explored through exceptionally accurate parity-violating electron scattering experiments. These trials deliver rigorous analyses of nucleon structure [18]. A diagram of the JLab accelerator with major components such as the linacs, recirculation arcs, and cryo-module locations is provided in Figure 1.5.

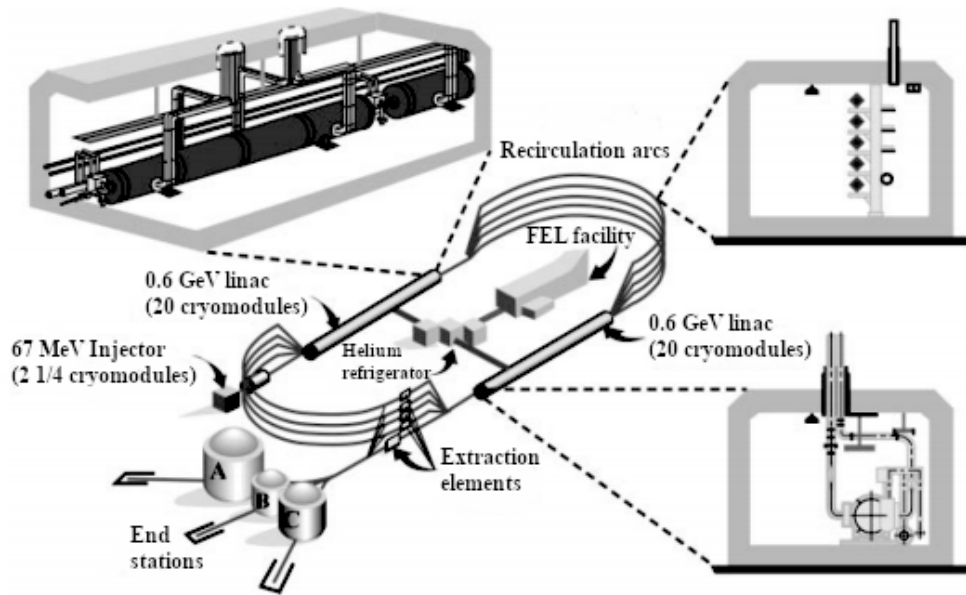


Figure 1.5: A layout diagram of CEBAF before the 12 GeV upgrade. The electron beam is generated with the injector which uses illumination on a photocathode. The beam is next accelerated in both superconducting linacs, which can recirculate the beam. The beam is then extracted to each of the experimental halls. Image from [17].

1.1.1 12 GeV Upgrade

The Jefferson Lab accelerator 12 GeV upgrade was built on the addition of 5 new cryo-modules to both linacs on each side of the racetrack-like design. Originally, the CEBAF structure allowed additional drift space towards the end of both linacs, therefore allowing space for the energy upgrade. The latest cryo-modules have 7-cell cavities (rather than the 5-cell cavities from the first CEBAF) which have enhanced surface treatments, allowing higher RF acceleration fields. Thus these cryo-modules can reach up to 100 MeV acceleration (contrasted 20 MeV in the first designs). Both linacs can now generate 1.1 GeV, and every recirculated beam gets an energy boost of 2.2 GeV. Improvements to the arc magnets and power supplies were required as well. The upgraded CEBAF is able to deliver beam to experimental halls A, B, and C at energies reaching at or in some cases above 11 GeV. In theory, beam is offered in multiples of the maximum 5-pass energy. The strength of the beams can amount to 85 μA while using beam polarization. In order to enable supply of the 12 GeV beam for Hall D, a fifth magnet arc is attached to the second recirculation arc, such that one beam may be accelerated across the north linac once more prior to delivery to experimental Hall D. Control of the extra cryo-modules required an improvement to the central helium liquifier capability [19].

The fundamental spectrometer capacity in Experimental Hall A was previously preserved with just the two HRS configurations, but other apparatuses have been built for further experiments specifically intended for improved measurement of nucleon form factors. Most notably, the Super BigBite Spectrometer assembled and located in Hall A. This is a bigger version of the effective BigBite Spectrometer influential in expanding the nucleon form factor measurements up to higher momentum transfer during the 6 GeV era. SBS utilizes the 48D48 dipole magnet with large area tracking Gas Electron Multiplier (GEM) detectors, timing scintillators, and particle identification detectors, including Cerenkov and calorimeter detectors. The solid angle acceptance is normally 50-100 msr, contingent on specifics of implementation, and the spectrometer is able to run at high luminosity [20]. In parallel, the physics program in Hall A will also consist of some high-precision parity violation experiments to deliver strict assessment for the standard electroweak model. This concludes the overview of the Jefferson Lab accelerator facility and the 12 GeV upgrade. The following sections provide a detailed summary of the formalism specific to nucleon structure and the electron scattering experiments performed at Jefferson Lab.

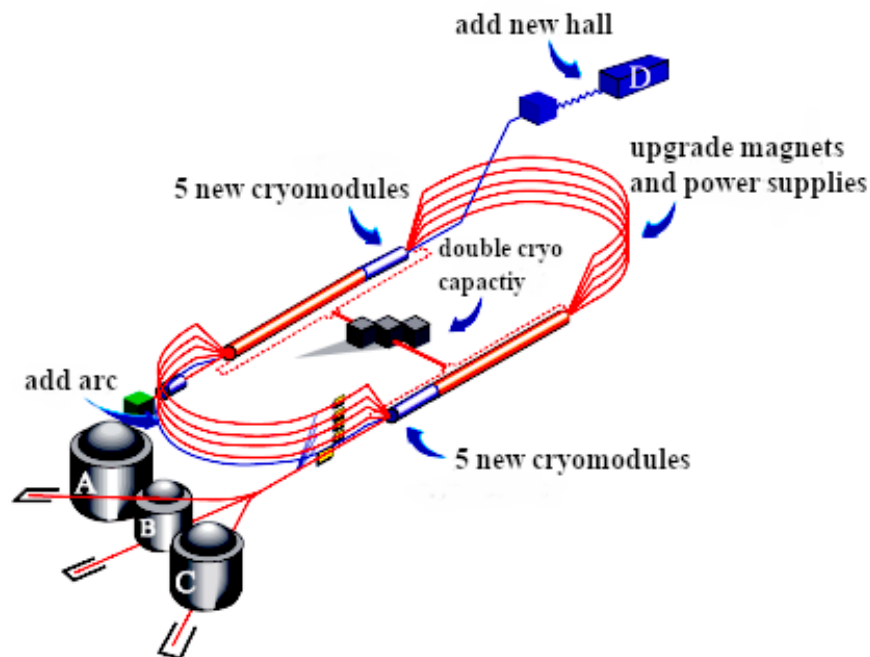


Figure 1.6: The essential diagram for the 12 GeV upgrade. With the upgrade of the accelerator system to deliver 12 GeV beam, the experimental technologies are improved to allow complete advantage to be made of the higher energy beam, including new detection systems and new Hall D. The setup for Hall A involved upgrades such as the installation of SBS. Image from [21].

1.2 Nucleon Structure and Electron Scattering Formalism

The spatial distributions of charge and magnetism in the nucleon are characterized by the electromagnetic form factors. The two form factors of a spin- $\frac{1}{2}$ object, G_E and G_M , in the basic non-relativistic portrayal, correspond to the Fourier transforms of the charge and magnetization's spatial distribution inside of the body. Since quarks are the charge carriers in the nucleon, these observables are both a probe of the underlying dynamics and directly related to the spatial distribution of quarks in the nucleon [22].

A revolution in the understanding of nucleon form factors was brought about by the development of electron beams with high luminosity and polarization, as well as novel polarized targets, recoil polarimeters, and large-acceptance detectors. The scientific text on the proton and neutron form factors has been completely revised in the last ten years as a result of experiments at Jefferson Lab. Now, physicists can isolate the contribution of strangeness in the nucleon and make cleaner, more accurate measurements of how the nuclear environment affects the internal structure of the proton and neutron thanks to the techniques that have enabled this dramatic resurgence of interest in the form factors [23].

1.2.1 Nucleon Structure

Studying the structure of the nucleon is an important component to comprehend the nature of matter because nucleons account for more than 99.9% of the mass of visible matter in the universe. The Standard Model, a very effective theory of strong and electro-weak interactions, serves as our framework. This theory's fundamental, spin- $\frac{1}{2}$ particles are six flavors of quarks and six leptons. Their fundamental properties are governed by a collection of gauge bosons, which include gluons, photons, and the W and Z bosons. Quarks are subjected to all three basic interactions. The electron, muon, and tau are sensitive to electromagnetic and weak interactions, but neutrinos are solely vulnerable to weak interactions. According to their masses, quarks are divided into two categories light quarks; up (u), down (d), and strange (s), and heavy quarks; charm (c), bottom (b), and top (t). Each quark has a one-third baryon number, and their electric charges are $+\frac{2}{3}e$ for u, c, and t quarks and $-\frac{1}{3}e$ for d, s, and b quarks. Such that e is the magnitude of the electron charge. Each quark has an antiparticle, or anti-quark, that has the same magnitude but opposite sign charge and baryon number. Furthermore, each quark has three different color charges via which it links to the gluons. Indeed, the entire foundation of the theory of strong interaction

inside the QCD standard model, is local gauge invariance under color changes [24].

The nucleon, being the lightest baryon, is the model of a system dominated by strong interactions. It has a baryon number of 1 and a spin of $\frac{1}{2}$. Early, simplistic depictions of the nucleon portrayed it as a simple system made of three quarks, with individual baryon numbers of $\frac{1}{3}$ adding up to unity and the quark spins combining to give the overall nucleon spin of $\frac{1}{2}$. One of the fundamental questions in nuclear and particle physics is how these elements organize themselves to form the nucleon. The light up and down quarks will be of key relevance in addressing nucleon structure. For example, the proton's valence quark content is two u-quarks and one d-quark (uud), but the neutron's is (udd) - as can be clearly shown by adding electric charges. Using high energy electron, muon, and neutrino beams, physicists have gained the most trustworthy knowledge about the interior structure of the nucleon. The electroweak interactions of those particle beams give a clearer probe of the nucleon's quark currents. Measurements of the proton and neutron magnetic moments revealed significant departures from the values anticipated for point-like Dirac particles, which were the first evidence of a composite structure of the nucleon. Until elastic electron scattering tests on the proton and deuteron began in the mid-1950s, the full spatial distribution of the electromagnetic current inside the nucleon was unknown. The scattering of thermal neutrons on electrons bound in closed-shell atoms provided the first signs of a non-zero charge distribution of the neutron [24]. The electromagnetic structural characteristics of the proton and neutron, sizes of their charge and current distributions, and electromagnetic polarizabilities, are currently understood with amazing precision. Elastic electron scattering and Compton scattering on the nucleon are the fundamental means for obtaining this information. Such information comes from scattering on deuterium targets or neutron-electron scattering tests for the neutron, which has a lifespan of less than 15 minutes [25].

1.2.2 Rutherford and the Coulomb Interaction

Rutherford made the nucleus discovery in 1911 by analyzing Geiger and Marsden's findings on the scattering of α -particles on an extremely thin gold foil. In this experiment the atom contains a nucleus of charge Ze , where Z is the atomic number of the atom, the nucleus can be treated as a point particle, and the nucleus is sufficiently massive compared with the mass of the incident α -particle that the nuclear recoil may be neglected. The laws of classical mechanics and electromagnetism can be applied such that

no other forces are present, and the collision is elastic. The closest approach distance, D , is determined by equating the initial kinetic energy to the Coulomb energy at closest approach for a collision between an incoming particle with kinetic energy T and electric charge ze ($z = 2$ for α -particle).

$$D = \frac{zZe^2}{4\pi\epsilon_0 T} \quad (1.1)$$

At this point the α -particle completely reverses direction, thus the scattering angle θ would be equal to π . However, the scattering angle will be less if the α -particle's line of incidence is closer to the nucleus than b , which is referred to as the impact parameter. The relation between b and θ is given by

$$\tan\left(\frac{\theta}{2}\right) = \frac{D}{2b} \quad (1.2)$$

The conservation of angular momentum, Newton's Second Law of Motion, and Coulomb's Law for the force between the α -particle and the nucleus are all used to give this relationship [26]. The quantity of incident particles arriving at the target per unit area per second is known as the flux, F , of incident particles. The number of particles, $dN(b)$, with impact parameter between b and $b + db$ is the flux multiplied by the area between two concentric circles of radius b and $b + db$. A formula can be written for the quantity of α -particles dispersed through an angle between θ and $\theta + d\theta$ after substitution by differentiating this relation.

$$dN(\theta) = F\pi \frac{D^2 \cos \frac{\theta}{2}}{4 \sin^3 \frac{\theta}{2}} d\theta \quad (1.3)$$

The number of scatterings between θ and $\theta + d\theta$ per unit flux, per unit range of angle, is known as the differential cross-section, or $d\sigma/d\theta$.

$$\frac{d\sigma}{d\theta} = \frac{dN(\theta)}{F d\theta} = \pi \frac{D^2 \cos \frac{\theta}{2}}{4 \sin^3 \frac{\theta}{2}} \quad (1.4)$$

The differential cross-section may be expressed in terms of a specific solid angle, Ω , that has a relationship to both the azimuthal angle and the scattering angle.

$$d\Omega = \sin \theta d\theta d\phi = 2 \sin\left(\frac{\theta}{2}\right) \cos\left(\frac{\theta}{2}\right) d\theta d\phi \quad (1.5)$$

The following equation describes the relationship between the number of events, the flux, the differential solid angle, $d\Omega$, and the differential cross section.

$$\frac{dN}{d\Omega} = F \frac{d\sigma}{d\Omega} \quad (1.6)$$

An integration over the azimuthal angle introduces a factor of 2π and substituting $d\theta d\phi$ for $d\Omega$ gives

$$\frac{d\sigma}{d\Omega} = \frac{D^2}{16 \sin^4 \frac{\theta}{2}} \quad (1.7)$$

Although the differential cross-section rapidly decreases with the scattering angle, it is still far larger than what previous models would have predicted.

As the scattering angle approaches closer to zero, the differential cross-section diverges, and the small scattering angle leads to a large impact parameter. The distance of the incident particle from any nucleus can increase up to a constraint of about half of the distance between the nuclei in the gold foil. The differential cross-section multiplied by the flux, multiplied by the number of nuclei in the area of the foil that is hit by the incident α -particles, is equal to the total number of particles that are scattered into a given solid angle [27] [28].

1.2.3 Electron Scattering

Electron and photon scattering on hydrogen and deuterium exposes a diverse spectrum of resonances that indicate excited states of the nucleon. There is a wealth of information available on the electric and magnetic multi-poles, as well as the form factors for transitions from the nucleon ground state to numerous such resonances. This type of information gives essential restrictions for building nucleon models. Elastic electron scattering may be used to investigate the global characteristics of charge and current distributions in nucleons. Figure 1.7 depicts the fundamental mechanism in the one-photon approximation. The one-photon approximation is excellent to around 1% accuracy because the electromagnetic interaction is regulated by the modest fine structural constant $\alpha = e^2/4\pi \approx 1/137$.

Using fundamental Quantum Electrodynamics (QED), the process illustrated includes the component electron current, the hadronic current J_{EM}^μ , and the exchanged photon with four-momentum transfer

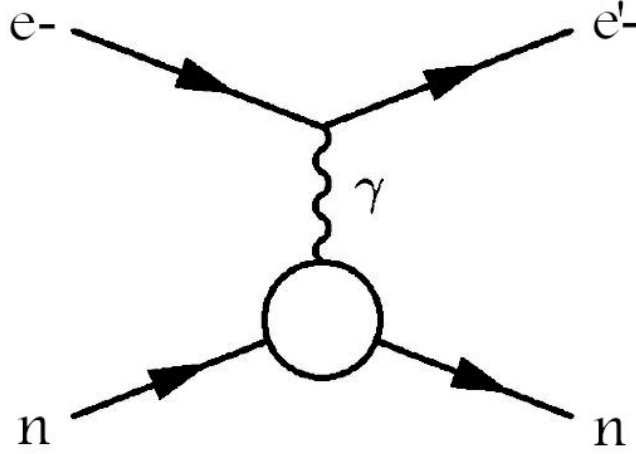


Figure 1.7: A schematic of the one-photon exchange mechanism is depicted for elastic electron-nucleon scattering showing resultant e' trajectory.

$$q = p - p' = P' - P \quad (1.8)$$

such that $p \equiv p^\mu = (\varepsilon, \vec{p})$ and $p' \equiv p'_\mu = (\varepsilon', \vec{p}')$ represent the four-momenta for the incident and scattered electron, and $P \equiv P^\mu = (\varepsilon, \vec{P})$ and $P' \equiv P'_\mu = (\varepsilon', \vec{P}')$ represent the nucleon four-momenta in the initial and final states respectively. In every case, four momentum is represented by the momentum in 3D dimensional space, \vec{p} or \vec{P} , and relativistic energy, ε .

Elastic scattering defines that the nucleon does not leave its ground state throughout the collision, meaning that the energy transfer written as:

$$v = \varepsilon - \varepsilon' = E' - E \quad (1.9)$$

and three-momentum transfer:

$$\vec{q} = \vec{p} - \vec{p}' = \vec{P}' - \vec{P} \quad (1.10)$$

are thus both taken in by the recoiling nucleon in their entirety, and the squared four-momentum transfer

$$q^2 = v^2 - \vec{q}^2 = -Q^2 < 0 \quad (1.11)$$

as a fundamental Lorentz invariant characteristic of this collision interaction [29].

Consider the elastic scattering of a relativistic electron off of a spinless, point-like particle with mass M and charge e . Let e represent the incident electron's energy within the laboratory frame and having the target at rest. In this process we ignore the electron mass in relation to its energy. The conservation of energy and momentum then requires that the scattered electron's energy, e' , be linked by a formulaic definition to its corresponding scattering angle θ in a given laboratory frame using the following equation.

$$e' = \frac{e}{1 + \frac{2e}{M} \sin^2 \frac{\theta}{2}} \quad (1.12)$$

with the squared four-momentum calculated for kinematics as:

$$Q^2 = 4ee' \sin^2 \frac{\theta}{2} \quad (1.13)$$

After that, a derivation leads to the Mott differential cross section that has the recoil component e'/e included.

$$\left(\frac{d\sigma}{d\Omega}\right)_{Mott} = \frac{\alpha^2}{4\epsilon^2} \frac{e'}{e} \cos^2 \frac{\theta}{2} \quad (1.14)$$

The elastic scattering from a point-like spin- $\frac{1}{2}$ target with a normal Dirac magnetic moment is next explored. Magnetic dispersion from the spin source introduces a new component, which increases the differential cross section at backward angles.

$$\frac{d\sigma}{d\Omega} = \left(\frac{d\sigma}{d\Omega}\right)_{Mott} \left[1 + \frac{Q^2}{4M^2} \times 2 \tan^2 \frac{\theta}{2}\right] \quad (1.15)$$

And with a spin- $\frac{1}{2}$ target using an expanded structure and the anomalous magnetic moment we get the Rosenbluth cross section:

$$\frac{d\sigma}{d\Omega} = \left(\frac{d\sigma}{d\Omega}\right)_{Mott} \left[F_1^2(Q^2) + \frac{Q^2}{4M^2} (F_2^2(Q^2) + 2(F_1(Q^2) + F_2(Q^2))^2 \tan^2 \frac{\theta}{2})\right] \quad (1.16)$$

This introduces the Pauli form factor $F_2(Q^2)$ and the Dirac form factor $F_1(Q^2)$. The former contains information on the target nucleon's anomalous magnetic moment. The Sachs form factors are sometimes more convenient:

$$G_E(Q^2) = F_1(Q^2) - \frac{Q^2}{4M^2}F_2(Q^2) \quad (1.17)$$

$$G_M(Q^2) = F_1(Q^2) + F_2(Q^2) \quad (1.18)$$

which are also named the electric G_E and magnetic G_M form factors. The Rosenbluth cross section can then be written in terms of these electromagnetic form factors:

$$\frac{d\sigma}{d\Omega} = \left(\frac{d\sigma}{d\Omega}\right)_{Mott} \left[\frac{G_E^2(Q^2) + \frac{Q^2}{4M^2}G_M^2(Q^2)}{1 + \frac{Q^2}{4M^2}} + \frac{Q^2}{2M^2}G_M^2(Q^2) \tan^2 \frac{\theta}{2} \right] \quad (1.19)$$

and this allows for the extraction of G_E and G_M by performing a Rosenbluth separation where

$$\frac{d\sigma/d\Omega}{(d\sigma/d\Omega)_{Mott}} = G_E(Q^2) + G_M(Q^2) \tan^2 \frac{\theta}{2} \quad (1.20)$$

would be plotted versus $\tan^2 \frac{\theta}{2}$ such that a straight line fit is generated.

The cross section for scattering electrons from a spin- $\frac{1}{2}$ target in the one-photon approximation can be written as

$$\frac{d\sigma}{d\Omega} = \eta \frac{\sigma_{Mott}}{1 + \tau} ((G_E)^2 + \frac{\tau}{\epsilon} (G_M)^2) \quad (1.21)$$

where η is the recoil factor, $\tau = Q^2/4M_p^2$, and ϵ is the longitudinal polarization of the virtual photon. The helicity conserving F_1 and non-conserving F_2 form factors can also be represented as simple linear combinations of the electric G_E and magnetic G_M form factors. These form factors for the proton and neutron are measured to investigate their electromagnetic structures.

Very little is understood about the magnetic form factor of the neutron at G_M^n for $Q^2 > 4 (GeV/c)^2$. Because the form factors are merely functions of Q^2 , they may be separated using the Rosenbluth approach, which involves taking cross section measurements at the same Q^2 but at various scattering angles to produce distinct linear combinations [30]. This concludes the general overview of physics performed at JLab, and the following chapter will provide an overview of the SBS in detail and the physics specific to its experimental program.

Chapter 2

Super BigBite Spectrometer

The JLab detectors in the four Experimental Halls (A, B, C, and D) offer a range of solid angles, ranging from several msr for CLAS, CLAS12, and GlueX to around 4-6 msr for focusing magnetic spectrometers like those in Halls A and C. For the large acceptance detectors, the maximum luminosity is constrained to a level of $10^{35} \text{ cm}^{-2}\text{s}^{-1}$ for CLAS12 and substantially lower for CLAS and GlueX. The Super-BigBite Spectrometer (SBS), offers a detector package capable of operating at higher luminosity, approximately $10^{39} \text{ cm}^{-2}\text{s}^{-1}$ for the GMn experiment, and yields an intermediate value of the solid angle of 70 msr [31]. The SBS magnets and detector package offer a versatile platform from which customized configurations and layouts for a variety of significant experiments can be assembled for optimal performance.

2.1 SBS Physics Overview

The magnetic form factor of a neutron is approximately as big as that of a proton and can be accurately measured. The results from single arm experiments, that are possible with pulsed accelerators, involve significant systematic uncertainties, which arise from the sub-detector systems and their ability to measure energy, position, and timing of particle tracks. Single arm (e, e') G_M^n measurements with Q^2 upwards of $10 (\text{GeV}/c)^2$ were performed with an uncertainty of 10-25% [32]. Durand offered a method for quantifying accurate G_M^n/G_M^p via detecting both the scattered electron and recoiling nucleon in coincidence and from there calculating the ratio of the cross sections for the two quasi-elastic processes, $(e, e' n)$ and $(e, e' p)$ [33]. With the advent of continuous-wave electron accelerators, this is possible. Numerous obser-

vations were made using the ratio technique, which is described in a later section, especially with recent JLab findings, reaching up to Q^2 of $4.5 (GeV/c)^2$ and using a 4 GeV electron beam [11]. Increasing to higher momentum transfer is critical, but it necessitates a larger beam energy and higher luminosity.

As the interface between theory and experiment, form factors are critical. Nucleon structure calculations may be assessed by their ability to accurately anticipate empirically available information on nucleon structure reflected in form factors. In general, polarization observables and structure functions will be important as well. In particular, lattice QCD predictions will ultimately have the power to provide significant predictions about hadronic structure. The proton and neutron form factors will provide a key to testing such predictions. Measuring the form factors of neutrons is more challenging because there is no free neutron target. Spin-asymmetry methods are utilized to extract the neutron's minute electric form factor as well as to measure the magnetic form factor, particularly at low Q^2 . However, at high Q^2 , quasi-elastic scattering from the deuteron is exploited to measure G_M^n . Because the deuteron is a loosely coupled system, high- Q^2 quasi-elastic scattering may be seen as a combination of scattering from a proton target and scattering from a neutron target.

2.1.1 Electromagnetic Form Factors

Experiments, like the physics program using SBS, that employ polarization observables, can yield more accurate results at higher momenta. Scattering of polarized electrons on hydrogen or deuterium, allows for the measurement of neutron recoil polarization. Now it would be helpful to look at the theory behind the derivation of the form factors measured using SBS. It is necessary to utilize some fundamental Dirac algebra when considering the electromagnetic current's nucleon matrix elements. Let $|N_s(P)\rangle$ represent the nucleon state such that $N = p$ references the proton, $N = n$ references the neutron, $s = \pm \frac{1}{2}$ represents the spin projection, and $P^\mu = (E, \vec{P})$ is the four-momentum. Thus the energy that a free nucleon has is $E = \sqrt{\vec{P}^2 + M^2}$, and the neutron and proton masses are $M_n = 939.57$ MeV and $M_p = 938.27$ MeV where $c = 1$. In order to satisfy the Dirac equation, written in the form

$$(\gamma_\mu P^\mu - M)u_s(P) = 0 \tag{2.1}$$

free nucleons are expressed using their spinors $u_s(P)$ in their explicit form

$$u_s(P) = \sqrt{E+M} \begin{pmatrix} \chi_s \\ \frac{\vec{\sigma} \cdot \vec{P}}{E+M} \chi_s \end{pmatrix} \quad (2.2)$$

such that $\vec{\sigma} = (\sigma_x, \sigma_y, \sigma_z)$ and the χ_s represent the fundamental Pauli spin matrices and the two-component spinors [34].

For the electromagnetic current, J_μ^{EM} , consider the matrix elements among the different nucleon states. With symmetry under space reflections and charge conservation, we get from the Lorentz invariance the most generalized form of that matrix element

$$\langle N(P') | J_{EM}^\mu(x) | N(P) \rangle = \bar{u}(P') [\gamma^\mu F_1^N(Q^2) + i\sigma^{\mu\nu} \frac{q_\nu}{2M} F_2^N(Q^2)] u(P) \quad (2.3)$$

and we can reduce using translational invariance

$$\langle N(P') | J_{EM}^\mu(x) | N(P) \rangle = e^{i(P'-P) \cdot x} \langle N(P') | J_{EM}^\mu(0) | N(P) \rangle \quad (2.4)$$

Rather than dealing with protons and neutrons directly, it is sometimes useful to consider their isospin symmetry properties using isoscalar and isovector combinations of the Pauli and Dirac proton and neutron form factors as

$$F_{1,2}^S = \frac{1}{2} [F_{1,2}^p + F_{1,2}^n] \quad (2.5)$$

$$F_{1,2}^V = \frac{1}{2} [F_{1,2}^p - F_{1,2}^n] \quad (2.6)$$

where S and V denote the use of isoscalar and isovector [35].

To obtain measurements of Dirac and Pauli form factors using elastic electron scattering with low momentum transfer we get values of the Sachs form factors G_E and G_M and use the equations from 2.5 and 2.6. Their normalization at Q^2 of zero can be provided by the nucleon charges and magnetic moments

$$G_E^p(0) = 1, \quad G_M^p = \mu_p = 2.793 \quad (2.7)$$

$$G_E^n(0) = 0, \quad G_M^n = \mu_n = -1.193 \quad (2.8)$$

such that $\mu_{p,n}$ are written in the unit of the nuclear magneton, $\mu_N = e/2M_p$. Their isoscalar and isovector combinations written as

$$G_{E,M}^S = \frac{1}{2}[G_{E,M}^p + G_{E,M}^n] \quad (2.9)$$

$$G_{E,M}^V = \frac{1}{2}[G_{E,M}^p - G_{E,M}^n] \quad (2.10)$$

will give the normalization for each

$$G_E^S(0) = G_E^V(0) = \frac{1}{2} \quad (2.11)$$

$$G_M^S(0) = \mu_S = 0.440 \quad G_M^V(0) = \mu_V = 2.353 \quad (2.12)$$

The departure of the neutron electric form factor G_E^n from zero suggests a nontrivial charge and current distribution in the neutron. Even though its whole charge vanishes, it still contains a positively charged core and a negatively charged cloud [36]. In studies of scattering using polarized electrons on hydrogen or deuterium targets for measuring recoil polarization, the precise angular dependency of the observed asymmetries allows one to map out the form factors in a way that minimizes reliance on the analysis models used. The approach used for the electromagnetic form factors during the SBS G_M and G_E experiments for the neutron and proton will be the ratio method - described in a later section.

2.1.2 Born Approximation

Consider the Lippman-Schwinger equation which defines the scattering in the form of particle waves as the following,

$$|\psi\rangle = |\phi\rangle + \frac{1}{E - H_0 + i\epsilon} V |\psi\rangle \quad (2.13)$$

such that a solution exists since the state vector $|\psi\rangle$ appears on both sides of the equation. Equation 2.13 can be written in coordinate space as

$$\psi(\vec{x}) = \frac{1}{(2\pi\hbar)^{3/2}} e^{i\vec{k}\cdot\vec{x}} - \frac{2m}{\hbar^2} \frac{e^{ikr}}{4\pi r} \int d\vec{x}' e^{-i\vec{k}'\cdot\vec{x}'} V(\vec{x}') \psi(\vec{x}') \quad (2.14)$$

at distances far away from the scattering where $r = |\vec{x}|$ and $\vec{k} = \vec{k}' \frac{x}{r}$, and this defines the wave-vector of the scattered wave. Here $|\vec{k}'| = \vec{k}$. Equation 2.14 is an integral equation for the unknown wave function, $\psi(\vec{x})$. Using perturbation theory is one way to solve Equation 2.13 by using a power expansion series in V , in the absence of the potential, $|\psi\rangle = |\phi\rangle$, or more accurately, $|\psi\rangle = |\phi\rangle + O(V)$. Thus the lowest first order approximation can be written as

$$|\psi\rangle = |\phi\rangle + \frac{1}{E - H_0 + i\epsilon} V |\phi\rangle + O(V^2) \quad (2.15)$$

If we neglect the $O(V^2)$, then the result is the first Born approximation [37]. This approximation is only useful in cases when the scattering is weak. Again, ψ can be replaced by ϕ in coordinate space using Equation 2.14 to get

$$\psi(\vec{x}) = \frac{1}{(2\pi\hbar)^{3/2}} [e^{i\vec{k}\cdot\vec{x}} - \frac{2m}{\hbar^2} \frac{e^{ikr}}{4\pi r} \int d\vec{x}' e^{-i\vec{q}\cdot\vec{x}'} V(\vec{x}')] \quad (2.16)$$

where $\vec{q} = \vec{k} - \vec{k}'$ is the momentum transfer that occurs in the scattering interaction. Equation 2.15 shows that the scattering amplitude is the Fourier transform of the potential such that

$$f(\vec{k}, \vec{k}') = -\frac{1}{4\pi} \frac{2m}{\hbar^2} \int d\vec{x}' e^{-i\vec{q}\cdot\vec{x}'} V(\vec{x}') \quad (2.17)$$

up to a factor of $(1/4\pi)(2m/\hbar^2)$. The result is valid for the first order solution in V . This expression also upholds the uncertainty principle such that in order to probe the structure of an object at small-scale values, it is necessary for the experiment to have a high momentum transfer, otherwise the Fourier transfer will average out the small-scale structure.

If the potential is central such that $V(\vec{x})$ is only a function of r which equals $|\vec{x}|$, then Equation 2.17 can be simplified to

$$f(\vec{k}, \vec{k}') = -\frac{2m}{\hbar^2} \frac{1}{q} \int_0^\infty dr r V(r) \sin(qr) \quad (2.18)$$

and the scattering angle depends only on $q = |\vec{q}| = |\vec{k} - \vec{k}'| = 2k \sin(\theta/2)$. Therefore, the equation is only a function of the polar angle θ such that $f(\vec{k}, \vec{k}') = f(\theta)$ [38]. The first order Born approximation is analogous to the one-photon exchange mechanism used for elastic electron scattering as shown in Figure 1.7, and it is the lowest order approximation for this interaction.

2.1.3 Ratio Method

The "ratio method" is based on the detection of both recoil protons and recoil neutrons. Even a simple nucleon-coincidence condition significantly reduces inelastic background. If particle detection, particularly neutron detection, is well understood, this approach is vulnerable to the fewest systematic errors because it benefits from significant cancelling of numerous types of systematic error that affect other techniques such as "proton-subtraction" or "proton-tagging."

The "ratio method" necessitates the measurement of both neutron-tagged, $d(e,e'n)$, and proton-tagged, $d(e,e'p)$, quasi-elastic deuteron scattering. Because several experimental errors, including target thickness, beam intensity, dead-time, electron trigger efficiency, electron acceptance, and the detection and reconstruction efficiency for the scattered electron track, cancel in creating the ratio,

$$R'' = \frac{\frac{d\sigma}{d\Omega} |_{d(e,e'n)}}{\frac{d\sigma}{d\Omega} |_{d(e,e'p)}} \quad (2.19)$$

and simultaneous measurements of both reactions give a significant decrease in systematic error. This is unaltered by factors such as target thickness, beam intensity, dead-time, electron trigger efficiency, electron acceptance, and the detection and reconstruction efficiency of the scattered electron track. With a modest and precisely calculated adjustment, ϵ_{nu} , this observed ratio of quasi-elastic cross sections may be utilized to calculate the ratio of elastic cross sections:

$$R' = \frac{\frac{d\sigma}{d\Omega} |_{n(e,e')}}{\frac{d\sigma}{d\Omega} |_{p(e,e')}} = \frac{R''}{1 + \epsilon_{nuc}} \quad (2.20)$$

The ratio of interest may be calculated by writing R' in terms of neutron form factors.

$$R' = \frac{\eta \frac{\sigma_{Mott}}{1+\tau} ((G_E^n)^2 + \frac{\tau}{\varepsilon} (G_M^n)^2)}{\frac{d\sigma}{d\Omega}|_{p(e,e')}} \quad (2.21)$$

$$R = R' - \frac{\eta \frac{\sigma_{Mott}}{1+\tau} (G_E^n)^2}{\frac{d\sigma}{d\Omega}|_{p(e,e')}} = \frac{\eta \sigma_{Mott} \frac{\tau/\varepsilon}{1+\tau} (G_M^n)^2}{\frac{d\sigma}{d\Omega}|_{p(e,e')}} \quad (2.22)$$

Given just the proton's elastic cross section at the relevant kinematics, this value of R allows G_M^n to be calculated [39] [40]. This concludes the overview of the physics background specific to the SBS experimental program. The following sections describe the relevant experiments of the SBS Hall A physics program.

2.2 SBS Hall A Physics Program

The SBS Hall A physics program includes five experiments of the ground-state electromagnetic form factors: GMn (E12-09-019) [11] and nTPE (E12-29-010) [41], which ran in parallel, GEn (E12-09-016) [2] and GEn-Recoil (PR12-17-004) [6], and GEp-Recoil (E12-07-109) [13]. These five experiments, together with a very precise measurement of GMp using the Hall A HRS Spectrometers, which are not part of the SBS Program, will collectively provide precise determinations of all four nucleon form factors with unprecedented reach in Q^2 . The figures-of-merit (FoM) of these measurements represent a significant improvement over all past nucleon EMFF measurement efforts. At the time of writing this thesis, the GMn, nTPE, and GEn experiments have completed data taking, and analysis of those experiments is working toward completion. The GEn-Recoil and GEp-Recoil experiments, which both require the SBS hadron arm polarimeter to be installed, have not yet taken data.

2.2.1 Neutron FF Experiments

The GEn experiment makes a measurement of the electric form factor GEn at high four-momentum transfer values of $Q^2 = 4.4, 6.6, \text{ and } 8.8 \text{ GeV}^2$ in double polarized semi-exclusive $^3\text{He}(e,e'n)$ scattering with quasi-elastic kinematics by measuring the transverse asymmetry, A , of the cross section. This quantity can then be used to extract the electric form factor using precise high Q^2 GMn data. The previous measurement of GEn at JLab provided data up to Q^2 of 3.5 GeV^2 [2]. Therefore at its highest

setting the new GEn experiment more than doubles the previously covered Q^2 range. Data for GEn at high Q^2 is necessary, in particular, to constrain spin-flip Generalized Parton Distributions (GPDs) at high momentum transfer. The experiment utilizes the polarized ^3He target and the polarized JLab beam at high beam energies. The electrons are detected in the SBS electron arm spectrometer with a new GEM based tracker and the neutrons in HCal. Because of the high kinetic energy of the neutrons, a high neutron detection efficiency with an excellent background suppression is needed. Separation of recoiling protons and neutrons is performed magnetically. This measurement significantly increases knowledge about a fundamental property of the neutron in a region where no data is available [2]. The detector setup for GEn and GEn-Recoil is the same except for addition of the polarimeter. In GEn-Recoil, electrons elastically scatter off neutrons in a liquid deuterium (LD2) target. Electrons are detected by the SBS electron arm while neutrons and their polarization are detected by the SBS hadron arm. Two polarimetry techniques are employed: charge-exchange $np \rightarrow pn$ and conventional $np \rightarrow np$ scattering. This is the first proof of principle validation for charge-exchange polarimetry against the conventional approach through direct comparison [1]. Plots of world data for EM neutron form factors are in Figure 2.1.

The GMn experiment made measurements up to a Q^2 of 13.5 GeV^2 . Its data will determine GMn by a detailed comparison of the un-polarized elastic cross sections of the two processes $d(e,e'p)n$ and $d(e,e'n)p$ by the ratio method described. It used essentially the same setup as GEn, with the exception that the target was the liquid deuterium and liquid hydrogen cryo-target. Like the other SBS form factor measurements, the GMn measurement in Hall A will provide excellent accuracy and reach in Q^2 , well beyond all competing efforts. The excellent statistical power of the Hall A GMn experiment is derived from many of the same factors that make the other SBS experiments so powerful: very high luminosity, an open-geometry spectrometer that is close to the target, and very good position resolution that permits strong suppression of accidental coincidences and inelastic events [11]. The nTPE experiment, which ran concurrently with and had the same setup as GMn, made a high precision measurement of the two-photon exchange contribution (TPE) in elastic electron-neutron scattering at a four-momentum transfer up to $Q^2 = 4.5 \text{ GeV}^2$. While significant efforts to study the two-photon-exchange have focused around elastic electron-proton scattering, the impact of TPE on neutron form factors was never examined experimentally. The nTPE experiment provides the very first assessment of the two-photon exchange in electron-neutron scattering, which will be important for understanding nucleon form factor physics [41].

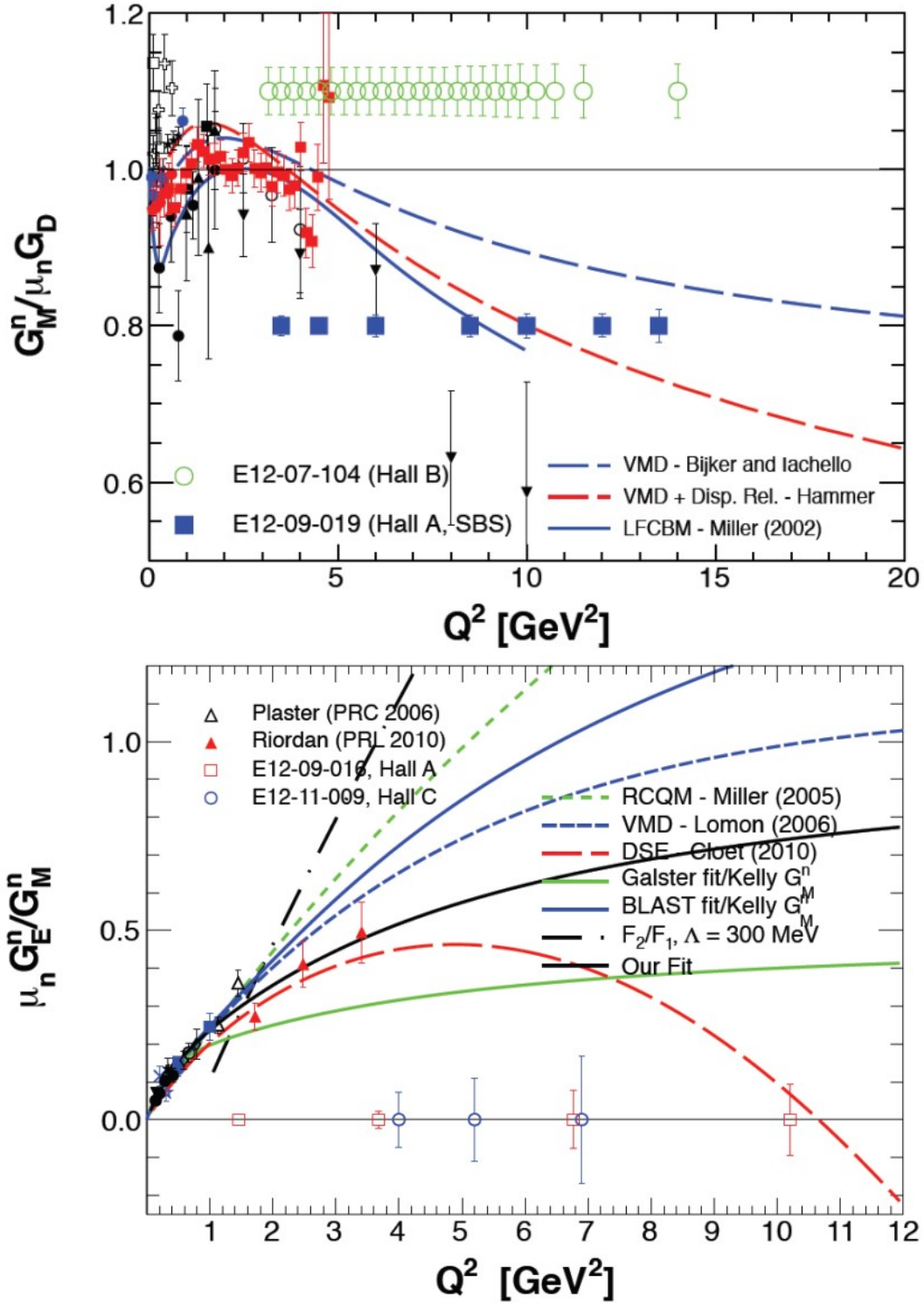


Figure 2.1: Two plots for world data on the neutron magnetic form factor G_M^n (top) and the neutron electromagnetic form factor ratio (bottom) with projected SBS statistical precision for the SBS G_M^n and G_E^n experiments. Trend lines and data marker are specific to each plot separately. Data markers for Hall A and C data are placeholders because these values have not yet been calculated, and are currently in the post-experiment analysis stage. Plots by A. Puckett [8].

2.2.2 Proton FF Experiments

The measurements of GEp at large Q^2 can be essentially improved in the recoil polarization experiments when a longitudinally polarized beam of electrons is scattered by unpolarized protons. For the one photon exchange mechanism, in the $e + p \rightarrow e + p$ reaction, the scattering of the polarized electrons results in a transfer of polarization to the recoil proton. From the polarized cross section it follows that the FF ratio can be extracted from the ratio of the measured polarizations. Practically, such a method has several advantages. First, only a single measurement is required for given Q^2 if both components can be measured at the same time. This allows to reduce the systematic errors associated with angle and beam energy change. Second, ambiguities related with the normalization of the absolute cross section also cancel in the ratio. Such experiments have been carried out at different values of Q^2 in JLab. Their results, for the first time, showed a clear deviation of the proton FF ratio from Rosenbluth measured values, starting from $Q^2 > 1 \text{ GeV}^2$ with much smaller statistical and systematic errors compared to previous similar measurements [12] [13].

The GEp-Recoil is the only proton form factor experiment in the SBS Hall A physics program and it will measure the electric form factor of the proton using the polarization-transfer method and the reaction $p(e,e'p)$. The polarization of the recoil proton will be measured using a single polarimeter instrumented with GEM trackers and a highly-segmented hadron calorimeter. The electron will be detected in coincidence by a large existing electromagnetic calorimeter. The target will be the standard Hall A liquid hydrogen (LH2) cryo-target. For GEp-Recoil, measurements will be made at three values of Q^2 : 5, 10, and 14.5 GeV^2 , thus nearly doubling the maximum value of past Q^2 achieved for previous GEp experiments. The measurement of the ground-state electromagnetic form factors becomes quite challenging at high momentum transfer because the effective rate drops as roughly E_{beam}^2/Q^{16} . The polarization-transfer method also requires very large statistics because of the relatively low analyzing power, approximately <0.1 , of the recoil polarimeter. The GEp experiment meets these challenges through a fairly innovative approach. The spectrometer in the proton arm is based on a large open-geometry dipole magnet that is placed quite close to the target, and at a fairly small angle; a configuration that provides a large solid angle at kinematics that have favorable statistics. The spectrometer will also be equipped with a recoil polarimeter that provides improved efficiency. There are several features of the GEp-Recoil experimental design that are favorable from the perspective of controlling systematic errors. The implementation

of the polarization-transfer method used involves measuring the ratio of the transverse and longitudinal proton polarizations. This eliminates the systematic errors coming from the beam polarization and the polarimeter analyzing power. Another source of systematic uncertainty is coincidences due to inelastic events. Here, the tight angular and momentum correlations between the elastic electron and the recoiling proton allows for a high degree of rejection [13].

2.3 SBS Design and Detectors

The ratio approach for extraction of GMn is dependent on the detection of both scattered neutrons and protons. In calculating the acceptance and detection efficiency of these particles, several sources of systematic error emerge. Nucleon acceptance errors can be decreased by matching neutron and proton acceptances so that they cancel in the ratio, just as the electron acceptance and efficiency. In Hall A, the momentum and angle of the scattered electrons is measured by the SBS electron arm, while the scattered neutrons and protons are detected by the SBS hadron arm. Nucleons scattered in the direction of the hadron arm detectors are deflected vertically relative to neutrons by the field of a large aperture dipole magnet positioned along the nucleon flight path.

The limitation of the solid angle for a spectrometer is a result of the difficulty of designing a high momentum magnetic spectrometer for operation at a small scattering angle. The High Resolution Spectrometer (HRS), for instance, in Hall A has a minimum angle of 12.5° and a solid angle of 6 msr. By using the septum magnet, a solid angle of 4 msr was achieved with a substantially smaller central angle of 6° . The main motivation behind the SBS is based on recent developments in tracking detector technology, namely Gas Electron Multiplier (GEM) chambers, which enable the use of tracking detectors at luminosities of $10^{39} \text{ cm}^{-2}\text{s}^{-1}$ in close proximity to the target at a relatively short distance of a few meters. This new tracker has an excellent spatial resolution of $70 \mu\text{m}$ in addition to its high rate capabilities [42].

Planning to use a magnet with a relatively small field integral at a few Tesla-meters that will produce a large solid angle is made possible by the improved spatial resolution in conjunction with the moderate momentum resolution of 1% necessary for several of the SBS experiments. A magnet is employed at small angles relative to the incident beam with a cut created in the mid-plane of the yoke to obtain the smallest possible angles. An iron dominated magnet can readily deliver a 2-3 Tesla-meter field integral

with a horizontal field direction. Figure 2.2 provides a whole schematic layout of SBS without the neutron polarimeter (NPol) and coordinate detector (CDet) because these detectors were not installed in Hall A for the G_M^n and G_E^n experiments.

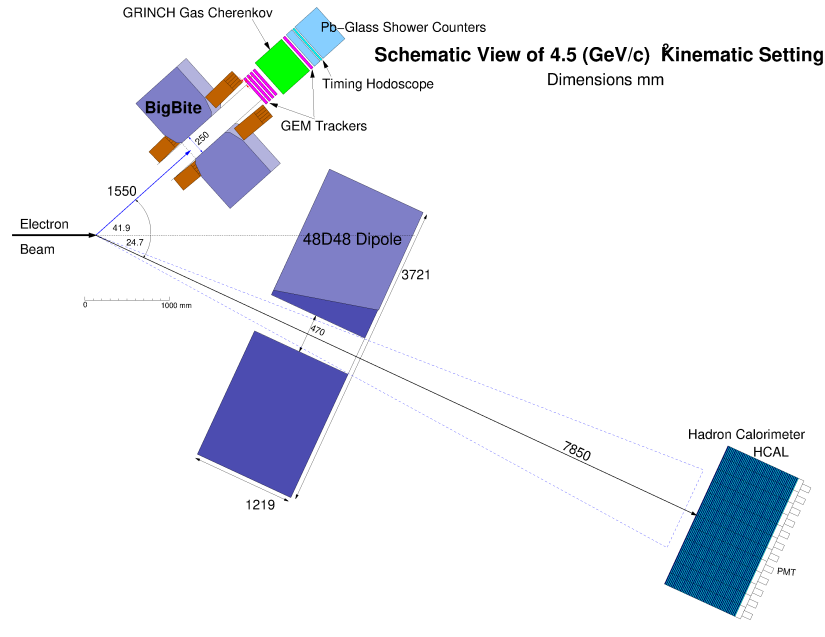


Figure 2.2: A layout diagram of SBS hadron (below electron beam) and electron (above electron beam) arms, including detectors: Timing Hodoscope (light blue), Pre-shower and Shower (light blue), GRINCH (green), GEMs (pink), Magnets (light purple), and Hadron Calorimeter (dark blue). The kinematic setting of SBS varies throughout the experiment run time. Image from [13].

2.3.1 Targets and Magnets

The targets for GMn and nTPE, which ran in parallel to GMn, were 10 cm long liquid deuterium (LD2) or liquid hydrogen (LH2) cells with 100 μm aluminum windows. This yielded around 1.7 g/cm^2 of target compared to approximately 0.054 g/cm^2 in the windows [31]. The target for the GMn and nTPE experiments contained several cells for target, beam-line, and optics calibrations, but the two target cells of most concern with data taking were the ones with liquid hydrogen and liquid deuterium. These are the two cells from which production data was collected. Production data is commonly used to refer to data taken while the beam is on and the target position is at one of the two aforementioned cells. The target cells can be rotated in or out of the beam line using a remote operation control system, external to Hall A, that keeps the target at 15° K. When the electron beam is not being delivered there is an empty target cell used during down time, and target cells are only rotated when no beam is being delivered to the target.

An enhanced polarized ^3He target was crucial for GEN, and GEN-Recoil uses an LD2 target. Novel target-cell design using convection for quick mixing between the target portion in the beam and target portion in which the ^3He nuclei are polarized means the new target withstands beam currents $>80 \mu\text{A}$. To fully benefit from these advancements in polarized ^3He technology, the convection design was essential. A liquid hydrogen target, 40 cm long, will be used in GEp-Recoil. The scattering chamber, with 100-cm diameter, accommodates such a target. A projected value of 800W is the expected beam heat load [42]. LH2 is used for proton scattering as it is the simplest proton target, and LD2 is used for neutron scattering as it is the simplest neutron target. ^3He is used for polarized experiments because it is easier to polarize.

The 20 ton dipole magnet labeled as BigBite in Figure 2.2 has a pole gap at 155 cm from the target center so the minimal central scattering angle that BigBite can achieve, which is constrained by the position of the exit beam line, is approximately 30° . The maximal integrated field is equal to 1.2 Tm. For GeV electrons the bend angle is comparatively small, estimated by the following.

$$\theta_e \simeq \frac{0.3 \int B \cdot dl}{p_e} \quad (2.23)$$

In Equation 2.23 the field integral, represented by the symbols $\int B \cdot dl$, is measured in Tm and the electron momentum, p_e , is measured in GeV/c [18].

The hadron arm dipole magnet, 48D48, is a warm coil magnet with an excitation current of 4 kA and a field integral of 3 Tm. By rotating the magnet 90 degrees, the magnetic field is directed in the horizontal plane, producing a vertical bend. With a deep incision in the iron yoke, the magnet is installed at tiny angles. Only a slight distortion of the magnetic flux flow in the yoke and the field distribution in the magnet gap is caused by the cut, which is parallel to field lines in the gap. The magnet consists of five iron slabs and weighs 100 tons total. The 48D48 magnet is used for neutron FF experiments to deflect high energy protons for clear identification of quasi-elastic electron-neutron events. The needed value of the field integral in the GEN and GEN-Recoil experiments is 1.7 Tm, but for GMn and nTPE it is 0.8 Tm. Two iron inserts are put inside the magnet for GEp-Recoil, which only needs a portion of the magnet aperture. Inserts minimize the vertical size of the pole gap at the entry, distance between poles, and acceptance. The field on the beam line is unchanged by the modification, but the field integral rises, and the spin rotation angle is closer to the ideal value of 90° [42].

2.3.2 Electron Arm

The electron arm of SBS is a non-focusing magnetic spectrometer with a high acceptance, approximately 70 msr, and it is used for the detection of electrons in the form factor experiments. It is constructed for high momentum measurements, with the dipole's entry aperture 1.55 m from the target and widely spread coordinate-measuring detector planes. The spectrometer is outfitted with GEM detector planes to accommodate the experiment's high luminosity. These detectors are accessible for use as BigBite tracking detectors and for later use in the polarimeter of the SBS hadron arm. The GEM detectors are built in a modular format that allows them to be customized to both the electron and hadron arms. Because of the higher resolution and low multiple-scattering guaranteed by the comparatively thin GEM detectors, the predicted momentum resolution is $\sigma_p/p = 1\%$. In both horizontal and vertical angles, the angular resolution is projected to be less than 1 mrad. The electron arm is a single-arm trigger, reducing the neutron and proton bias and assuring the trigger efficiency cancels for the ratio, R. The BigBite electromagnetic calorimeter (BBCal) made of lead-glass is utilized for the experiment's trigger [39]. This allows for a reasonable single-arm trigger rate of less than 5 kHz. The Timing Hodoscope (TH) which is a sub-detector of the electron arm is described extensively in Chapter 3. Descriptions of other electron arm detectors important to this thesis are in the following sections.

Gas Electron Multipliers (GEMs)

The Gas Electron Multiplier (GEM) technique, developed by Sauli in 1997, offers an affordable option for large-area monitoring in a high-rate setting. The GEM is built upon the multiplication of gas avalanches within tiny holes etched on a Kapton foil with a thin coating of copper on both sides. Because of the avalanche's confinement to the hole, signals appear relatively quickly, with a 10–20 ns rise time [43]. For high gain and operational stability, many GEM foils, which act as amplification stages, can be cascaded. Secondary avalanches are less likely to form in cascaded GEM chambers because of the GEM foils' comparatively low transparency [43]. All of these characteristics lead to extremely high rate capabilities of up to 100 MHz per cm² and superb position resolution which is a function of the instantaneous rate. Because the GEM trackers provide a higher counting rate ability, there is an increased experimental luminosity which can be reached [42].

Front GEM trackers use triple-foil GEM modules which are $40 \times 50 \text{ cm}^2$ in size, assembled in groups of three, providing a coverage of $40 \times 150 \text{ cm}^2$ for each tracking plane. The 2D readout strips are tilted at 0.4 mm giving a coordinate resolution of 0.070 mm . Readout of these strips measure the strip charge at a sampling rate of 40 MHz , 25 ns per sample, such that the start time can be determined within $\sim 5 \text{ ns}$ accuracy [13]. The back GEM tracker is comparable with the front end GEMs, but for the back these modules are $60 \times 50 \text{ cm}^2$ in coverage such that the single plane is assembled from 4 modules providing a coverage of $60 \times 200 \text{ cm}^2$. The tilt of these readout strips is exactly as the front GEMs [13].

Three amplification steps are present in a chamber section assembly. A drift foil, three GEM foils, and a readout board are included, and all components are arranged on top of a layer of honeycomb material. The Permaglass TE630 frames with a width of 8 mm hold the foils with active areas of $40 \times 50 \text{ cm}^2$ [42]. For sturdiness and optimum foil spacing, spacers are placed inside the frame. The spacers are placed at the GEM boundaries, with a width of less than 0.5 mm . They make a small contribution to the chamber's inactive area. In contrast to the read-out of the final two chambers, which is ordered along U and V directions (45° and -45° to the dispersive direction), the first two chambers are read out along X and Y (0° and 90° to the dispersive direction). Strips with a $400 \mu\text{m}$ pitch are chemically etched on a PC board for the readout boards. The widths of the strips in the two directions are selected such that the X and Y (or U and V) strips share the charge equally [42]. Diagrams of the GEMs are in Figure 2.3.

The cathode foil on one side and the anode read-out board serve as a barrier for the gas of a chamber section. The GEM chamber parts of one chamber are installed between two robust aluminum frames [44]. Some dead zones between sections are acceptable. However, to achieve optimal effectiveness, these regions are reduced as much as possible by putting the GEM foils on thin polyglass frames. In order to prevent obstacles from blocking the GEM chamber active regions, the front-end electronics are positioned perpendicular to the chamber plane behind frames, which places them well out of the way. Estimates place the overall dead area at less than 5% of the whole active plane [44]. The GEMs provide crucial particle tracking data used in the performance analysis of the TH detector, especially when analyzing the TH detector's tracking efficiency, which is calculated relative to the GEMs. The position of the particle tracks in electron arm detectors can be projected from the GEM data. This allows for a predicted hit position in the TH detector to be projected and compared to the measured location of a particle track by the TH. This comparison provides a means for calculating a tracking efficiency for the TH detector.

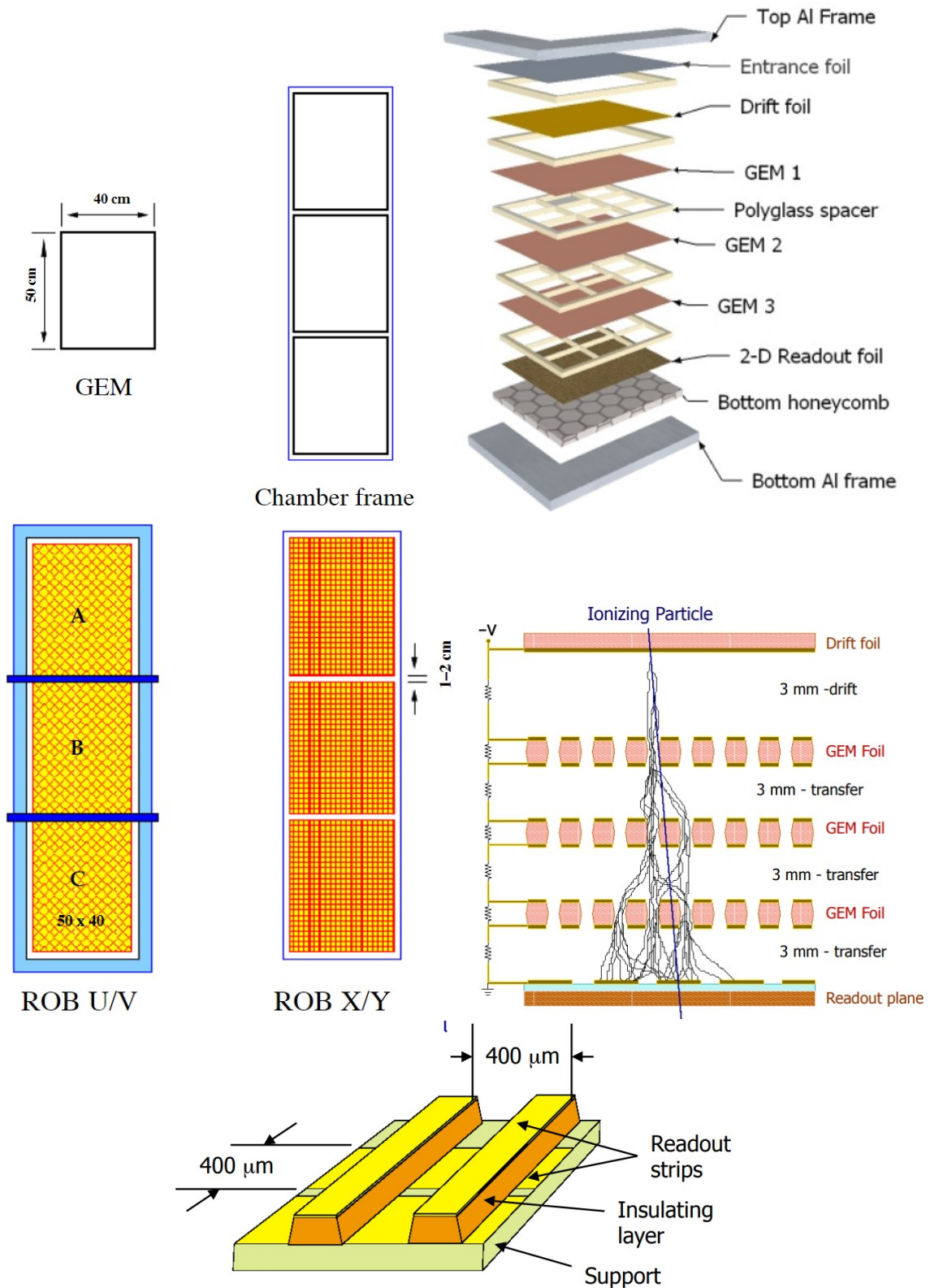


Figure 2.3: Several diagrams of the GEMs with a single GEM (top left) dimensions, a GEM chamber layer frame of three GEMs, stack of single GEM chamber components (top right), GEM layers with readout boards (ROB) using the U/V and X/Y strips design (bottom left), particle cascade in the three-layer GEM foils filled with gas (bottom right), and readout board layout (bottom). Diagrams from [42].

Pb Glass Calorimeter (BBCal)

The electron arm includes lead glass pre-shower (PS) and shower (SH) detectors with long axes perpendicular and parallel, respectively, to the electron trajectory and the correlation of their signal amplitude gives an extra method for differentiating electrons from other particles. The form factor experiments use BBCal, a lead-glass electromagnetic calorimeter, for a number of reasons that are unique to these experiments [20]. To identify the elastic reaction events during the run-time of production data taking, and reduce the physical inelastic background, the data taken from BBCal is coupled with the reconstructed proton parameters, so that elastic events can be singled-out in the analysis. Mapping diagrams of the PS and SH calorimeter block arrays, not to scale, are in Figure 2.4.

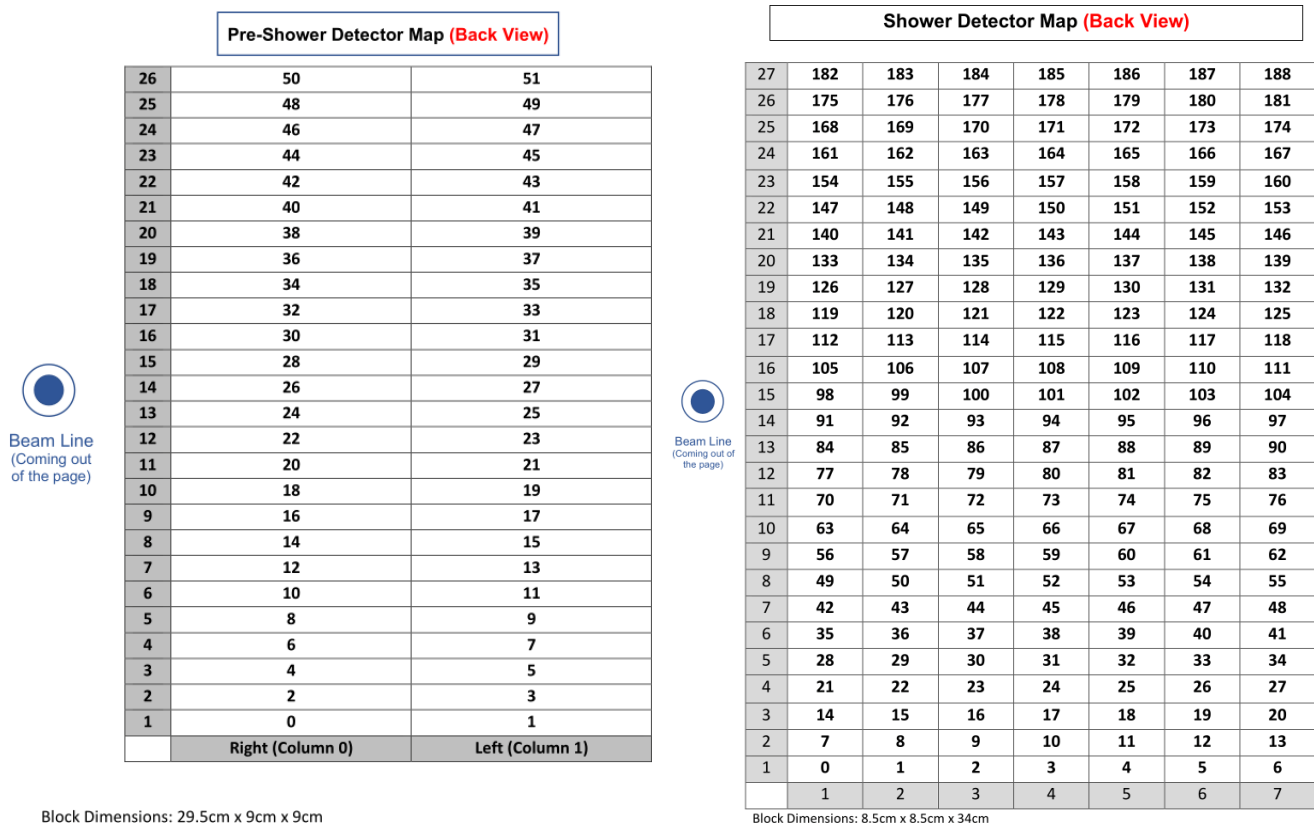


Figure 2.4: Calorimeter block arrays with numbering and Pb glass block positions for the PS (left) and SH (right) detectors which comprise BBCal showing the direction of the incident scattered electron coming out of the page. Therefore, this perspective is from the back of the two BBCal detectors relative to the target. Diagrams by P. Datta.

BBCal is built of two different sized TF1 lead glass blocks. The shower's 189 lead glass modules, each measuring $8.5 \times 8.5 \text{ cm}^2$, and 37 cm in length, are arranged in 27 rows and 7 columns. The pre-

shower is made of $52.9 \times 9 \text{ cm}^2$, in an array of 26 rows and 2 columns, 37 cm in length, lead glass modules that are arranged transversely to the spectrometer's center. In order to meet the requirements of the SBS form factor experiments, the following upgrades were made to BBCal: building of a permanent UV light box in front of the lead glass, replacing the 4" Al absorber with an 8" Al absorber, and using a new power supply system of 58 LeCroy HV cards in 4 LeCroy HV crates [42]. The diagram in Figure 2.5 provides a layout for the electron arm. The GRINCH detector was not used for analysis results in this thesis therefore it is not described here, but more information can be found in [6]. BBCal provides energy, and momentum data crucial for defining physics cuts which are used in the performance analysis of the Timing Hodoscope. These physics cuts help differentiate among different types of particle tracks, like electrons and pions, which can be characterized by their energy-momentum ratio. Cuts can be applied to separate electrons from elastic electrons using data from the HCal. This detector is described in the following section for the SBS hadron arm.

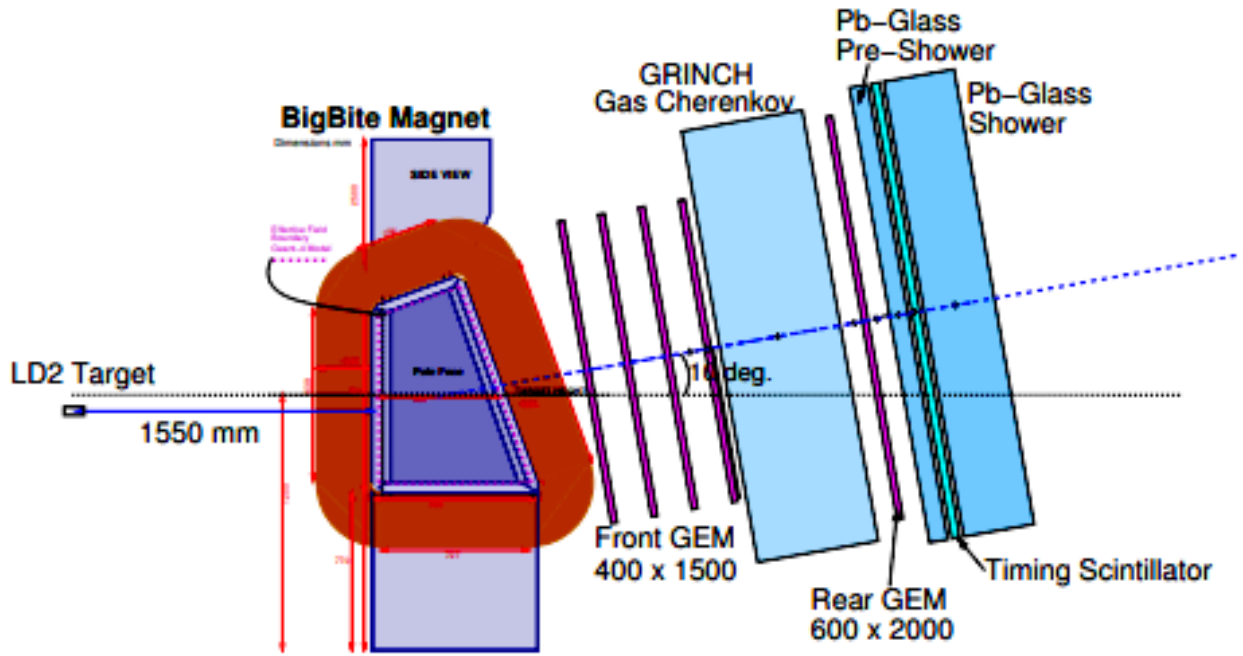


Figure 2.5: A layout diagram of the BigBite electron arm showing the component detector subsystems, including the BigBite magnet, GRINCH, GEM layers, TH detector, and the BigBite calorimeter comprised of the shower and pre-shower. The LD2 target chamber in the diagram can be interchanged with the LH2 target chamber. The dashed black line shows the scattered electron trajectory with the BigBite magnet off while the dashed blue line shows the scattered electron trajectory with the BigBite magnet turned on. Diagram from [2].

2.3.3 Hadron Arm

The hadron arm is comprised of the 48D48 dipole magnet, and the HCal detector. The subdivided hadron calorimeter (HCal) is optimized to track and measure nucleons with momenta within 1.5 - 10 GeV/c at high efficiency. The EMFF experiments deal with approximately 10 picobarn (pb) cross sections, hence the luminosity should be as high as feasible for significant scientific results. The high energy of the recoil nucleon is fully exploited in the trigger and detector arrangement for high luminosity conditions. Depending on the measurement, the energy of the nucleon in the EMFF experiments ranges from 2 to roughly 10 GeV. The substantial proton energy in GEp-Recoil makes it possible to utilize a 3–4 GeV energy threshold in HCal without suffering a major decrease in detection performance. HCal has a strong position resolution useful for data interpretation [13]. The polarimeter and Coordinate Detector (CDet) excluded in Figure 2.2 were not used for data taking in either the GMn, nTPE, or GEn experiments, all of which have completed their experiment run-time schedules. The data presented in this thesis focuses on the performance of the Timing Hodoscope, and only uses data taken during the GMn experiment. Therefore, the following section only covers the HCal detector and its purpose.

Hadron Calorimeter (HCal)

The modular architecture of the SBS HCal detector comprises 242 blocks grouped in an 11 x 22 matrix. Forty iron and scintillator plates are interspersed between layers to form a single module. The iron and scintillator plates have thicknesses of 5 mm and 20 mm, respectively. The plates' cross-sectional area is $142 \times 146 \text{ mm}^2$. A wave shifter is used to gather the scintillator's light. The wave length shifting light guide has a 1200 mm length, a 1050 mm active length, and a 3 mm thickness. A calorimeter module has a total length of 1450 mm, an active length of 1000 mm, and a 150 kg weight. The iron plates, wavelength-shifting light guide, and scintillator are contained in a rectangular container with a cover, both made of steel sheets measuring 1.4 mm thickness. High light yield and consistent light collecting over the scintillator surface are the primary criteria for the scintillating plates. Given that the scintillator will be subjected to radiation of high intensity, a strong radiation resistance is also essential for its long-term experimental operation [42]. A single calorimeter block is shown in Figure 2.6.

The linearity of the HCal as a function of particle energy, momentum ratio, and its energy and spatial

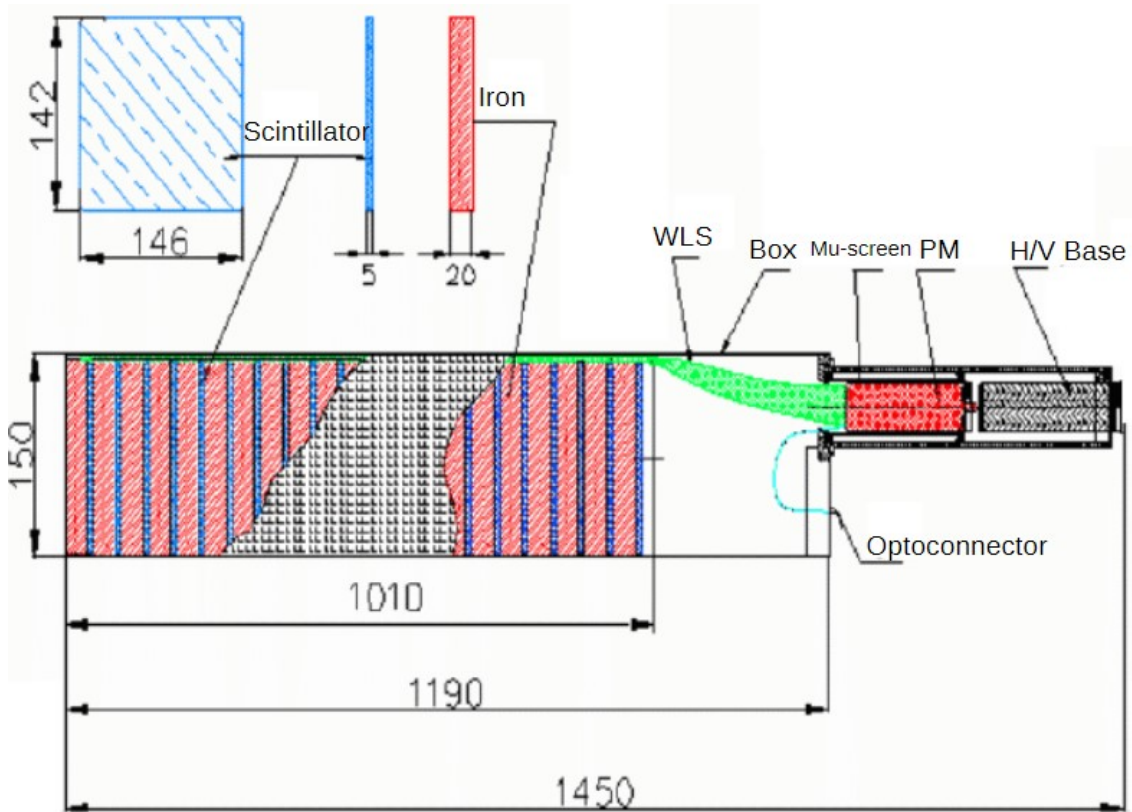


Figure 2.6: A diagram of a single HCal block, with all measurements in mm, pointing left toward the target. These blocks are arrayed in an 11 x 22 matrix to make HCal. Diagram from [42].

resolutions, are its key features. The HCal has a 5.5 m^2 total active area. The kinematical concentrating of quasi-elastic nucleons at the high momentum transfer of the form factor experiments will ensure that HCal is useful enough despite the larger distance from the target to the detector. The hadron calorimeter features a high granularity of $15 \times 15 \text{ cm}^2$, a time resolution of 1.5 ns, a coordinate resolution of 2 cm, as well as a high energy threshold. The HCal is an effective neutron detector for the neutron FF experiments thanks to all these important characteristics. For the HCal detector, the energy threshold in the timing channel may be set significantly higher at 1 GeV, which is better than an entirely scintillator-based neutron detector. This allows for a two orders of magnitude decrease in background rate. With HCal positioned at the end of the SBS hadron arm detector package, it will be used to trigger the DAQ, in coincidence with the signals from the BBCal used as the electron detector to register the elastic electron. The sensitivity of HCal between protons and neutrons is comparable and measurement of the efficiencies is dependent on the applied energy thresholds. The peaked pulse-height, from the energy passed into the scintillator sheets, allows thresholds at high settings so low energy background from the experimental trigger is filtered out [45]. The HCal provides crucial position data for defining physics cuts which isolate elastic

electron particle tracks, and these cuts are used in the performance analysis of the TH detector. Images for the SBS electron and hadron arms are in Figure 2.7. Figure 2.8 provides a side view of the SBS hadron arm with no polarimeter or coordinate detector, as the setup was for the first three SBS experiments.

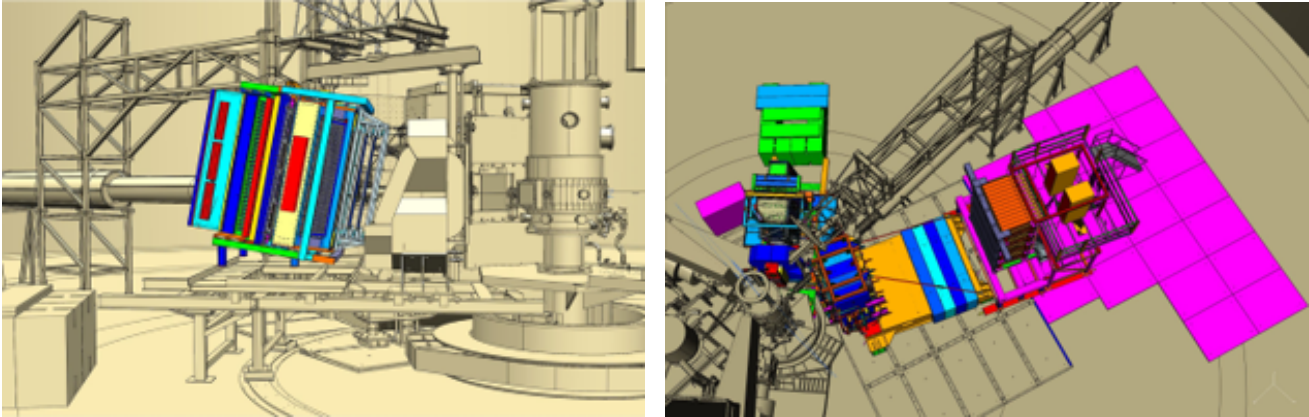


Figure 2.7: Two diagrams of the SBS electron (left) and hadron (right) arms with target and detector frames installed in Hall A. These images include both SBS arms with the electron arm left of the beam-line and the hadron arm to the right, showing the setup for the GMn, nTPE, and GEn experiments, which exclude the SBS hadron arm polarimeter and coordinate detector. Images courtesy of the SBS Collaboration at JLab.

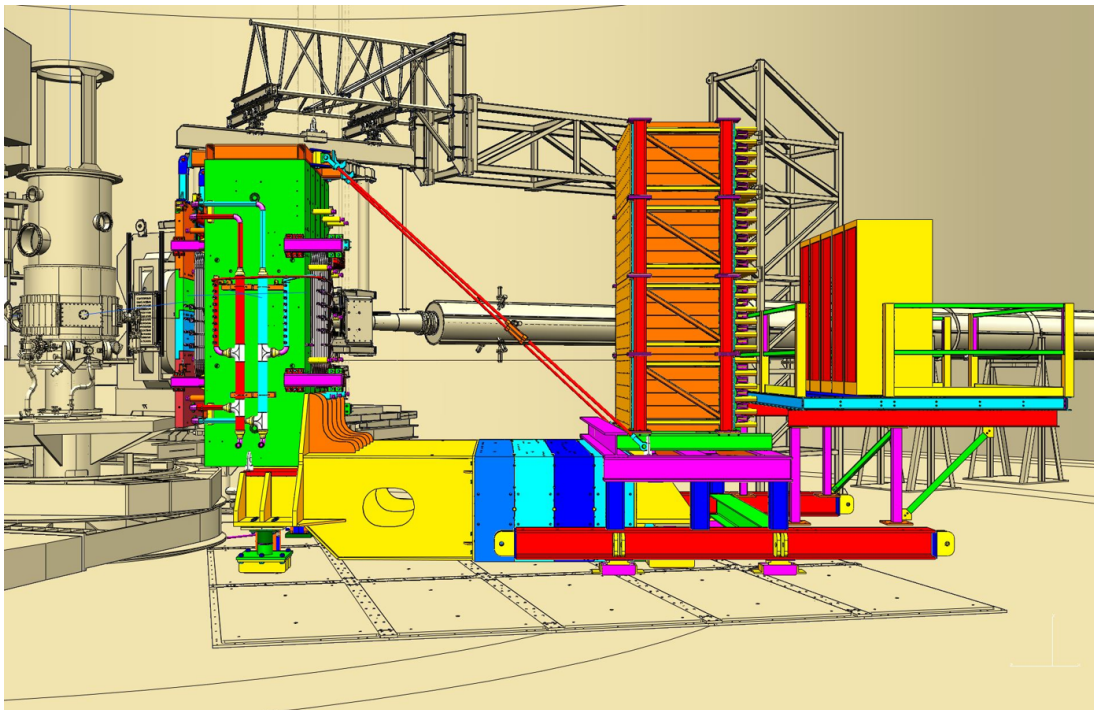


Figure 2.8: An image showing just the SBS hadron arm, excluding the polarimeter and coordinate detector. The HCal is represented by the stack of orange colored blocks. The 48D48 dipole magnet is shown in green, positioned close to the target. Image courtesy of the SBS Collaboration at JLab.

Chapter 3

TH Detector Design and Major Components

The TH detector principal role is to give high precision time stamping of scattered electrons, and this proves especially useful for two arm ($e, e'N$) measurements taken during the G_M^n experiment. The e' hit time in the TH may be utilized to calculate nucleon time of flight in the SBS electron arm. The TH will also offer pulse height information, which proves useful in distinguishing minimum-ionizing particles from low energy background, as well as hit location information. This proved useful in resolving tracking ambiguities in the high-rate GEM systems [2].

3.1 BigBite TH Detector Design

The BigBite TH detector is a vertical stack of 90 plastic scintillator bars placed between the pre-shower and shower lead glass arrays. The mean time from the two photo-multiplier tubes (PMTs) attached to each end of a $25 \times 25 \times 600$ mm³ bar is used to calculate position independent timing for each bar. The horizontal hit position is determined by the time difference between the two left and right side logic signals. The TH encompasses the whole coordinate range of the lead glass arrays. Its job is to give an accurate timing reference for minimum-ionizing particles over the whole range of particle momenta studied by the BigBite detector package. It is designed to be capable of high-rate operation without placing any substantial limitations on the luminosity that the BigBite spectrometer can tolerate during the scheduled SBS electromagnetic form factor measurement experiments.

Attached to each end of the 90 TH scintillator bars are 180 light guides which alternate in shape

between curved and straight to account for spacing between the PMTs and their shielding. The light guides are attached to the scintillator bars via ultraviolet light treated optical glue, and on the opposite side, the light guides are positioned flush against the faces of their respective PMTs using the PMT housing and a series of screws to hold each PMT assembly in place such that there is no space between the PMT face and its corresponding light guide. The scintillator bars are stacked one on top of the other such that the only space between them is <0.1 mm caused by the light-tight wrapping used on the scintillator bars to prevent external light from seeping into the detector. A series of metal supports and plastic ties hold the entire detector scintillator bar plane flush against the BigBite detector package frame such that there is no discrepancy in the angle of the focal plane of the TH detector relative to the other detector subsystems, nor the polarized target. A stand-alone diagram of the fully assembled TH detector without the surrounding frame is provided in Figure 3.1 for reference. The perspective in Figure 3.1 is from the target on the side closest to the beam line, which is the right side of the TH detector. TH detector requirements are provided in Chapter 4.

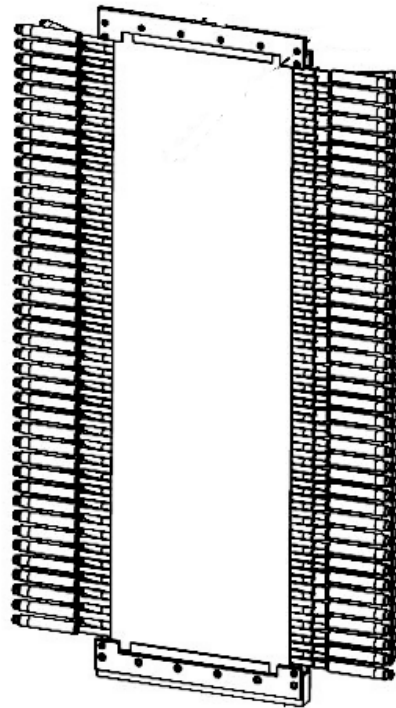


Figure 3.1: A 3D diagram of the TH detector showing central plane made of stacked scintillator bars, which are attached to light guides and PMTs. The PMTs are inside individual housing assemblies, which are made light-tight. In the BigBite frame, the TH detector is installed between the PS and SH detectors of the BBCal. Diagram courtesy of the SBS Collaboration.

The PMTs are connected to custom-made bases, and each PMT high voltage may be modified independently. The signals from each PMT are extracted and routed to specialized amplifier-discriminator front-end cards. The signals from the front-end cards are then read out to VME-based CAEN multi-hit TDCs, which are connected to the NINO cards. This allows the hit times to be extracted, as well as providing some raw pulse height information that can be reconstructed using the NINO card time-over-threshold capability; for example, the vertical bar number and the time difference between the two signals extracted from the PMTs at either end of the bar can be used to calculate the raw position of an electron hit on the TH detector. Each component of the TH detector from the scintillating material, to the PMTs, and the readout electronics work together to provide a system by which the TH can be tested, calibrated, and analysed for use in the high momentum electromagnetic form factor experiments. The following sections provide some background information on the major hardware components of the TH detector.

3.1.1 Scintillating Material

When activated by ionizing radiation, a scintillator displays scintillation, which is emitted fluorescent light from the material. Once impacted by an incoming particle, luminescent materials absorb the energy and re-emit it in the form of light. When a scintillator is connected to an electronic light sensor, such as a photo-multiplier tube, a scintillation detector is formed. Using the photoelectric effect, PMTs absorb light produced by the scintillator and re-emit it in the form of electrons [46].

Some of the many desirable qualities of scintillators, depending on their application, could include high or low density, quick operation speed, low cost, radiation hardness, production capability, light output efficiency, and operational parameter durability. Temperature affects the light output and scintillation decay time of most scintillators, but at room temperature, this dependency for the TH scintillators is disregarded because it is minimal. The density of the Eljen EJ-200 scintillator bars used for the TH detector is lower density, near that of water, at 1.023 g/cm^3 [47]. A high operating speed is required for optimal time and position spectra resolution. Time measurement precision using a scintillation detector is proportional to $\sqrt{\tau_{scint}}$, where τ_{scint} is the decay time. Short decay duration is critical for measuring time intervals and operating in quick coincidence circuits. In physics, short reaction time allows for detection of unique particle interaction events in the material [48]. The scintillators used in the TH have a decay time of 2.1 ns and rise time of 0.9 ns [47]. Figure 3.2 is a plot of the scintillator emission spectrum.

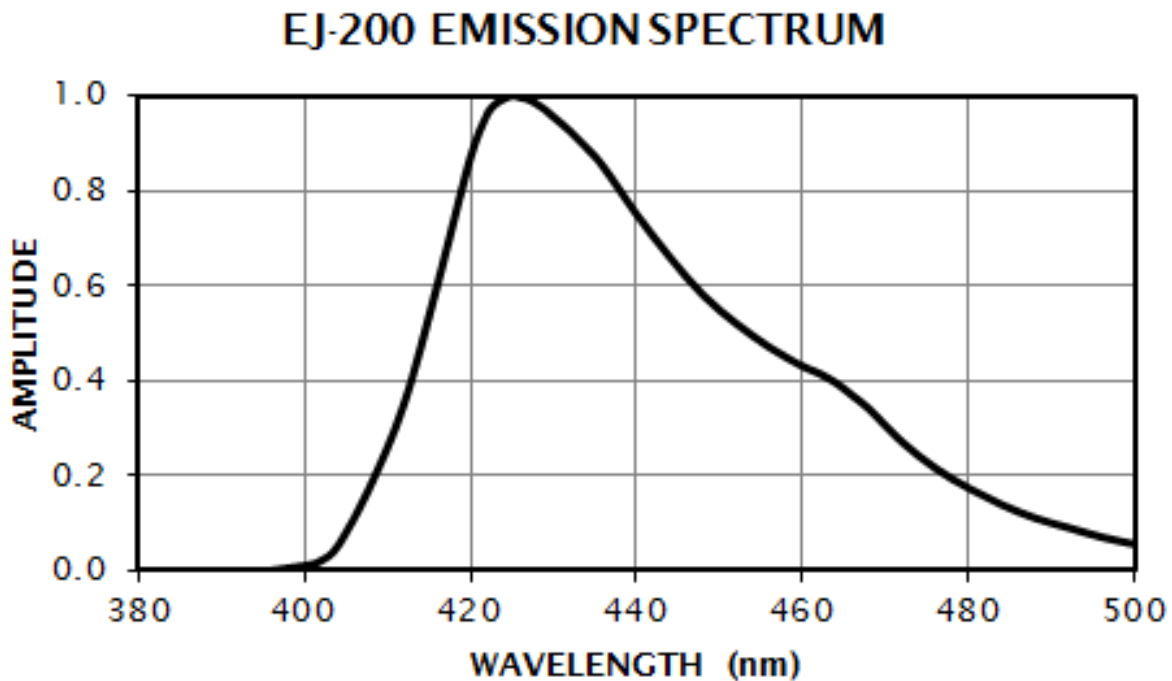


Figure 3.2: A plot of the Eljen EJ-200 scintillator bar emission spectrum with measured wavelength versus amplitude. This plot shows the peak wavelength occurring at 425 nm. Plot from [47].

A high efficiency for converting the energy of incident radiation into scintillation photons, transparency to its own scintillation light for good light collection, efficient particle detection, linearity over a wide range of energy, a short rise time for fast timing applications such as coincidence measurements, and a short decay time to reduce detector dead-time are all desirable properties in a good detector scintillator. The light output is the most crucial of the above-mentioned parameters since it impacts both the detector's efficiency and resolution. The efficiency is the ratio of detected particles to the total number of particles entering the detector, and the energy resolution is the proportion of the full width at half maximum of a specific energy peak to the peak position. Because light output is a direct consequence of the type of incident particle and its energy, the type of scintillation material employed for a certain application is heavily influenced by the particles being detected [48].

The term "plastic scintillator" typically refers to a scintillating material in which the primary fluorescent emitter is suspended in the base, a solid polymer matrix. Plastic scintillators have a relatively low light output and a fairly fast signal, but arguably their most significant benefit is their capacity to be fashioned into any desired shape with a high degree of resilience using molds [48]. Anthracene is the colorless crystalline aromatic hydrocarbon used in the TH scintillator bars giving them a light output of

64%. Their scintillation efficiency is ten thousand photons per 1 MeV, they have a wavelength of maximum emission peaking at 425 nm, and their pulse width at full width half maximum is 2.5 ns [47]. A plot of scintillation versus particle energy for different incident particle types is provided in Figure 3.3. The most interesting set of data points from Figure 3.3 is the data corresponding to the electrons since the TH detector is used in the electron arm of the SBS. For the kinematic settings in the GMn experiment, the energy of the scattered incident electron ranges from 1.5-3.5 GeV and the energy deposit spectra of the elastic electrons peaks in the range of 8-13 MeV. This range of energy deposit corresponds to an average scintillation value of approximately 10^5 photons produced per elastic electron track particle interaction event in the scintillating material.

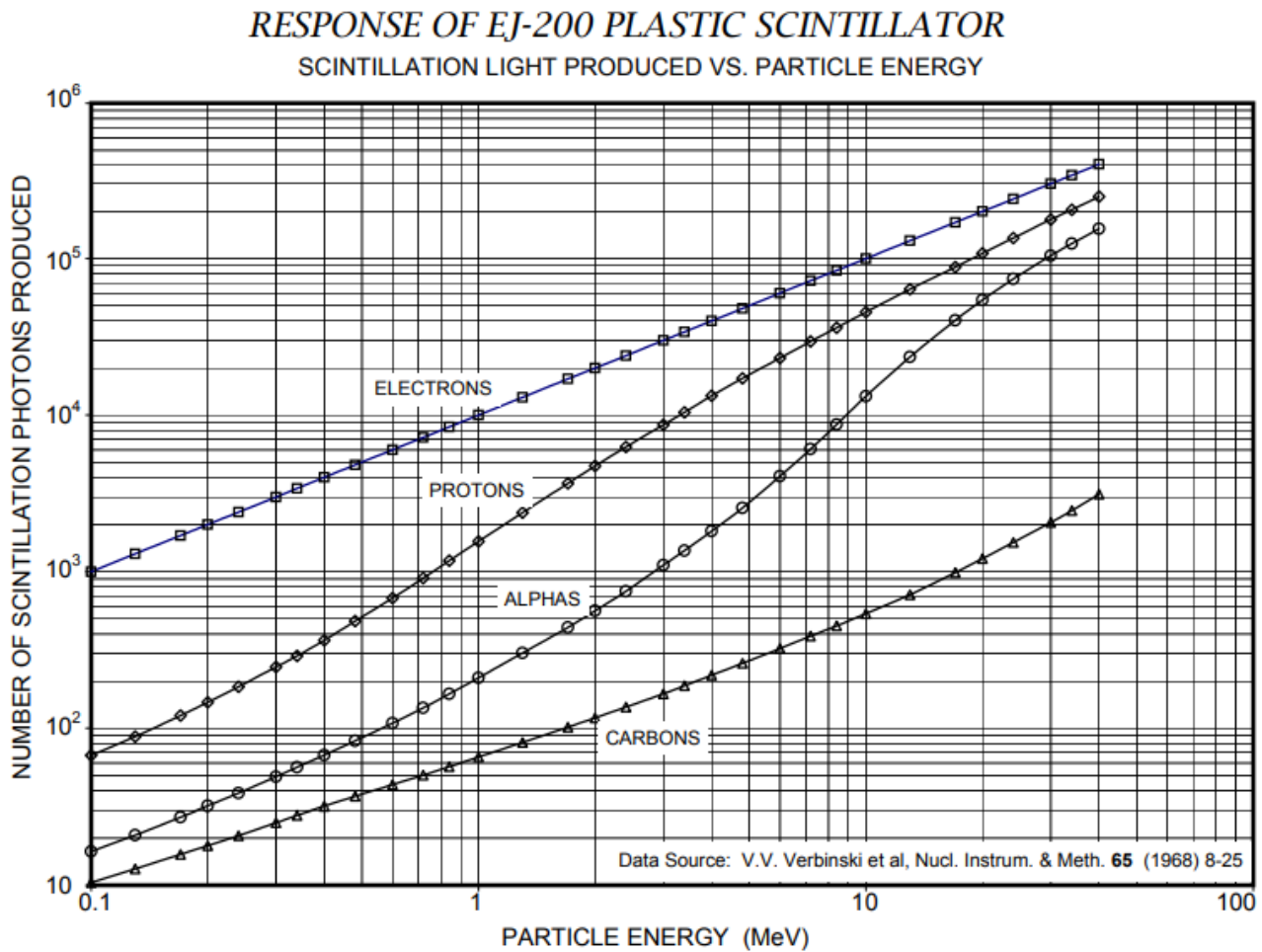


Figure 3.3: A plot showing how the TH detector scintillator bars respond to the energy of the particles detected given by the number of scintillation photons produced. This plot shows electrons outputting more photons per MeV thus making this specific scintillating material optimal for use in the BigBite electron arm of SBS. Plot from [47].

3.1.2 Photo-multiplier Tubes

An input window, a photo-cathode, focusing electrodes, an electron multiplier constructed of dynodes, and an anode are all standard components of a photo-multiplier tube, which has a vacuum tube design. The external photoelectric effect causes photo-electrons to be released into the vacuum when light enters into a photo-multiplier tube via the input glass window lens, stimulating the electrons in the photo-cathode to generate an electric output signal. The focusing electrode accelerates and concentrates photo-electrons before they arrive at the first of several dynodes and multiply through secondary electron emission. At each dynode in the electron multiplier, the secondary electron emission is repeated. Finally, the last group of secondary electrons are multiplied by the last dynode one final time and retrieved from the anode [49]. A general diagram of a typical photo-multiplier tube is provided in Figure 3.4 with all the main components labeled.

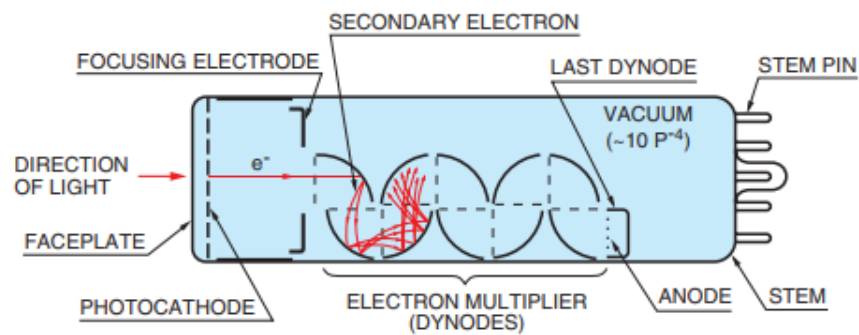


Figure 3.4: This diagram shows the internal construction of a general photo-multiplier tube design with light incident on the PMT face plate and photo-cathode turned into electrons which are multiplied by the dynodes and output as a signal pulse. Image from [50].

The two main types of photoelectric conversion are "external photoelectric effect," where photo-electrons are released from a material into the vacuum, and "internal photoelectric effect," where photo-electrons are stimulated into a material's conduction band. The former effect is exhibited by the photo-cathode, whereas the latter is exhibited by the photo-conductive or photovoltaic effect [49].

Photo-multipliers of type ET-9142 are used to capture and read out scintillation light from the TH bars, most capable at 200-600 nm which matches the emission spectrum in Figure 3.2. These PMTs feature an outside diameter of 28 mm, a blue-green sensitive bialkali cathode with a diameter of 25 mm, ten linear-focusing dynodes, and a typical gain of 10^6 . The linear focused design of the high stability

SbCs dynodes allows for excellent linearity and timing [51]. A mu-metal shield, an insulating sleeve, and an exterior conductive layer are placed on the glass envelope of the PMT. Typically, the multi-electron pulse rise time at the anode is 2 ns or less. The PMTs and bases are housed in Al housings that hold the PMTs flush against the light guides while a high voltage is given to the PMT pins through a bespoke base. Additional protection against stray magnetic fields from the BigBite dipole magnet is offered by an external mu-metal cylinder that is located outside of the aluminium housing [52]. Diagrams of PMTs used for the TH detector, their internal circuitry, and housing assembly are in Figures 3.5 and 3.6. PMT bases and assembly were design by J. Annand and A. Shahinyan.

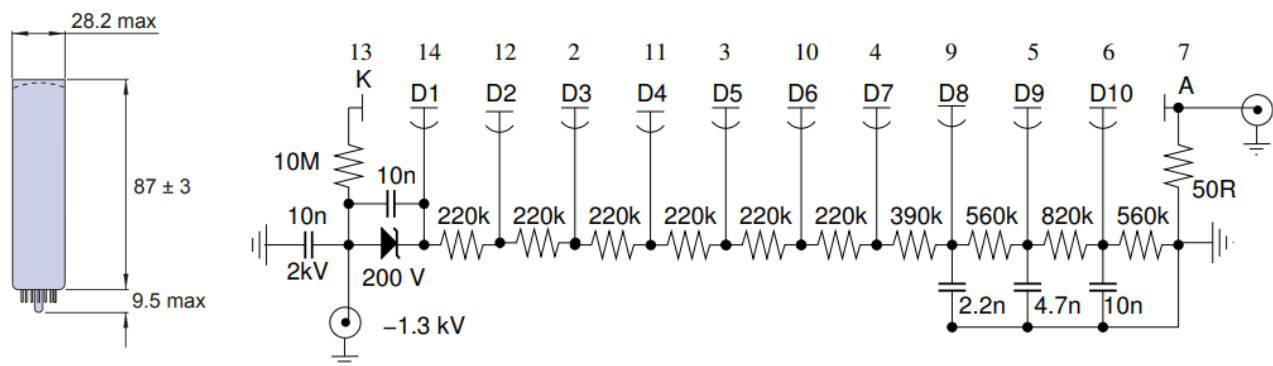


Figure 3.5: The left diagram shows the physical measurements in mm of the ET-9142 PMTs used for the TH detector and the right diagram is a schematic of the internal circuitry showing all 10 dynodes, anode, and resistors. Diagrams from [51] (left) and by J. Annand and P. S. Lumden [52] (right).

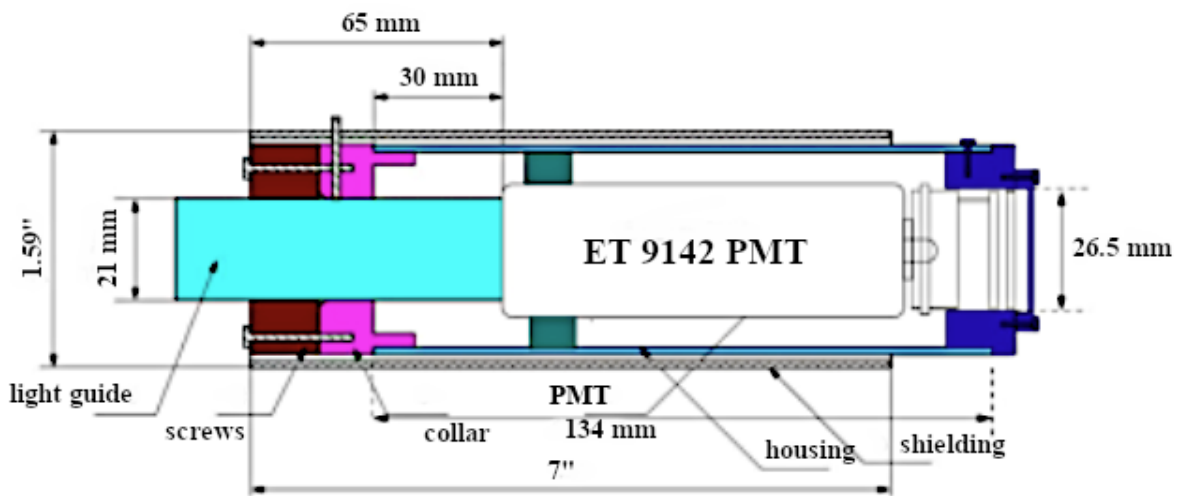


Figure 3.6: A schematic of the ET-9142 PMT installed inside a unit of the PMT housing assembly with measurements showing depth of light guide (light blue) within the housing. Image by J. Annand and A. Shahinyan.

3.1.3 NINO ASIC Amplifier-Discriminator Cards

A fast front-end amplifier discriminator with minimum noise rate is required for the extremely accurate measurement of time. There are 12 NINO ASIC amplifier-discriminator cards for the TH detector and each card contains 16 signal channels. Six NINOs are positioned on either side of the TH detector stack, near to the PMTs. Each NINO card requires about 1.3 A and needs 5 V of power. An essential low-noise, wide-bandwidth circuit that is based on a balanced common gate circuit arrangement serves as the NINO's input stage. Four identical cascaded amplifiers that are tuned for delay and noise rate provide the appropriate signal amplification [52].

A voltage difference provided using two symmetrical inputs of a DC stabilization feedback circuit—which also serves as the common mode rejection circuit—sets the NINO threshold. A completely differential circuit is designed from input to output to provide a high immunity to power supply noise and ground noise. The channels of the NINO chip receive biasing currents and voltages from a common biasing block. The differential input stage's two input devices are biased similarly to a transistor. As a result, the reference resistance value and the input devices' impedance are matched. The output stage is an open-drain differential circuit with current switching between a channel's two outputs, and made to be compatible with LVDS receivers. The correlation of pulse width with the front edge time-walk is linear, and the pulse width measurement can thus be used to correct for the time drift of the front edge due to the discriminator time-walk effect [52]. The NINO cards were designed by J. Annand. A block diagram of the NINO ASIC chip logic flow for a single channel is provided in Figure 3.7.

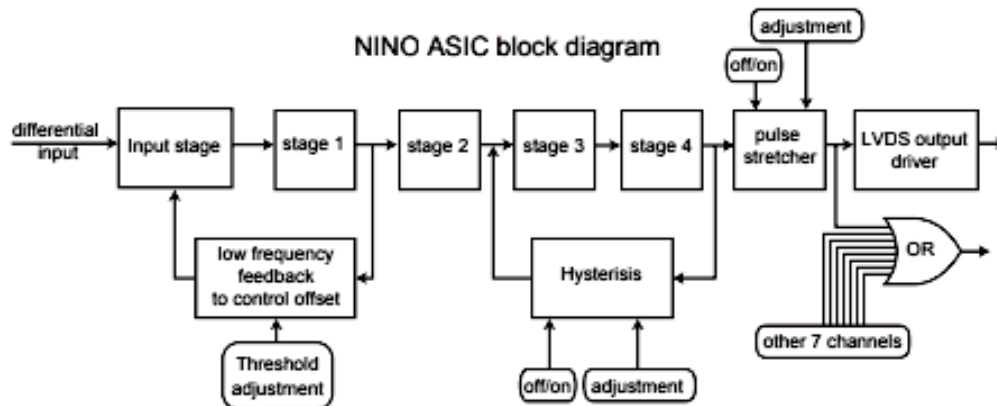


Figure 3.7: A block diagram of the NINO ASIC showing the logic behind the information flow for a single channel in the electronic chip. Diagram form [53].

For the input stage of the NINO ASIC amplifier-discriminator card shown in Figure 3.8, the input current pulse enters the first M1 transistor's source, exits through the drain, and then enters the source of the second M2 transistor. The current pulse will subsequently emerge from M2's drain, but at that point the impedance is significantly higher than it was at the input. This current charges the capacitance on the drain. The rise time of this signal is determined by the properties of the transistor itself, and the fall time is determined by how long it takes the capacitance to recharge [53].

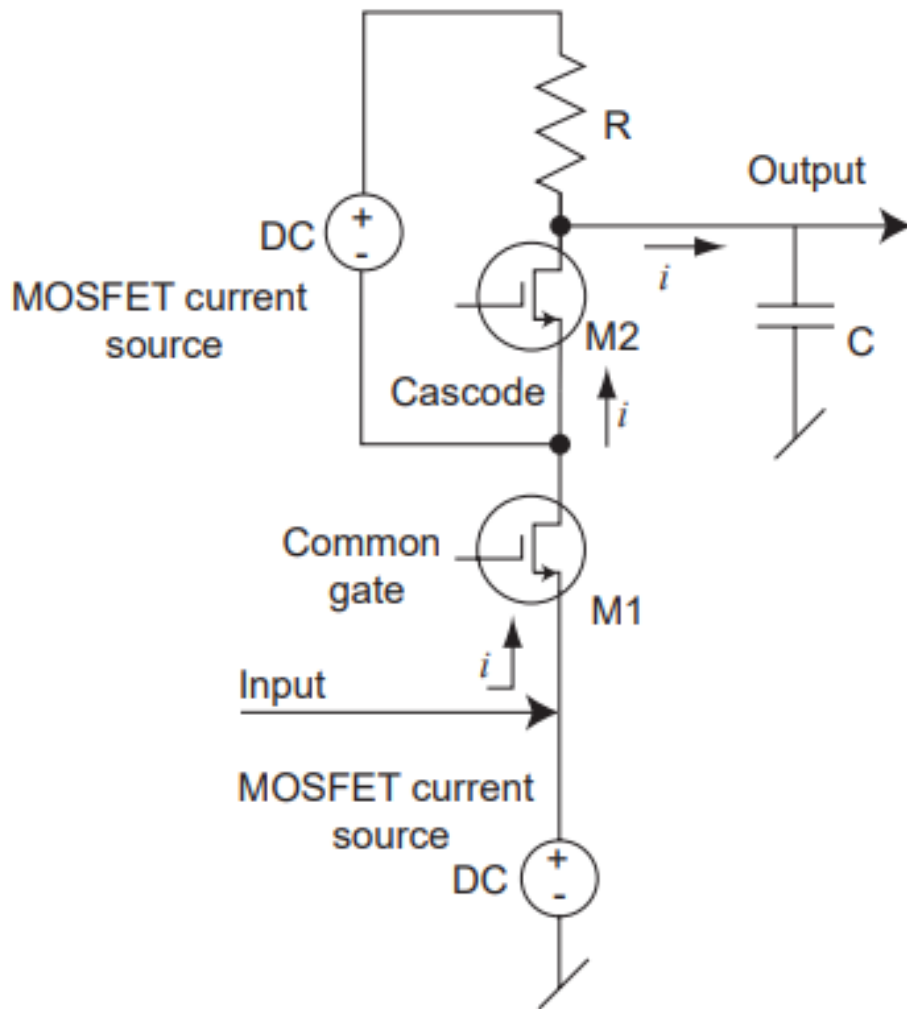


Figure 3.8: A schematic of the NINO ASIC amplifier-discriminator chip input stage showing signal input and output, current source, and common gate. Diagram from [53].

In the photograph from Fig 3.9, we can see an example of the NINO ASIC amplifier-discriminator card version used for the TH detector. This type of NINO has 16 input coaxial connectors where the PMT signal enters. The connectors are housed in a box of metal shielding to protect the amplifiers from

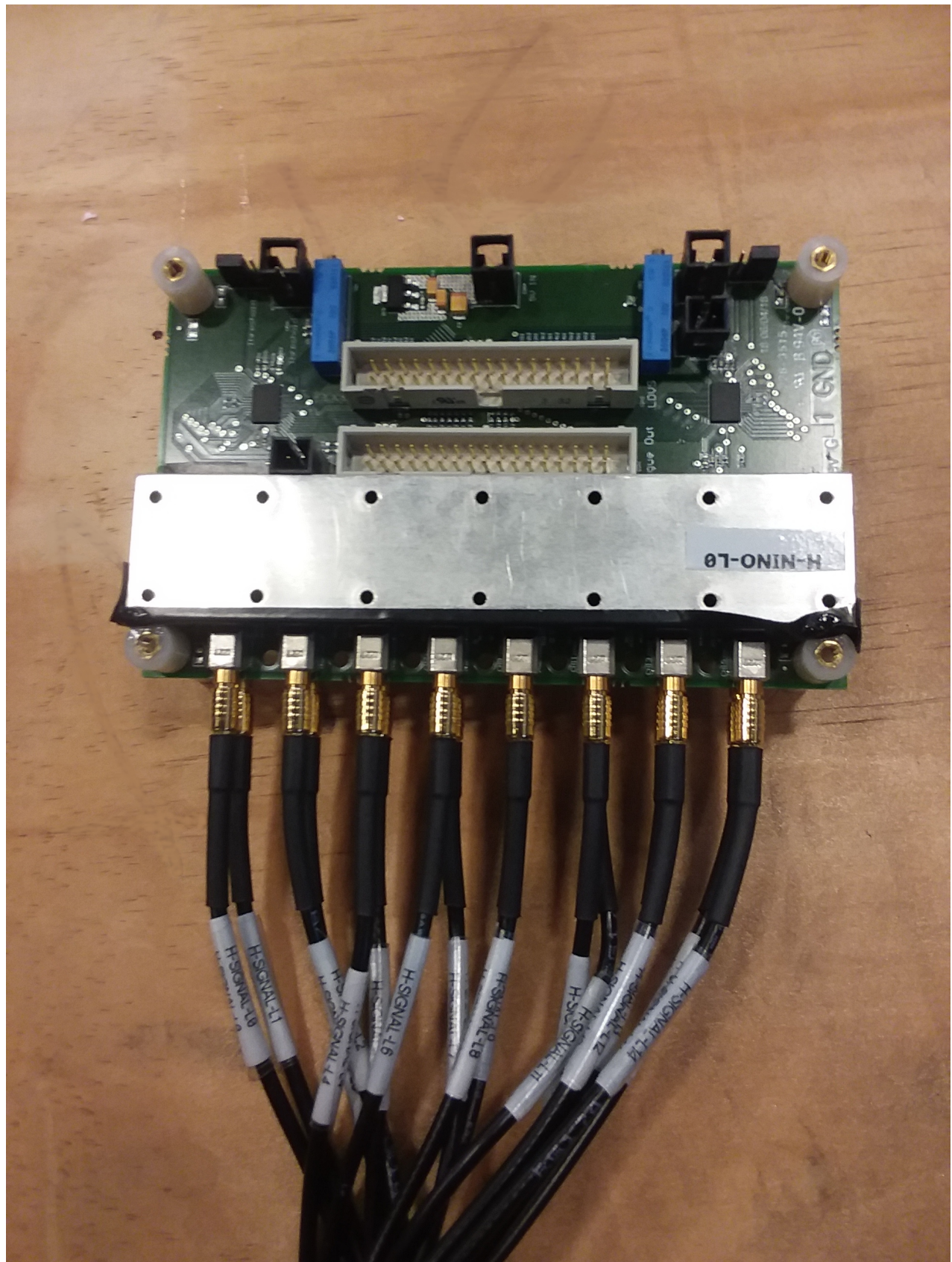


Figure 3.9: A photo of the specific 16 coaxial input connector NINO ASIC amplifier-discriminator card version. This version is particular to the TH as NINO card designs can vary as needed to accommodate different input signal cable connectors. Photo by R. Marinaro.

RF background and it doubly acts as additional support to prevent damage as the gold connection pins from the signal cables to the NINO were found to be somewhat fragile. Two sets of 17-pair connector pins at the center of the NINO output the logic (TDC) and analogue (ADC) signals from the NINO card to the data acquisition system. Each NINO outputs 16 channels of TDC and ADC signals connected to 16 corresponding PMTs with the 17-pair pin in each 34 pin set acting as a ground. The whole NINO card is grounded with four screws attaching the NINO card to the BigBite detector package frame which shares a common ground. Power is supplied to the NINO card via the black power supply connector pins and thresholds are set using blue prism-shaped adjusters which have a set range between 1.3-1.9V. The NINO card thresholds can be checked using a voltmeter connected to the adjacent threshold measurement pins, and the low voltage (LV) supplied to the NINO card can be similarly measured at the NINO using the base of the power supply pins and ground. Measured LV supplied to each of the 12 NINOs from a common power supply varied from 4.95-5.2V across the TH detector. Circuit diagrams of the NINO ASIC amplifier-discriminators used for the TH detector are provided in Appendix B. The diagrams from figures in Appendix B show how the input signal from the PMT to the NINO is amplified and split into analogue and logic signals which can be read out by the data acquisition system to provide particle identification, tracking and timing information.

3.1.4 High and Low Voltage

Low voltage for the NINO cards is provided by an KEYSIGHT N5744A DC supply. It is housed in the electronics racks in the electronics bunker in Hall A as shown in Figure 3.10. An LV distribution panel which comprises a series of fuses has been installed on the TH detector frame to feed the 5V required for operation to each NINO card. The LV distribution box is labelled H-LV-DISTRIBUTION with a diagram showing its internal wiring in Figure 3.11. Each NINO card is supplied by a single 2 meter 20 AWG cable with a Molex LLC 0050579402 connector at the NINO card connection end, and soldered directly to the TH detector frame LV distribution panel at the other end. A table of the cable mapping connecting the NINOs and the LV distribution panel is provided in Appendix C.

Each NINO card line is fused at 1.5 A. Because of a voltage drop along the supply lines the LV power supply is set to +7.13 V which delivers +4.8-5.0 V at the NINO card (its optimal operating voltage range). The total current drawn is 15.77 A. Each NINO card, connected individually, draws the expected 1.3 A.



Figure 3.10: A photo of the KEYSIGHT LV power supply unit mounted in an electronics rack in the bunker used to power the NINO cards. The power supply on top is used for the TH detector, the other is for the GRINCH. Photo by R. Marinaro.

The NINO discriminator threshold is set via an external voltage in the range 1.25- 2.00 V. The current drawn is typically 1-2 mA. Normally, the NINO cards will all operate at the same nominal threshold, which was set to 1.6V divided over sixteen channels per NINO for the entirety of the G_M^n experiment.

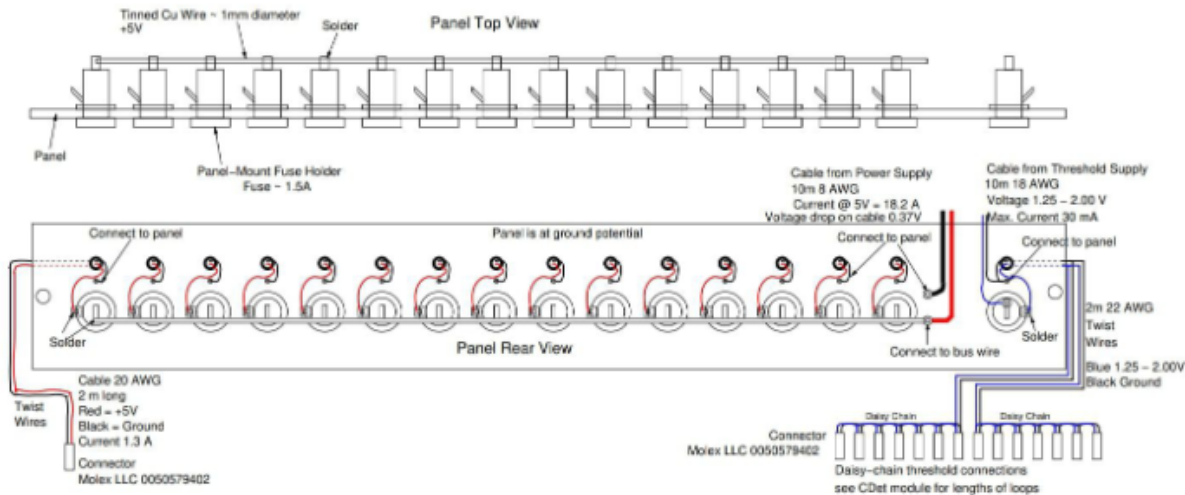


Figure 3.11: A diagram of the TH detector frame LV distribution box which splits the power from the KEYSIGHT power supply unit to the individual NINO cards. Diagram from [52].

High voltage (HV) for the TH detector during the G_M^n experiment was supplied by a CAEN SY1527LC mainframe, equipped with 4 A1932A, 48-channel, HV distributors. HV is output on a 52-pin Radiall 691803004 connector and is transported to a distribution panel via a multi-way HV cable, which has

corresponding Radiall 691803002 connectors at each end. The cable has 48 HV lines, 2 ground lines and 2 lines for a safety interlock circuit. Each line has a high dielectric strength insulator, and when the safety interlock is broken the HV is turned off automatically. An outer Cu-braided sheath provides mechanical protection and electromagnetic shielding for the multi-way cables going to the four HV distribution boxes on the TH detector frame. Connecting the HV mainframe to the PMT bases includes 4 60m braided 48-channel multi-way cables connected to 4 HV distribution boxes on the BigBite detector frame with the 52-pin Radiall connectors. There are 180 individual 4m HV cables that bring the individual high voltages from the distribution boxes to the PMT bases. The 4m HV cables connect to the HV distribution boxes with CAGE 0541 type D-01 3-pin connectors, and attach to the PMT bases with custom, 2-pin connectors. Images of the front and back of the HV main frame are provided in Figure 3.12. These images show the 48-channel multi-way cables connected to the back of the HV mainframe. Spools of additional HV cable length laid between the electronics bunker and the TH detector frame were housed in the electronics bunker next to the rack holding the HV mainframe. A table of the mapping of the labels for the entire TH detector HV system is provided in Appendix C. A further description of how the entire detector data acquisition system and electronic components work together to provide a functioning TH detector as installed in Experimental Hall A at JLab is provided in the following section.

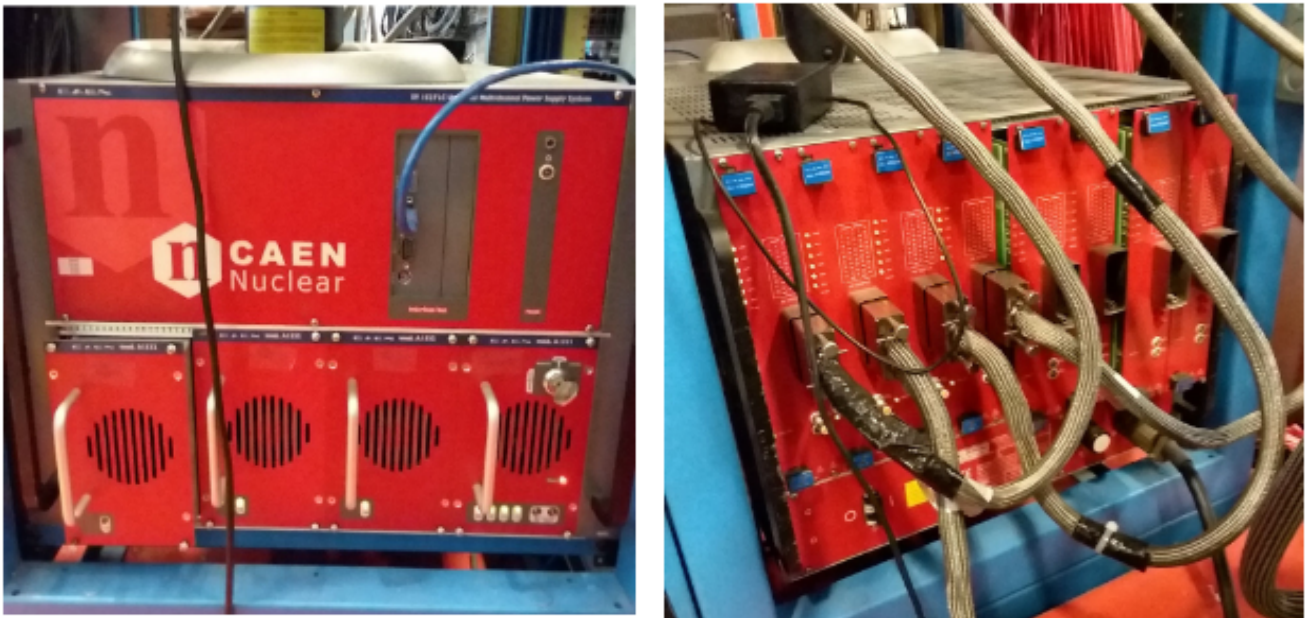


Figure 3.12: Front and back photos of the HV mainframe, which was installed in the electronic racks in the Hall A SBS bunker, used for the TH detector to power the 180 PMTs. Photos by R. Marinaro.

3.2 Data Acquisition

Before delving into the specifics of the data acquisition systems used for the TH detector, an enumerated list of DAQ components and photos will be useful. The wires, cables, electronic panels, and front end electronics that make up the TH detector are listed in Appendix D. Each NINO card is labelled in the form H-NINO-## where the first # is either L or R corresponding to the left or right side of the TH detector frame, and the second # goes from 0 to 5 depending on where the NINO is located top to bottom on the frame with 0 at the bottom and 5 at the top. The NINO cards are further identified with serial numbers stamped on the bottom right side. Serial numbers for NINO cards are in Table 3.1.

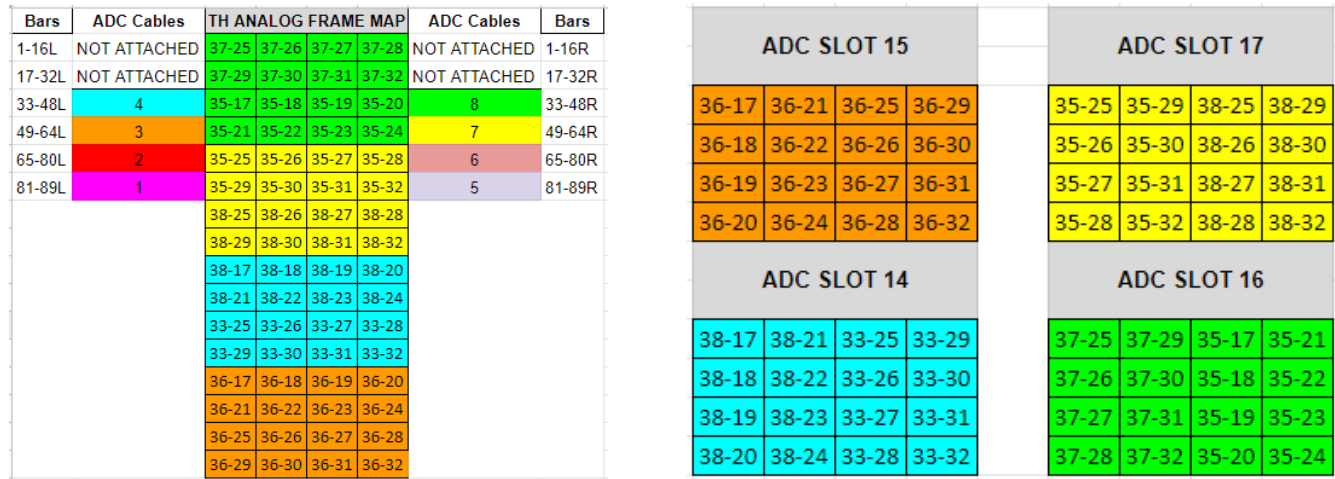
Table 3.1: NINO serial numbers corresponding to the NINO card labels.

Left Side		Right Side	
NINO	Serial	NINO	Serial
H-NINO-L0	18-06/04/18	H-NINO-R0	44-06/04/18
H-NINO-L1	31-06/04/18	H-NINO-R1	6-06/04/18
H-NINO-L2	38-06/04/18	H-NINO-R2	22-06/04/18
H-NINO-L3	14-06/04/18	H-NINO-R3	1-06/04/18
H-NINO-L4	51-06/04/18	H-NINO-R4	23-06/04/18
H-NINO-L5	50-06/04/18	H-NINO-R5	30-06/04/18

Input numbering for the NINO is sequential for the top and bottom connection pins. Even numbered inputs are on top (side where the ADC and TDC ribbon cables connect) and odd numbers on the bottom, opposite side. Bars 1-16L and 1-16R go to inputs 0-15 on H-NINO-L0 and H-NINO-R0 respectively, and so on. Mapping of the scintillator bars to cable to NINO card input is in Appendix E. All 180 TDC digital outputs from the NINO card are connected to the TDC patch panel (TH LOGIC) on the detector frame. The ADC analogue outputs from the NINO card, however, which are used for commissioning purposes, only use a subset of 64 channels (4 NINO cards). Only 64 ADC channels are connected to the ADC patch panel (TH ANALOG) on the TH detector frame at any time. A map of the TDC and ADC patch panel labels is provided in Appendix E.

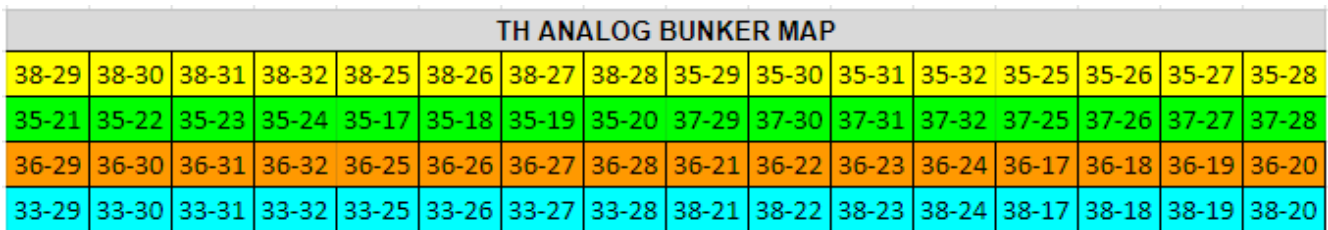
At the TH detector frame ADC patch panel, the signals from each ADC ribbon are converted to individual signals, with the 17 pin connection terminating to ground. The 64 ADC signals are then carried to the ADC patch panel in the electronics bunker. Then they are connected to the inputs of the FADCs in a DAQ VME crate. Previously CAEN v792 ADC readout modules were used during commissioning of

the detector with cosmic ray data before Experimental Hall A installation, but were swapped with FADCs before the beginning of the G_M^n experiment due to rate concerns. A color coded map of the ADC channel labelling is provide in Figure 3.13 for a typical G_M^n run taken using the middle third of the detector where the event rate is highest. The mapping in these figures is an example of how the ADC channels are setup during the G_M^n experiment, but different combinations of bars and cables can be used. The order of cables remains constant from detector to electronics bunker.



(a) TH detector frame TDC patch panel.

(b) ADC DAQ crate slot numbers.



(c) Electronics bunker ADC patch panel.

Figure 3.13: The ADC slot number refers to the position of each FADC readout module in the DAQ crate. The same crate houses the TDC v1190 readout modules.

The digital signals (LVDS) from each NINO card are carried to the TDC patch panel on the TH detector frame labelled TH LOGIC. From there the signals continue to an LVDS-ECL level translator repeater (LTR) in a separate electronics rack in the bunker. The level converter has its own power supply. After passing through the LTR, the ECL signals are brought to the TDC patch panel in the electronics bunker. The outputs from that TDC patch panel are connected to two CAEN v1190A multi-hit TDC readout modules via Robinson Nugent P50E-068-P1-SR1-TG type (34+34) signal connectors. Each component label is provided in Appendix E, and a colour coded mapping is given in Figure 3.14. Pictures of various electronics hardware are provided in Figures 3.15, 3.16, 3.17, and 3.18.

Bars	TDC Cable	TDC FRAME MAP	TDC Cable	Bars
1-16L	1-16L	81-89R	1-16R	1-16R
17-32L	17-32L	65-80R	17-32R	17-32R
33-48L	33-48L	49-64R	33-48R	33-48R
49-64L	49-64L	33-48R	49-64R	49-64R
65-80L	65-80L	17-32R	65-80R	65-80R
81-89L	81-89L	1-16R	81-89R	81-89R
		81-89L		
		65-80L		
		49-64L		
		33-48L		
		17-32L		
		1-16L		

(a) TH detector frame TDC patch panel map.

LVDS to ECL Level Translator Repeater Map											
1-16L	17-32L	33-48L	49-64L	65-80L	81-89L	1-16R	17-32R	33-48R	49-64R	65-80R	81-89R

(b) TDC level translator repeater map.

TDC BUNKER MAP											
1-16L	17-32L	33-48L	49-64L	65-80L	81-89L	1-16R	17-32R	33-48R	49-64R	65-80R	81-89R

(c) TDC electronics bunker patch panel map.

TDC Slot 2					TDC Slot 3				
D	Ref		81-89L	C	D	Ref		81-89R	C
	Ch. 127		65-80L			Ch. 127		65-80R	
B	49-64L		17-32L	A	B	49-64R		17-32R	A
	33-48L		1-16L			33-48R		1-16R	

(d) DAQ crate TDC v1190 slot and readout modules input map.

Figure 3.14: Color coded maps of the TDC labelling used from the TH detector frame patch panel to the TDC v1190 readout modules in the DAQ crates. The readout inputs A, B, C, and D correspond to the physical position of the connection points to the v1190s further discussed in the next section.

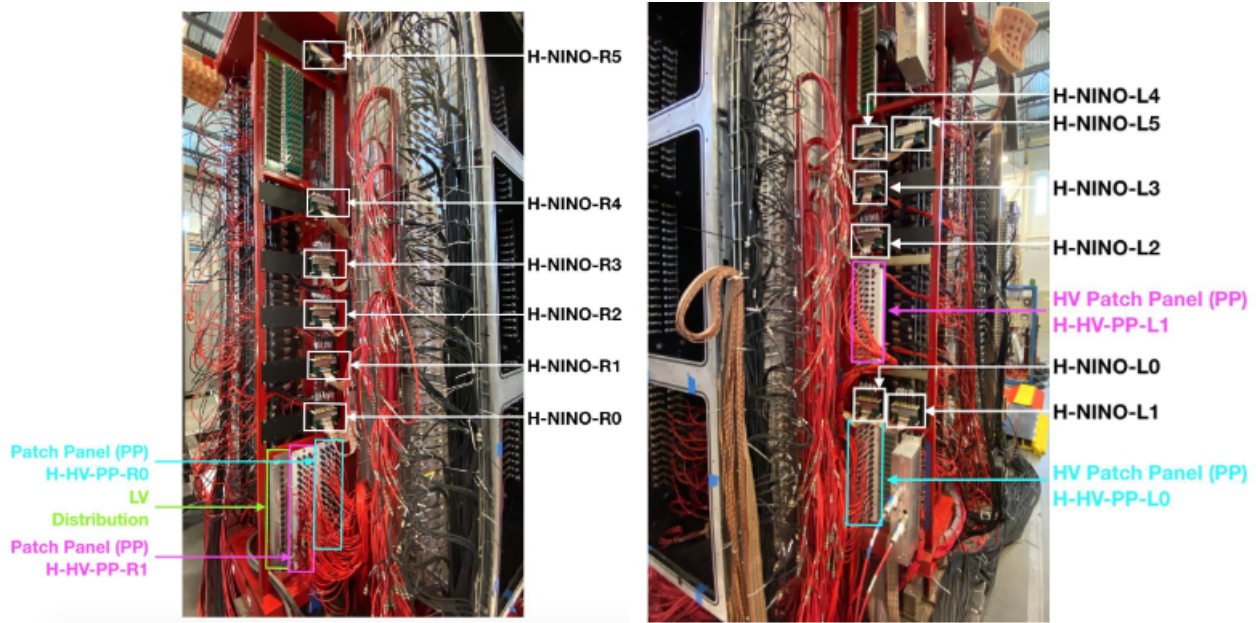


Figure 3.15: Two photos with labels showing where the NINOs, and distribution boxes are located on the TH detector frame. The NINOs are mounted to the frame with metal screws that provide grounding to the frame which has a common ground for all electronics attached to the BigBite frame. Photos by R. Marinaro, and labels by R. Montgomery.

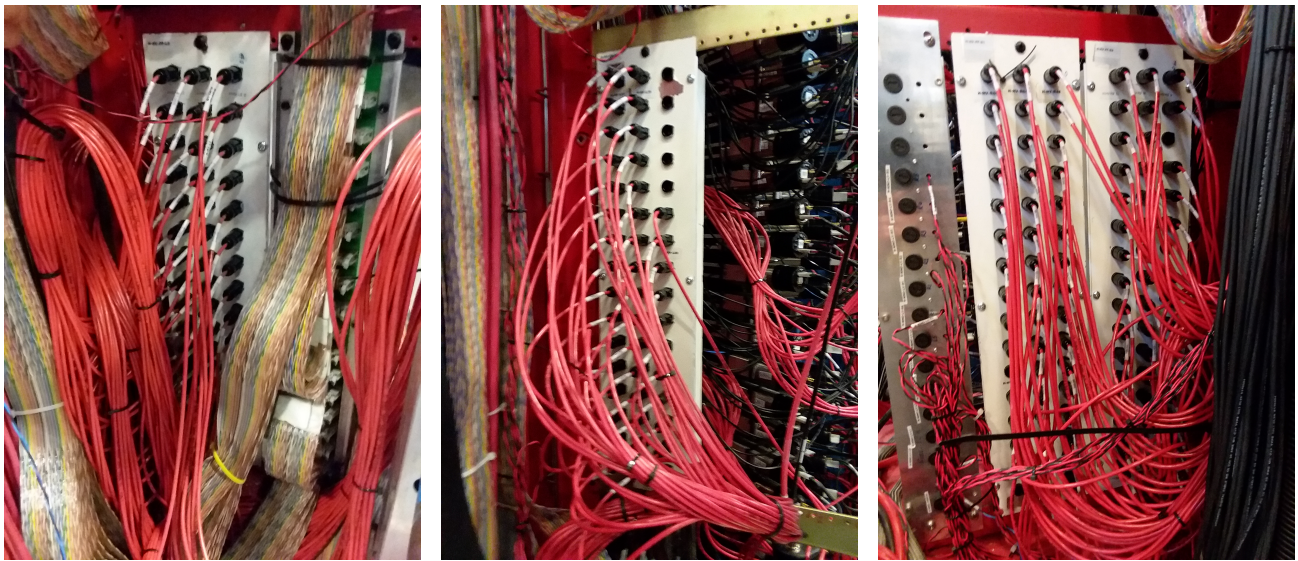


Figure 3.16: Three photos showing the TH detector HV distribution boxes H-HV-PP-L0 (left), H-HV-PP-L1 (middle), and H-HV-PP-R0 and -R1 (right). Photos by R. Marinaro.

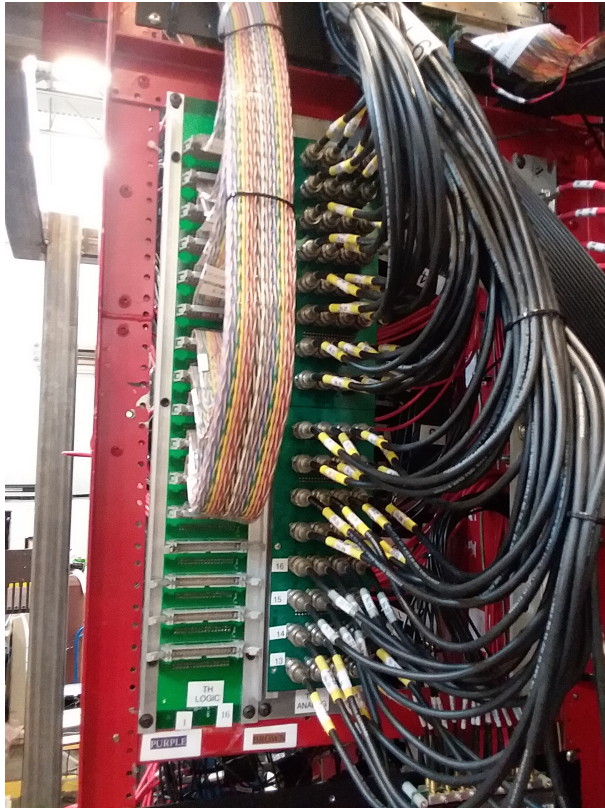
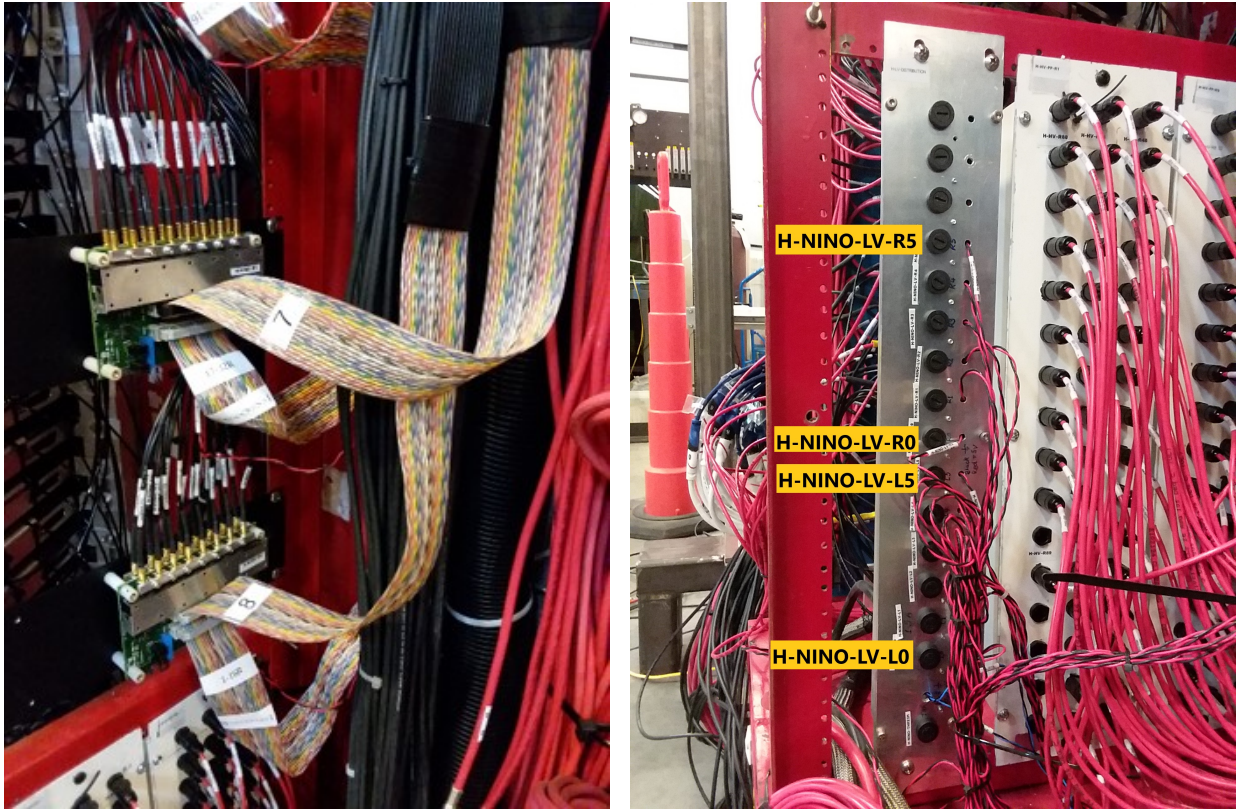


Figure 3.17: A photo of two NINOs mounted to the detector frame with ADC and TDC ribbon cables installed (top left), the LV distribution box (top right), and the TDC and ADC patch panels at the TH detector frame (bottom). Photos by R. Marinaro.



Figure 3.18: Two photos of the level translator repeater (left) and the TDC patch panel (right) both located in the electronics bunker racks. Photos by R. Marinaro.

3.2.1 Readout Modules and Trigger

Detector hit times in the TH detector are recorded in digital signals by TDC v1190s and the amplitudes of the analogue signals are recorded by FADCs. The TDC CAEN v1190s are multi-hit devices. An example is shown in Appendix F. Timing with respect to a trigger signal are recorded in 128 channels, but in order to achieve the best resolution one channel must be reserved as a reference channel which is subtracted from hit channels. The reference channel used for the TH detector is a copy of the BigBite calorimeter trigger signal. The BigBite calorimeter trigger is used as it covers the entire acceptance plane of the TH detector, and is most reliable. The trigger logic for the SBS form factors experiments uses the BBCal pre-shower and shower detectors. There is not a one-to-one relationship between the sum of two rows from the pre-shower and the sum of two rows from the shower because the geometry of the pre-shower and shower blocks is not precisely the same.

NIM electronics modules are employed to process the signals from the BigBite pre-shower and shower modules in order to generate the trigger. It is first necessary to amplify these signals. This is accomplished for the shower using a 7-sum/amplifier custom module, which accepts the signals from 7 modules (1 row) from the shower as input. Through 500 ns delay cables, a duplicate of each shower module's signal is transferred to the SBS electronics bunker to be recorded by FADCs. Several PS 776 16-channel amplifiers are used to amplify the signal for the pre-shower. Through 500 ns delay wires, one copy of the signal from the amplified pre-shower modules is delivered to the SBS electronics bunker to be

recorded by FADCs. A passive splitter splits the second copy. In 4x(4-in/4-out) fan-in/fan-out modules (Lecroy 428F or PS 740) the split pre-shower signals are summed. Each sub-trigger of the fan-in/fan-out for the pre-shower summing receives the signal from pre-shower row “n” on the left and right, and the signal from pre-shower row “n+1” from the left and right. Each sum of two row sub-triggers from the pre-shower is summed with the sums of the corresponding shower sub-trigger rows. This summing is made with 4x(4-in/4-out) fan-in/fan-out modules. The sums of the signals from the pre-shower and shower for each group of corresponding sub-triggers from both detectors are passed into PS 706 16 channel discriminators. Each discriminator channel outputs a gate signal if the amplitude of the final sum it receives as an input is above the set discriminator threshold. Then, the discriminator signals are placed through a "or" logic, using PS 754 Quad logic units 4x(4-in/4-out), which causes a trigger for data acquisition if at least one discriminator generates a gate signal [54].

The TDC v1190s are programmed to readout both the leading and trailing edges of the input logic signal such that a time over threshold (TOT) value for every digital signal is recorded. A time window of acceptance, with respect to the trigger signal, of the individual hits is programmed and hits precede to the trigger, avoiding the need for long delay cables. TOT provides a means to record the amplitudes of scintillations from the TH detector, but TOT is related to integrated charge in a non-linear fashion and must be calibrated against the measured charge. Thus the FADC readout modules are necessary. A standard gated ADC will require considerable delay on the analogue signals from the NINO card, so the coaxial cables are essential. The same crate houses the TDC v1190s and FADC readout modules as well as readout modules for other BigBite electron arm detectors [52]. The Robinson Nugent P50E-068-P1-SR1-TG connectors, which are compatible with standard 17-pair twist and flat cable, allows for the adapting of one high density connector into two 1” 17+17-pin header-type connectors. This is used to combine inputs from two ribbon cables carrying 16 signals into one 32 channel slot on the v1190s. Channels for the cable adapters are labelled CH0 - CH15 on one input and CH16 - CH31 on the adjacent input as seen in Appendix F, and a DAQ flow chart is in Figure 3.19.

Two CAEN v792 ADC readout modules were used for the TH detector prior to Hall A installation since the Flash-ADCs (FADCs) were still being procured. This is only important as some of the initial commissioning for the TH detector before moving it to Hall A was completed with the v792s. A diagram of a v792 is provided in Appendix F. They were connected to slots 4 and 5 in the same VME crate housing

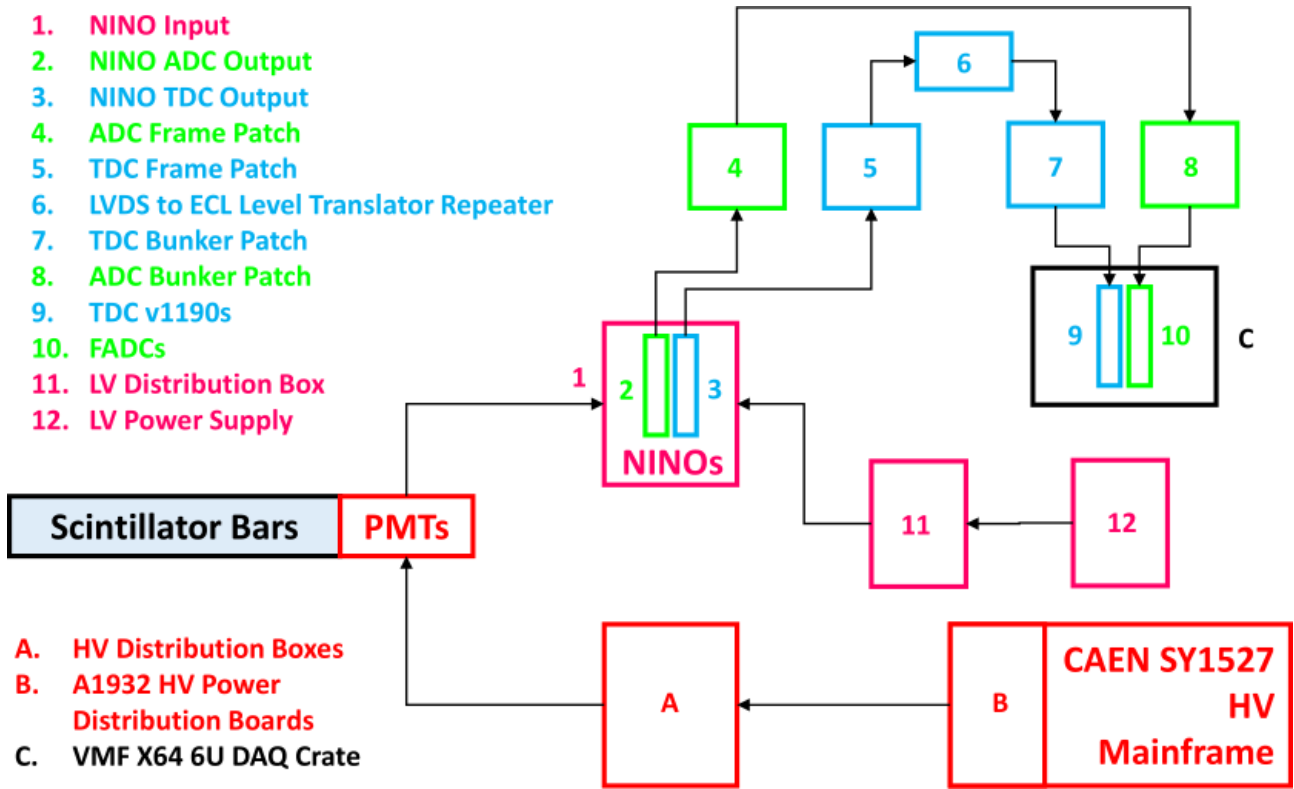


Figure 3.19: A flow chart diagram of the DAQ system going from scintillator bars to DAQ crate, and including the HV (red) and LV (pink) power supply systems for the PMTs and NINOs respectively. The path for ADC and TDC signals are in green and blue respectively.

the v1190s respectively. Again, the v792s were replaced with the FADC readout modules, diagram provided in Appendix F, before the G_M^n experiment began. The v792s are only relevant when discussing pre-installation commissioning studies of the TH detector. All data taken after installation involving calibration and performance analysis during the GMn experiment used the FADC readout modules. The FADCs are connected to slots 14-17 in the VME crate. The next section details the software and analysis structure of the TH detector used in conjunction with the data acquisition system.

3.2.2 Software and Analysis Structure

The SBS analysis software is based on Podd [55], the standard C++/ROOT-based Hall A analysis framework, and uses the ROOT-based “panguin/OnlineGUI” for online monitoring plots during experiment run-times. The existing structure can be broken down into four separate repositories: sbs-offline [56], sbs-replay [57], g4sbs [58], and libsbsdig [59]. The sbs-offline repository is the main software repository for SBS specific libraries and source code. It includes raw data decoders for all the readout modules used

by the various detector data acquisition systems including the TDC v1190s and FADCs used for the TH detector [60]. All of the detector class structure is housed in this repository which provides the information for detector geometries and definitions for the desired data variables to be generated during replaying of the raw EVIO data files. The EVIO data files are generated using CODA which is a control software for starting and stopping data runs during experiment production data-taking. The configuration used by CODA can be specialized for different detector groupings to produce raw data files for specific setups. Raw data-files are output to a temporary directory at the end of each data run, and the raw data-files are moved to cache disks and tape for long-term storage.

The sbs-replay repository is for storing analyzer database files, replay scripts, analysis and calibration macros, and online GUI configuration files. This repository is needed to do the actual analyzing of the EVIO raw data files, turning them into analyzed ROOT files which have a tree structure [60]. Each branch of the data tree corresponds to desired data variables for the various detectors. The analyzing of the raw data files is performed by the Hall A analyzer which is used in conjunction with executing replay scripts. Replay scripts can be specialized in how they are written for creating a ROOT file specific to detector sub-systems or for all detectors together. They can also be specialized for specific experiment configurations. The replay scripts read in text files from the sbs-replay database where values for various cuts and calibration values are stored for all the detector sub-systems. Once the desired ROOT file is generated, analysis studies can be performed for detector commissioning, calibration, and performance, as well as physics analysis for the experiments.

The last two repositories are for the purpose of simulation. The g4sbs repository provides all the necessary software for a GEANT4 based simulation of the SBS detectors and experiments. It was used during the simulation of the TH detector performance analysis provided in Chapter 5. The libbsdig library is for digitization of simulation output. It translates the g4sbs output, such as hit time, position, and energy deposit, into simulated raw detector signals, and populates hit data structures used during the reconstruction. Its purpose is to test and develop reconstruction algorithms on simulated events using identical algorithms to those used for real data. This repository is crucial for performing high-rate tracking studies using the simulation software [61]. Figure 3.20 shows a software flow chart.

The TH detector has its own macros specific to the needs of the commissioning, calibration, and performance studies completed thus far. The sbs-replay repository houses the database files specific to

the TH detector which hold all the cut and calibration values used in the replaying of the detector ADC and TDC data [62]. The SBS detectors also utilize an EPICs based control software. For the TH detector, EPICs is used to control the HV settings and power. EPICs graphical interfaces were developed and implemented for all the HV under EPICs control for use during experiment data taking. These interfaces include the ability to backup and restore HV settings. For each HV channel of the various SBS detectors, a voltage difference EPICs signal is provided. Alarm limits are placed on these signals such that a notification will alert via the alarm handler if a channel trips off or if the actual voltage provided by the channel differs from the set voltage. By default, a minor alarm is raised if the monitored voltage is more than 25 volts above or below the set voltage, and a major alarm is raised if the voltage is more than 50 volts away from the set voltage. These limits may be changed for individual channels using the alarm handler. Every high voltage mainframe is assigned a unique crate mainframe number. EPICs Process Variables (PVs) for HV channels have a consistent form, independent of hardware. The form matches the built in EPICs on the mainframes. Using consistent PV name convention allows for GUIs that are independent of hardware. This concludes the overview of TH detector design and data acquisition. The following chapter outlines TH detector construction, installation, commissioning, and calibration.

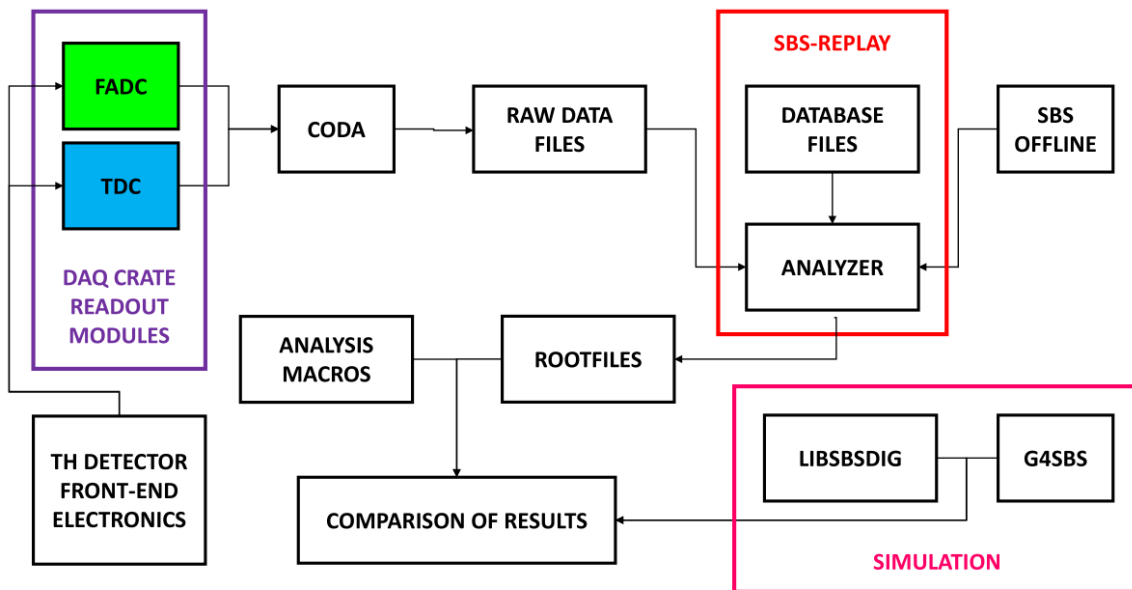


Figure 3.20: A flow chart diagram of the analysis software process going from the TDC and FADC readout modules to sbs-replay using sbs-offline, and final analysis. This diagram includes the simulation software repositories as well.

Chapter 4

TH Construction, Installation, Commissioning, and Calibration

The main components of the TH detector are the ninety $25 \times 25 \times 600 \text{ mm}^3$ EJ-200 plastic scintillator bars acting as the active material of the TH detector for detecting light from particle events, the 180 ET-9142 photo-multiplier tubes with custom bases used to transfer light from the scintillator bars into charged electrical signals, and the twelve NINO ASIC amplifier-discriminator cards which output the PMT signals into both analogue (ADC) and timing logic (TDC) signals. Detailed descriptions of these three main components and their purposes in experimental nuclear physics are provided in Chapter 3. The TH detector and its operation requires an understanding of the procedure for: how the detector arrived at its final construction, and the steps taken during the installation of the TH detector as part of the BigBite electron arm package in JLab Experimental Hall A. Following the completion of the TH detector construction, and installation, a series of studies were completed to determine the detector's readiness for use in the GMn experiment. This process is called commissioning. This process analyzes as much data as possible concerning the ADC and TDC signals from every channel in the detector to confirm their expected and proper operation. Also, there is the need to optimize the TH detector system by looking at the HV settings of the PMTs with regard to charge normalization, and gain matching. Following these preliminary commissioning studies, the calibration of the detector became the main focus. This involves optimizing data gathered from cosmic ray and beam-on-target particle interaction events or hits to account for any and all timing discrepancies among the several TDC channels.

4.1 SBS TH Detector Requirements

Before construction of the TH detector could be undertaken, a set of detector requirements and expectations were determined for quantifying the successful operation of the TH detector during the GMn experiment run-time. Considering the TH detector's main function is to provide particle timing information, it is crucial to note that the time resolution, based on the time difference, was expected to be less than or equal to 300 ps for each scintillator bar, meaning that the overall average time resolution of the TH detector should not exceed that value. This value of 300 ps is called the intrinsic time resolution of the TH detector. Other than for particle timing data, the TH detector can be used to track particle position. The expected horizontal position resolution of each scintillator bar should be less than 2.7 cm, based on the intrinsic time resolution, and the average horizontal position resolution of the whole TH detector was not expected to exceed that value. The vertical position resolution was expected to be less than or equal to 2.5 cm (the width of the scintillator bar) which is an unchangeable vertical position resolution limitation constrained by the physical geometry of the scintillator bars. The TH detector is also expected to have a certain efficiency that should be as close as possible to 100% in terms of particle tracking which can be calculated using track matching analysis by comparing particle event interactions in the TH detector with those events that are also recorded as having occurred in the GEM tracking layers.

Additionally, the physical requirements for the TH detector in terms of its design and construction are crucial for understanding its successful assembly and operation. Each individual scintillator bar must be prepared such that it is light-tight, meaning that no external light leaks into the detector. This confirms that the only light being detected by the PMTs from the scintillator bars is originating internally from the particles interacting with the scintillating material and not from an external source. The method used for making the bars and PMT housing light-tight is provided in the following section. The bars must be aligned to the center of the BigBite package detector frame such that the TH detector is positioned central to the main axis of the other BigBite detectors. To secure the scintillator bars, a means of holding the bars to the BigBite package detector frame must be engineered such that the bars will not slide around when moving the BigBite platform from one kinematic setting to another. There is also a need to consider the structural integrity of the detector as a whole, specifically between the joints where the scintillator bars and the light guides meet. These connection points between the light guides and scintillator bars

are fragile and a detailed procedure for improving the connecting of those components is provided in the following section. To obtain clear ADC and TDC distributions for every channel, the high voltage supplied to each PMT and the threshold settings, which discriminate out unwanted low signals and noise, on each NINO must be optimized using analyzed detector cosmic ray and production data. These clear distributions prove that every channel is working properly and ready for use during the GMn experiment run-time. The following sections detail the construction and installation of the TH detector.

4.1.1 Repairs Procedure

After the first attempt at a complete assembly of the TH detector it became apparent over the course of a few months and after having several joints break that the optical glue joints holding the PMT housing and light guides to the scintillator bars was not sufficiently strong enough to withstand long term use. A means for strengthening the joint between the light guides and scintillator bars was proposed such that both surfaces would be roughened with industrial sandpaper. The optical glue would fill in the ridges created by the sandpaper on both the surface of the scintillator bar and the light guide such that there would be minimal degradation in the light transference between the two components. A test setup was constructed using a red laser pointed at a miniature photo-cathode detector which was connected to an ammeter to measure a current. Different configurations were used to test the effects of roughening the surface starting with a baseline value of the current produced by the laser without any light guides up to having two light guides roughened and attached together with UV-cured optical glue. A diagram of the various test configurations are provided in Figure 4.1.

Table 4.1 provides a summary of measured electric current values and changes in light guide transparency among the different configurations. A single light guide was found to have a transparency of 86.7% and this value reduces to 65.9% with two light guides, but when the two light guides are glued together the transparency rebounds to 81.9%. A single light guide with one end roughened using the 400 grade industrial sandpaper has a transparency of 25.3% and this value drops to 19.2% with two light guides each with one side roughened, but when the two roughened surface are attached with the UV-cured optical glue the transparency jumps up to 81%. This shows that the roughening of the two surfaces with the UV-cured glue compared to the two smooth surfaces only accounts for a difference of 0.9% transparency. Thus, the roughening proved to have minimal affect on the transference of light because the

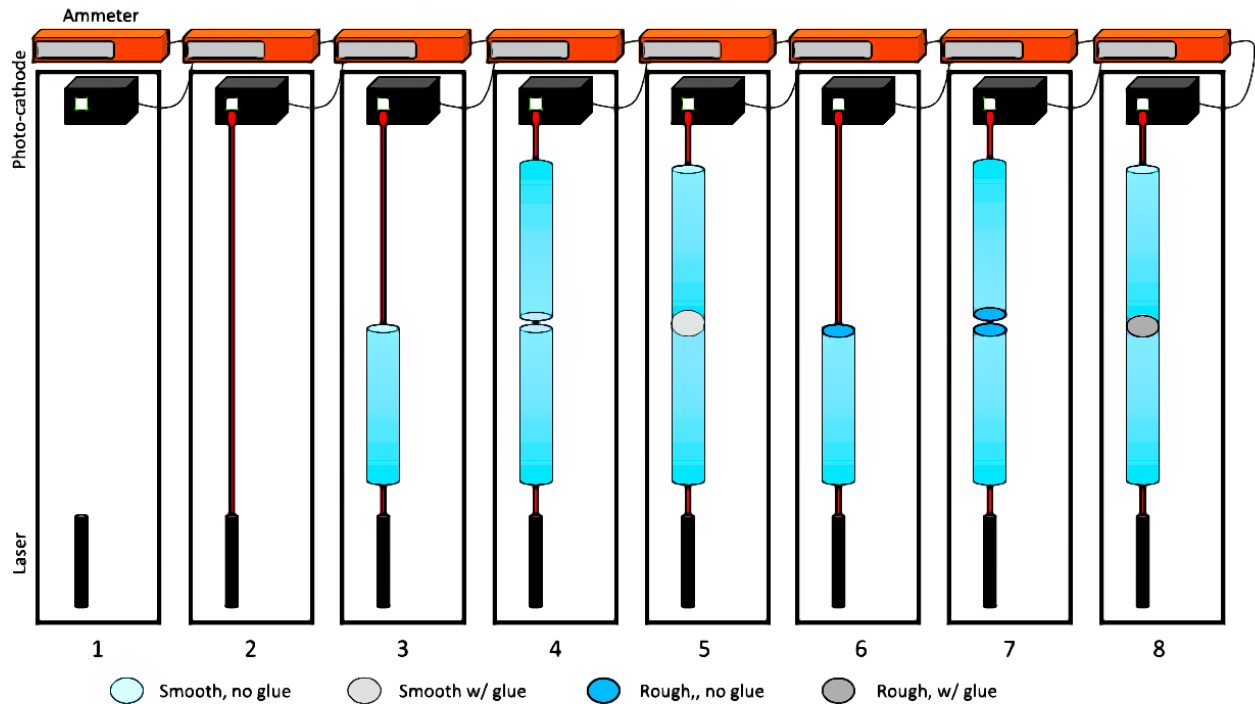


Figure 4.1: Laser tests in light-tight black box: resting no laser (1), no light guide (2), smooth light guide (3), two smooth light guides (4), two smooth light guides glued together (5), light guide roughened one side (6), two light guides roughened one side (7), two light guides roughened one side glued together (8).

optical glue fills in the roughened ridges of the light guide surface. This also makes the joint stronger, and the next test determines by how much.

The diagram in Figure 4.2 provides a schematic of the setup used to test the strength of the glue joint between two smooth-surface light guides versus those that were roughened with the 400 grade industrial sandpaper. Weights varying from 4-8 kilograms were used at 2.5 cm, 11 cm, and 24 cm, which equals the closest-end, middle, and furthest-end of the light guide from the glue joint. The test shows that not even at 24 cm with 8 kg of weight equaling a force of 35 N and a torque of approximately 8.5 Nm could break the glue joint for roughened surfaces. Next, attempts were made to break the joint by leaning on the light guide and hitting the light guide with padded metal poles, and still the joint would not break. Considering the glue joints without roughening would break with a moderate touch, it is plain to see that at a minimum the strength of the glue joint between the smooth and roughened surfaces has increased approximately by a factor of ten. Only after soaking the glue joint in isopropyl alcohol would the light guides break off. A decision was made to forego repeating the laser and stress test using 200 or 300 grade sandpaper since

Table 4.1: List of values for the measured currents and transparency of the different light guide configurations for the laser test.

Laser Test Results		
Light Guide Configuration	Measured Current (uA)	Transparency (%)
1. Resting, No Laser	0.018 ± 0.003	N/A
2. Laser, No Light Guide	3.311 ± 0.015	100
3. Single Light Guide (smooth)	2.632 ± 0.015	86.7
4. Double Light Guide (smooth)	2.141 ± 0.018	65.9
5. Double Light Guide (smooth, glued)	2.626 ± 0.018	81.9
6. Single Light Guide (rough)	0.882 ± 0.012	25.3
7. Double Light Guide (rough)	0.672 ± 0.011	19.2
8. Double Light Guide (rough, glued)	2.619 ± 0.016	81.0

the 400 grade provides adequate strength in the glue joint with minimal loss in light guide transparency using UV-curved optical glue. Convinced that the glue joints were strong enough for long term ware with minimal decrease in light guide transparency, attention was turned to disassembling and reassembling all the detector components using the following procedure.

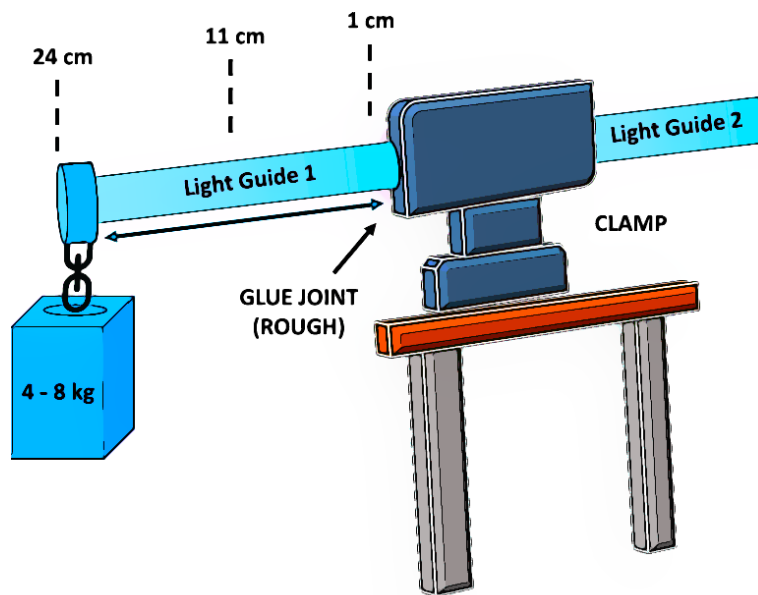


Figure 4.2: Diagram of stress test setup using clamp bolted to a table. Smooth-surface light guides would break with only a moderate touch, but after roughening, the glue joint became significantly stronger.

First, all the previously assembled PMT housings were removed, outer light-tight coverings removed, and light guides removed from scintillator bars. Upon removing the light guides from the scintillator bars, a fair amount of hardened optical glue remained on the light guides. Thus, the light guides were

soaked in isopropyl alcohol to remove excess glue. The ends of the light guides to be attached to the scintillators were roughened with the 400 grade sandpaper in the same clamp used for the stress test. The light guide ends that rest flush with the PMTs were left smooth. Both ends of the scintillator bars were roughened as well with the same sandpaper in the same clamp. Care was taken to roughen the surfaces of the light guides and scintillator bars using an equal number of passes across the surfaces, and alternating the movement of the sandpaper so that no biasing pattern would form on the surface. The roughened ends of the scintillators were next attached to the roughened ends of the light guides using a bespoke precision alignment apparatus to hold the scintillator and light guides in place so the optical glue could be cured for thirty seconds with a pedal-operated, hand-held UV light source. Figure 4.3 provides a diagram of the alignment apparatus used during the application of the UV-cured optical glue. Reflective mylar sheet was wrapped around the scintillator and light guides, followed by black industrial wrapping paper. These were secured around the light guides and scintillator assemblies using a durable clear tape. The purpose of this wrapping was to make the individual scintillator bar and light guide assemblies light-tight.

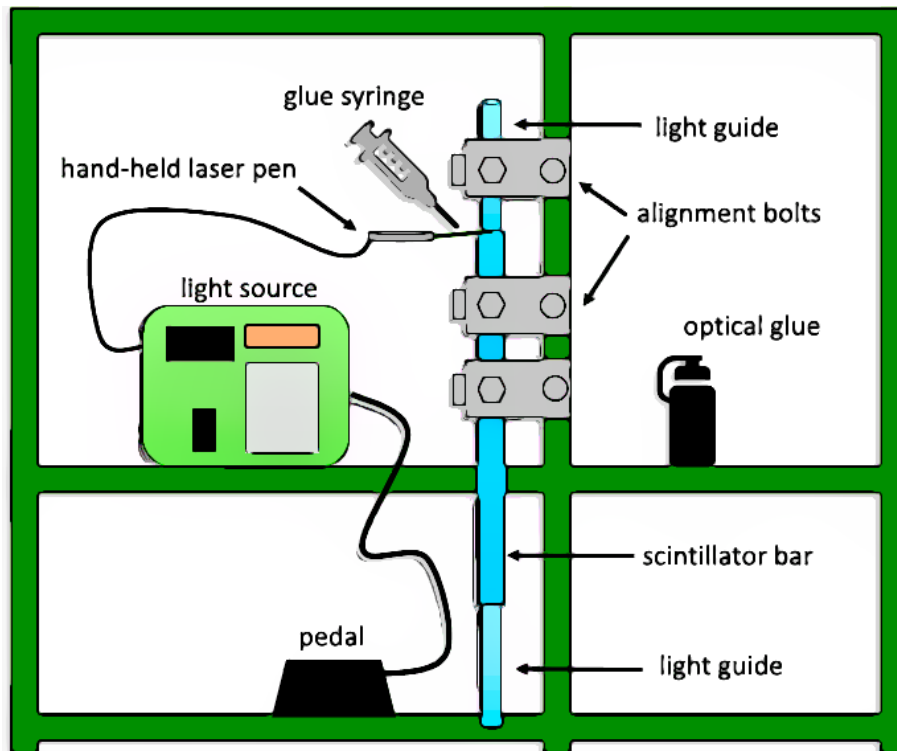


Figure 4.3: Diagram of the precision alignment apparatus used during the gluing of the roughened light guides to the roughened scintillator bars. Only a drop of optical glue 5 mm wide and 1 mm high was needed to cover the whole contact surface between the light guide and the scintillator bar. Optical glue was stored in a sealed container to prevent drying.

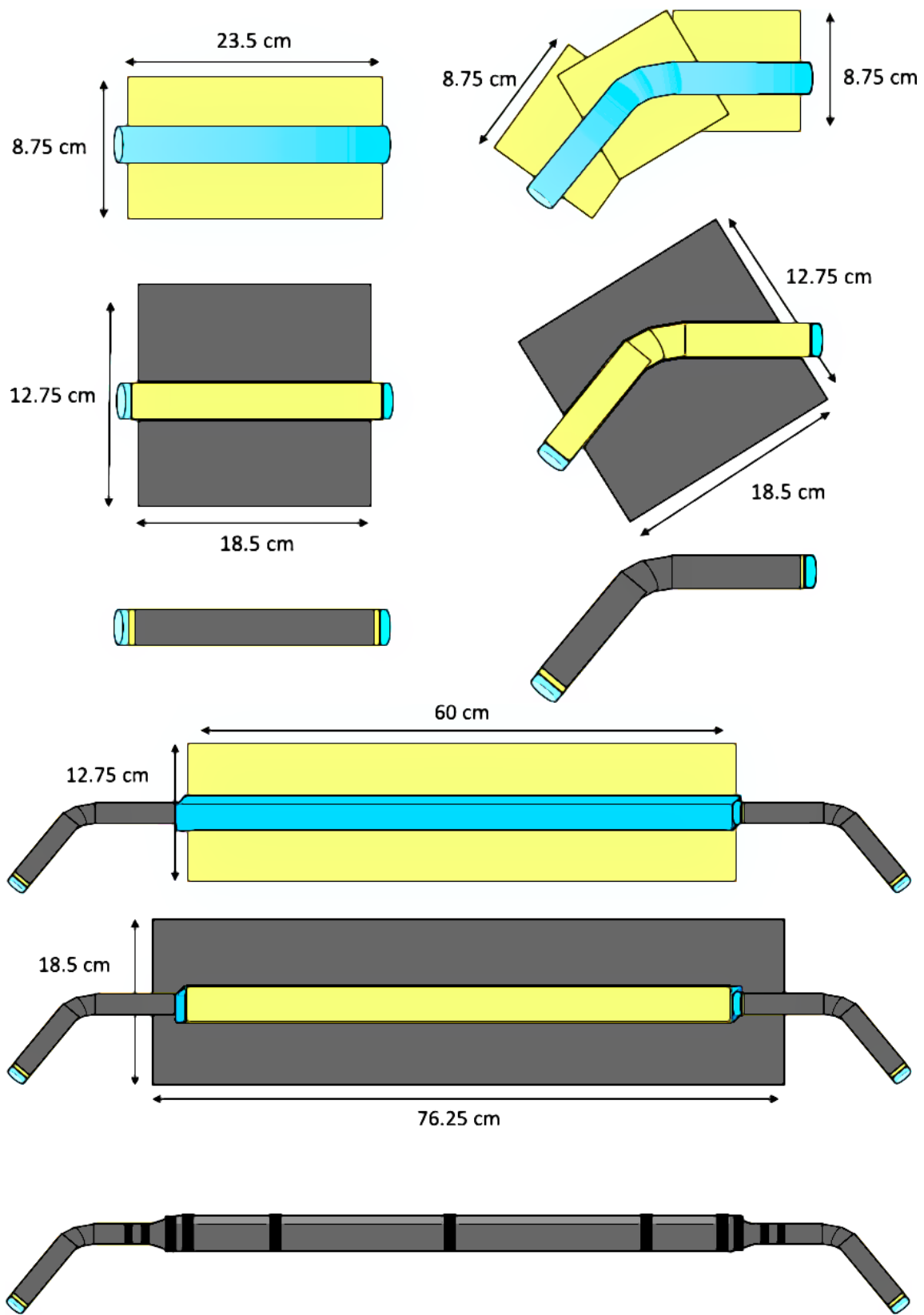


Figure 4.4: Diagrams of the wrapping procedure for both straight and curved light guides, and scintillator bars with dimensions. The final wrapping thickness leaves only a <0.5 mm gap between the stacked scintillator bars. The light guide is shown in blue, the yellow is the mylar wrap, grey is the industrial wrapping paper, and black is electrical tape.

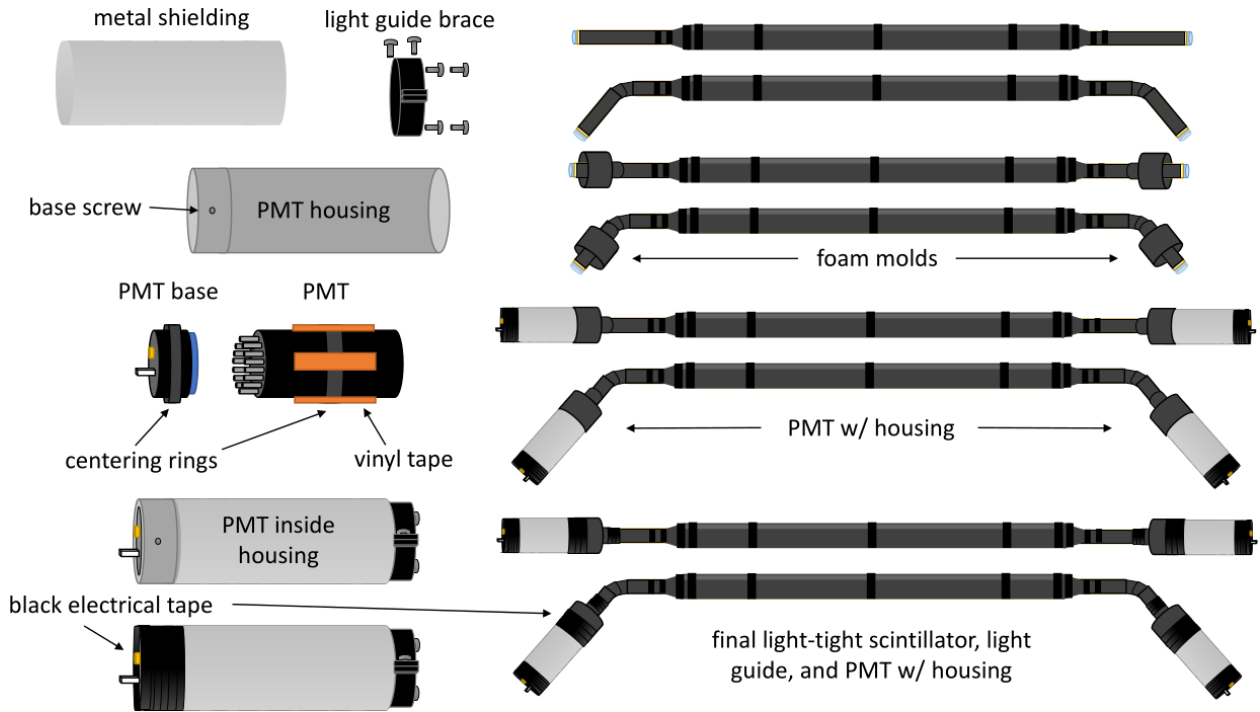


Figure 4.5: A diagram of the PMT inside the housing and attachment to light guides using a brace and screws which were tightened once the PMT and light guide were inserted in the housing.

Several diagrams of the wrapping procedure and dimensions can be seen in Figure 4.4. The black industrial wrapping paper around the scintillator bar was cut longer than the bar so an overhang could be folded down towards the light guides and secured with black electrical tape to make the scintillator bar light-tight. The light guides were then made light-tight by inserting their exposed ends into the assembled PMT housing which were then made light-tight using a foam material and more black electrical tape. A diagram of the PMT housing with PMT inside can be seen in Figure 4.5. Finally, an additional support beam, attached at the back of the bars relative to the target, was attached to each scintillator light guide assembly with either electrical tape for curved light guides or aluminium straps for straight light guides.

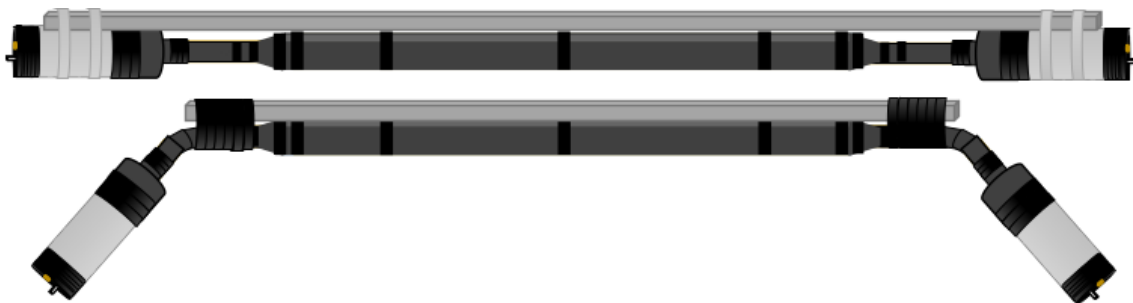


Figure 4.6: A diagram of the final light-tight scintillator bar, light guides, and PMT housing assemblies with added support bars to further prevent roughened glue joint from breaking.

Figure 4.6 shows the fully completed scintillator bar, light guides, and PMT housing assemblies. The assemblies were then tested individually for light-tightness using a high voltage power supply going to each PMT with a signal cable from the PMT to an ammeter which measured the base current output by the PMT at 500V. This base current could not exceed 10 nA for confirmed light-tightness. A high power flash light was used to pass over and around the tested assemblies to find holes or leaks in the wrapping or housing. Leaks were plugged with more electrical tape.

After confirming light-tightness for each assembly, each PMT was tested at operational high voltages ranging from 700V to 1150V. Currents on the ammeter, and signal amplitudes on an oscilloscope were checked to be within reasonable values over the specified high voltage range such that the current would be somewhere between 0.2 μ A to 0.4 μ A of current and 100 mV to 400 mV for the amplitude. An external trigger scintillator was used to observe cosmic ray event signals on the oscilloscope. PMTs that behaved outside these limits at operational high voltages were replaced and set aside to ensure some initial uniformity among all the PMTs. Ultimately, only a handful of PMTs would need to be replaced. Fortunately, the design of the housing was made such that easy removal and replacement of PMTs could be done without completely disassembling the PMT housing.

A final normalization of the PMT signals using ADC data for gain matching would be completed after complete assembly of the detector scintillator bar stack and that process is covered in a later section. The scintillator bar, light guides, and PMT housing assemblies were then stacked in the BigBite detector frame, with the assemblies secured to the frame using additional angled support brackets with straps to tie down the housing flush with the angled supports shown in Figure 4.7. These angled support brackets ensure that each individual scintillator bar assembly is aligned flush with the flat BigBite detector frame and the bar above and below such that the focal planes of the TH detector match with those of the other BigBite detectors. Special attention was given to the position right to left of each assembly with measurements taken on both sides to confirm that each scintillator bar protruded equally on both sides of the BigBite detector frame. Any sizable misalignment would cause unwanted discrepancies in the data between the various BigBite detectors. Upon finishing the re-stacking in Fall 2020, the TH detector had returned to the state it was in at the end of 2018 prior to the smooth glue joints breaking. After roughening, reassembling, re-stacking, and the addition of the further support bars and angled brackets, the TH detector was ready for long term use in Experimental Hall A as seen in Figure 4.7.

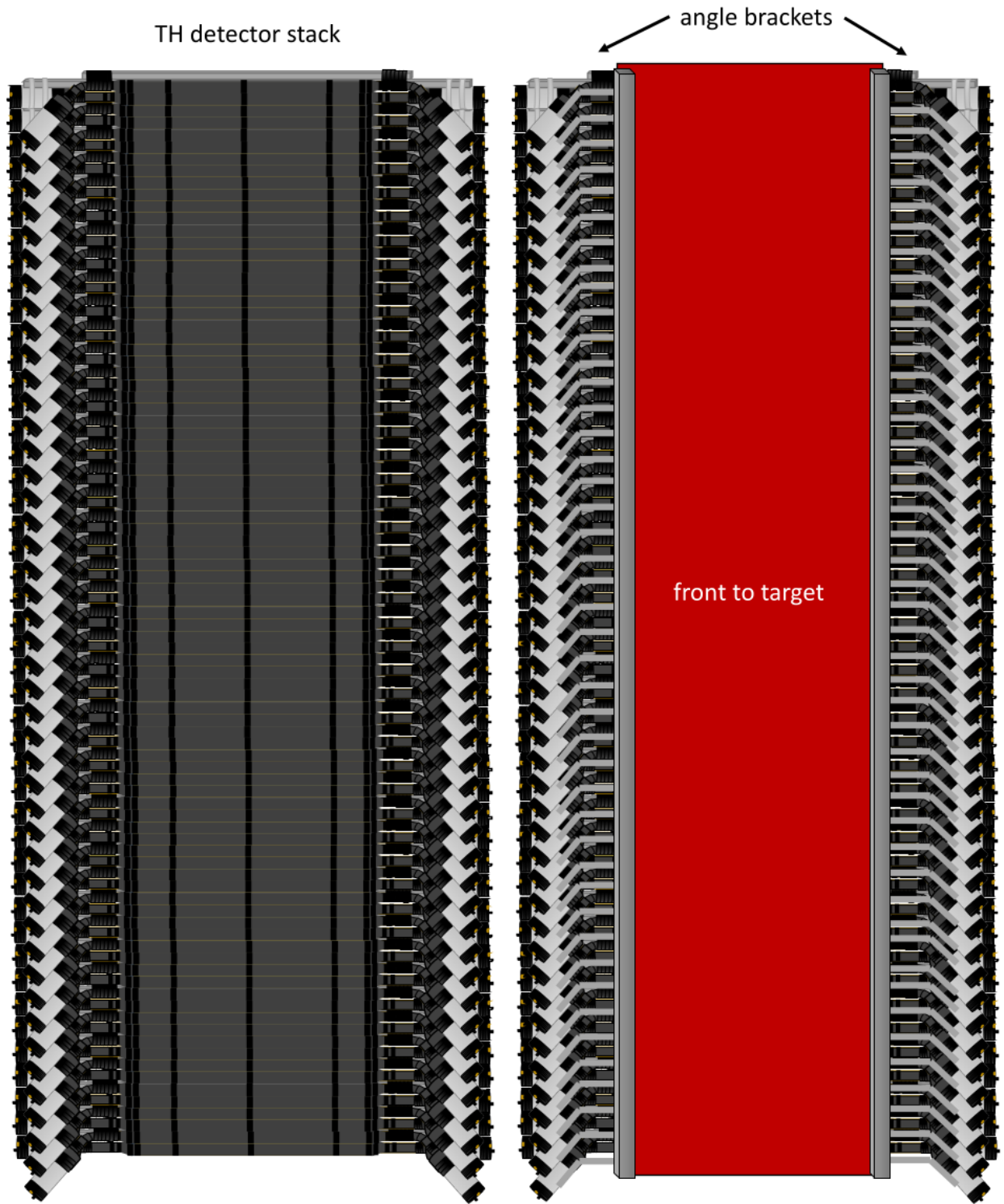


Figure 4.7: Two images of the fully stacked and assembled TH detector. The left image shows what the detector looks like without the detector frame to hold it up. The right image shows a portion of the red detector frame and the angled brackets which the TH scintillator bars are attached. This allows for the bars to be stacked without falling over. The angle brackets also help alleviate some of the weight pressing down on the scintillator bars at the bottom of the stack. The right image is what the target would see if it had a direct line-of-sight to the TH and no other detectors were blocking the TH from the target.

4.1.2 Experimental Hall A Installation

For the TH detector, several front-end electronics were attached to the BigBite frame surrounding the TH detector. Starting at the PMTs, these front end electronics include 180 signal cables coming from the PMTs, the twelve NINO cards (NINOs) which those signal cables connect with, and 8 ADC and 12 TDC 34-pin 17-pair flat ribbon cables from the NINOs to the ADC and TDC patch panels. The seventeenth pair in the ribbon cables is for ground. Only 8 ADC ribbon cables (4 for each side of the TH) were made since the DAQ ADC modules can only read out 64 channels at a time with only two ADC ribbon cables being used on each side per data run. Spare ADC ribbon cables were left plugged into the NINOs at the top of the detector frame. After the patch panels, another set of twelve TDC ribbon cables continues on. The ADC patch panel takes in four (2 from each side of the TH) 34-pin 17 pair ADC ribbon cables in one side and out the other side comes 64 individual coaxial cables which correspond to the 64 channels being read by the DAQ FADC readout modules. Both the twelve TDC ribbon cables and 64 ADC coaxial cables continue on to the data acquisition system (DAQ) which was already covered in a Chapter 3. All twelve TDC ribbon cables coming from the patch panel are used per data run since the DAQ TDC modules have the capacity to read all 180 channels.

As for the high voltage (HV) starting from the PMT, there are 180 red 2-pin HV cables coming from the PMTs connected to four 48-channel HV distribution boxes (2 on each side of the detector). On each side, one of the HV distribution boxes corresponds to the lower 48 PMTs and the second box connects to the top 42 PMTs. The second distribution box on each side of the TH has spare HV channels which were used as back-up channels to replace troublesome HV distribution box connections, or HV channels that were unreliable. Each of the four HV distribution boxes have one multi-coil HV cable going to the HV mainframe which was covered in the previous chapter. Additionally, the NINOs have their own low voltage power supply cables. All twelve of those NINO power supply cables connect from the NINOs to one low voltage (LV) distribution box attached to the right side of the TH detector frame. This LV distribution box has one LV power supply cable which connects to a LV power supply. This covers all the front-end electronics and cables that are physically attached or connected to the BigBite detector package frame. All HV, LV, and signal cables at the frame were tied down and secured, and given enough slack such that cables would not become easily disconnected. Figure 4.8 provides a comprehensive diagram of the electronics surrounding the TH detector on the BigBite frame.

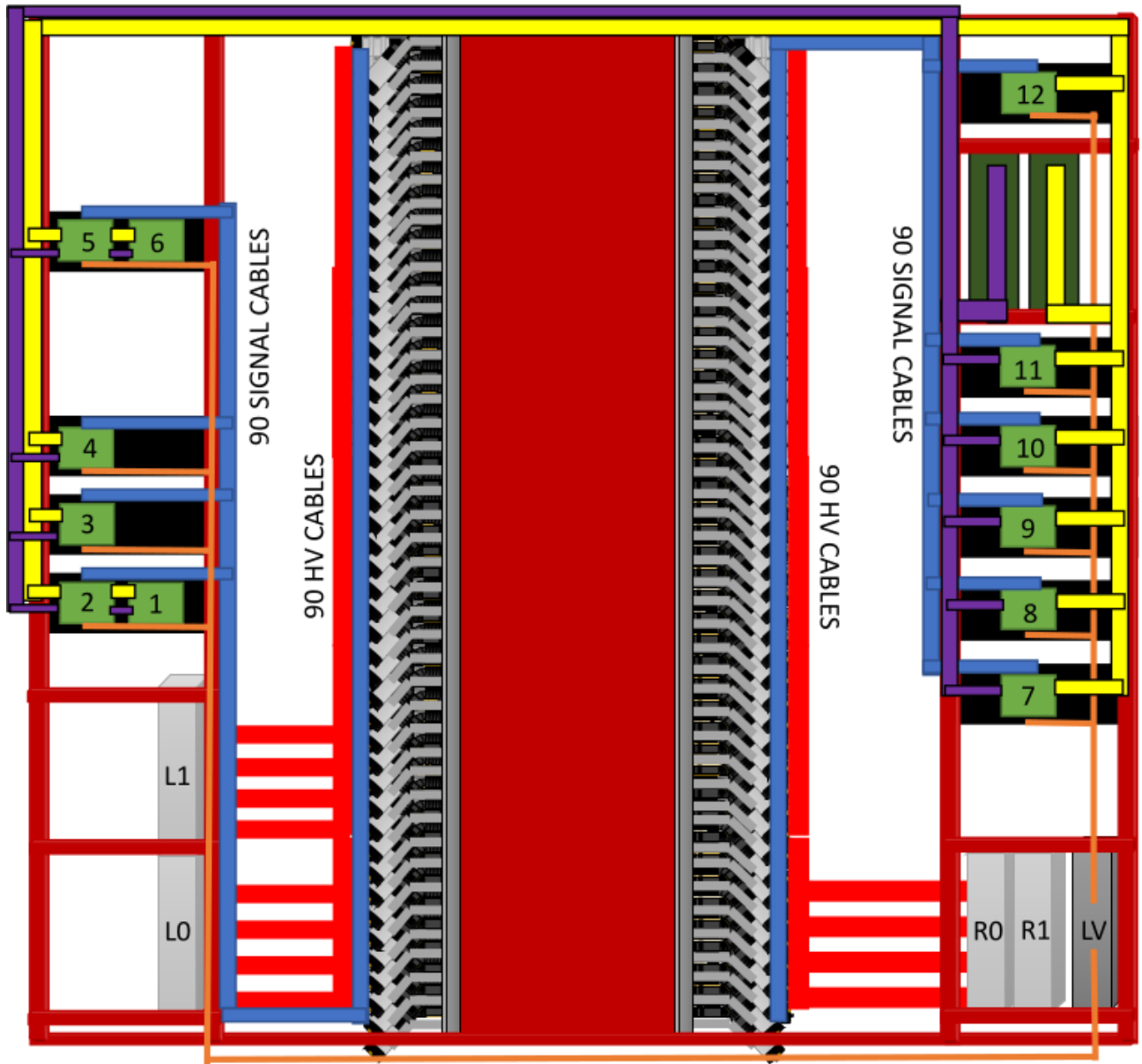


Figure 4.8: The HV distribution boxes (light grey) are attached to the frame (dark red) and are labeled L0, L1, R0, and R1 corresponding to the right and left side and bottom (0) 48 channels or the top (1) 42 channels. Individual PMT HV cables (bright red) go from the PMTs to the HV distribution boxes. The individual signal cables (blue) go from the PMTs to the NINOs (light green) labeled 1-12. NINO 1 corresponds to bottom left 16 PMTs, 6 to top left, 7 to bottom right, and 12 to top right. The individual LV NINO power supply cables (orange) go from the LV distribution (dark grey) to the NINOs. ADC ribbon cables (purple) and TDC ribbon cables (yellow) connect the NINO analogue and logical output to the ADC and TDC patch panels (dark green). Cable lengths are provided in Appendix D.

The TH detector scintillator bar stack, front end electronics, and DAQ were initially assembled in the JLab TEDf building High Bay room. This is where the TH detector and DAQ went through its first stages of commissioning, which is detailed in the following section. During Summer 2021 the BigBite detector package and DAQ electronics were moved to Experimental Hall A. The BigBite electron arm was placed on the BigBite platform with the TH detector included. The DAQ electronics were moved to an electronics bunker which acts as shielding for the DAQ electronics to protect them from radiation damage. The layout of SBS in Experimental Hall A can be seen in Figure 4.9. All HV, LV, ADC coax, and TDC ribbon cables were run below the BigBite platform, under the Left High Resolution Spectrometer (LHRS), and to the electronics bunker. A few meters of slack was left at the BigBite platform to allow extra cable length for when the platform moves to different kinematic setting angles relative to the beam-line. Extra cable length was bundled up, and hung on mounted wall hooks in the electronics bunker.

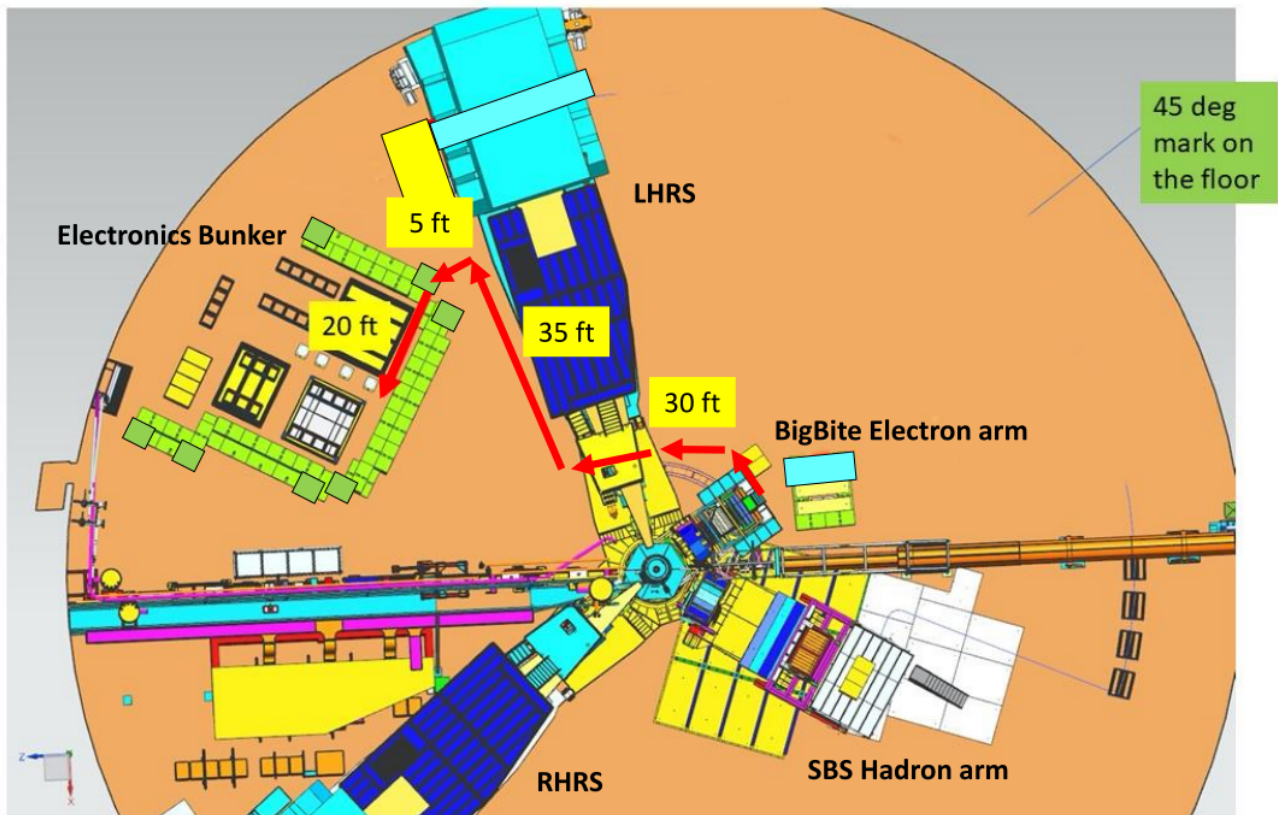


Figure 4.9: The cable path for the HV, LV, ADC coax, and TDC ribbon cables are show by red arrows. The total laid cable length from BigBite to the bunker is 90 ft with an additional few feet of laid cable at BigBite for slack and inside the bunker to reach the electronics. Additional cable length was coiled and stored in the bunker. The TDC ribbon cables were run through a flexible rubber conduit for protection. Image courtesy of the SBS Collaboration at JLab.

A new cable connected from the LV power supply in the electronics bunker to the LV distribution box at the TH detector frame had to be created since the old LV power supply cable would not reach from the TH detector frame to the bunker. Additionally, a set of twelve TDC ribbon extension cables were made because the TDC ribbon cables came up approximately ten feet short of the TDC level-translator repeater (LTR) in the electronics bunker. Photos of the fully installed BigBite electron arm, including the TH detector and TH DAQ system can be seen in Figures 4.10, 4.11, and 4.12. After the TH detector and its DAQ were constructed and repaired, but before and during the detector installation in Hall A, the commissioning of the TH detector took place to prove its readiness for use in the G_M^n experiment. This process is detailed in the following sections as well as the calibration of the detector, which was initially completed as a "rough" calibration during the experiment, but was eventually finalized. This concludes the overview of the TH detector construction and installation.

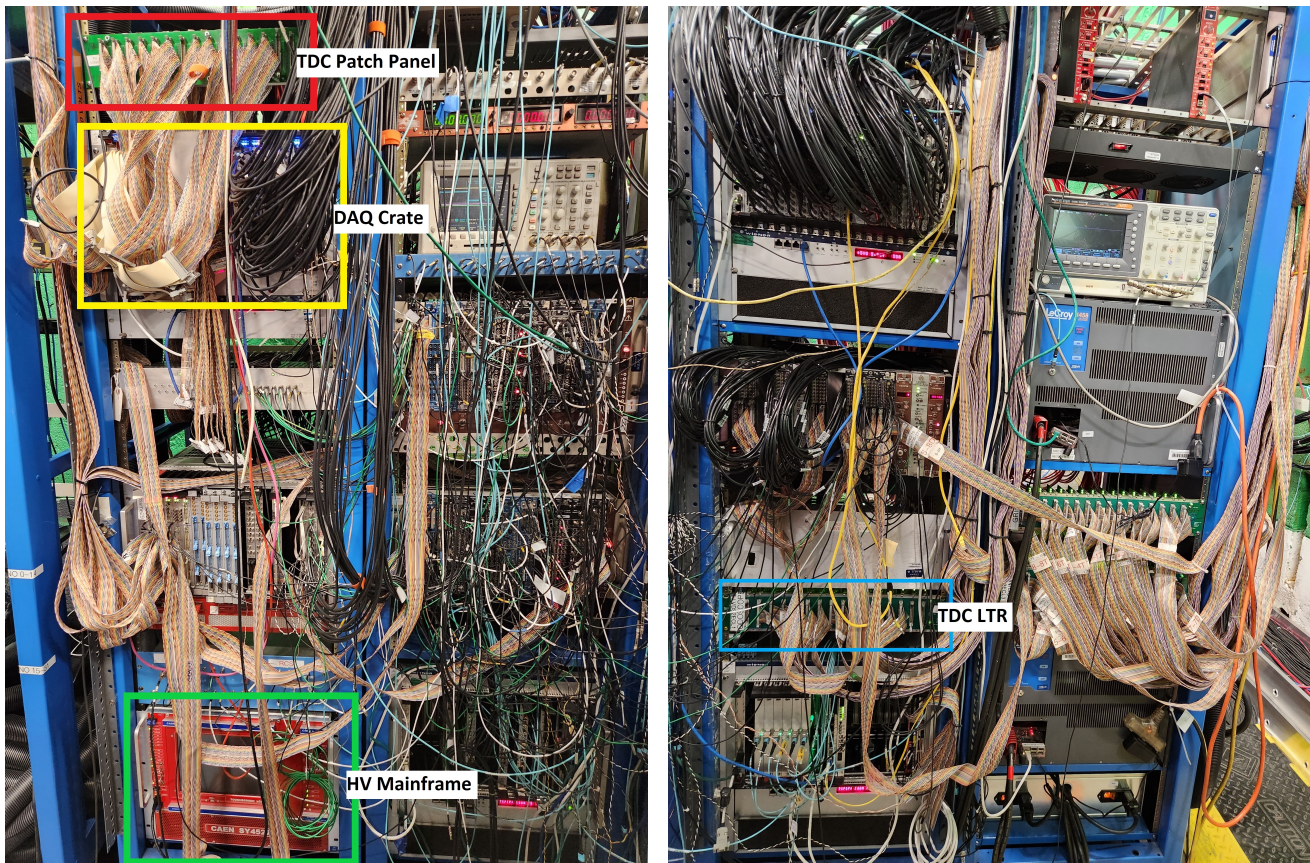


Figure 4.10: A photo of the left half of the electronics racks (left) housing the TH detector TDC and ADC bunker patch panels, the DAQ crate, the LV power supply, and HV power supply, and the right half of the electronics racks (right) housing the LTR and other BigBite detector DAQ modules. Photos by R. Marinaro.

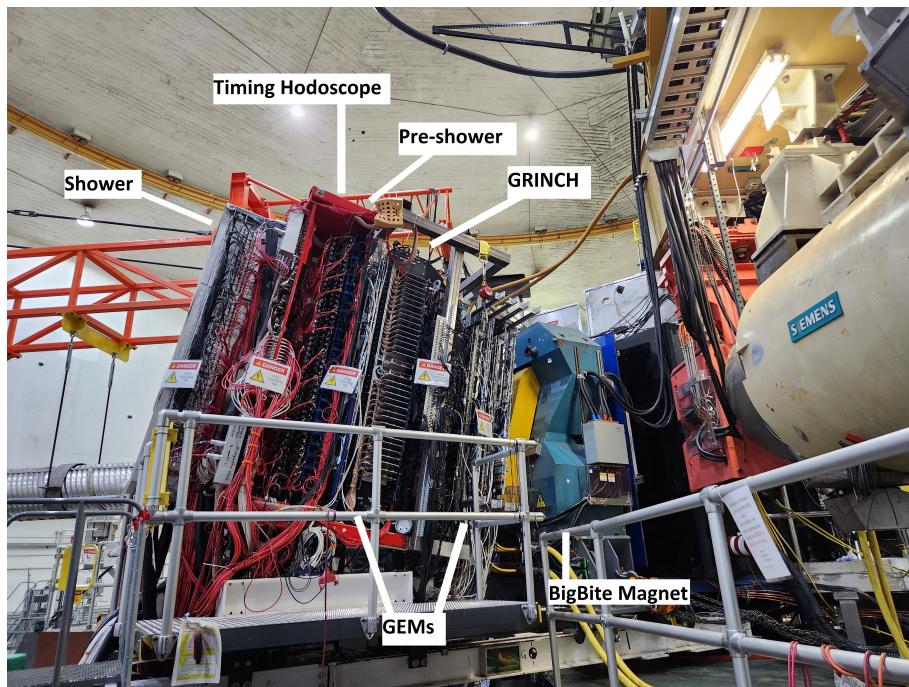


Figure 4.11: A side profile photo of the BigBite electron arm as it is currently, fully installed in Experimental Hall A. Photo by R. Marinaro.

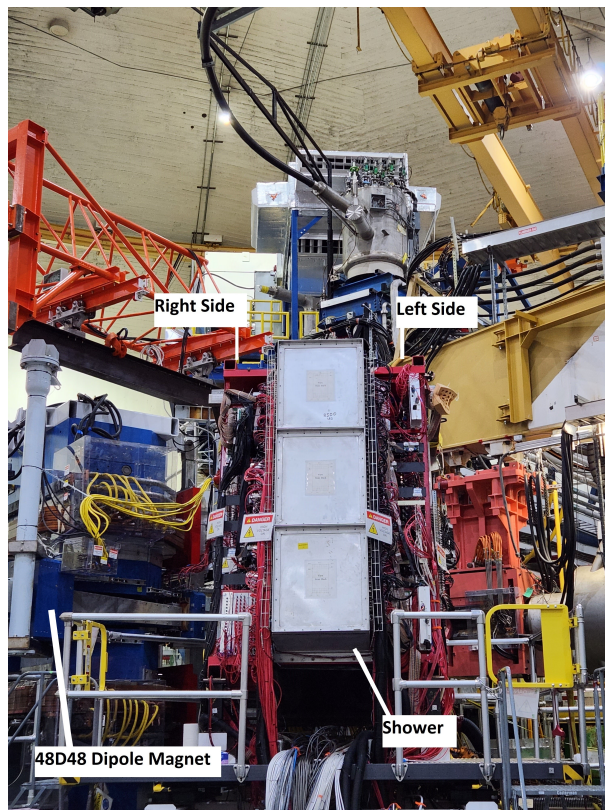


Figure 4.12: A photo of the back-view for the BigBite electron arm looking in the direction of the detector stack towards the target hidden on the other side of BigBite. Platforms on either side allow for access to the PMTs, and NINOs during experiment down time where troubleshooting takes place for any malfunctions of the TH detector of which there were next to none. Photo by R. Marinaro.

4.2 TH Commissioning Studies

Commissioning for all the TH detector ADC and TDC channels begins with first checking that correct signals are present from PMT to readout modules using an oscilloscope. Signals were checked directly from the PMT, directly from the NINOs, and at every patch panel on the detector frame and in the electronic racks. Any components not showing correct signals or no signals were either fixed or replaced. Initially, the TDC signals were unreliable until a grounding issue with the level translator-repeater (LTR) could be fixed. Noisy or missing channels were typically caused by poor connections, or faulty PMT bases. Once these few hardware issues were fixed, testing and analysis of the ADC and TDC data began.

4.2.1 ADC Testing and Analysis

The first step in testing the ADC channels of the TH detector is to confirm that every ADC channel has the expected shape to its distribution. A good plot for an ADC distribution will show a distinct pedestal made of noise or other electrical static coming from the signal channel and a secondary peak which represents the actual ADC signals. For a clean separation between the pedestal and the ADC signals, cuts are applied to the ADC of adjacent channels such that their ADC signals for the same event are above a minimal threshold. This guarantees that only particle tracks which pass all the way or mostly through the scintillator bar are being plotted. These cuts remove events where the particle track only passes through a corner or a small portion of the scintillator bar. Events where the particle track only passes through a small part of the scintillator bar are undesirable for the purposes of commissioning analysis because these sort of events make it difficult to get a clean separation between the pedestal noise and the actual ADC signals. The lack of clean separation makes the task of fitting the ADC distribution impractical and will also incorrectly skew fits to the ADC signal distribution away from the correct value for parameters like the distribution mean. An example of 16 good, analyzable ADC distributions is in Figure 4.13. The ADC distribution plots like those in Figure 4.13 were generated for every channel in the TH detector using the v792 ADC readout modules, which were later replaced with the FADC, and cosmic ray data with a large scintillator external trigger. The x-axis is an ADC converted value for the actual amount of charge in each signal read by a microprocessor which takes in the digital signal voltage and converts that digital signal into a number calculated using a reference voltage.

PMTs 48-63L: ADC bin vs. Hits

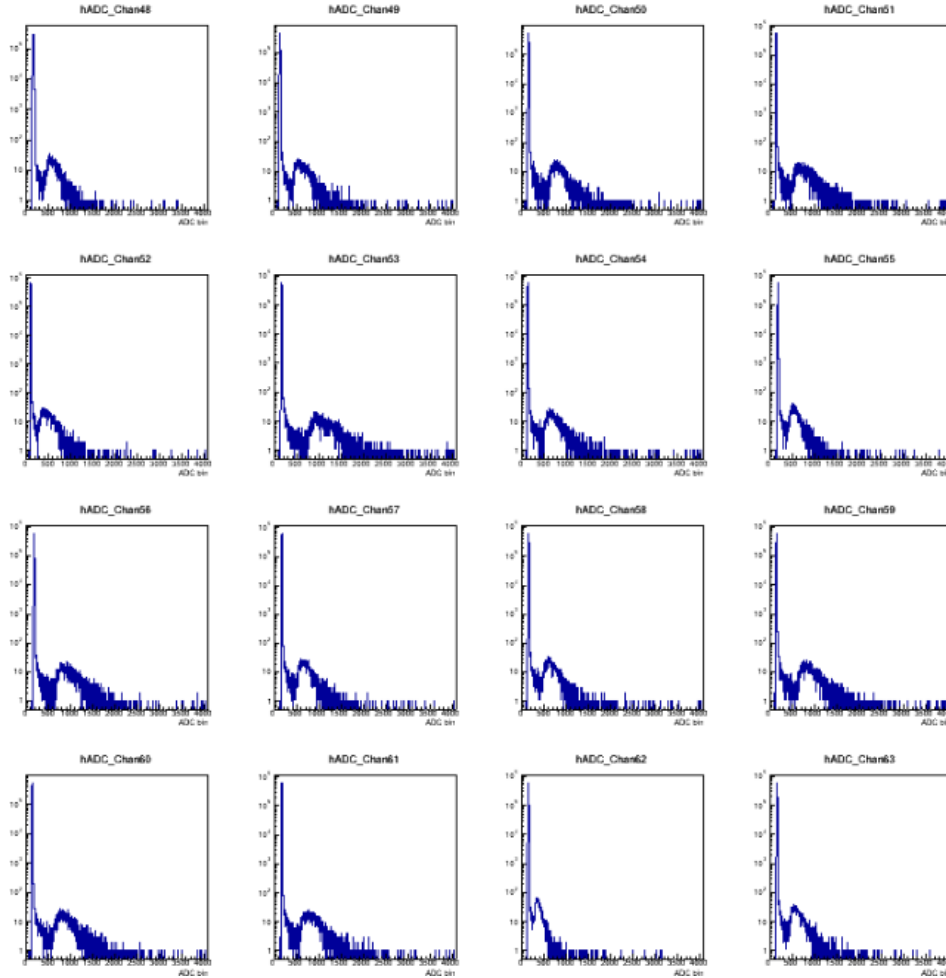


Figure 4.13: A plot of 16 good ADC distributions with pedestal and ADC signal peaks cleanly separated using minimal ADC cuts on the ADC signals from adjacent scintillator bar ADC channels, which ensures that only particle tracks from events that pass all or mostly through the scintillator are being plotted. These plots were generated using cosmic data before installation in Hall A using a large external trigger scintillator positioned on top of the detector frame.

Charge Normalization

After confirming all ADC channels present, and working appropriately, attention was given to a study of charge normalization for each channel. The first step in this study is pedestal subtraction such that the pedestal peak is centered at zero. This study was also completed using cosmic ray data with an external large scintillator trigger and the v792 ADC modules. To subtract the pedestal, a Gaussian fit was applied to the pedestal peak as in Figure 4.14, the mean of the pedestal Gaussian fit was recorded as in Figure 4.15, and the ADC distributions were re-plotted with the pedestal mean subtracted from the distribution. This centers the pedestal mean at zero, and shifts the whole distribution to its correct ADC bin value.

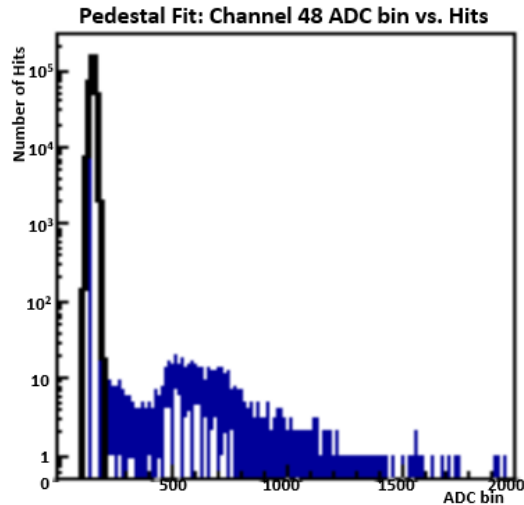


Figure 4.14: A plot of the ADC distribution for channel 48 left (48L) showing the Gaussian fit to the pedestal. Once the mean is subtracted the whole distribution shifts down by an amount equal to the mean of the fit. This was repeated for all ADC channels left and right.

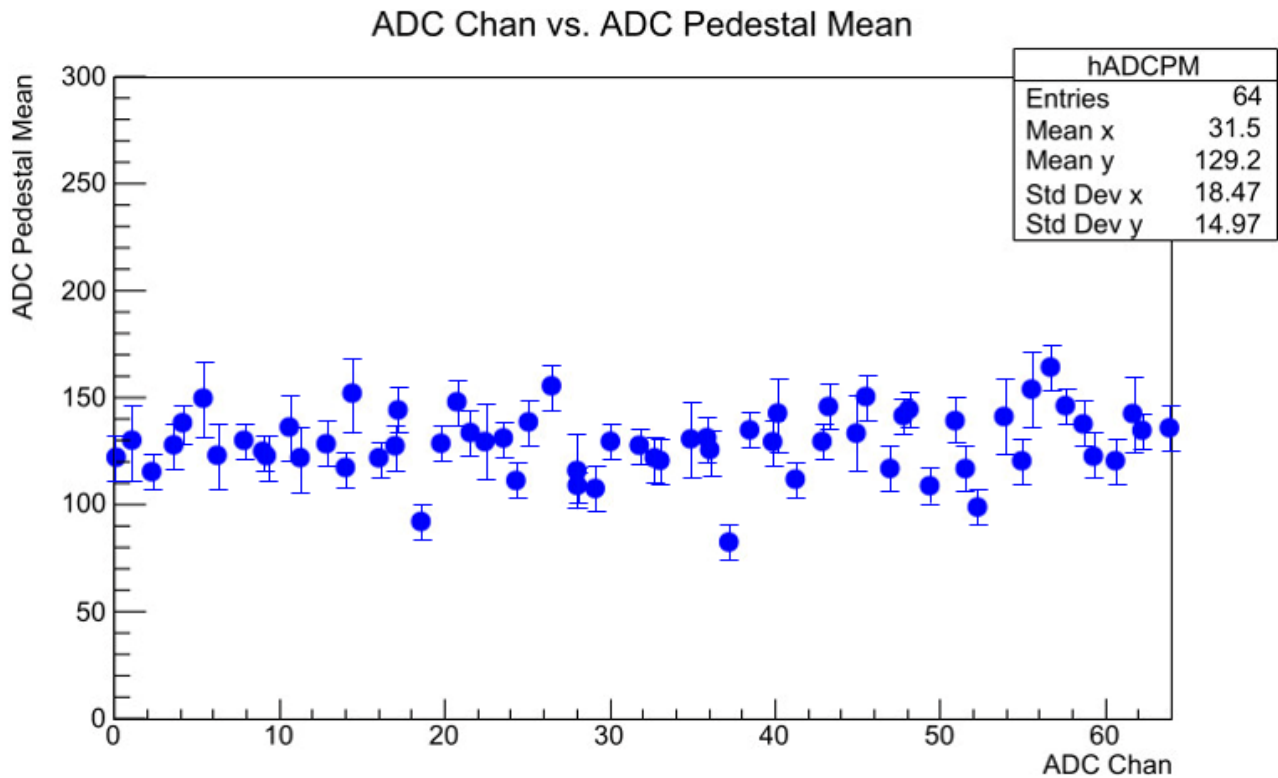


Figure 4.15: A plot of the pedestal Gaussian fit mean values for the set of 64 middle, bars 33-64 left and right, channels of the TH detector using cosmic ray data with the v792s and large external scintillator trigger. Similar plots were generated for every ADC channel to confirm an initial uniformity of the pedestal means across the whole TH detector.

The second step is removing the pedestal from the ADC distribution plots for a clean fit of the ADC signal peak. The pedestal is removed by placing a pedestal cut at three RMS (standard deviations) above the mean of the pedestal Gaussian fit. The ADC signal peak is fit with a Landau function. The peak of the Landau fit on the ADC signal peak is called the ADC MPV (most probable value). Once the starting ADC MPV for all channels are recorded, the HV value for every channel is adjusted to normalize all ADC channel MPVs to one value in ADC bin. The chosen optimal ADC bin value was decided to be 300 since this ADC bin value was seen on the oscilloscope as equating to an ADC signal which has a time over threshold (TOT) of 15-20 ns. The optimal operating range of the NINO cards in terms of TOT is 10-20 ns. Thus, an ADC normalized bin value of 300 sets all channel HV values to be optimized to have an ADC MPV towards the higher end of the NINO card TOT optimal operating range. Having the signals on the higher end of this range is good for two reasons: the signals are within the optimal TOT operating range and the signals are large enough to be distinctly separated from the pedestal noise. Plots of this charge normalization process are shown in Figures 4.16, 4.17, and 4.18.

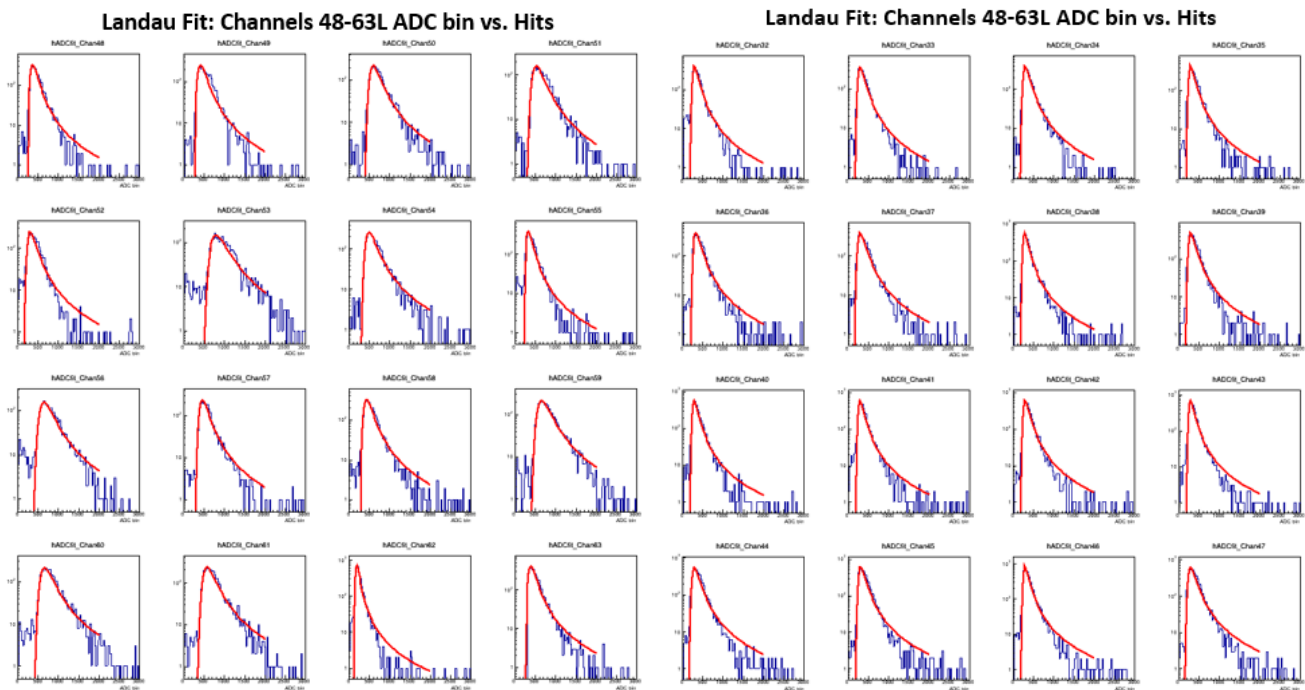


Figure 4.16: The left set of 16 plots (in a 4x4 array) in this figure show the Landau fit for a set of 16 ADC distributions with pedestals subtracted and removed. These plots are far less uniform than the set of 16 plots on the right which were generated after adjusting the HV settings for a successful optimized charge normalization.

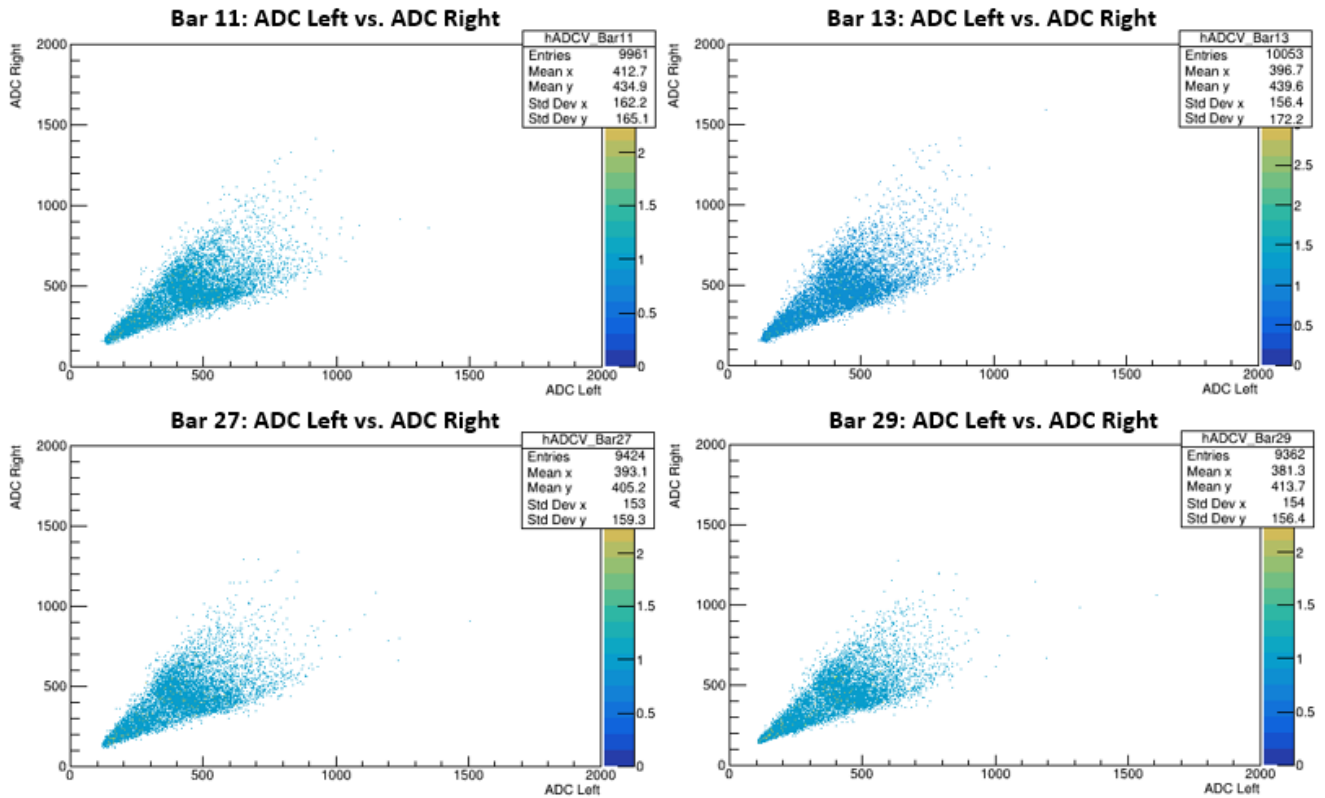


Figure 4.17: Four plots from Bars 11, 13, 27, and 29 showing the ADC distributions left and right for each bar plotted against each other after charge normalization. These plots show a strong correlation and uniformity by their tight cone shape, which further underscores the success of the ADC distribution charge normalization process. The only cuts applied here are ADC neighbor cuts to ensure cosmic tracks that pass all the way through the scintillator bar.

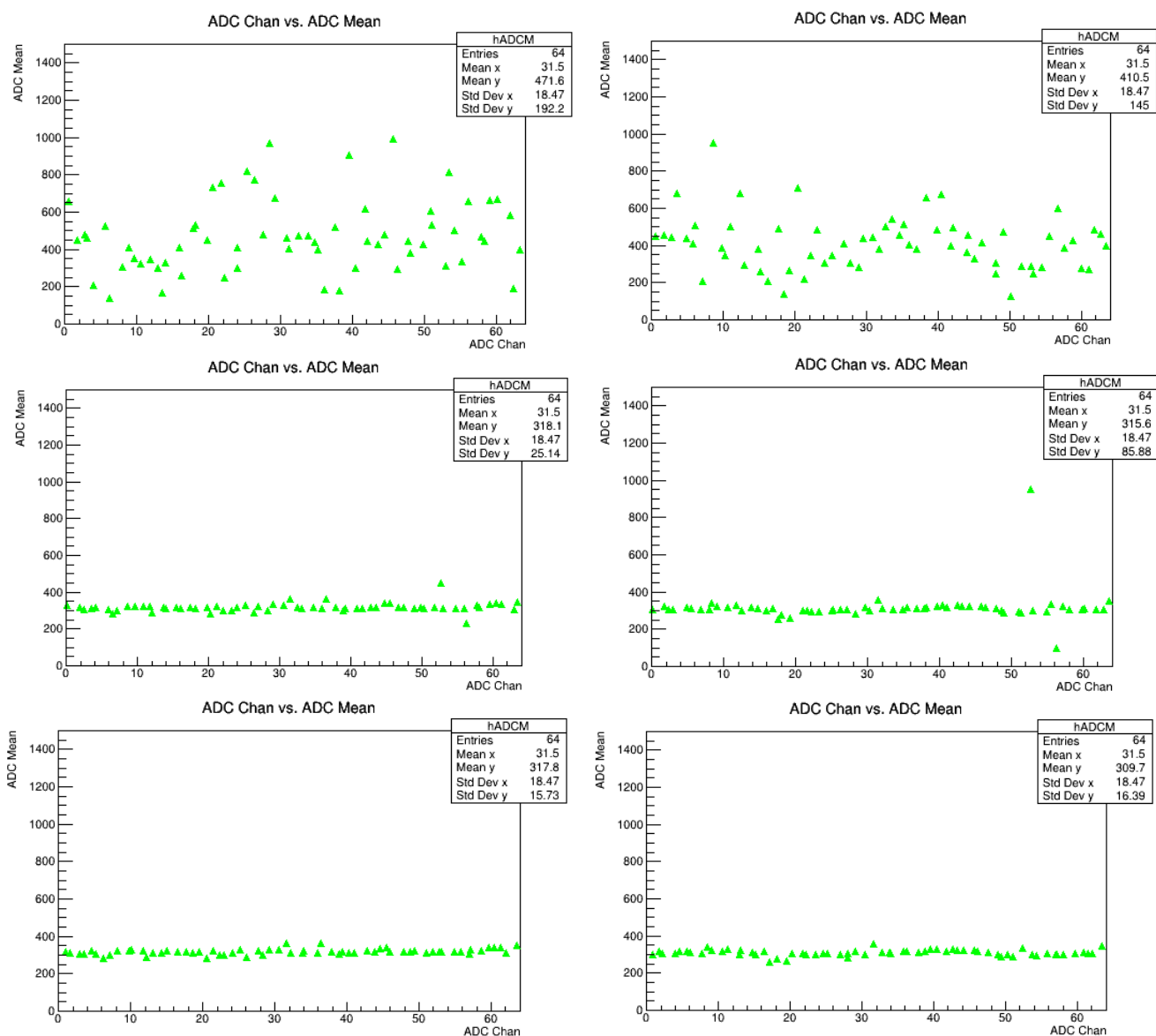


Figure 4.18: Six plots of ADC Means or MPVs from the Landau fits on the ADC distributions. The first column of plots shows charge normalization for the lower third of the detector progressing from the initial ADC MPV values at the top to their final values at the bottom. The second column shows, similarly, charge normalization for the middle third of the detector. This process was repeated for the upper third with similar behavior and results as in the plots shown above. These plots were generated using cosmic ray data with the ADC v792 readout modules and a larger external scintillator trigger.

As seen from the bottom two plots in Figure 4.18, the study for charge normalization of the ADC distributions was successful in normalizing all ADC channel landau fit MPVs to a value of 300 ADC bins. This process took several rounds of adjusting the HV settings until all channels were set to their optimal HV values. The optimal HV values were recorded in Appendix G, and used for the TH detector during the G_M^n experiment. Some adjustments were made for a final set of HV values once an analysis of the TH detector rates could be completed because the rates were estimated to be running above the recommended limit. Therefore it was necessary to drop the HV values by 50V across the whole detector toward the end of the G_M^n experiment run schedule.

ADC Multiplicity

Other than looking at the ADC distribution plots directly, another means of confirming that several ADC channels in the TH detector are functioning properly is with a single plot of 64 ADC channels and their multiplicities. ADC Multiplicity for the TH detector is the number of signals recorded during a single opening of the ADC gate, prompted to open by the input trigger. Often, when the gate is open, the ADC readout modules record two or more signal pulses, one being the desired signal, and the other(s) coming from background accidentals. Some channels will have more events with >1 multiplicity and missing channels will show no hits. Multiplicity allows for checking several missing or noisy ADC at once.

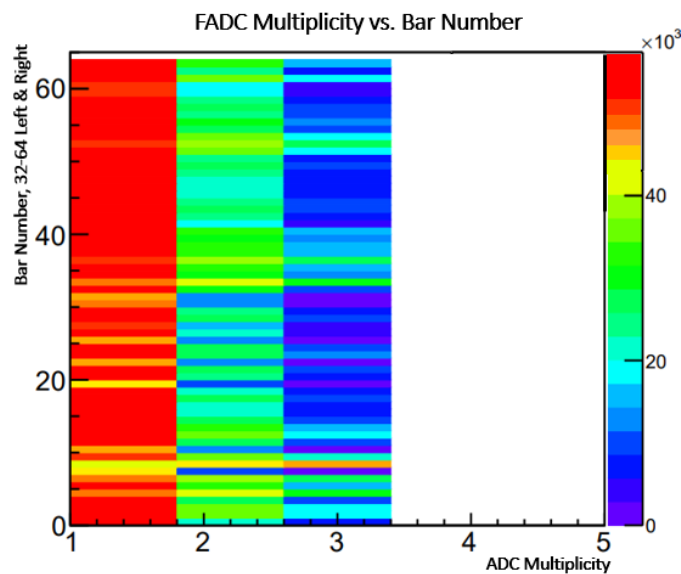


Figure 4.19: A plot of ADC multiplicity where on the y-axis 0-31 corresponds to bars 33-64L and 32-63 to bars 33-64R. These bars are the middle third of the TH detector. This plot was generated with beam-on-target data and using the BigBite calorimeter trigger and FADC readout modules.

Relative Gain Curves

The ratio of the anode current to the photocathode current, G , is the gain or current amplification of a PMT. It fluctuates according to the power of the supplied voltage and the ratio:

$$\frac{G_2}{G_1} = \left(\frac{V_2}{V_1}\right)^{\alpha N} \quad (4.1)$$

Here G_2 and G_1 are gains at supply voltages V_2 and V_1 , respectively; α is a coefficient (0.6 to 0.8) determined by the material and geometry of the dynode; and N is the number of dynodes. For the ET-9142 PMTs used for the TH detector, the expected gain taken from the data sheet is 10^6 where $\alpha = 0.8$ at a nominal 50 A/lm (lumens) with 10 dynodes. Gain curves are often shown as straight lines with a slope of aN since they are typically plotted on log-log coordinates. Once the gain at one high voltage is known for individual tubes, data sheets provide the usual value of the slope, making it simple to compute the gain at any supply voltage, or vice versa. For the ET-9142, for instance, aN is approximately 8.0, so the gain will almost double for a 10% voltage increase. These data sheets provide gain curves which are based on ideal operation of the PMTs, so it is best to produce gain curves for each PMT as their performance will vary. Experiment scheduling did not allow for measurement of the absolute gain for the TH detector PMTs, but relative gain curves were fitted for all PMTs to plots of the FADC amplitudes in mV versus high voltage setting which ranged from 700 to 1000 volts as shown in Figure 4.20. A table of all FADC mV values versus HV setting for each PMT is provided in Appendix H.

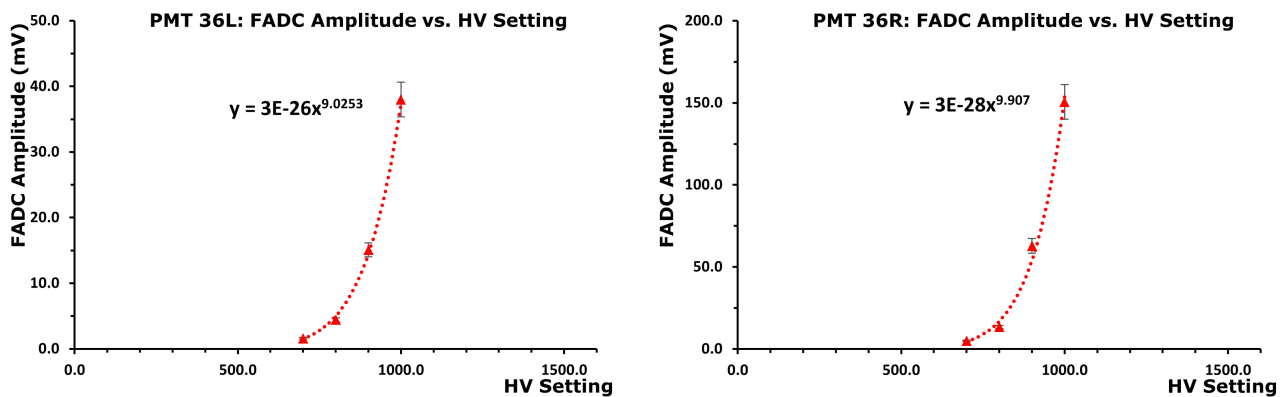


Figure 4.20: Two plots for PMTs left and right attached to bar 36 showing the relative gain curves fitted to FADC amplitude most-probable-values (MPVs) extracted from landau fits to the mV distribution from each PMT. This process was completed for all TH detector PMTs and the parameters of their relative gain curve power-law fits were recorded.

4.2.2 TDC Testing and Analysis

The first step in testing the TDC channels of the TH detector is to confirm that every TDC channel has the expected shape to its distribution. A good plot for a TDC distribution will show a single peak which represents the actual TDC signals. This peak then has to be corrected using the reference signal input into the TDC v1190 readout modules using channel 127 from the trigger. This corrects the timing of the signal which has to pass through all the cables and electronics to its correct time. There were some initial setbacks in terms of troubleshooting issues with the TDC channels, but all channels were confirmed to work properly after fixing a grounding issue with the level translator-repeater which converts the TDC signals from LVDS to ECL. The incorrect grounding caused an offset to the TDC signal baseline which shifted the signal up or down, making the TDC distributions either disappear or incredibly noisy. An example of a reference corrected TDC distribution after alignment is in Figure 4.21, and a 2-D plot of all TDC distributions versus PMT number after Hall A installation, but before alignment, is in Figure 4.22. The data shown in Figure 4.21 is from an SBS-4 kinematic setting cosmics data run, but before calibration of the TH detector was completed, therefore it is a plot of raw TDC leading edge data.

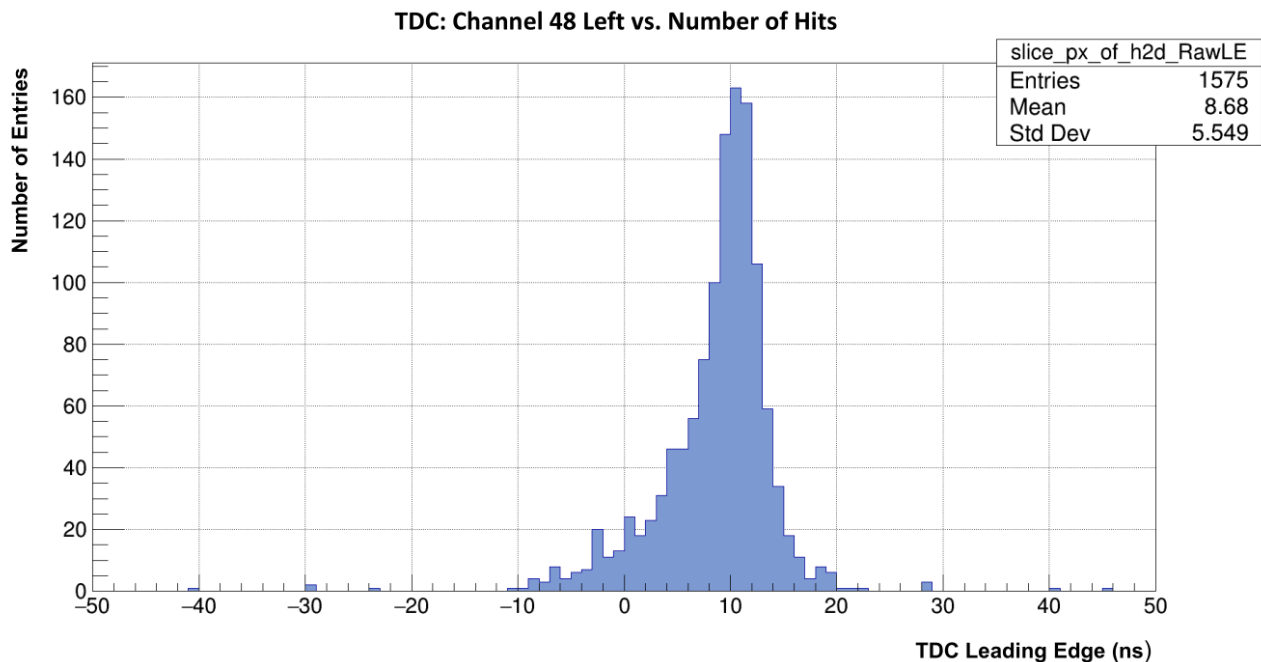


Figure 4.21: An example plot of a corrected, not calibrated TDC distribution from after Hall A installation during the SBS-4 kinematic setting of the GMn experiment. This plot was generated with cosmic ray data using the BBCal trigger after alignment. Here the peak represents the center of the scintillator bar.

TDC: Leading Edge Time vs. PMT number

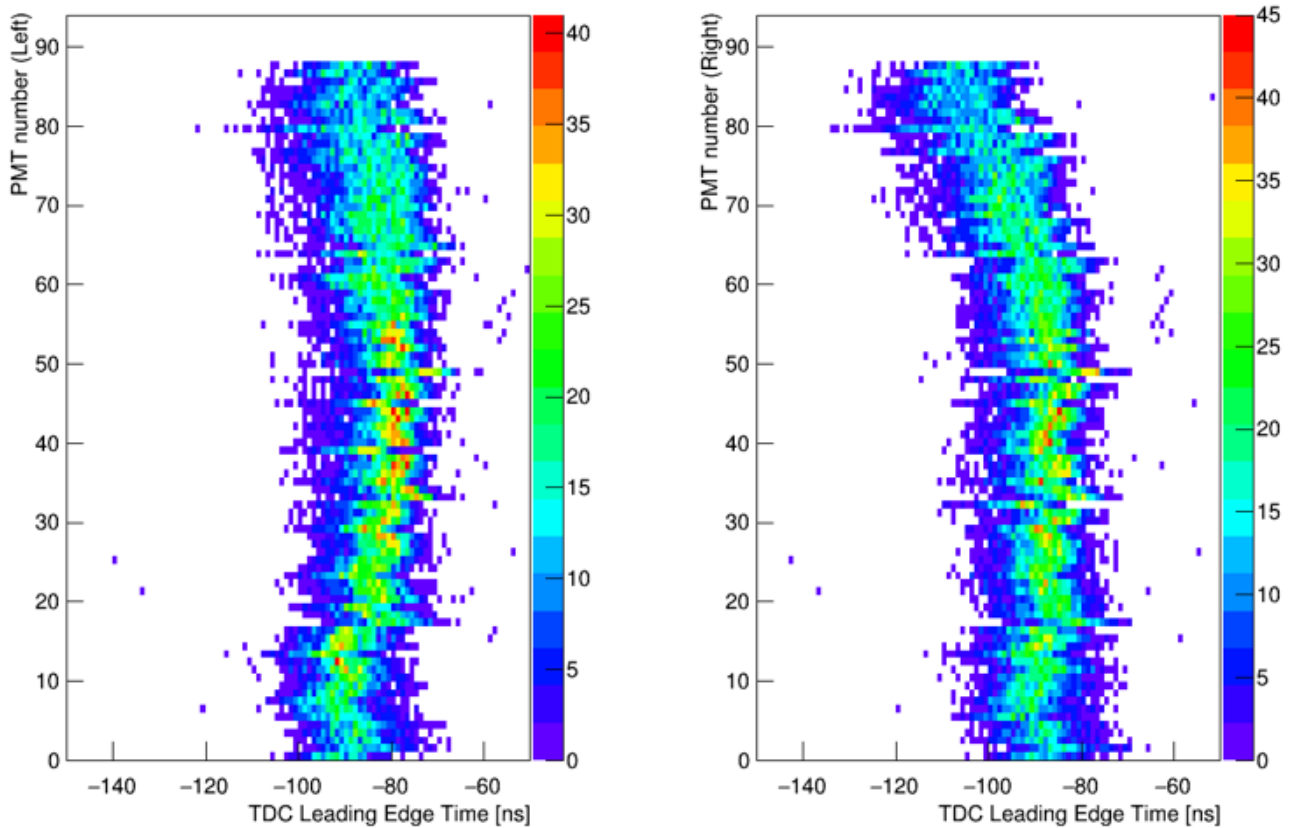


Figure 4.22: Two plots showing the TDC distributions for every channel plotted against their PMT number for the left and right side of the TH detector. Monitoring plots like these are used during the experiment run time for quick checks as time passes and more data runs are taken to confirm there are no missing or noisy TDC channels. These plots were generated with cosmic ray data after installation in Experimental Hall A using the BigBite calorimeter trigger before alignment.

Mean Time

To calculate the mean time of a single bar, the average of the TDC leading edge distributions from the left and right side PMTs for each bar is plotted. This represents the mean time for a single bar for every event recorded from both the left and right PMTs connected to each scintillator bar via the light guides. This calculation comes into consideration when calculating the horizontal position of each event and horizontal resolution for each scintillator bar. This horizontal position calculation is also used in particle tracking which can be compared to the trajectory of the particle track measured by the GEMs. A plot of mean time distributions versus scintillator bar number is provided in Figure 4.23. Data for scintillator bars toward the top of the TH is less reliable due to the lower number of events occurring in that region and this is likely an effect of the BBCal trigger.

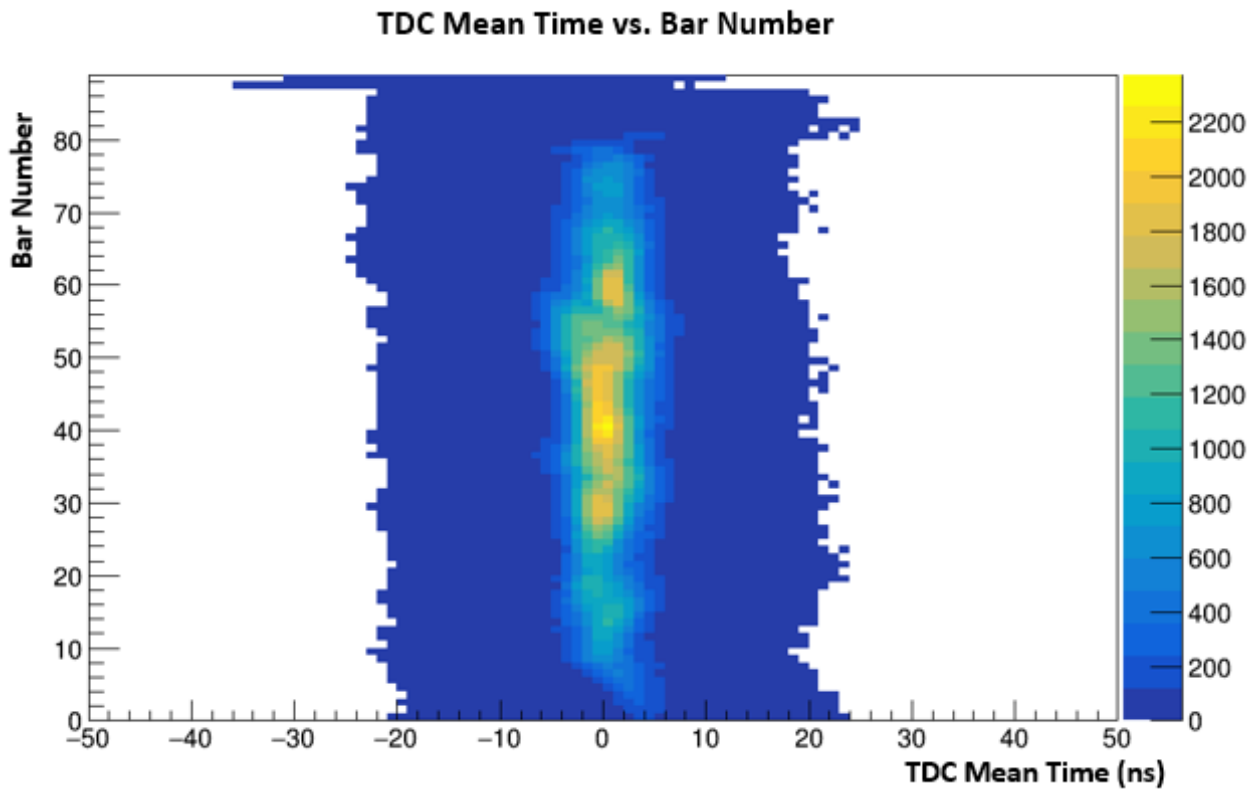


Figure 4.23: An example plot of the TDC mean time leading edge distributions versus bar number using SBS-4 kinematic production data and the BBcal trigger.

Time Difference

To calculate the time difference for a single bar, the difference of the TDC leading edge distributions from the left and right side PMTs for each bar is plotted. This represents the time difference for a single bar for every event recorded from both the left and right PMTs connected to each scintillator bar via the light guides. This calculation, like, the mean time, comes into consideration when calculating the horizontal position for each event and horizontal resolution for each scintillator bar. A calculation of the time resolution is also based on the time difference. This time resolution calculation could also be based on the mean time but using the time difference provides better time resolution. Using the time difference rather than the mean time to calculate the TH detector time resolution provides a better time resolution by approximately a factor of 2-3 on average across all the G_M^n experiment kinematic settings. More on the time resolution analysis is provided in the corresponding section in Chapter 6. A plot of time difference distributions versus scintillator bar number is provided in Figure 4.24, showing the same low event statistical effect for bars at the top of the TH likely caused by the BBcal trigger.

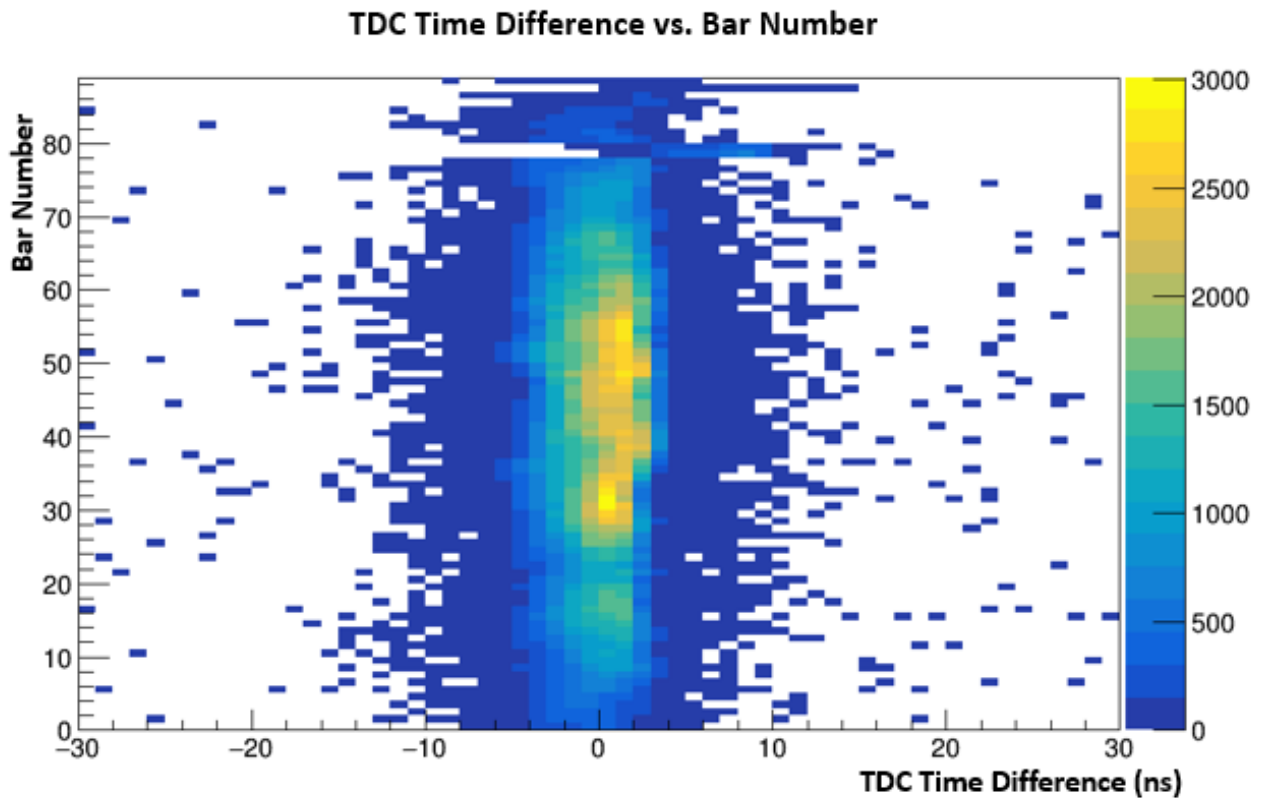


Figure 4.24: An example plot of the TDC leading edge time difference distributions versus bar number using SBS-4 kinematic production data, an LH2 target, and the BBcal trigger.

Time Over Threshold

To calculate the time over threshold for an individual TDC channel the TDC trailing edge for each signal is subtracted from the TDC leading edge. This gives a distribution of widths for the TDC signals in nanoseconds. The time over threshold distribution can then be plotted against the TDC to see the time-walk effect. When plotted against the ADC distribution, there is a curved shaped and when plotted against the TDC there is a more elongated blob shaped. For the plots of TOT versus TDC a linear fit can be applied to get parameters of the distributions that help in correcting the time-walk effect. After applying these fits, the TDC data can be corrected using the linear fit parameters during the calibration. The specific parameters of the linear fit that are used during the calibration are the intercept and slope. A portion of the calibration studies detailed in a later section is dedicated to this correction. Example plots of the fits applied to the time over threshold distribution versus the ADC and TDC distributions are provided in Figures 4.25, and 4.26. The plot shown in Figure 4.27 is another useful plot for identifying missing or noisy PMT channels based on their TOT distribution.

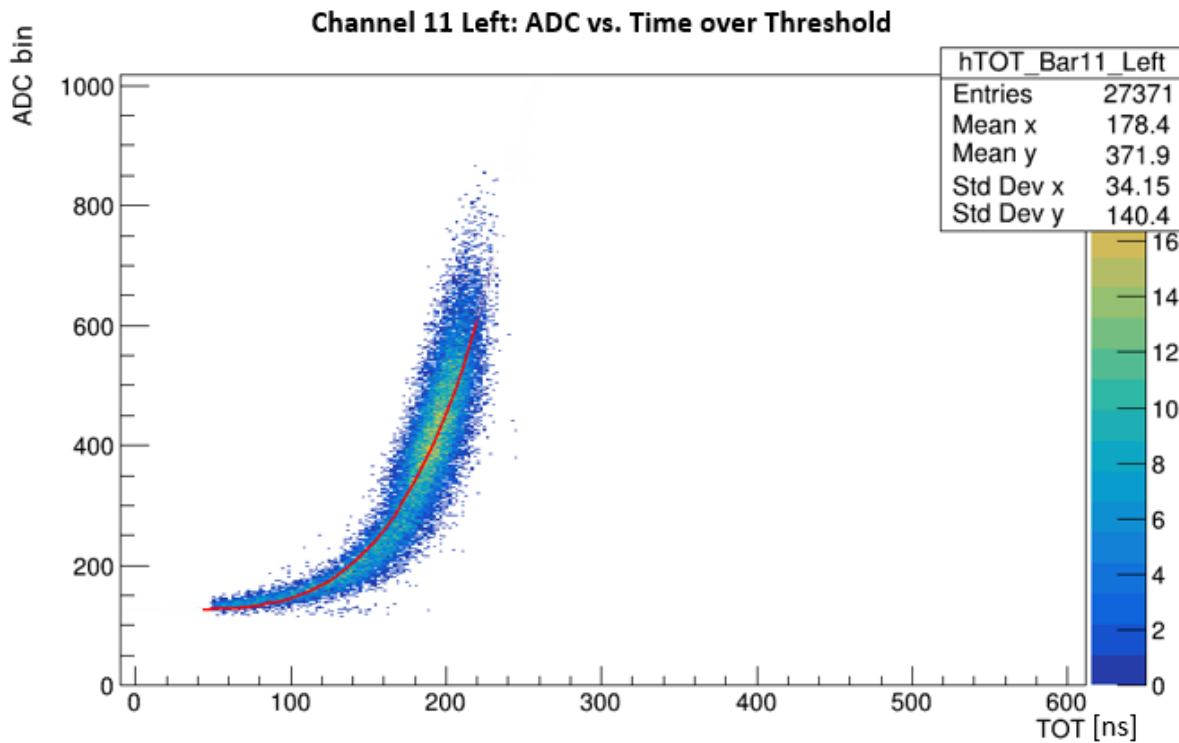


Figure 4.25: An example plot of a time over threshold distribution versus ADC distribution for a single channel using cosmic ray data with the FADC readout modules and the BigBite calorimeter trigger after Hall A installation. The fit used is an exponential function.

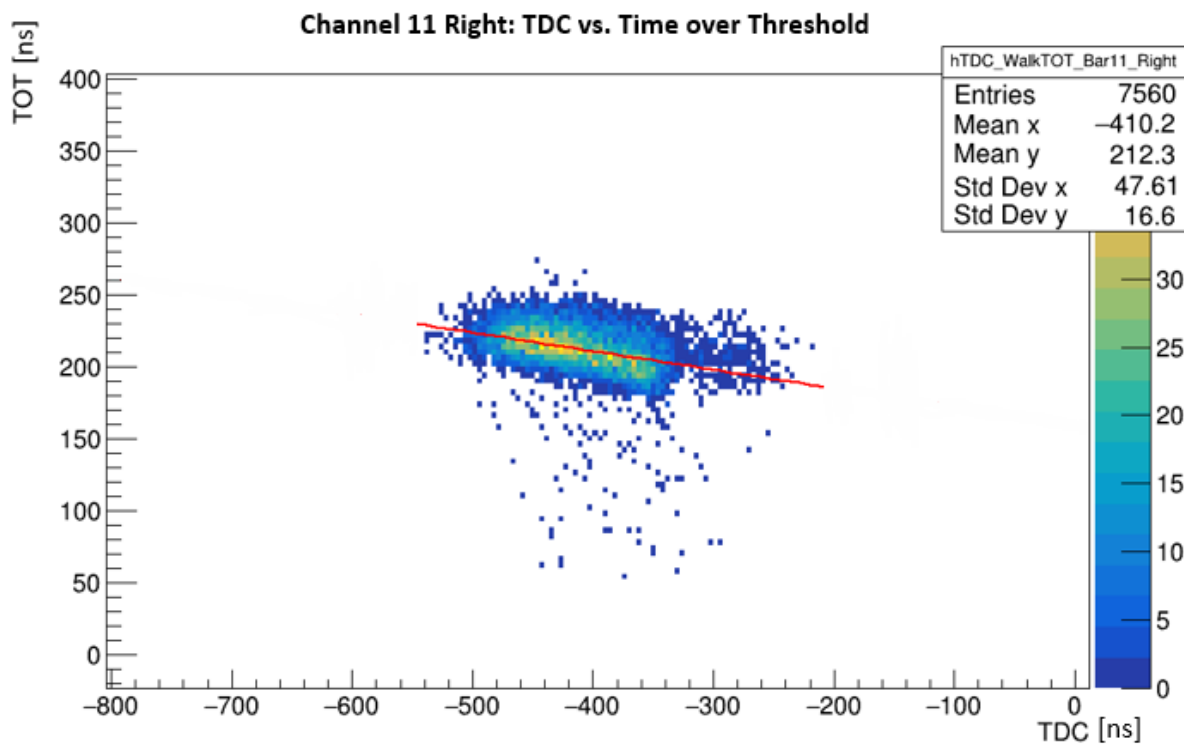


Figure 4.26: An example plot of a time over threshold distribution versus TDC distribution for a single channel using cosmic ray data and the BigBite calorimeter trigger after Hall A installation.

Time over Threshold: TDC TOT vs. PMT number

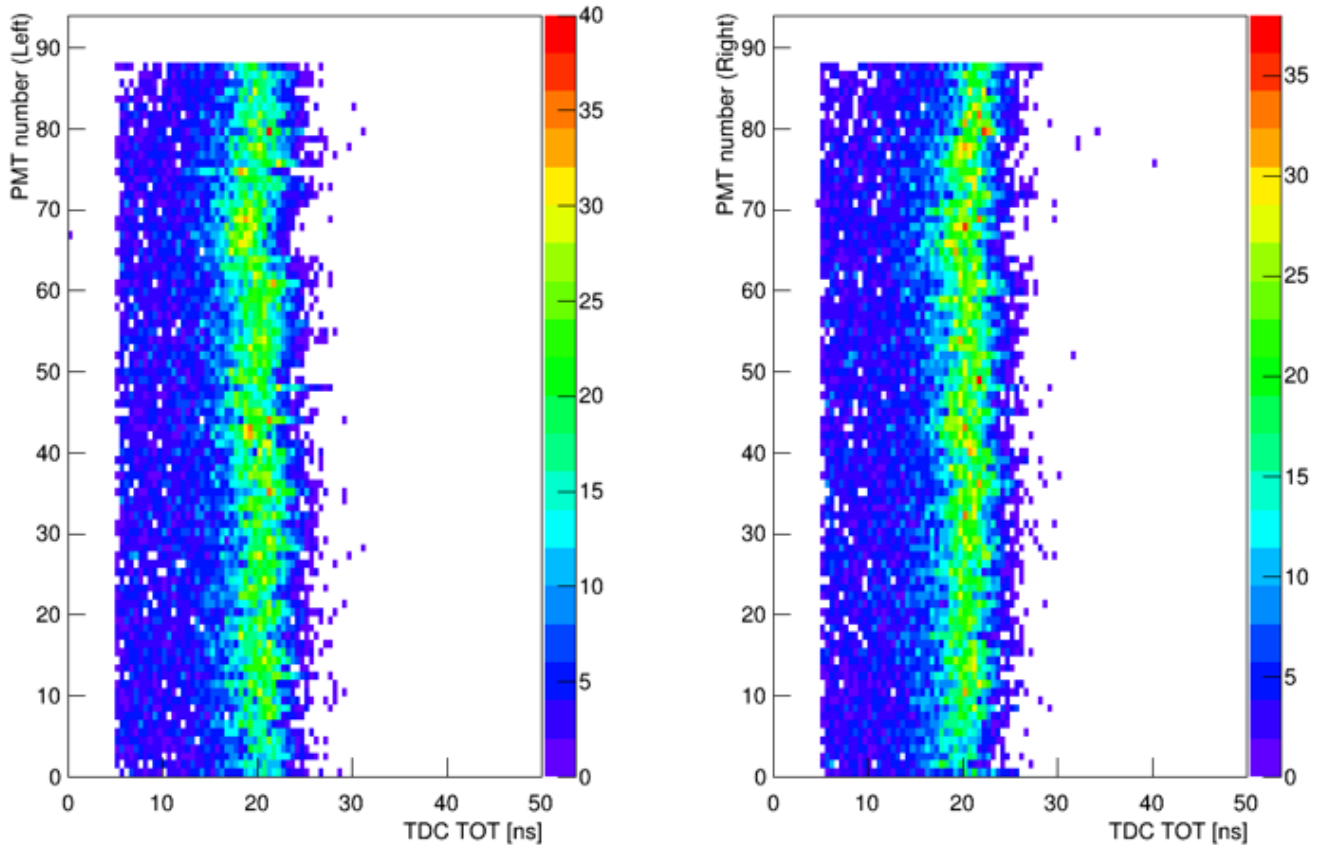


Figure 4.27: An example monitoring plot of the time over threshold distributions versus PMT number using cosmic ray data and the BigBite calorimeter trigger after Hall A installation. This plot is useful during experiment run time to monitor all TDC channels and their time over threshold distributions making missing or noisy channels easy to identify.

TDC Multiplicity

Other than looking at the TDC distribution plots directly, another means of confirming that several TDC channels in the TH detector are functioning properly is with a single plot of all 180 TDC channels and their multiplicities. As previously defined, multiplicity for the TH detector is the number of signals recorded during a single opening of the TDC gate, which is prompted to open by the input trigger. Often enough, when the gate is open, the TDC v1190 readout modules record two or more signal pulses, one being the signal corresponding to a desired particle interaction event in the detector, and the other(s) coming from background accidentals, which increase with rate. The signal closest to zero in the distribution is selected as the desired signal. If a channel is missing, it will show no hits. Therefore, multiplicity allows for checking several TDC at once. Figure 4.28 shows an example plot of TDC multiplicity.

TDC Multiplicity vs. Bar Number

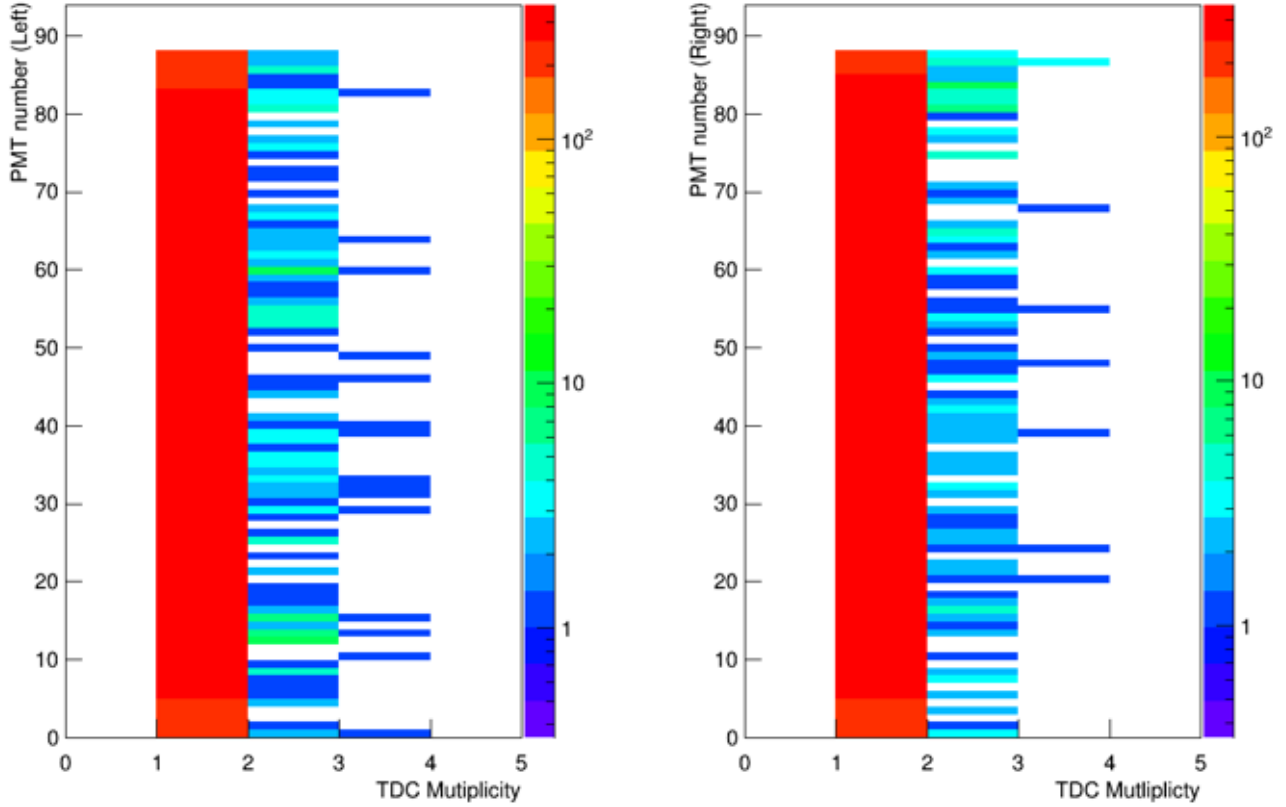


Figure 4.28: A plot of TDC multiplicity for all 180 channels of the TH detector. This plot was generated with cosmic ray data and using the BigBite calorimeter trigger and FADC readout modules after Hall A installation.

4.3 TH Calibration Studies

After commissioning the TH detector, and confirming that all of its channels were operational and ready for use in experimentation, a series of calibrations were made to the TH detector timing data in the first few weeks of the G_M^n experiment. These calibrations are intended to correct the timing data. They account for various physical and electronic effects which skew the timing data such that, without calibration, it is not true to the real timing of particle interaction events occurring in the scintillating material of the detector. Each calibration improves the tracking efficiency, and time and position resolutions, making the TH detector more useful in terms of its most important purpose which is to provide timing information for the calculation of form factors. Arguably, the two most important plots for visual confirmation that the TH detector is well calibrated are shown in Figures 4.23 and 4.24, using first cosmic and later production data. These plots show fully calibrated distributions of mean time and time difference versus bar number. With some exceptions for bars at the top and bottom of the TH where events occur less, thus lowering

the usable statistics, and the reliability of the BBCal trigger at the TH detector extremes is lower, the distributions are mostly uniform. The uniformity of these plots is key to maximizing the performance of the TH in terms of track matching efficiency, and time and position resolutions. It is important to note some calibrations are implemented on a PMT by PMT basis and others on a bar by bar basis.

The calibrations presented were completed using only data from runs in the kinematic setting run group named SBS-4. There are six major kinematic setting run groups (SBS-4, SBS-7, SBS-11, SBS-14, SBS-8, and SBS-9), and each corresponds to a certain distance and angle at which the SBS hadron arm and BigBite electron arm were set. The distance is measured from the target and the angle is relative to the beam line. The number of passes around the accelerator which determines the energy of the beam measured in GeV also varies by kinematic setting as shown in Table 4.2. Since the SBS-4 kinematic setting has the lowest Q^2 and beam energy, SBS-4 was chosen as the most reasonable kinematic setting from which to extract calibration values. Eventually, calibration values will be extracted and implemented in the database files for all six of the major SBS kinematic settings. A table of values for all of the calibrations are provided in Appendix I.

Table 4.2: List of six SBS kinematic settings in run-time order from top to bottom, and their corresponding kinematic values. Additional comments on added shielding and HV changes are in Table 5.1.

Setting	$Q^2(\text{GeV}/c)^2$	$E_{beam}(\text{GeV})$	$\theta_{BB}(\text{deg})$	$d_{BB}(\text{m})$	$\theta_{SBS}(\text{deg})$	$d_{SBS}(\text{m})$	$d_{HCAL}(\text{m})$
SBS-4	3.0	3.7	36.0	1.80	31.9	2.25	11.0
SBS-7	10.0	8.0	40.0	1.85	16.1	2.25	14.0
SBS-11	13.6	10.0	42.0	1.55	13.3	2.25	14.5
SBS-14	7.5	6.0	46.5	1.85	17.3	2.25	14.0
SBS-8	4.5	6.0	26.5	2.00	29.9	2.25	11.0
SBS-9	4.5	4.0	49.0	1.55	22.5	2.25	11.0

4.3.1 Timing Cuts

The three majors cuts on the TDC data readout by the TDC 1190s cuts are for defining the TDC good timing, the TDC window, and the time over threshold distributions. The first cut for TDC good timing accounts for the events where more than one TDC signal is recorded. For an event with TDC multiplicity greater than 1, there must be a means for discriminating which of the multiple TDC signals is the true signal for that event. This is done by fitting a Gaussian function to the TDC distribution to find the TDC

time mean and then choosing the signal which has a TDC value closest to the mean of the TDC distribution. This process is also implemented for the reference TDC channels for both TDC 1190 modules. The value for multiplicity timing cut on the reference signals remains the same throughout the calibrations, but the TDC good timing cut on the individual TDC channels changes as more calibrations are implemented. Since the alignment of the TDC distributions detailed in the following section shifts the mean of the TDC distributions to be centered at zero, the TDC good timing cut also eventually gets closer to zero with the TDC distribution mean as a result.

Less complicated are the cuts on the TDC window and the time over threshold distributions which simply narrow the accepted range of events being used. Cuts on the TDC window help remove TDC values that fall well beyond what could be considered real events within the given length of the scintillator bars. The cuts on the TOT distributions remove a large amount of signals where the time over threshold value falls so low that the signal could not correspond to a real event in the detector. After TDC alignment the TDC window cuts were set at -20 to 20 ns and the TOT distribution cuts were set at 7 to 30 ns. These cuts are implemented in the replaying of the evio data files using the Hall A analyzer, which is when the data files are converted to analyzable ROOT files.

4.3.2 TDC Alignment

The calibration for aligning the TDC distributions corrects discrepancies among the various channels for their timing caused by slight variances in the propagation of signals through the electronics and cables from the scintillator bars to the readout electronics. This calibration is implemented on a PMT by PMT basis by fitting the TDC distributions with a Gaussian, extracting the mean, and then applying an offset by subtracting the mean from the distribution. This centers the distribution at zero. In this correction, zero represents the center of the TH detector. As further cuts were applied, the alignment calibrations were adjusted in a cyclical process until the final alignment values were determined after a few rounds of calibration and subsequent re-calibration. Plots of the TDC distributions versus PMT number for both the left and right side of the TH detector are provided in Figure 4.29. These plots show improved uniformity when compared to similar plots from Figure 4.22. Both figures show data taken with cosmic ray data, and the calibration for TDC alignment was redone with production data from the SBS-4 kinematic setting once the GMn experiment began.

TDC Alignment: TDC Leading Edge vs. PMT Number

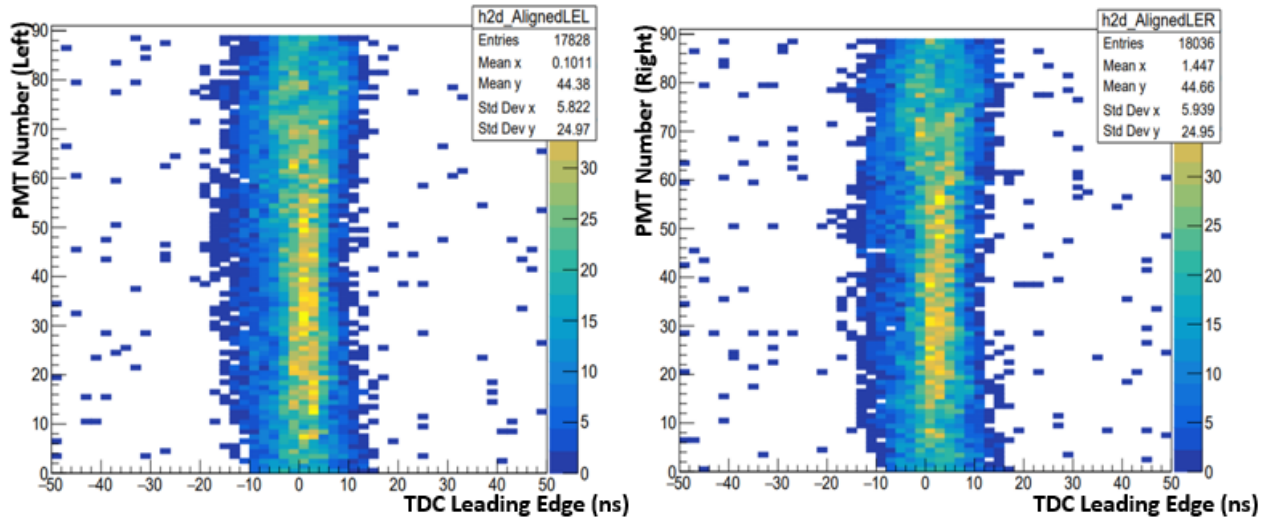


Figure 4.29: Two plots of TDC leading edge time versus PMT number left and right after TDC alignment. This data was taken from an SBS-4 cosmic data run in Hall A using the BBCal trigger.

4.3.3 Time-walk Correction

The time-walk effect is a shift in timing which arises due to the finite rise time of the PMT analog pulse. For any given event, signal pulses with different amplitudes pass above the discriminator threshold at different times. Essentially, the time-walk effect defines the difference in time delay between large and small hits. Figure 4.30 gives a visual description of the time-walk effect.

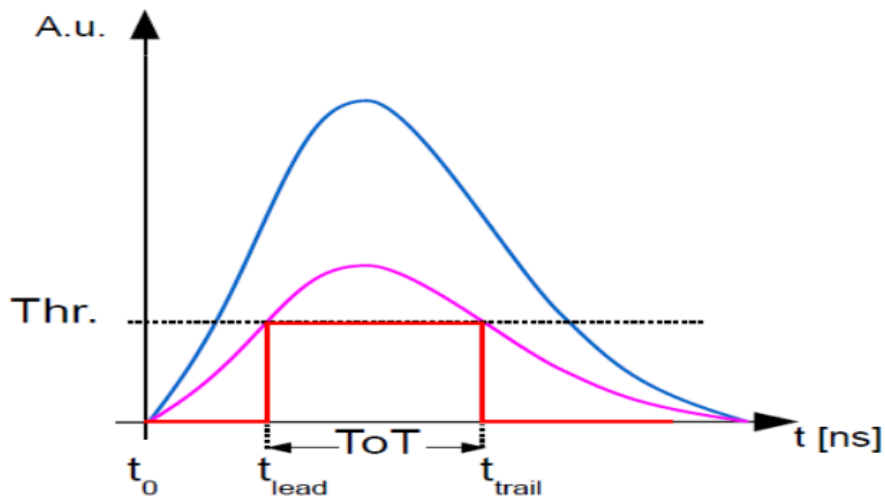


Figure 4.30: The difference in time for the leading edge of the blue versus the purple pulse is the result of the time-walk effect which causes the time over threshold (TOT) to be shorter for smaller signals and longer for larger signals. Image from [63].

As shown in Figure 4.26, the time-walk effect skews the TDC data. Since the primary purpose of the TH detector is to provide timing information, the time-walk correction was applied to the TDC data only. This makes the calibration simpler as the relation between the TDC and TOT is linear. Therefore a linear function is fitted to a plot of the TDC versus TOT and this function gives two parameters of interest which are the slope and the intercept. Both parameters are input into the TDC database file as time-walk calibration values. The slope and intercept of the linear fit allow for all TDC leading edge values to be corrected to zero no matter the size of the signal pulse. Example plots and a description of the fitting process are provided in Figure 4.31 and 4.32 using SBS-4 data with an LH2 target and BBCal trigger. Segmentation of TOT by bin provides for a more accurate linear fit when applied to the Gaussian fit extracted means. As TOT increases, the mean and sigma from the Gaussian fit to the TDC distribution from each TOT segment becomes less reliable due to lower stats as events at larger TOT is less than in the center of the TOT distribution as shown by the TDC maximum plotted versus TOT bin segment.

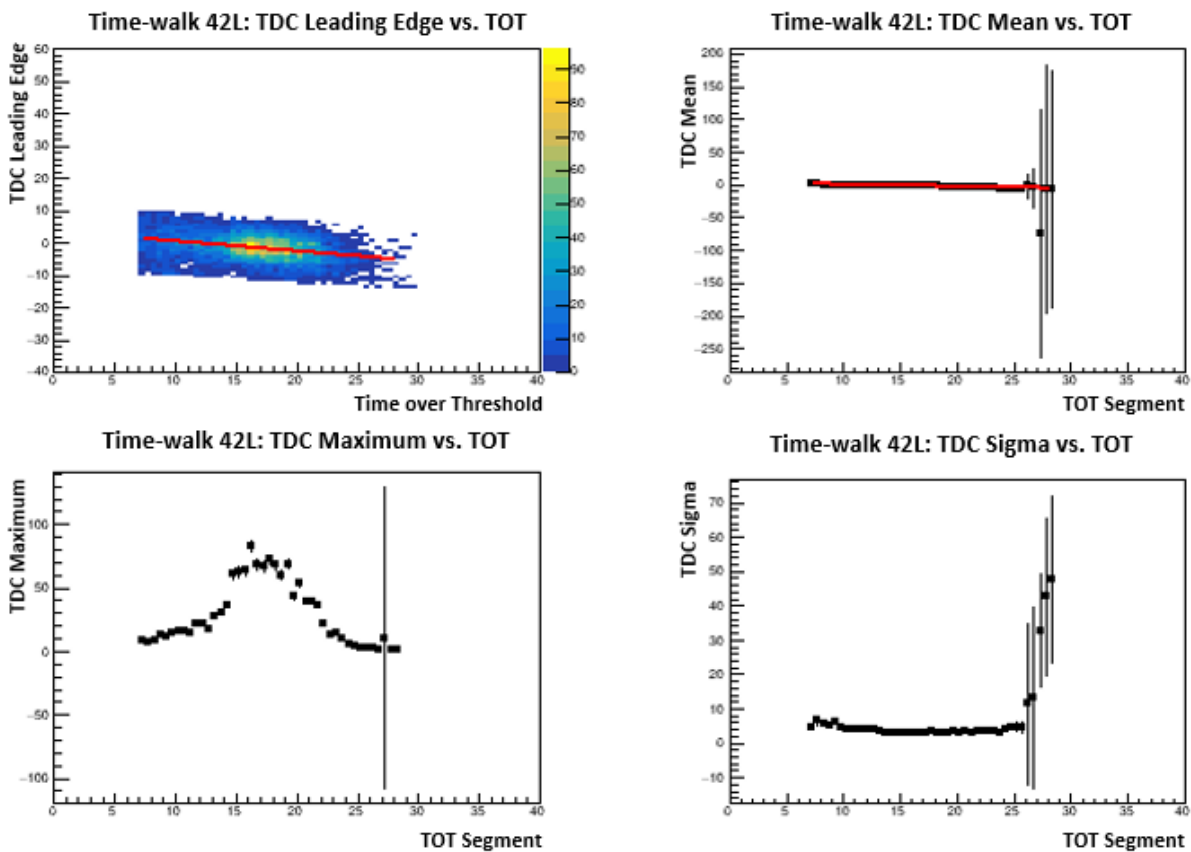


Figure 4.31: Four plots including TDC leading edge versus TOT (top left) for PMT 42, left side. The other three plots are the mean (top right), maximum (bottom left), and sigma (bottom right) parameters taken from Gaussian fits applied to the TDC distributions for one bin segments of the TOT.

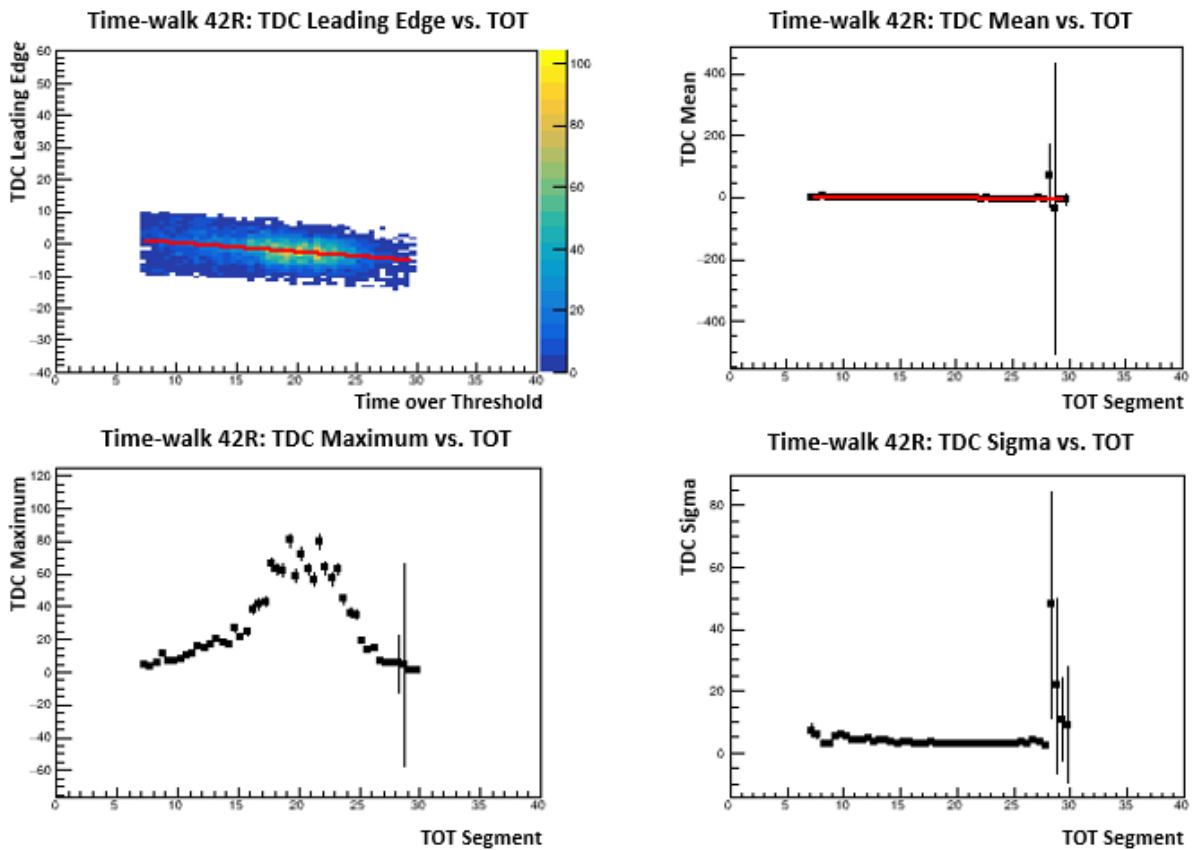


Figure 4.32: Four plots including TDC leading edge versus TOT (top left) for PMT 42, right side. The other three plots are the mean (top right), maximum (bottom left), and sigma (bottom right) parameters taken from Gaussian fits applied to the TDC distributions for one bin segments of the TOT.

For a better visual understanding of the time-walk correction being applied to the TDC leading edge data, consider the plots from Figures 4.31 and 4.32 with the time over threshold plotted versus the TDC leading edge. This plot has a slight downward slant that should be flat and centered around a TDC leading edge value of zero. Just as the TDC alignment calibration corrects the TDC distribution to be centered at zero, the time-walk correction adjusts this slanted behavior such that the TDC distribution is centered at zero relative to the TOT. The time-walk correction was applied to all PMTs and their calibration values taken from the slopes and intercepts of the linear fits to the TDC distribution means versus TOT segment were recorded in the TDC database file.

4.3.4 Time Difference Offset

Just as the TDC distributions were aligned to be centered at zero, the TDC difference, which is the difference in time measured by both the right and left side PMTs for a single bar, spectra were aligned to

zero. The TDC difference offset is applied on a bar by bar basis, and accounts for discrepancies in the electronics corresponding to the left and right side of each scintillator bar. Ideally, the TDC difference between left and right side channels for each individual bar should be centered at zero since most particle interaction events occur in the center of the TH detector. To extract the time difference offset from the data a plot of time difference versus horizontal position along the bar is generated. The time difference is calculated as the left side TDC leading edge minus the right side TDC leading edge for each bar. This calculation of time difference was further improved on by using only events corresponding to one cluster, a cluster size greater than one, and a cluster width no greater than two. A cluster is defined as an event which generates sizable signals in more than one scintillator bar for both the left and right side PMTs. Doing this allows for better precision in calculating the time difference since more bars are used which helps filter events which exist farther out on the extremes of the time difference distributions, allowing for a more refined, tight and narrow peak in the TDC time difference spectrum for fitting. Cutting on the cluster width such that the width is less than two guarantees that the bars in the cluster are close enough together to provide reliable data.

The horizontal position along the bar is calculated by first converting to a transport coordinate system. The x-direction points in the dispersive direction of the detector and the y-direction points in the non-dispersive direction, along the bar. For each scintillator bar of the TH detector, the transport coordinate y-position is calculated by projecting the particle track trajectory for a given event out from the GEM layers and to the location of the TH detector. This is done by using the known distance between each of the detectors and the BigBite magnet, and the trajectory angles of the particle tracks passing through the SBS electron arm as measured by the GEMs during the momentum reconstruction, which involves back-tracing of the particle trajectory from the detectors, through the magnet, and back to the target.

Further cuts were applied to the data such that only events corresponding to elastic electrons were used to generate the plots of TDC time difference versus transport coordinate y-position. These elastic electron cuts involve cutting on energy momentum measured by the pre-shower and shower detectors in the BigBite package, and other particle momentum values which are further detailed in Chapters 5. The reason for using a transport coordinate system is because it makes for a simpler calculation of particle hit position in the detector and for position resolutions which are provided in Chapter 5. Figure 4.33 provides example plots for two different scintillator bars, one bar from the lower region and one bar from

the middle region of the TH detector, of TDC time difference versus transport coordinate y -position. Here, y -position is projected from the GEMs, and the gradient gives the speed of light in the bar. A linear fit is applied to each plot and the intercept gives the time difference offset which is recorded as a calibration value in the TDC database file. This same process of fitting is applied to every scintillator bar in the TH detector.

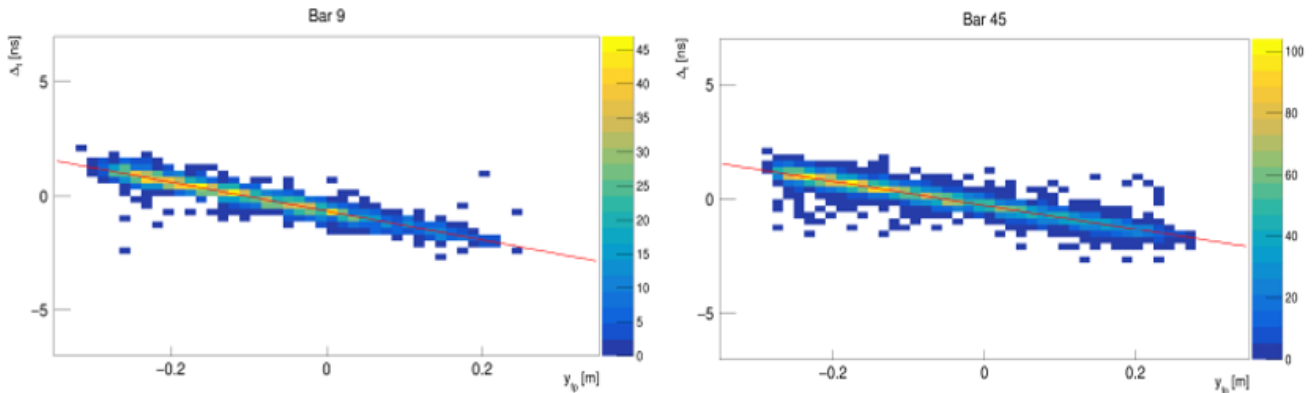


Figure 4.33: Two plots of TDC time difference versus transport coordinate y -position for bars 9 (left) and 45 (right). This data was collected using a run from SBS-4 with an LH2 target and a beam of 3.5 μ A. The BBcal trigger was used. Cuts correspond to cluster number, size, and width, and for ensuring only elastic electrons were applied.

4.3.5 Scintillation Velocity Correction

The scintillation velocity correction accounts for slight discrepancies in the refractive index belonging to each of the scintillator bars. Ideally, the speed of light through the scintillating material would be constant, but minute impurities in the structure of the material can affect the time difference spectrum, causing a slight slant to the data as in Figure 4.33. This slant can be corrected by using the slope taken from the same fit to the TDC time difference versus transport coordinate y -position plot seen in Figure 4.33 as a calibration value for the scintillation velocity correction. Just as the time-walk effect causes a slant to the TDC versus TOT plots, variance in scintillator velocity causes a slant to the plot of TDC time difference versus transport coordinate y -position. Extraction of the slope from Figure 4.33 gives the error and this was repeated bar by bar for all scintillators in the TH as shown in Figure 4.34. The slope values were recorded as the scintillation velocity correction calibration values in the TDC database file.

Scintillator Velocity Correction vs. Bar Number

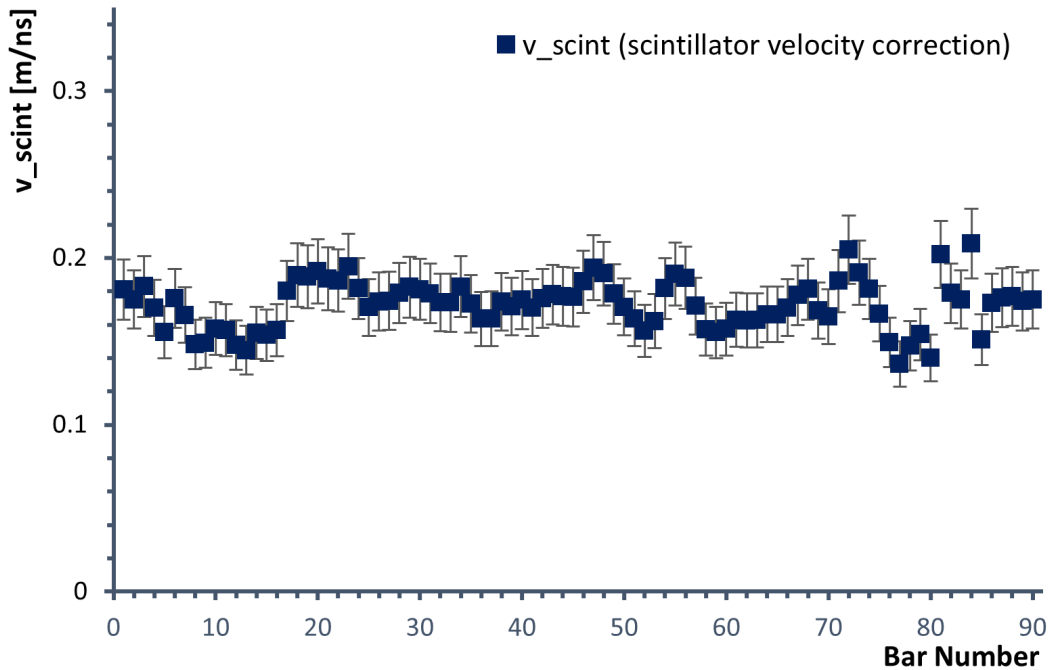


Figure 4.34: A plot of scintillator velocity correction values from the slope of the fit to the TDC time difference versus transport coordinate y-position. These calibration values are plotted versus bar number.

Further calibrations that could be considered for improving upon the performance studies of the TH detector include a time-of-flight correction which was proposed using timing data taken from the HCal detector. A time-of-flight correction intends to correct for discrepancies in timing between two different planes at various locations in the system of detectors, and that are placed at different distances from the target. In this case the two planes would be the TH detector and HCal, and this calibration would improve timing measurements with respect to both the SBS hadron arm where HCal is located, and the BigBite electron arm where the TH detector is located. Another calibration to consider is a radio-frequency (RF) alignment of the TH detector TDC data with the electron beam. This RF alignment would ideally improve timing of the TH detector relative to the beam. Due to time constraints the only calibrations included in the performances studies detailed in Chapters 5 were the timing cuts, TDC alignment, time-walk correction, time difference offset, and scintillation velocity correction. These calibrations proved to be sufficient for the purposes of a comprehensive TH detector performance analysis because, as is shown in Chapters 5, the tracking efficiency compared to the GEMs is above 95% for all six kinematic settings of the G_M^n experiment and the time and position resolutions are of an equal quality.

Chapter 5

TH Performance Studies for G_M^n Experiment

This chapter details studies of the TH detector performance during the running of the GMn experiment. These studies include analysis of energy deposit, average cluster size, occupancy, rates, accidentals, pile-up, tracking efficiency, position resolution, and time resolution. Before discussing performance studies, an overview of the physics cuts for all-tracks, electrons, and elastic electrons used to differentiate between the different particle groups is provided followed by a section on the simulation of detector performance, which provides a baseline for comparison between the simulated versus the real data. The TH detector performance analysis provides important insight for characterizing how well the detector measured various particle parameters, but most importantly for timing as that is the TH primary function, and especially for elastic electrons, which are ultimately the primary focus of the SBS electron arm for measuring the electromagnetic form factors in conjunction with data collected by detectors from the SBS hadron arm.

Following the analysis of energy deposit and average cluster size, focus shifted towards analyzing the TH detector rates, track matching efficiency, resolution for both the vertical and horizontal position, and time resolution. The same physics cuts for all-tracks, electrons, and elastics apply to the timing performance studies for rates, track matching efficiency, and position and time resolutions. Analysis of the rates, tracking efficiency, and resolutions was implemented across all six SBS kinematic settings. Rates are expected to increase with luminosity, which is dependent on the beam current and the type of target used. Also, the beam energy, which varies across the six kinematic settings, must be considered when analyzing detector rates. Evidence of pile-up, which is a term for defining a maxing-out of the

detector rates, was investigated as concerns arose during the G_M^n experiment run-time that the TH detector operational rate limit of 2.5 MHz, which was determined relative to the maximum rates of the GEMs, was surpassed at some of the higher momentum kinematic settings. As rates increase with higher Q^2 , the track matching efficiency in relation to the GEMs should decrease, due in part to the increased radiation from the beam-line. Resolutions should worsen at higher Q^2 , generating larger showers, and thus a larger Molière radius from the pre-shower interacting in the scintillating material, making it more difficult for the TH detector to measure the timing of an event. Considering all expected trends in the data, an analysis of TH detector performance commenced.

Kinematic Setting	Comments
SBS-4	No Comments
SBS-7	No Comments
SBS-11	Additional Shielding Installed
SBS-14	No Comments
SBS-8	Additional Shielding Installed
SBS-9	All TH HV Values Lowered by 50V

Table 5.1: List of six SBS kinematic settings and comments on adjustments made regarding shielding added between the beam-line and BigBite magnet, and changes to the TH HV value settings.

5.1 Definition of Physics Cuts

Before conducting the TH detector performance analysis a series of physics cuts were defined for differentiating groups of certain particle types by looking at data taken from the various SBS and BigBite detectors. These distinct particle groups are named all-tracks, electrons, and elastics. The purpose of these cuts is ultimately to get a purely elastic electron data set which is the data set specific to the measurement of the electromagnetic form factors. The all-track particle group includes cuts on the reconstructed track parameters at the target on the y-position, and the angles θ_{tgt} and ϕ_{tgt} . This is following the transport coordinate system such that the positive z-axis goes along the BigBite central axis, the positive x-axis goes vertically down along the face of the TH detector, and the positive y-axis goes to the left along the length of the TH detector scintillator bars. The x-position and y-position at the target are defined as the coordinates of the intersection of the reconstructed trajectory with the coordinate focal plane perpendicular to the BigBite central axis containing the origin. The angles θ_{tgt} and ϕ_{tgt} measured in radians are the

track slopes dx/dz and dy/dz respectively, and are the tangents of the in-plane and out-of-plane angles of the trajectory. These all-track cuts remove, for the most part, data which does not correspond to either electron or pion tracks.

Following, and in addition to, the all-tracks cuts, another layer of cuts are applied to differentiate data which represents only electron tracks. Figure 5.1 provides two helpful plots of how these electron track cuts are applied. First, a cut on the energy-momentum ratio where the energy in GeV is measured by the pre-shower (PS) detector for a track divided by the momentum of the track in GeV/c is applied to the data such that the ratio is greater than a pre-set value.

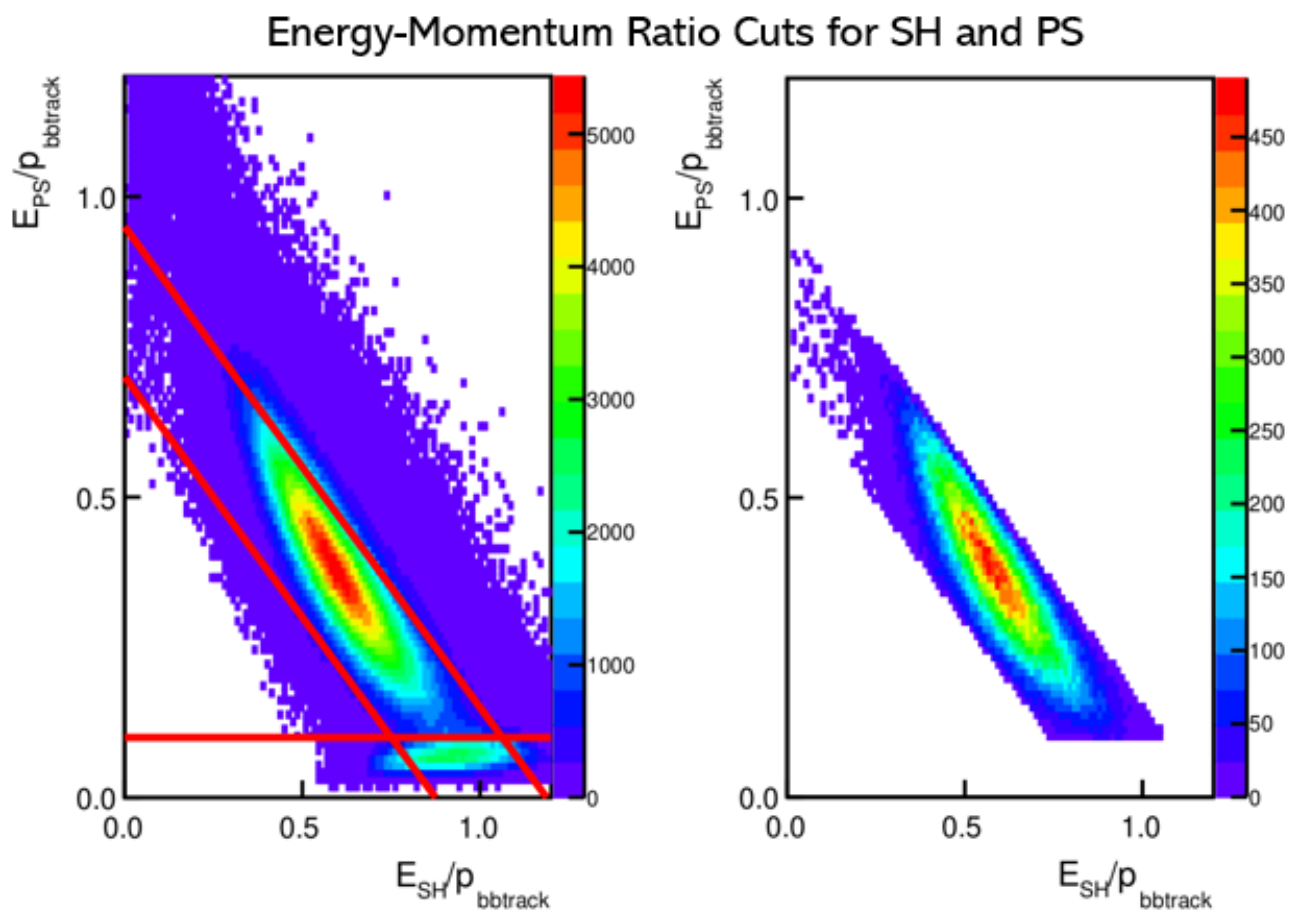


Figure 5.1: Two plots showing before (left) and after (right) applying energy-momentum ratio cuts for both PS and SH detectors to ensure only electron tracks, thus cutting out lower energy pions.

The momentum is calculated during the momentum reconstruction process using optics variables which are calculated from particle track hit positions and trajectories provided by the BigBite detectors. The optics values were obtained by using a method based on singular value decomposition. In spite

of the complexity of the optics, positions and momenta at the target are precisely reconstructed from the coordinates measured in the detectors by means of a single back-tracing matrix. The technique is applicable to any similar magnetic spectrometer and any particle type, and a description of it can be found in [64]. Another two cuts are applied to the energy-momentum ratio as measured by the shower (SH) detector to be within pre-set minimum and maximum values. The three cuts as shown in Figure 5.1, are adjusted slightly up or down for each kinematic setting to better fit the data.

The final layer of physics cuts for elastic electrons are applied to the hadron x-position and y-position of particle track clusters as measured by HCal. First, distributions of the measured minus the predicted position in both x and y are generated. The x-position and y-position are provided by HCal and measured in mm using the transport coordinate system. To calculate x_{pred} , the predicted x-position, and y_{pred} , the predicted y-position, Equations 5.1 and 5.2 were used. These predicted distributions were subtracted from the measured to get distributions for both δx and δy , which represent distributions of the measured

$$x_{pred} = -(d_{HCal})(\sin \phi_{HCal}) \quad (5.1)$$

$$y_{pred} = (d_{HCal})(\sin \theta_{HCal}) \quad (5.2)$$

minus the predicted x-position and y-position respectively. The angles θ_{HCal} and ϕ_{HCal} measured in radians are the track slopes dx/dz and dy/dz respectively, and are the tangents of the in-plane and out-of-plane angles of the trajectory as measured by HCal. The value of d_{HCal} measures the distance between the HCal detector and the target. The cuts on these position difference spectra in both x and y define a range using pre-set means and sigmas which eliminate non-elastic electron tracks. Figure 5.2 provides example plots showing the effect these cuts have on the position difference spectra comparing all-tracks in blue to elastics in red. In these plots, the x-direction is vertical and the x-distribution is offset from zero due to particles being deflected by the SBS magnet and HCal not being at beam height.

The last elastics cut is applied to a spectrum of the momentum difference, which is the measured momentum of the track minus the expected momentum. The expected momentum is calculated using the beam energy, E_{beam} , mass of the proton M_p , and θ_z , where θ_z is calculated using the values for total

Elastics: Position Difference Cuts for HCal

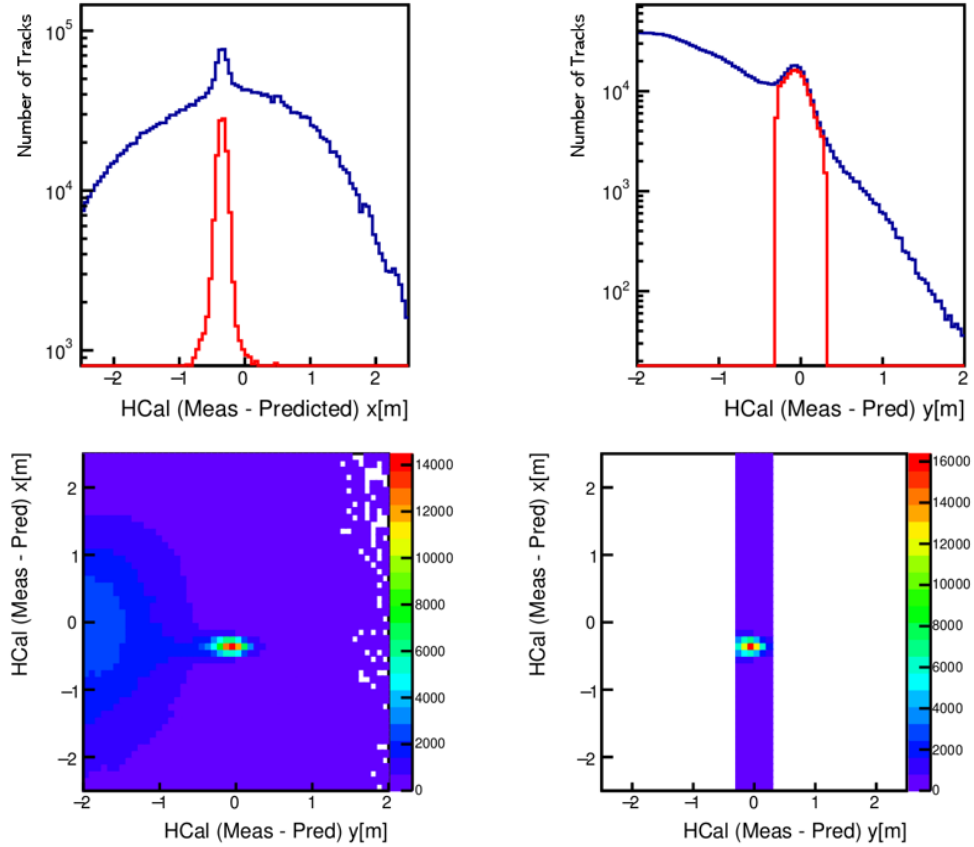


Figure 5.2: Two plots (top) showing all-tracks (blue) and elastics (red) with HCal position difference cuts applied, and plots of all tracks (bottom left), and elastics (bottom right).

momentum p and the momentum in the z -direction, p_z , as measured by BBCal. Equation 5.3 defines the calculation of θ_z and Equation 5.4 provides the formula for the expected momentum, p_{exp} .

$$\theta_z = \cos^{-1} \frac{p_z}{p} \quad (5.3)$$

$$p_{exp} = \frac{E_{beam}}{1 + \frac{E_{beam}}{(M_p)(1 - \cos \theta_z)}} \quad (5.4)$$

The plots provided in Figure 5.3 show the momentum difference distributions for all-tracks in blue and elastics in red. A final momentum difference cut is applied to the elastics distribution with a mean center at zero and a pre-set value for the sigma which provides a range that acts as the cuts above and

below zero for the elastics momentum difference distribution. This completes the definition of cuts for all-tracks, electrons, and elastics. The momentum difference cut applied to the elastic momentum difference distribution in red from Figure 5.3 accounts for any non-elastic electron tracks which were not removed by the HCal position difference cuts. A smaller secondary peak, representing leftover deep-inelastic scattering events, is seen in the elastics momentum difference distribution, but this is cut out by the elastics momentum difference cut such that the distribution of data considered for elastics analysis is better centered around zero. Figure 5.4 provides a comparison of several plots for the momentum, θ_{tgt} , ϕ_{tgt} , and y_{tgt} distributions for all-tracks plotted in blue and elastics plotted in red. All physics cuts categorized into all-tracks, electrons, and elastics are implemented similarly for each kinematic setting with adjustments to beam energy, and spectrometer angles which vary. Also, adjustments are made by eye to the energy-momentum ratio, position difference, and momentum difference cuts as deemed necessary such that the cuts would best fit the data as it is plotted for each kinematic setting.

Momentum Difference: All-Tracks and Elastics

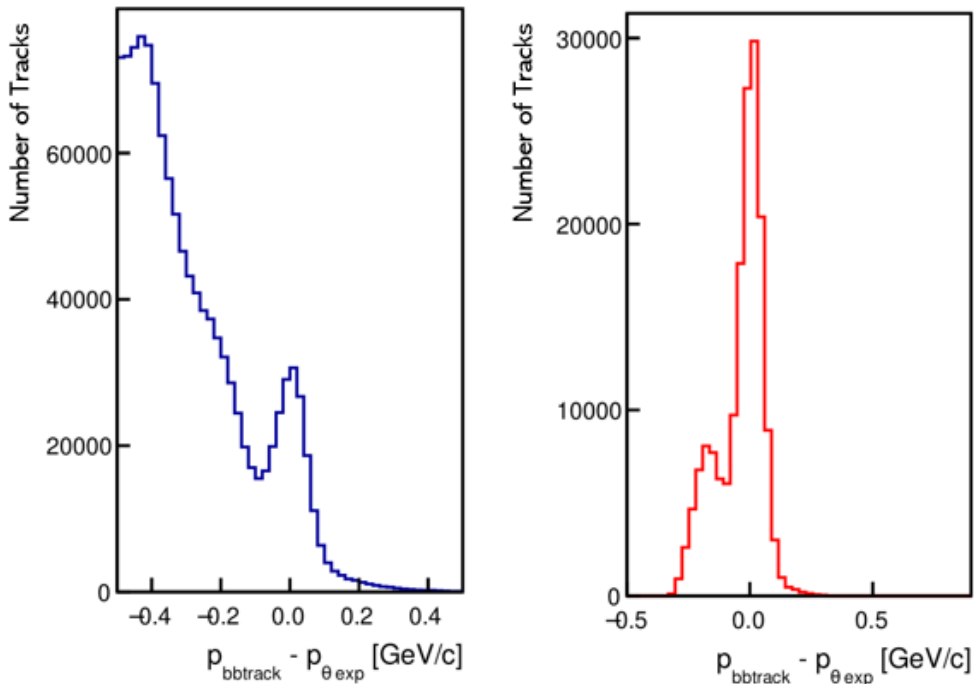


Figure 5.3: Two plots of all-tracks momentum difference distribution (blue) and elastics (red). The data shown is from SBS-4 kinematic setting runs 11547 and 11548 using an LH2 target with 3.5 uA beam. These plots were generated for all six of the SBS kinematic settings to optimize the physics cuts, so each could be specifically tailored to the data set being analyzed.

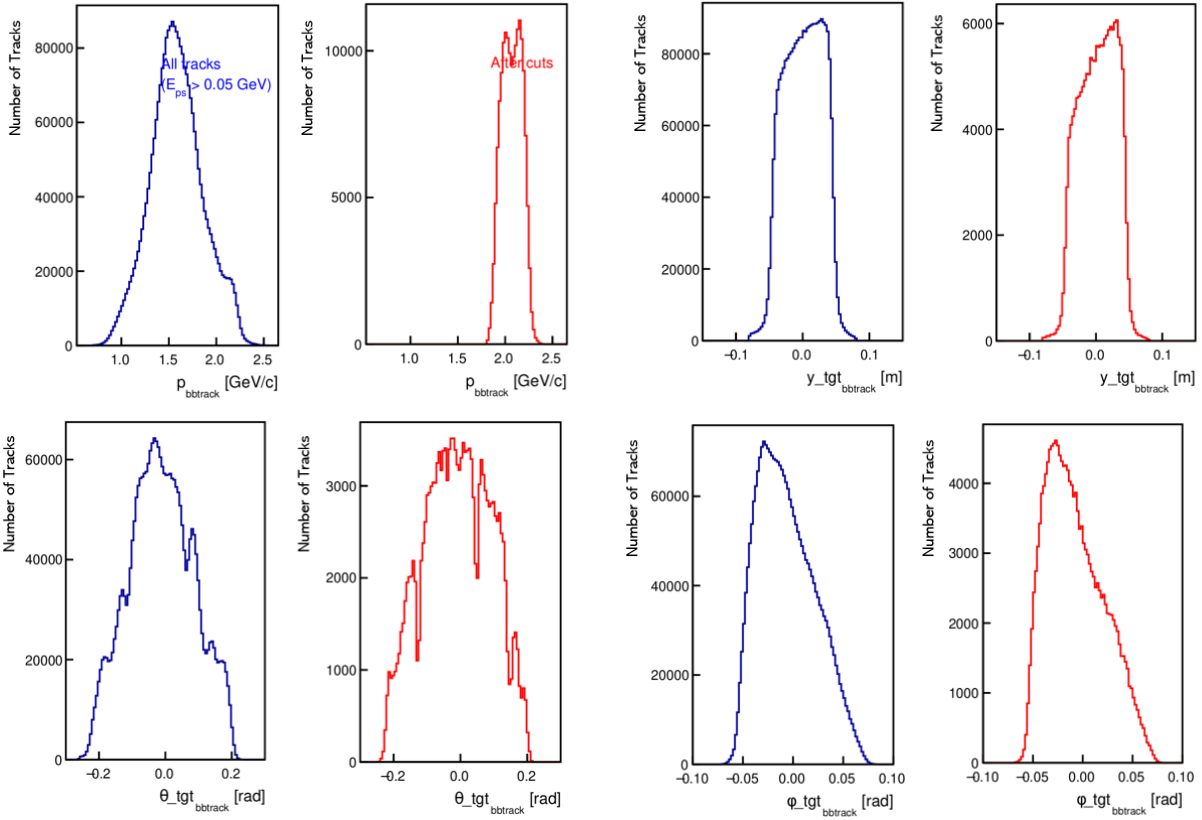


Figure 5.4: Several plots comparing all-tracks (blue) and elastics (red) distributions for track momentum, y-position at the target, and the angles θ_{tgt} and ϕ_{tgt} measured at the target, which were generated using the BBCal trigger and a 3.5 uA beam on an LH2 target from SBS-4 runs 11547 and 11548.

5.2 Simulation for Detector Performance

A simulation using GEANT4 software was used to predict how the TH detector performs in Hall A. GEANT4 is a platform for simulation of the passage of particles through matter using Monte Carlo methods [65]. The simulation utilized an electron source with energy in GeV incident on a block of lead glass resembling the PS detector geometry. Behind the PS detector, the TH detector, constructed of 90 plastic scintillator bars, in the simulation was positioned and set to record energy deposit and the x-y position of particle tracks in a Cartesian coordinate system. The TH was placed behind the PS to match the Hall A setup. This decision for detector placement was originally made over concerns of rates. The PS acts as a shield lowering rates, but degrades resolution as the performance analysis shows. The incident electron energy was varied between 1-3.5 GeV in 0.25 GeV increments to see how the mean energy deposit and spread in the x-y position of particle tracks changes. Intuitively, mean energy deposit of all tracks in the shower of particles should increase with increased energy of the incident electron.

Figure 5.5 provides a visual of the simulation in action, comparing a shower of particle tracks coming from the incident electron interaction in the PS detector to the TH detector for both a 1 and 3 GeV electron. In the images of the simulation, the green lines represent neutral charged particles, the red lines represent negatively charged particles, and the blue lines corresponding to tracks of positive particles. The PS detector is presented by the block outlined in pink and the 90 scintillator bars are shown with a blue outline. The view of the simulation in the images from Figure 5.5 are from behind and left of the TH detector when looking toward the origin of the incident electron, which in Hall A would be the target. By eye, it is apparent that the shower of particles for a 3 GeV electron versus a 1 GeV electron is much larger and wider in terms of the spread and number of particle tracks hitting the TH detector. This larger shower will correspond to a wider spread in the x-y distribution for tracks hitting the TH detector which will degrade the timing resolution. The timing resolution is directly linked to how well the TH detector is able to measure the mean position in the y-direction which in a transport coordinate system goes along the length of the scintillator bar. The intrinsic time resolution of the detector must also be taken into consideration when calculating the actual time resolution and this value has an expected value of 300 ps based on the geometry and design of the detector, and prior simulation of the TH detector without the PS included. The showering effect, caused by the PS detector, on the spread of particle tracks entering the TH detector will degrade the time resolution. A quadrated sum calculates the actual time resolution which will be >300 ps by an amount that varies with the energy setting of the incident electron.

The plot from Figure 5.6 shows the distribution in the y (horizontal) and x (vertical) for a 1 GeV electron over fifty-thousand events. This plot is created by setting the incident electron angle effectively equal to zero such that the spread in the horizontal and vertical directions are only affected by the showering effect from the PS detector. Therefore, the showers for every incident electron are centered at (0,0) which corresponds to the center of the TH detector. Projections of the horizontal and vertical distributions at zero for fifty-thousand events of 1 GeV incident electrons are provided in Figure 5.7, which also shows the Gaussian fit used on those distribution to extract a value for the 1-sigma standard deviation of the Gaussian fit. This 1-sigma is measured in centimeters. To convert this value to time, the 1-sigma is divided by the speed of light through the scintillator bar which is approximately 18 cm/ns [66]. This provides a time resolution relative to the shower of particles, and that value is used in quadrature with the intrinsic time resolution to give an actual time resolution for the scintillator bars in the TH detector.

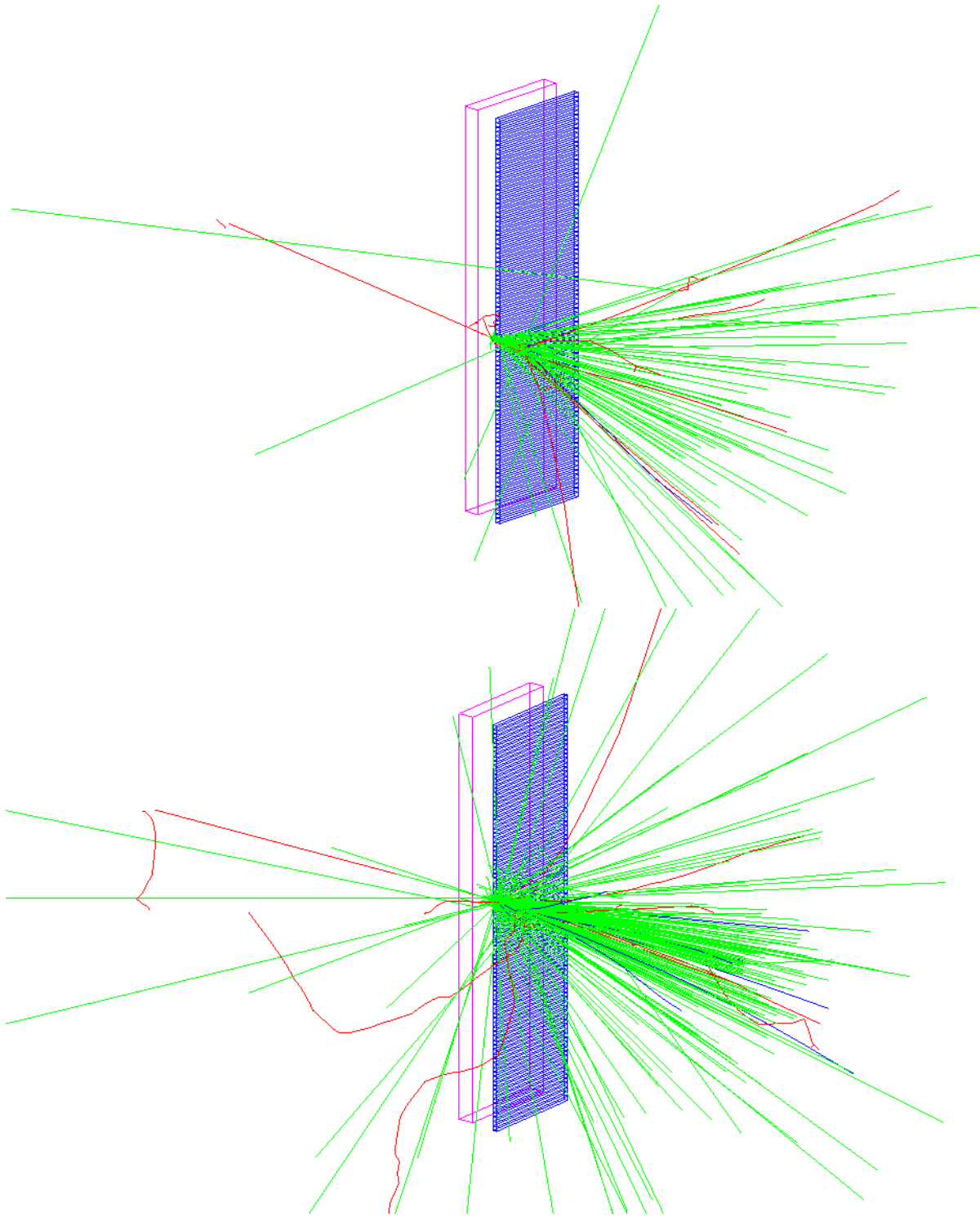


Figure 5.5: Two images comparing visually the showering of particles created by the interaction of a 1 GeV (top) and a 3 GeV (bottom) electron in the PS and how that shower looks when passing through the TH detector. The spread of the particle shower is much larger and creates a greater number of shower particles at 3 GeV than at 1 GeV for the incident electron. This larger particle shower at the 3 GeV setting will degrade the timing resolution of the TH detector compared to a smaller shower produced by an electron energy of 1 GeV.

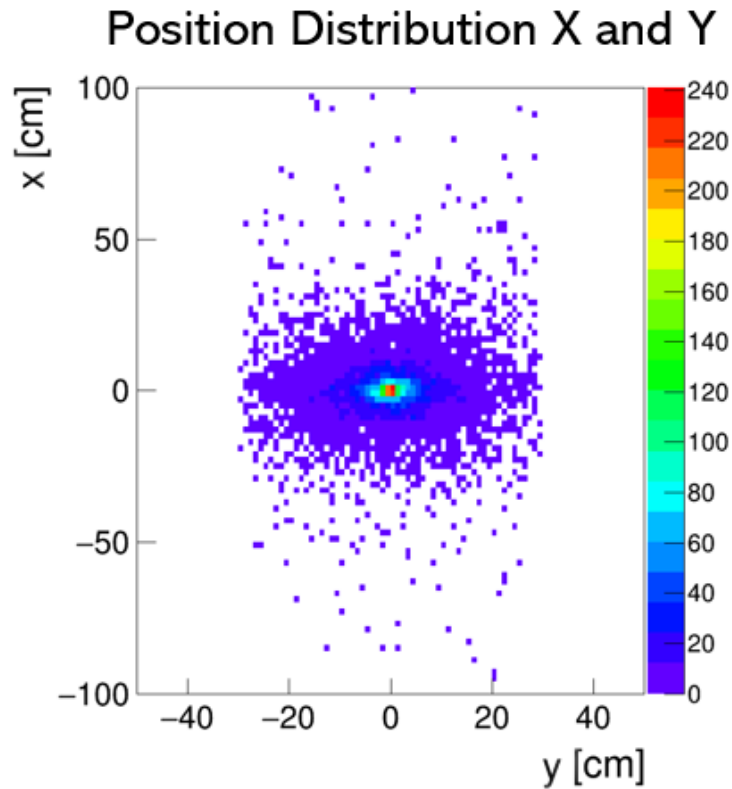


Figure 5.6: A plot showing the position distribution in both the horizontal (y) and vertical (x) directions for fifty-thousand 1 GeV incident electrons at a very small angle, and with a cut to remove photons. This plot corresponds to the analyzed, not the Monte Carlo generated, events from the simulation.

Position Distribution vs. Number of Entries

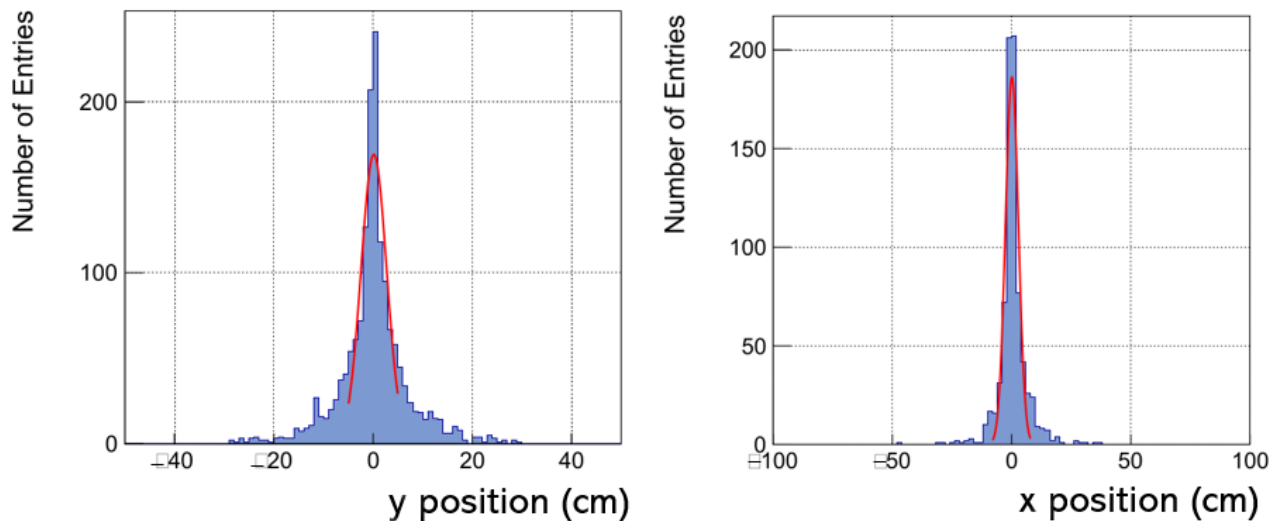


Figure 5.7: Two plots of projections of the y (left) and x (right) distributions center at (0,0) in a transport coordinate system. These plots were generated using fifty-thousand 1 GeV incident electrons and are one dimensional projections of the 2D plot from Figure 5.6. These distributions are a result of multiple scattering which is Lorentzian in shape, but close to the center the distribution can be fitted with a Gaussian function if the tails on either side are excluded.

Figure 5.8 shows a plot of 1-sigma values from Gaussian fits to the plots in Figure 5.7 over a range of GeV from 1-3.5 GeV for particle track energy of the incident electron. The second plot is the time resolution which is a combined value of the particle shower time resolution calculated from the 1-sigma values for the horizontal position distributions and the intrinsic time resolution of the TH. It is sufficient to plot only horizontal resolution because the spreads in the vertical and horizontal directions are symmetrical for simulated data. The plots in Figure 5.8 include measured data for comparison from the six SBS kinematic settings. Resolution for both position and time worsens at higher GeV values for incident electrons. The measured and simulated data match in the range of 4-6 cm for horizontal resolution and 450-800 ps for time resolution over the same GeV range. Extraction of resolutions gives the errors for the experimental data, and simulated data errors come from Poisson statistics of the Monte Carlo.

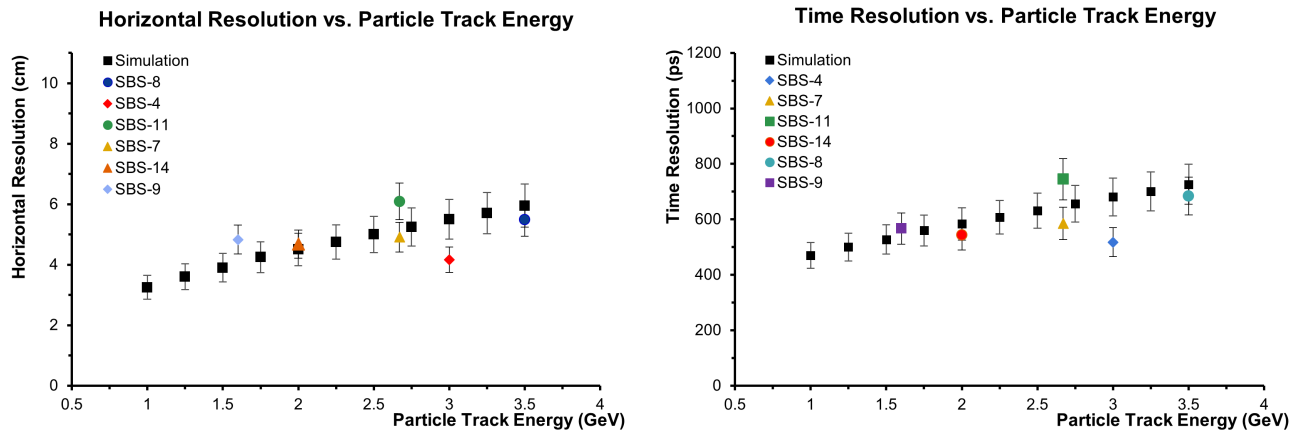


Figure 5.8: Two plots of horizontal position distribution 1-sigma values and combined time resolutions over a range of GeV for the incident electron particle track using fifty-thousand events. The data in black is from the stimulation only, and the other data points are from measured data collected during the running of the GMn experiment.

The plot from Figure 5.9 shows that as the energy in GeV of the incident electron particle track used in the simulation increases the mean energy deposit of the particles in the shower that passes through the TH detector also increases; because more individual particles hits come from the PS, which sum up hitting at the same time therefore creating larger energy deposit. The real data matches this trend. Based on all the trends from Figures 5.8 and 5.9, it can be concluded that as energy deposit increases so do the position and time resolutions. These plots were generated with cuts to remove photons created in the particle shower because this provides a cleaner distribution of the position and energy deposit spectra for fitting, as was done for the plots in Figures 5.7.

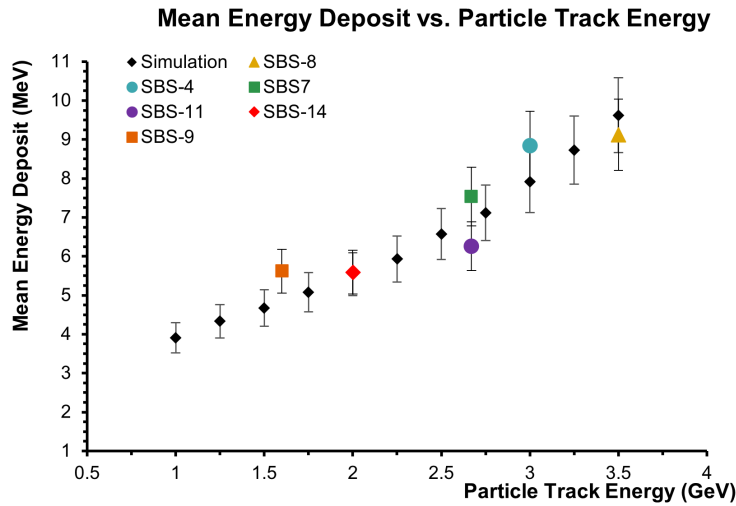


Figure 5.9: A plot of mean energy deposit for particle showers created by an incident electron over a range of GeV particle track values from 1-3.5 GeV with 0.25 incremental steps. The black data points are only simulated data, and the other data points are from real data taken during the GMn experiment.

5.3 Energy Deposit

To analyze the energy deposit in the TH detector a calculation of expected deposited energy by a cosmic muon using the known energy lost by a muon passing through a certain density, 2 MeV per g/cm^3 [67], the density of the scintillator bars, 1.02 g/cm^3 [47], and the thickness of those bars, 2.5 cm, provides a value of 5 MeV. The FADC readout modules provide data for amplitude measured in mV of the signal corresponding to an event. Thus, a conversion factor is needed to translate from mV to MeV. Assuming the particle track passes mostly through the entire bar, we also know the mean of the FADC amplitude distribution in mV should be equal to 5 MeV as well. Therefore, using a set of ADC cuts, like those used in the charge normalization study, to guarantee only a distribution of cosmic muon events whose tracks pass fully through the scintillator bars, the conversion factor can be calculated by dividing the mean of the FADC amplitude distribution in mV by 5 MeV. PMT numbers for the middle third of the TH detector, their conversion factors, and mean FADC amplitudes in mV are provided in Table 5.2. The values in Table 5.2 are calculated using ADC cuts, same as those used for the charge normalization study completed during the TH detector commissioning, to ensure that only particle tracks which pass fully through the scintillator bars are used. This provides clean separation between the pedestal and the ADC signal peak, which allows for better fitting of the data.

The reason for using the mean of the FADC mV distributions rather than the most probable value

Table 5.2: FADC mean amplitudes measured in mV and their corresponding PMT number and MeV conversion factors. These values were calculated using cosmic data of more than 350K events total for all 64 PMTS connected to the FADC readout modules from run 11610 of the G_M^n experiment at the SBS-4 kinematic setting using only particle tracks that pass fully through the scintillator bars. The average error for conversion factors is ± 0.6 and ± 0.8 for the means.

FADC Amplitude Means (mV) and MeV Conversion Factors					
PMT	Conversion Factor	Mean (mV)	PMT	Conversion Factor	Mean (mV)
32L	9.23	46.16	48L	9.1	45.5
33L	10.8	54.21	49L	8.81	44.04
34L	10.45	52.28	50L	8.37	41.86
35L	10.32	51.58	51L	8.33	41.64
36L	10.83	54.2	52L	9.32	46.61
37L	10.06	50.3	53L	9.9	49.49
38L	10.4	51.97	54L	8.59	42.98
39L	8.3	41.57	55L	9.64	48.23
40L	11.87	59.36	56L	10.1	50.5
41L	10.45	52.3	57L	9.05	45.24
42L	8.86	44.3	58L	9.64	48.21
43L	10.15	50.77	59L	9.2	45.9
44L	12.04	60.21	60L	11.82	59.1
45L	11.1	55.6	61L	9.6	48.1
46L	10.49	52.44	62L	9.43	47.14
47L	9.2	46.13	63L	8.31	41.54
32R	10.1	50.38	48R	9.3	46.5
33R	10.46	52.3	49R	8.37	41.9
34R	10.1	50.48	50R	9.23	46.14
35R	10.54	52.7	51R	9.6	47.98
36R	10.33	51.66	52R	10.64	53.2
37R	9.34	46.7	53R	9.2	46.17
38R	9.78	48.9	54R	9.92	49.6
39R	10.4	51.95	55R	9.9	49.67
40R	10.6	52.9	56R	9.65	48.23
41R	9.37	46.8	57R	9.85	49.27
42R	9.79	48.94	58R	9.45	47.24
43R	9.03	45.16	59R	9.08	45.42
44R	9.43	47.17	60R	9.7	48.47
45R	9.53	47.67	61R	9.55	47.77
46R	9.53	47.6	62R	9.36	46.79
47R	8.8	49.1	63R	10.83	54.16

(MPV) of a Landau function fitted to the mV distribution is because the mean provides a large enough MeV conversion factor for each bar such that the MeV converted mean of the FADC amplitude distribution falls below 5 MeV as expected. The MPV from a Landau function fitted to the mV distribution was not large enough to provide a conversion factor that gave a MeV converted FADC amplitude distribution mean below 5 MeV likely due to the Landau fits being skewed too low when plotted on the histograms by lower energy events not filtered out of the data. Figure 5.10 shows a plot of the FADC amplitude means measured in mV. These means in mV are on average 10 mV higher in value than the MPVs taken from the Landau fits to the same FADC amplitude spectra. The means in mV are divided by the theoretical energy deposit of 5 MeV already calculated for full particle tracks to generate the MeV conversion factors for each PMT. Figure 5.11 provides a plot of the conversion factors. Uncertainties in mean energy deposit come from the extraction of the distribution means, and these are taken into account when calculating the conversion factors whose main source of uncertainty comes from the FADC means in mV.

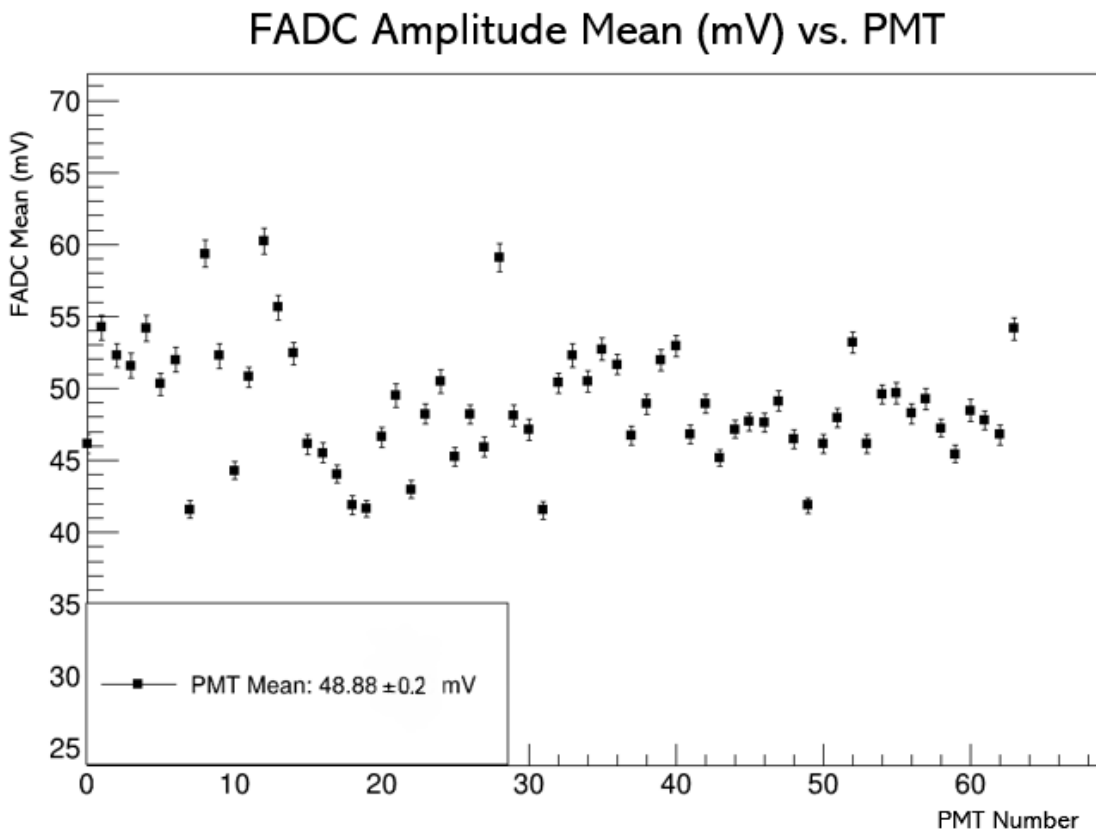


Figure 5.10: A plot showing means for left PMTs (0-31), and right PMTs (32-63) for the 32 middle scintillator bars of the TH detector. The average of these means for SBS-4 is 48.88 ± 0.2 mV. The FADC data used was taken from cosmic data run 11610 at the SBS-4 kinematic setting.

FADC Conversion Factor vs. PMT

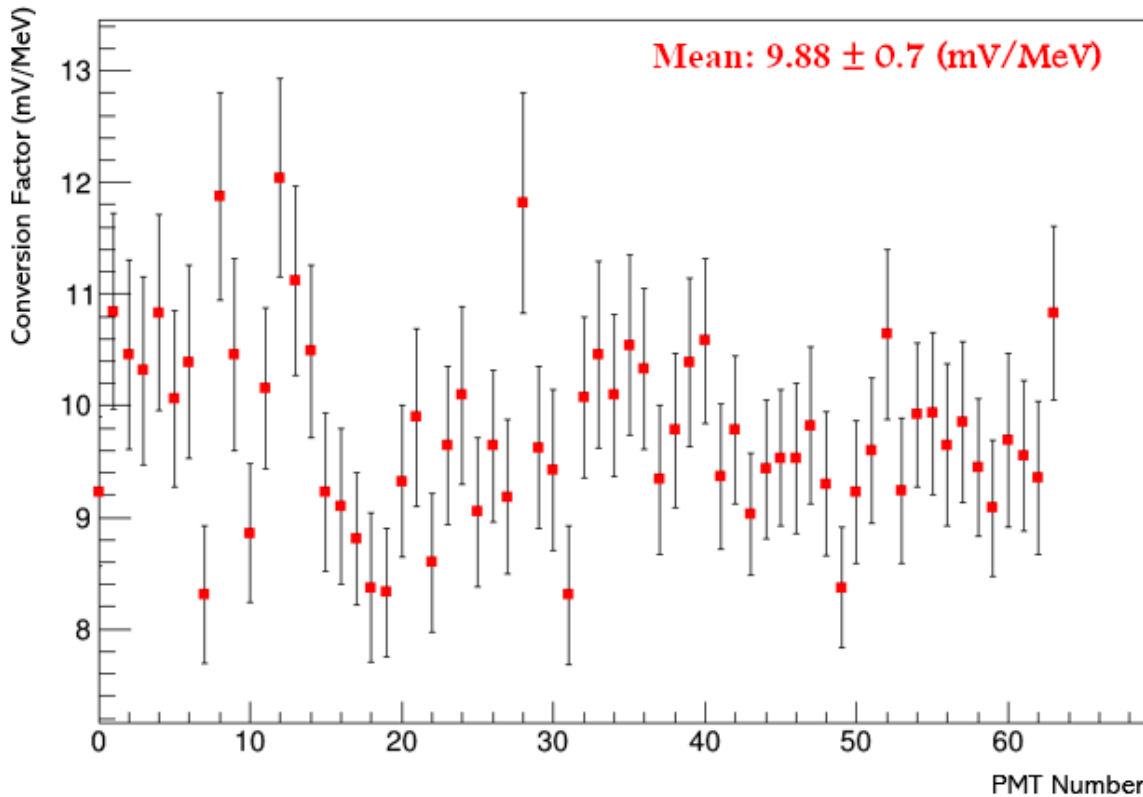


Figure 5.11: A plot of the MeV conversion factors for each of the 64 PMTs in the middle third of the TH detector. In this plot left PMTs are represented by PMT number 0-31 and right PMTs correspond to PMT number 32-63.

Using the conversion factors taken from Table 5.2, plots of the MeV corrected FADC amplitudes are generated for each PMT such as the example plot for PMT 7, which corresponds to scintillator bar PMT number 39L, provided in Figure 5.12. This plot shows the MeV corrected distributions with just the ADC cuts, TDC good timing, and TDC multiplicity cuts in black, added TDC window cuts on the leading edge in blue, and added time over threshold cuts in red. All the TDC cuts are the same as those defined in the TH calibration studies. These three layers were generated to show how the TDC timing cuts affect the FADC amplitude distribution, making the mean slightly higher with each additional timing cut. The three histograms corresponding to these three layers of cuts plotted on top of each other showing the effect of the cuts on the FADC MeV corrected distributions. The distributions peak just below 5 MeV because the means rather than the MPVs of the FADC mV distributions were used for the conversion to MeV. The plot shown in Figure 5.12 was repeated for all 64 PMTs in the middle third of the TH detector that were connected to the FADC readout modules during the G_M^n experiment.

FADC Amplitude MeV Corrected

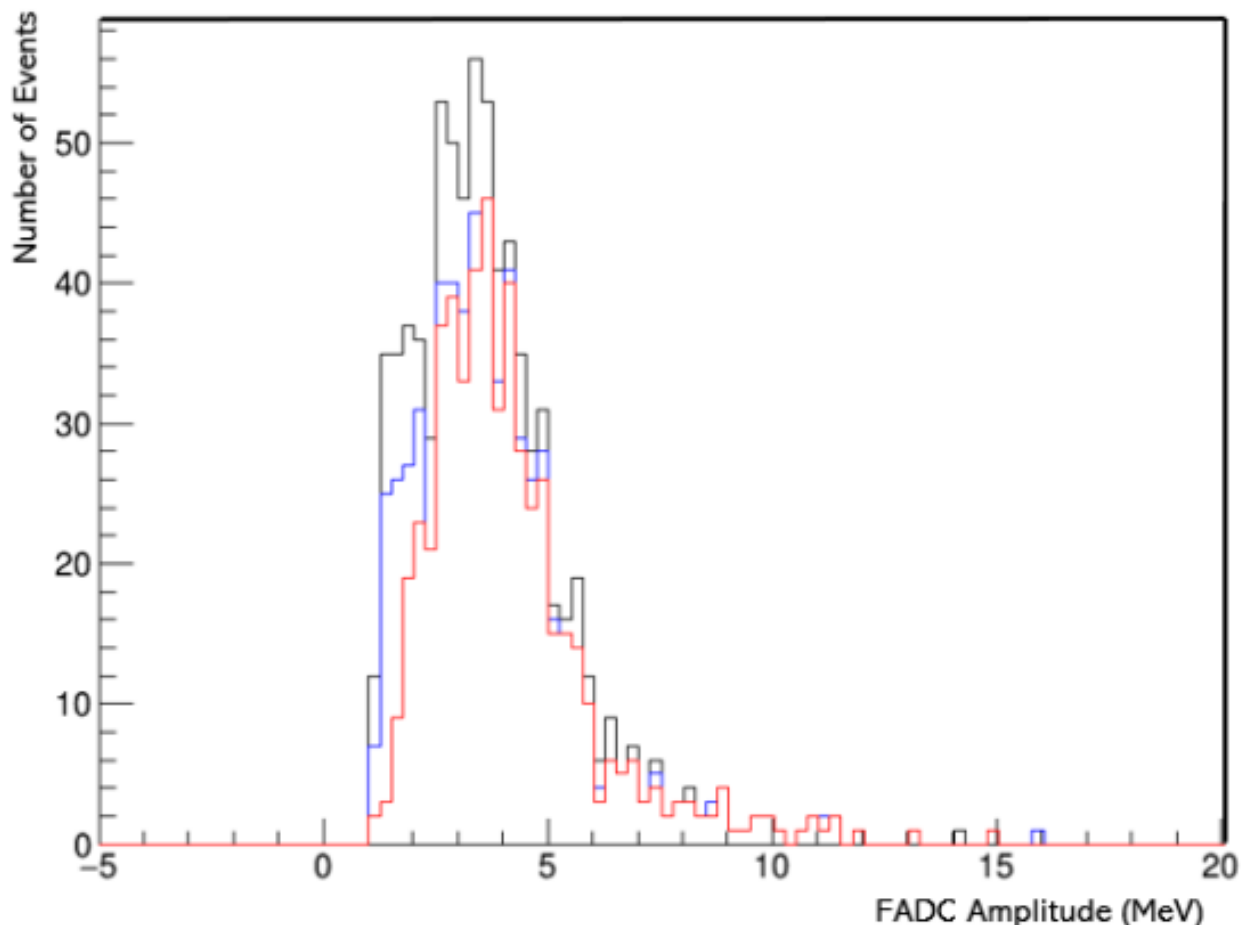


Figure 5.12: An example plot for PMT 7, corresponding to PMT number 39L, of an FADC MeV corrected amplitude distribution. This histogram has three layers: a distribution with just the ADC cuts, and TDC multiplicity cuts (black), another distribution with added TDC window cuts (blue), and a third distribution with added time over threshold cuts (red).

A plot of the means for each layer of the histograms like for those in Figure 5.12 is provided in Figure 5.13. With each layer of additional cuts, the mean for each PMT increases slightly showing how the TDC timing and TOT cuts discriminate events not corresponding to full particle tracks. The average mean for each layer of cuts goes from 4.0 MeV with only ADC cuts, TDC good timing cuts, and TDC multiplicity cuts, to 4.13 MeV with added TDC window cuts, and to 4.31 MeV with added TOT cuts. All 64 FADC amplitude MeV means with all cuts applied are listed in Table 5.3. As expected, the means in MeV from Table 5.3 fall below the analytically calculated value of 5 MeV. Since the maximum energy the muon could deposit in the full width of the scintillator is constrained to be below 5 MeV, it follows that the mean in MeV would peak just below the expected upper bound for the theoretical energy deposited.

Table 5.3: FADC mean amplitudes measured in MeV and their corresponding PMT number. These values were calculated using cosmic data of more than 350K events from runs 11610 for SBS-4 and 13701 for SBS-9 of the G_M^n experiment. This list of MeV mean values is take from the distributions which include all three layers of TOT, TDC window, and ADC and TDC timing cuts. The average error for the means is ± 0.1 MeV for SBS-4 and ± 0.05 MeV for SBS-9.

FADC Amplitude Means (MeV)							
SBS4				SBS9			
PMT	Mean	PMT	Mean	PMT	Mean	PMT	Mean
32L	4.05	48L	3.94	32L	3.01	48L	3.07
33L	4.448	49L	4.32	33L	3.52	49L	3.59
34L	4.495	50L	4.14	34L	3.42	50L	3.43
35L	4.101	51L	3.9	35L	3.19	51L	2.99
36L	4.46	52L	4.36	36L	3.49	52L	3.41
37L	4.429	53L	4.33	37L	3.46	53L	3.46
38L	4.597	54L	4.14	38L	3.545	54L	3.2
39L	4.137	55L	4.13	39L	3.03	55L	3.23
40L	4.62	56L	4.21	40L	3.59	56L	3.29
41L	4.67	57L	4.19	41L	3.5	57L	3.28
42L	4.26	58L	4.21	42L	3.46	58L	3.28
43L	4.6	59L	4.06	43L	3.72	59L	3.2
44L	4.496	60L	4.65	44L	3.485	60L	3.6
45L	4.48	61L	4.135	45L	3.487	61L	3.2
46L	4.67	62L	4.245	46L	3.92	62L	3.32
47L	4.63	63L	4.166	47L	3.93	63L	3.36
32R	4.3	48R	4.23	32R	3.1	48R	3.04
33R	4.6	49R	4.09	33R	3.36	49R	3.04
34R	4.39	50R	4.31	34R	3.26	50R	3.29
35R	4.357	51R	4.14	35R	3.24	51R	3.18
36R	4.38	52R	4.4	36R	3.31	52R	3.24
37R	4.29	53R	4.15	37R	3.3	53R	3.236
38R	4.32	54R	4.3	38R	3.42	54R	3.18
39R	4.245	55R	4.21	39R	3.1	55R	3.185
40R	4.37	56R	4.275	40R	3.32	56R	3.23
41R	4.3	57R	4.21	41R	3.16	57R	3.123
42R	4.325	58R	4.14	42R	3.3	58R	3.145
43R	4.416	59R	4.1	43R	3.44	59R	3.149
44R	4.4	60R	4.22	44R	3.43	60R	3.19
45R	4.185	61R	4.1	45R	3.2	61R	3.19
46R	4.476	62R	4.22	46R	3.36	62R	3.1
47R	4.647	63R	4.38	47R	3.43	63R	3.24

FADC Amplitude MeV Corrected Means

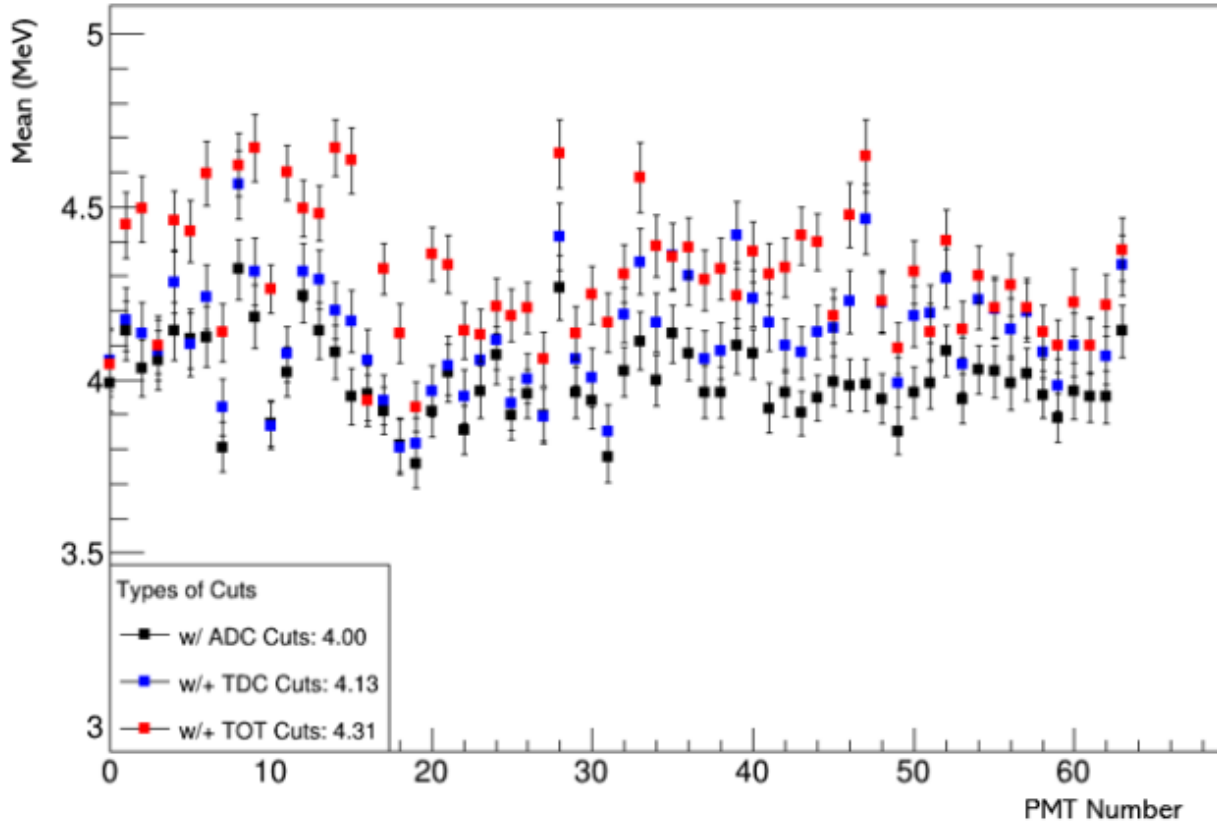


Figure 5.13: A plot of the means for each addition of cuts to the FADC MeV corrected amplitude distributions. Plotted are means, all of which include the TDC multiplicity cut, TDC good timing, and the ADC cuts (black), added TDC window cuts (blue), and added time over threshold cuts (red). The average MeV FADC amplitude mean for SBS-4 with all cuts is 4.31 MeV.

All data shown thus far for the cosmic muon energy deposit portion of this analysis was collected using a trigger on the BigBite calorimeter detector in Experimental Hall A and no changes were made to the high voltage (HV) settings during the data run 11610 at the SBS-4 kinematic setting. This same cosmic muon energy deposit analysis was applied to cosmic data run 13701 from the SBS-9 kinematic setting. The SBS-4 and SBS-9 kinematic settings were the first and last, respectively, kinematic settings during the G_M^n experiment run time. Throughout the experiment run time slight changes were made to TH detector HV settings, specifically a 50V drop across all channels before the start of the SBS-9 kinematic setting run period, and other changes to shielding around the target and magnets. These HV changes and shielding additions were implemented over concerns of detector rates running too high, but changes to the HV settings also affect the energy deposit spectra. Therefore, a comparison of the MeV means from SBS-4 and SBS-9 was done, and those values are all compiled in Table 5.3. The same conversion

factors calculated using the SBS-4 cosmic data were used to analyse the SBS-9 cosmic data to see the effect. Figure 5.14 shows the FADC amplitude means for SBS-9 in mV and Figure 5.15 provides the MeV corrected means for SBS-9 with the three layers of ADC and TDC good timing, TDC window, and TOT cuts applied in the same way as for SBS-4. Comparing the average of the mV and MeV FADC amplitude means between SBS-4 and SBS-9 shows the 50V drop in HV across all PMTs corresponds to an average 10 mV and 1 MeV drop in the means. This makes sense because the average conversion factor sits around 10 mV/MeV, so a 10 mV decrease in the average mean across all channels would result in a 1 MeV decrease as well. Thus, the 50V drop across all PMTs connected to ADC channels resulted in an average 1 MeV decrease in measured energy deposit across the same range of channels. The 50V drop across all HV channels in the TH occurred at the start of the SBS-9 run period, and only effected the data from that setting and not data from any of the other SBS kinematic settings.

FADC Amplitude Mean (mV) vs. PMT

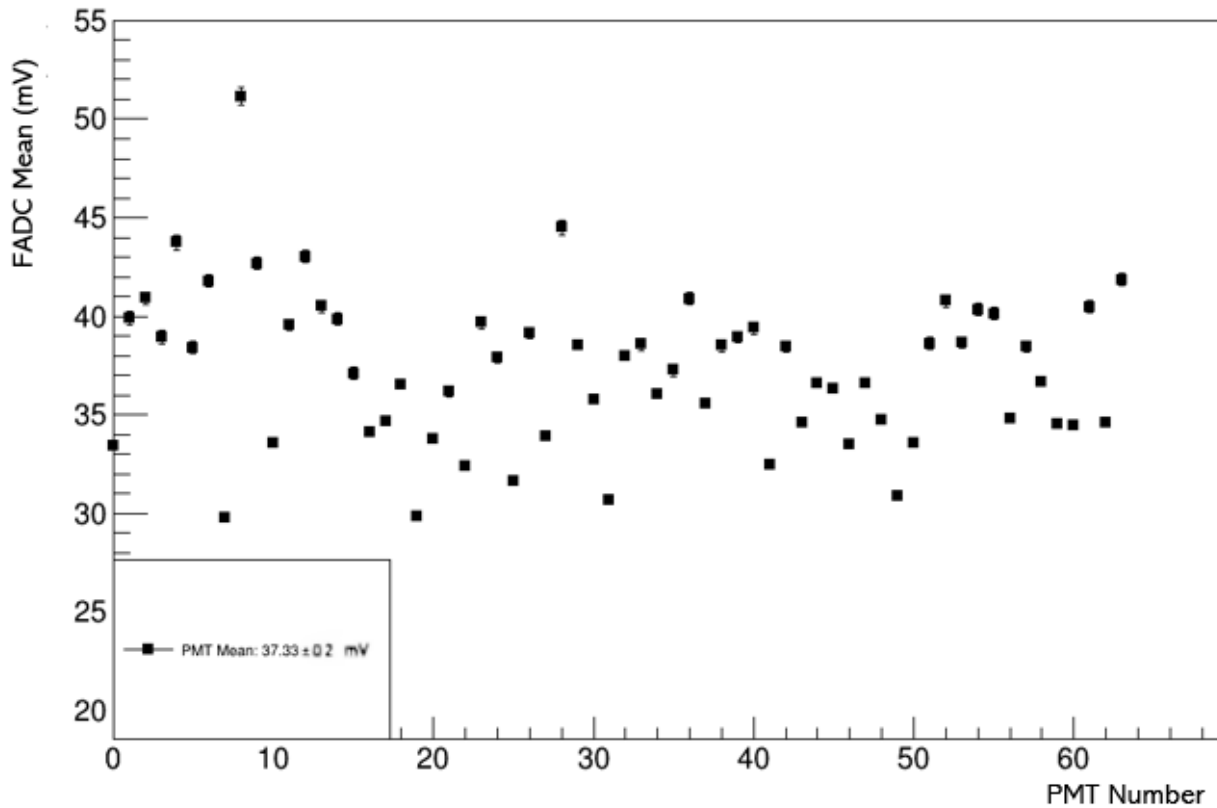


Figure 5.14: A plot showing Means for left PMTs (0-31), and right PMTs (32-63) for the 32 middle scintillator bars of the TH detector. The average of these means for SBS-9 is 37.33 ± 0.2 mV. The FADC data used was taken from cosmic data run 13701 at the SBS-9 kinematic setting.

FADC Amplitude MeV Corrected Means

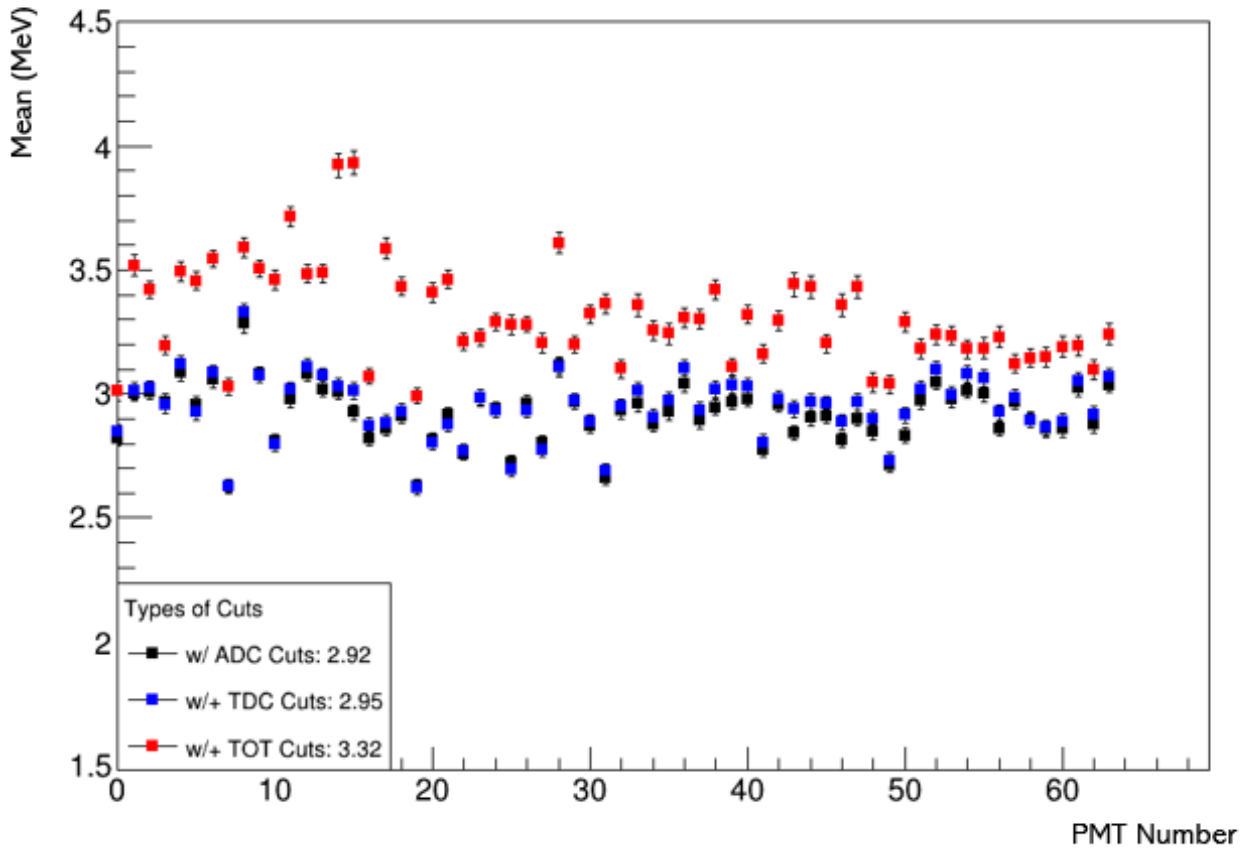


Figure 5.15: A plot of the means for each addition of cuts to the FADC MeV corrected amplitude distributions. Plotted are means, all of which include the TDC multiplicity cut, TDC good timing, and the ADC cuts (black), added TDC window cuts (blue), and added time over threshold (TOT) cuts (red). The average MeV FADC amplitude mean for SBS-9 with all cuts is 3.32 MeV.

The minimum value from the plots of the FADC mV and MeV corrected amplitude distributions give a quantity for the minimum mV and MeV thresholds for each PMT. Two lots of these minimum thresholds in mV and MeV per PMT are provided in Figures 5.16 and 5.17 for the SBS-4 and SBS-9 kinematic settings respectively. The minimum for each PMT in MeV is extracted from the plot of the MeV corrected FADC amplitude with all ADC and TDC cuts applied represented by the red line in Figure 5.3. Plots in Figures 5.16 and 5.17 show the minimum ionizing energy threshold does not vary with the 50V drop between SBS-4 and SBS-9. This is expected because the minimum ionizing energy should not vary with PMT HV setting and the NINO thresholds were constant throughout at 1.6V. Though the minimum changes on the order of a few hundredths of an MeV or a few tenths of a mV for the PMT, the average minimum ionizing energy for all 64 ADC channels is constant around 7.5 mV or 0.75 MeV.

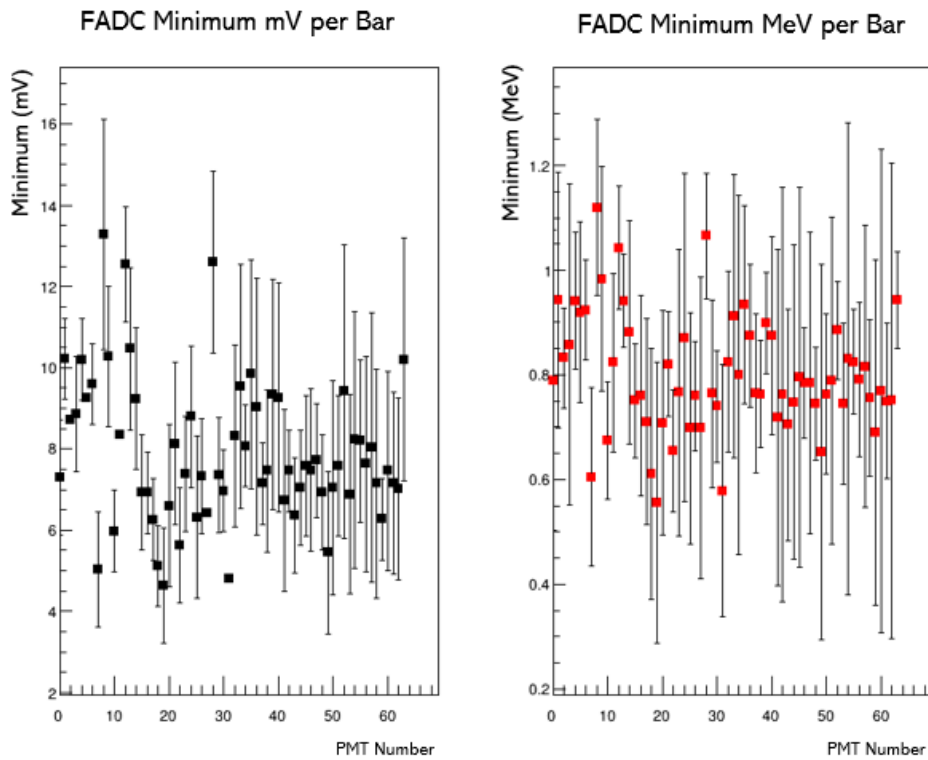


Figure 5.16: Two plots of the FADC mV (left) and MeV corrected (right) amplitude distribution minimum thresholds for each PMT connected to ADC channels from SBS-4 cosmic run 11610. These plots provide a basis for deciding where to set the minimum ionizing energy threshold for the TH detector.

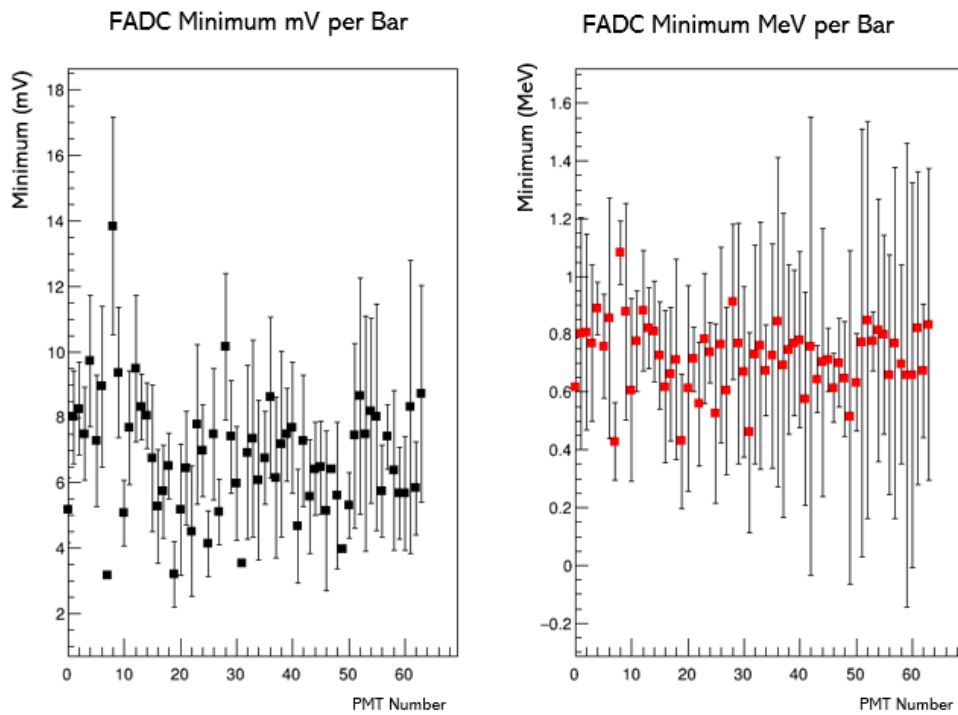


Figure 5.17: Two plots of the FADC mV (left) and MeV corrected (right) amplitude distribution minimum thresholds for each PMT connected to ADC channels from SBS-9 cosmic run 13701. These plots provide a basis for deciding where to set the minimum ionizing energy threshold for the TH detector.

Using the conversion factors plotted in Figure 5.11, the same energy deposit analysis can be applied to beam-on-target data from each of the six G_M^n kinematic settings to get an average mean FADC amplitude value in MeV across all 64 PMTs connected to the FADCs from the middle third of the TH. This can be done for FADC amplitude spectra using data for all particle tracks, just electron tracks, and just elastic electron tracks. The cuts to define those three groups are the same as previously defined for all tracks, electrons, and elastics. A plot of average FADC amplitude mean in MeV across all six kinematic settings using the three different layers of physics cuts is provided in Figure 5.18. The average mean FADC amplitude values for SBS-9 are the lowest among the six kinematic settings for each layer of physics cuts and this is because of the 50V high voltage drop across all channels which occurred before the start of the SBS-9 run period. The average for all-track data points from Figure 5.18 is 7.3 ± 0.1 MeV, 9.6 ± 0.1 MeV for electron tracks, and 10.8 ± 0.2 MeV for elastics. Since the all-tracks data points include lower energy particles such as pions, these data points would naturally have lower energy deposit values than data which only includes electrons, and the same for only elastic electrons compared to all electrons. Data variance is because of the different number of minimum-ionizing particles due to specific track momenta of scattered particles.

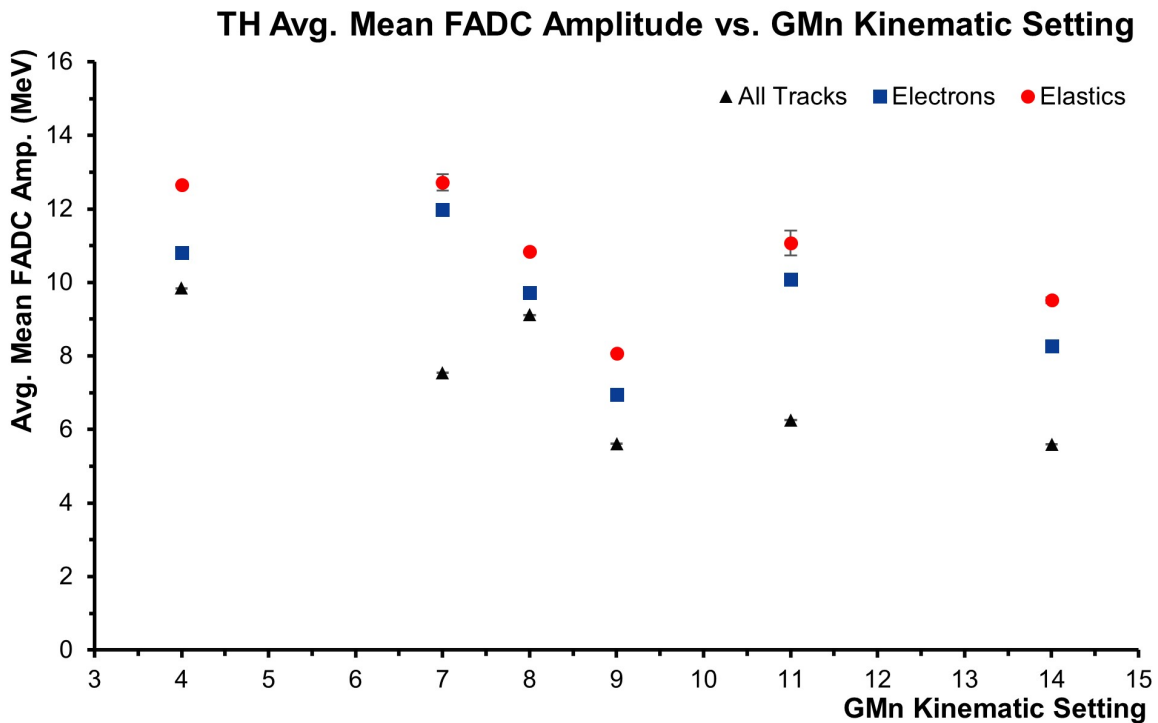


Figure 5.18: A plot of average mean FADC amplitude in MeV across all 64 PMTs connected to the FADC modules for each kinematic setting and with different layers of physics cuts.

5.4 Average Cluster Size

Cluster size is calculated by looking for events in the TDC data where signals were recorded for one or multiple neighboring bars simultaneously. The cluster size is always greater than or equal to one, and tends to be less than four bars in size. A constraint is also placed on the analysis of the cluster sizes such that the scintillator bars in a cluster must be within the same four scintillator bar block. Any signals recorded outside that block of scintillator bars will not be included in the value of the cluster size. In Figure 5.19 the elastics layer of physics cuts has the highest average cluster size since high energy particles will create a larger shower size in the pre-shower which sits just in front of the TH detector in the BigBite package. This larger shower size will create a larger spread of hits across multiple scintillator bars for a bigger cluster size. Similarly, the all tracks data points which include lower energy particles such as pions will generate smaller showers in the pre-shower, less hits across fewer scintillator bars in the TH detectors, and thus a smaller cluster size. The average of the all track data points from Figure 5.19 is 1.589 scintillator bars, for electron tracks the value is 1.92, and 2.06 for just elastic electrons.

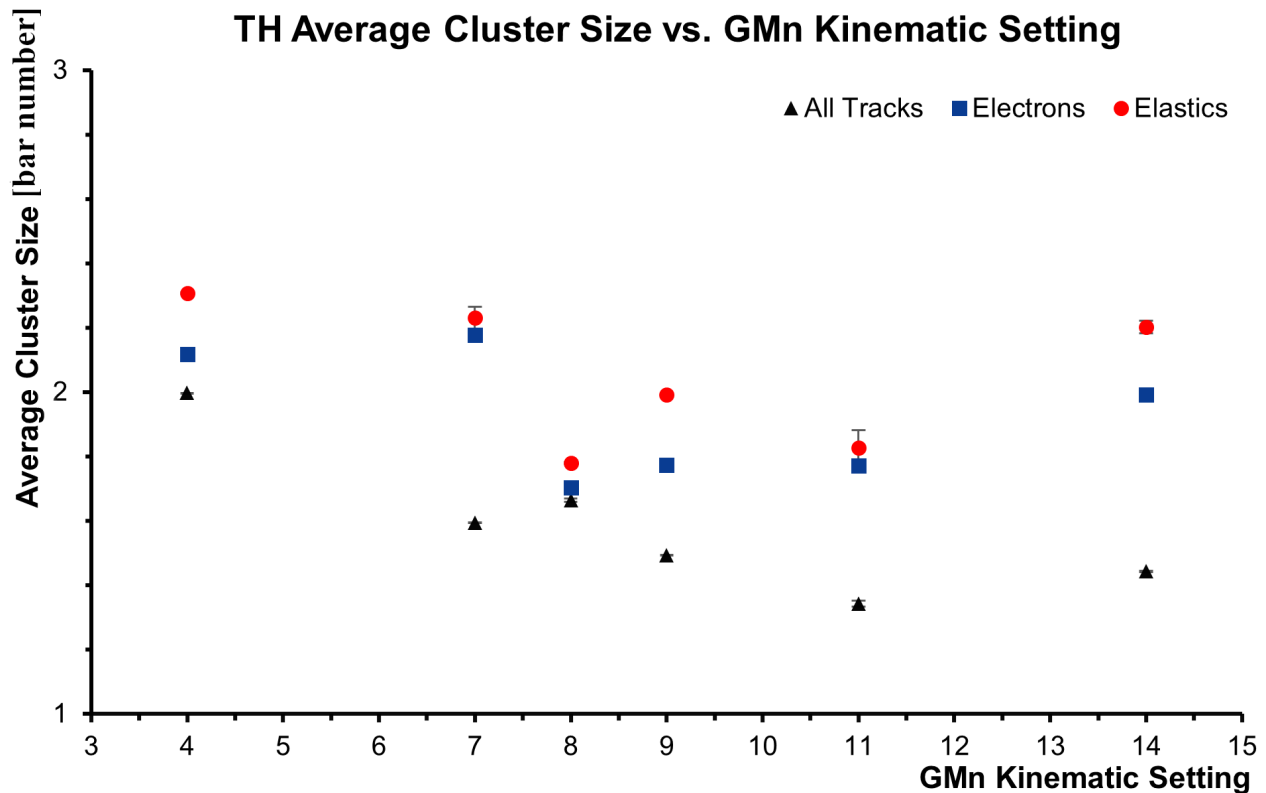


Figure 5.19: A plot of average cluster size across all TH detector PMTs connected to the TDC v1190 readout modules for each kinematic setting and with different layers of physics cuts.

Figure 5.20 provides six plots of the cluster size distributions for the entire TH detector across the six SBS kinematic settings starting with SBS-4 at the top left and ending with SBS-9 on the bottom right, going in timeline order as shown going from top to bottom of Table 4.2. These six plots are for only elastics data represented by the red data points in Figure 5.19. The SBS-8 kinematic setting shows the lowest mean and SBS-4 shows the highest mean for the average cluster size distributions. Cuts on the cluster sizes for each kinematic setting kept the distributions within the range of 1-4 scintillator bars per cluster. The means for average cluster size increase with GeV of the incident elastic electron like the means for the energy deposit. This makes sense since both cluster size and energy deposit should increase for higher GeV, specifically for the cluster size because of the larger particle shower coming from the PS detector into the TH detector for higher GeV particle tracks.

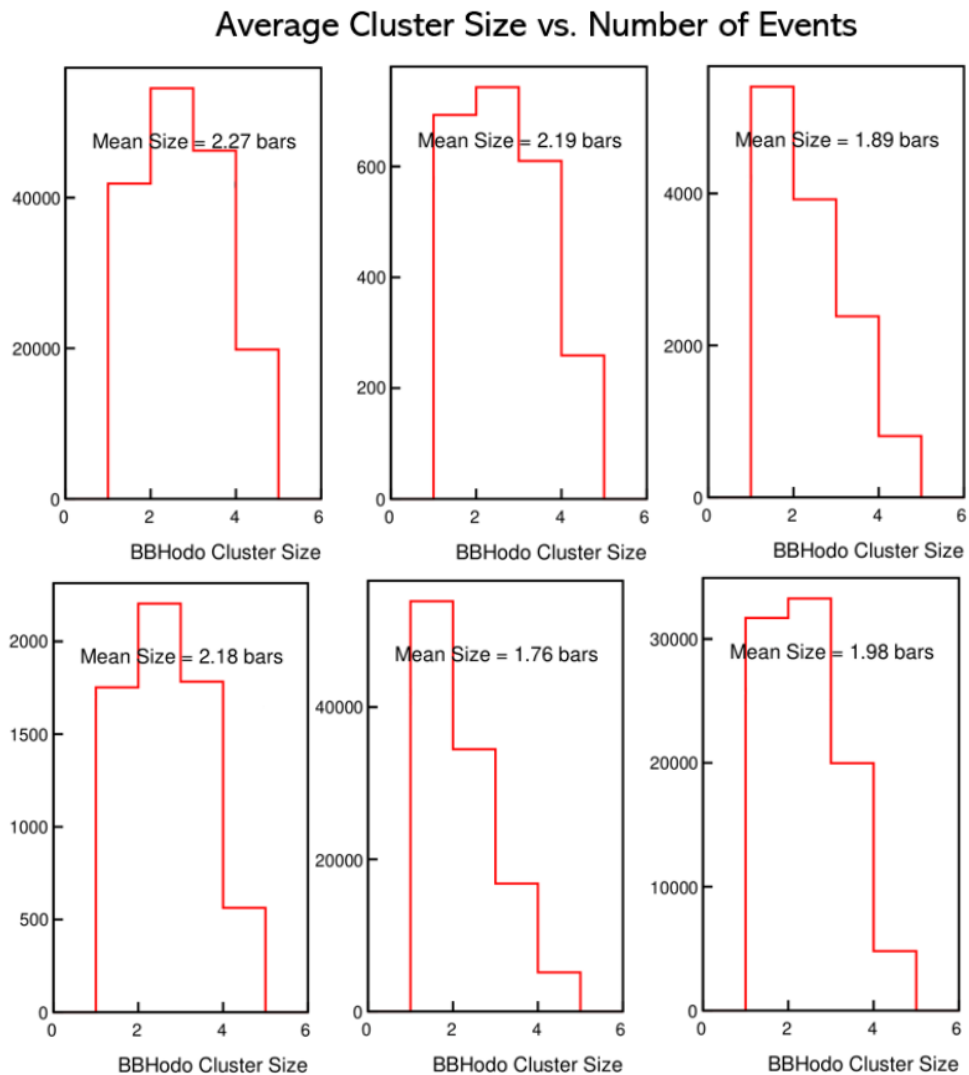


Figure 5.20: Six plots of the average cluster size distributions for SBS-4 (top left), SBS-7 (top middle), SBS-11 (top right), SBS-14 (bottom left), SBS-8 (bottom middle), and SBS-9 (bottom right).

5.5 Occupancy and Rates

The occupancy for the TH detector can be defined on a PMT or bar level basis, but in either case, it refers to the total number of hits recorded by an individual PMT, or by both PMTs connected to the same bar, given a number of replayed events in the analyzed ROOT file. If an event is recorded in the data file generated, which includes data for all SBS detectors, but is not recorded as a hit in the TH detector, then the event does not count toward the total occupancy for any TH detector channel. Figure 5.21 shows a plot of the occupancy as the number of hits versus the bar number. Occupancy for both left and right side PMTs for each bar are shown in red and blue. Hits which meet the coincidence cut such that there are hits recorded in both the left and right side PMTs, and that are within a narrowed TDC window cut, compared to the red and blue which are over the whole TDC window, are shown in black for each scintillator bar. The red and blue data is mostly accidentals from background.

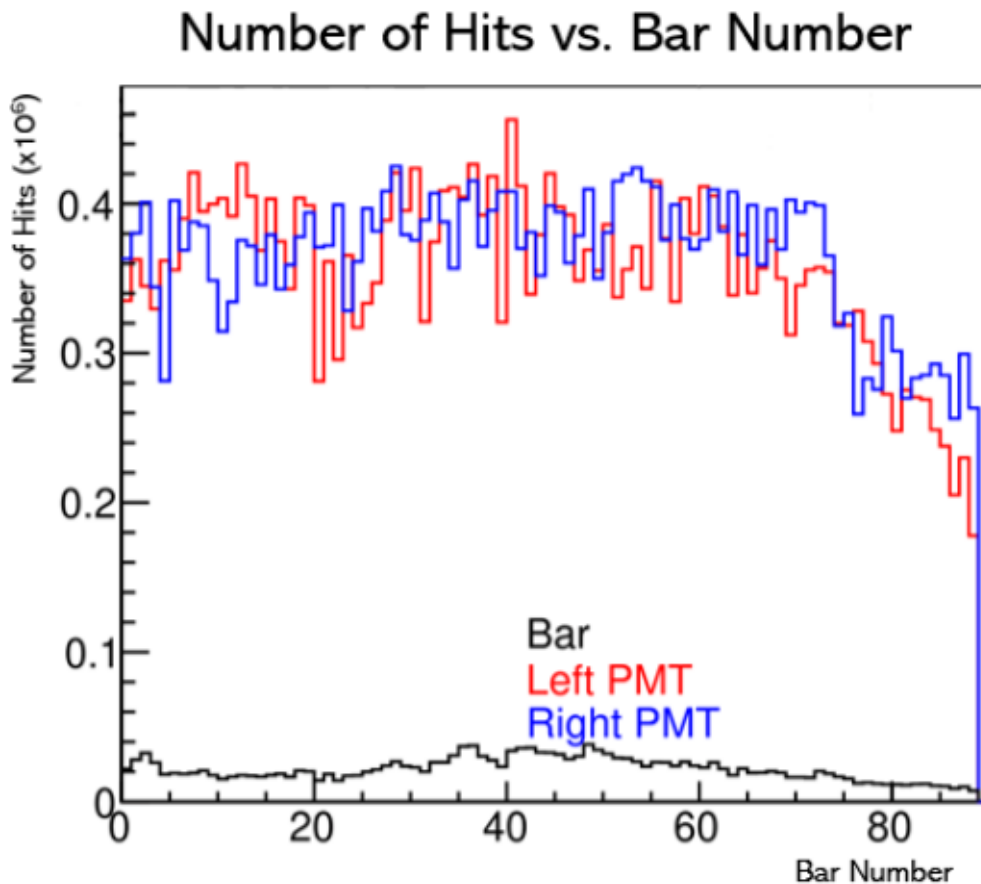


Figure 5.21: A plot of occupancy versus bar number using data from an 11 uA beam on an LD2 target from SBS-11 run 12946 with the BBCal trigger for 500K events. The black line is coincidence events between left and right PMTs for each bar within a narrowed TDC window.

The occupancy in Figure 5.21 for PMTs toward the top of the TH detector drop off slightly because there are less particle tracks which scatter from the target in that region. This causes the BBCal trigger to fire less for events toward the top of all BigBite package detectors, and this is a common trend not unique to the TH detector. However, the number of hits with regard to bar coincidence for these top bars remains fairly consistent, with less of a dropping off effect when compared to scintillator bars toward the middle and bottom where particle tracks are slightly more abundant. The plot shown in Figure 5.21 was used for monitoring purposes during the G_M^n experiment run-time and helped identify PMTs which were running at output levels either too high or too low for normal operation. This would help identify noisy or missing channels, signaling that an adjustment was needed. Plots of occupancy versus bar number were generated for each run across all six SBS kinematic settings.

A study of rates was developed as a means for reviewing the TH detector's performance and to determine how well the experiment run-time conditions adhered to the recommended operational restriction of keeping individual scintillator bar rates below 2.5 MHz, an estimate based on DAQ trigger electronics capability. Rates were monitored for the G_M^n experiment run-time, but a comprehensive review was employed to see how rates changed with kinematic setting, and with the addition of shielding and changes to HV settings at different stages. The rate for a single scintillator bar is defined as the number of hits, or occupancy, divided by the number of events recorded by the event handler for the run being analyzed, which gives us a hits ratio. The hits ratio is divided by the TDC window size, measured in microseconds, to give the rate for the scintillator bar. Bar 40, which is located directly in the middle of the TH detector, was chosen as a representative for the rates study since it is positioned where hits, and therefore the rate, are likely to be the highest compared to the rest of the TH detector. The rates analysis was conducted with varying beam energy for different SBS kinematic settings, and luminosity, which is a function of beam current and target type. For each setting the beam energy is constant and only electron-neutron luminosity, "eN" in $\text{cm}^{-2}\text{s}^{-1}$, changes. Figure 5.22 provides six plots of rates across different luminosity values for each of the six SBS kinematic settings. Beam current values were taken from experiment run-time condition records which may have varied slightly during the selected SBS runs used for the rates analysis due to beam tripping, The beam current values shown on these plots are average values over their corresponding run, and beam tripping was infrequent, so average beam current values are sufficient for estimated rate analysis. Rates were calculated using fifty-thousand event replayed ROOT files.

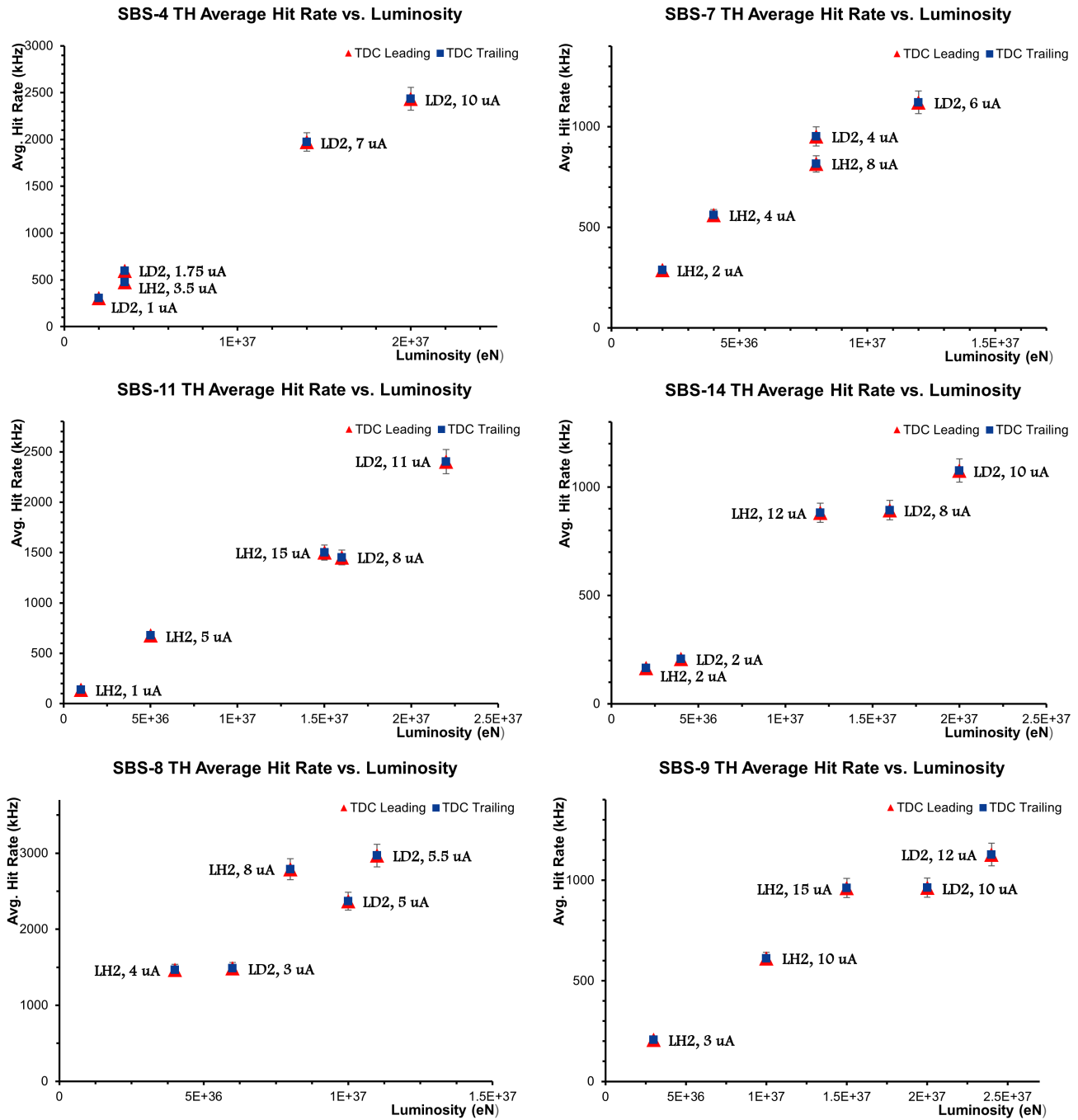


Figure 5.22: Six plots of scintillator bar rates versus luminosity for each of the SBS kinematic settings. These plots are arranged in timeline order, going from top left to bottom right. The target type and beam current are labeled next to their corresponding data points for each run used in the rates analysis. The highest rates recorded from SBS-4 and SBS-11 come close to exceeded the recommended 2.5 MHz upper limit, while SBS-8 surpasses this value by roughly a few hundred MHz. The symbol eN represents electron neutron scattering luminosity with units of $\text{cm}^{-2}\text{s}^{-1}$.

The rates were calculated using both the leading and trailing edge TDC data to investigate the possibilities of discrepancies between the leading and trailing edge signals which could have been caused by some internal bias within the TDC 1190 readout modules. From the plots, it is plain to see that the leading and trailing edge rates are consistent with each other, proving any concern over biasing between the leading and trailing edge within the TDC 1190 readout module to be unfounded. From Figure 5.22, SBS-8 is shown to have the highest rates, which precipitated the decision to lower the HV values by 50V across all PMTs before the beginning of SBS-9. Between certain data points, specifically during SBS-11 and SBS-8, the luminosity increases, but the rates either stay the same or decrease, which is counter to what would be expected. But in these cases, shielding was added between the target and the BigBite magnet, and this accounts for that discrepancy because the added shielding would have a decreasing effect on the rate. Including changes to the shielding, a decrease in the TDC window from 2 micro-seconds to 1 micro-second occurred before the highest rate data point in SBS-11. The TDC window was then adjusted again to 1.2 micro-seconds before the start of SBS-14. This is important to note since it is the TDC window size which the hits ratio is divided by that gives the value for the rate. Two more plots are provided in Figure 5.23 which show the rates where the luminosity is relatively constant within a narrow range for both low and high luminosity versus SBS kinematic setting, which varies the beam energy.

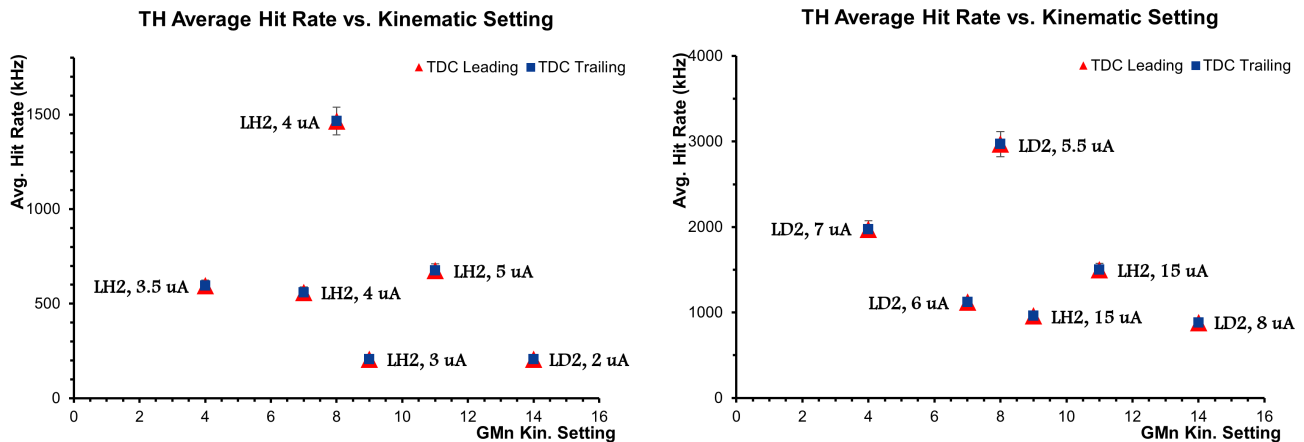


Figure 5.23: Two plots of the average hit rate versus kinematic setting with relatively constant luminosity at both low (left) and high (right) values within a narrow range. SBS-8 holds the highest rates for both data sets because it has the smallest BigBite angle relative to the beam-line. This shows that a significantly greater numbers of particle tracks originating from the beam-line and not the target are interacting with the TH detector at this kinematic setting, causing the rates to increase drastically.

The plots from Figure 5.23 were generated for the purpose of observing how beam energy and spectrometer angle affect rate. At both the low and high luminosity, SBS-8 has the highest rate which would be unexpected given that it has neither the highest Q^2 nor the highest beam energy of the six kinematic settings. What sets SBS-8 apart is its small BigBite angle relative to the beam-line which puts the TH detector closer to the beam than any of the other five kinematic settings. This is why the rates are significantly higher for SBS-8 compared to the other SBS kinematic settings. The range for low luminosity data runs used in Figure 5.23 are within $3\text{-}5 \times 10^{36}$ eN and $1.2\text{-}1.5 \times 10^{37}$ eN for the high luminosity data runs. Figure 5.24 provides a combined rates plot of those shown in Figure 5.22 with the SBS kinematic settings in timeline order for each of the run groups starting with SBS-4 on the left and ending with SBS-9 on the right. From Figure 5.24, it is easier to compare the SBS kinematic settings based on how they performed in terms of their rates. The effect of the 50V drop to the HV values across the whole TH detector is visible in the large difference in rates between SBS-8 and SBS-9.

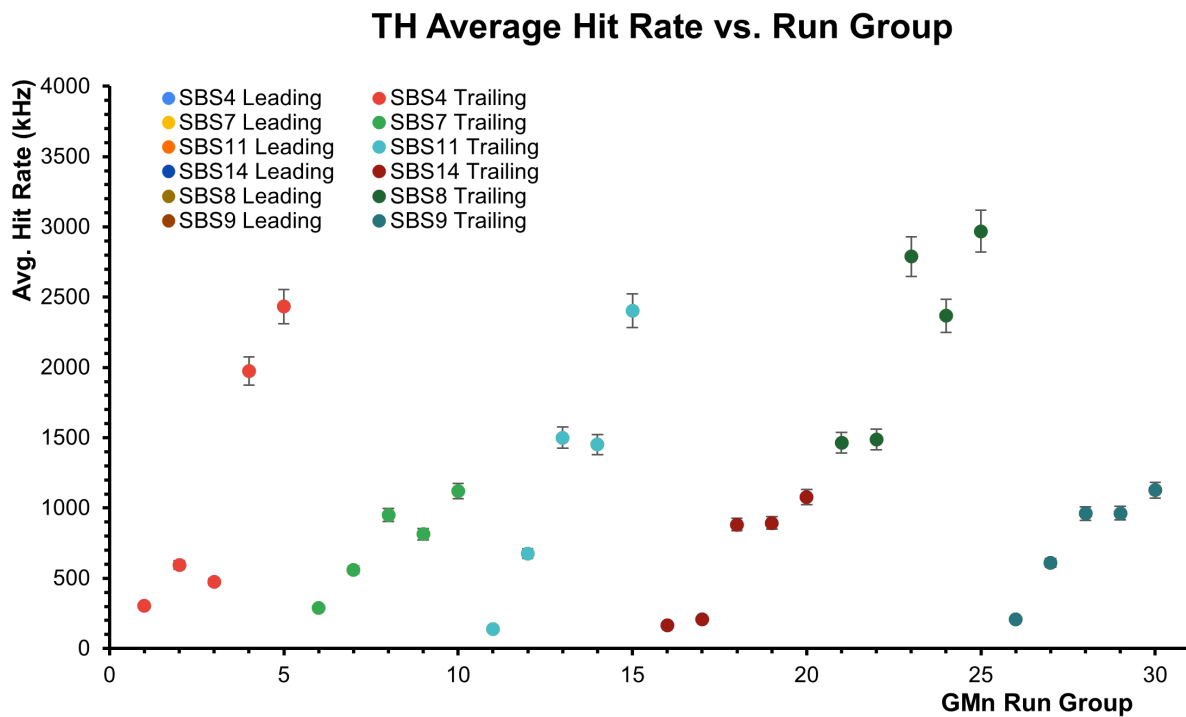


Figure 5.24: A combined plot of all rates for each of the six SBS kinematic settings during the G_M^n experiment in timeline order from left to right, segmented by run group with luminosity increasing from left to right for each group of runs, which go left to right on the plot in the same order from top to bottom of Table 5.1. SBS kinematic settings 4, 11, and 8 boasted the highest rate values which pushed the TH detector right up and slightly past its limit in terms of its performance relative to the recommended range of operation. Leading and trailing data points overlap.

5.6 Accidentals and Pile-up

Complementary to the rates analysis, a study of the accidental ratios over different luminosity for each of the six SBS kinematic settings was implemented. The structure of this accidental ratios study was exactly the same as for the rates. An accidentals ratio is defined as the number of hits corresponding to particle track events originating from the target and recorded by the TDC 1190 readout module for a certain scintillator bar divided by the number of hits in that same peak which do not correspond to particle track events originating from the target. Thus, accidentals are events in the TDC peak which correspond to background radiation mostly from the beam-line. Like the rates, the accidentals ratios should increase with luminosity for the same reason as the rates increase with luminosity. The number of accidental hits varies with beam energy and proximity to the beam-line where there is the most background. Beam energy and BigBite angle vary with kinematic setting, so accidental ratios were calculated for each setting separately, while varying luminosity. Figure 5.25 provides a visual for how the accidentals ratio is calculated for scintillator bar 40, which was used as a representative for the purposes of the study. The ratio is calculated by dividing the blue shaded region of the peak by the whole shaded region of the peak, which is the red plus the blue region.

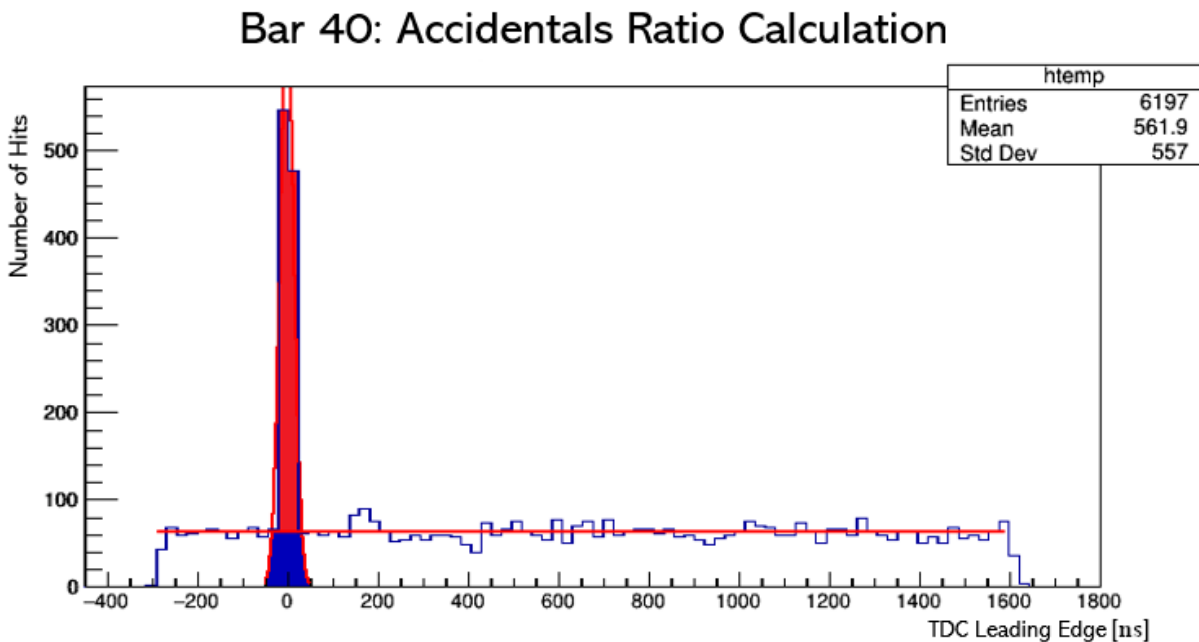


Figure 5.25: An example plot of the accidentals ratio calculation for scintillator bar 40. This same plot was generated and used for the calculation of the ratio for each of the same five data runs of the six kinematic settings used in the rates analysis. The red straight line is an average of the background hits without the peak included.

Plots of the accidental ratios for the six kinematic settings with varying luminosity are provided in Figure 5.26. These data points correspond to the same beam current and target type for the same runs used in the rates analysis shown in Figure 5.22, thus the luminosity for each data point used in the accidental ratios study is the same as in the rates study. The accidental ratios were calculated using only TDC leading edge time data because, as was shown in the rate analysis, there is no difference in the number of hits due to any biasing between the leading and trailing edge of the TDC signal, thus it is sufficient to focus only on the leading for the accidentals ratio calculation. The highest of the accidental ratios shown in Figure 5.26 reach values just below 0.4 for SBS-4, SBS-7, SBS-11, and SBS-14, while the highest ratio for SBS-9 reaches just above 0.3. The accidental ratios from SBS-8 tend to be more uniform than the other kinematic settings, and this is likely because of its closer proximity to the beam-line as shown by θ_{BB} in Table 4.2. It shows that for SBS-8 the beam-line, which is at a constant energy for the kinematic setting, has a greater effect on how much the ratio varies with luminosity since the background coming from the target is more drowned out by background from the beam-line than at other kinematic settings.

Similar, to the rates study, two plots of accidental ratios for groups of low and high luminosity, across the six kinematic settings are provided in Figure 5.27. The beam current and target type for the data points shown in both the high and low luminosity plots for Figure 5.27 are exactly the same as those used for the plots of the high and low luminosity rates plots in Figure 5.23, and therefore the luminosity is the same for each matching data point. SBS-4, SBS-7, and SBS-11 tend to have higher ratios in the group of kinematic settings, while SBS-9 and SBS-14 tend to have lower ratios. Figure 5.28 provides a plot of accidental ratios, which is a combined plot of the six ratio plots in Figure 5.26, that are grouped in timeline order starting with SBS-4 and ending with SBS-9. For all of the SBS kinematic settings, excluding SBS-8, the highest ratio calculated fails to exceed more than 0.4, which is still a large portion of TDC leading edge peak. Notably, the 50V drop before the start of SBS-9 has no major effect on the accidental ratios for that kinematic setting compared to the other kinematic settings, which is in stark contrast to what was seen in the rates study. However, the accidentals are more effected by the background radiation in Hall A, which is highly dependent on the beam energy, and luminosity of the target, and not directly effected by the operation of the PMT, so the drop in the HV values would not be expected to have that great of an effect on the accidental ratios for SBS-9. The addition of shielding at points throughout the G_M^n experiment run-time does not have the same decreasing effect on the accidental ratios as with the rates.

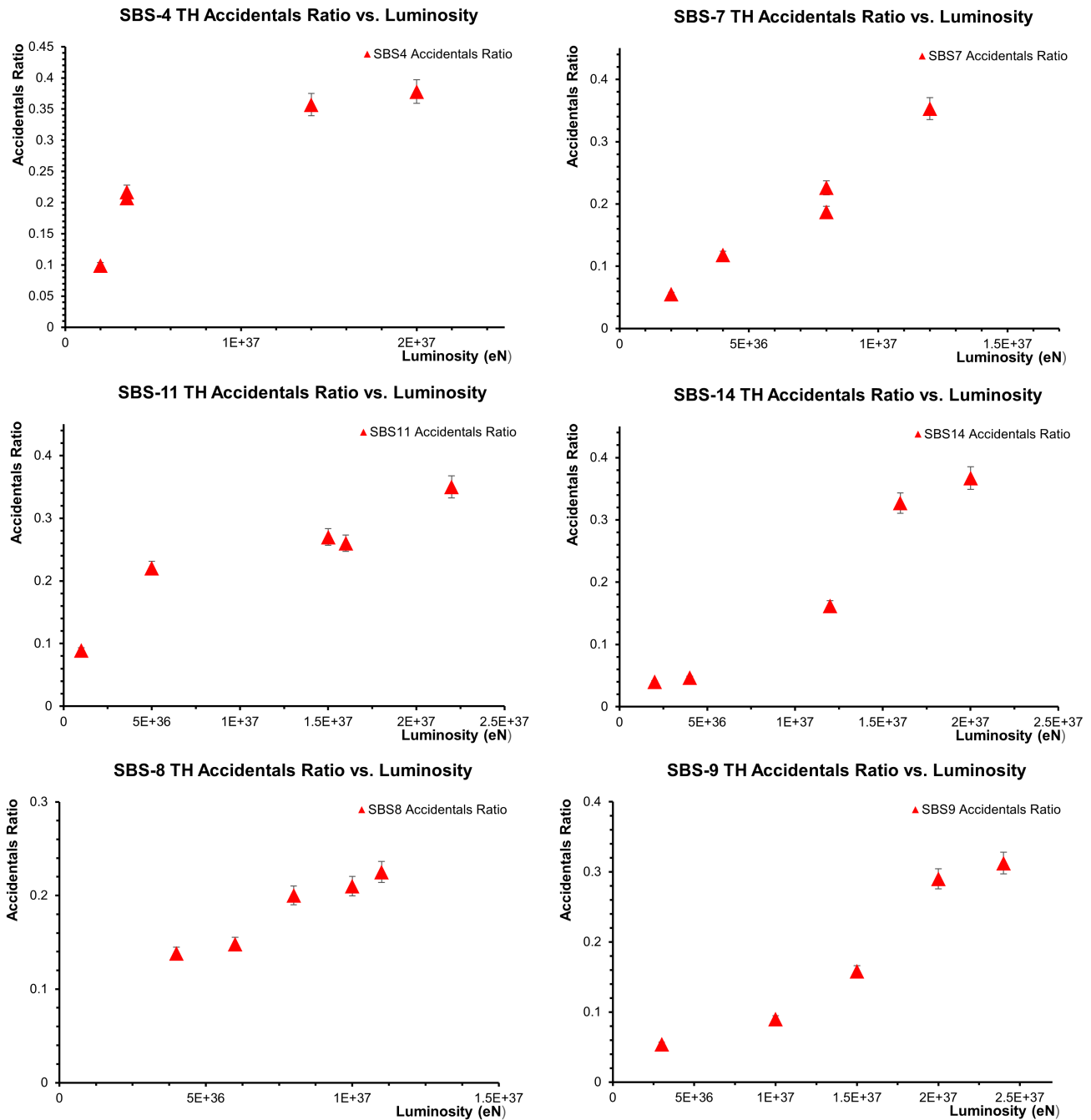


Figure 5.26: Six plots of scintillator bar accidental ratios versus luminosity for each of the SBS kinematic settings. These plots are arranged in timeline order, going from top left to bottom right. The target type and beam current are the same for each data point as those used in the rates analysis. The highest ratios recorded from SBS-4, SBS-7, SBS-11, and SBS-14 come close to a value of 0.4, while SBS-8 reaches slightly above a ratio value of 0.2. The symbol eN represents electron neutron scattering luminosity with units of $\text{cm}^{-2}\text{s}^{-1}$.

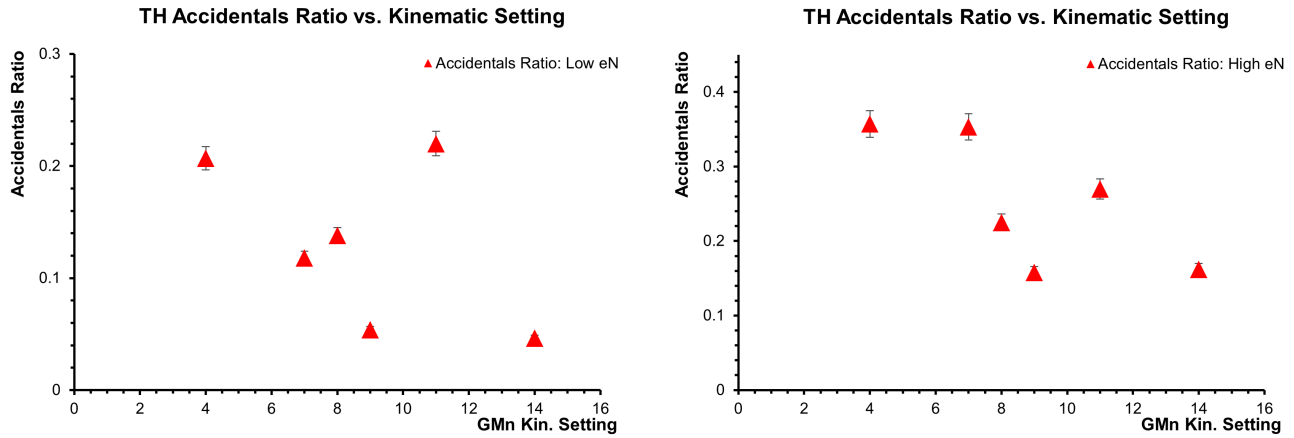


Figure 5.27: Two plots of the accidental ratios versus kinematic setting with relatively constant luminosity at both low (left) and high (right) values within a narrow range. SBS-8 shows a more constant ratio value when comparing both data sets. This shows that a significantly greater amount of background originating from the beam-line and not the target is interacting with the TH detector at this kinematic setting causing the ratio to be comparatively less affected by changes in the target luminosity. The left plot is from low luminosity runs and the right is from high luminosity runs.

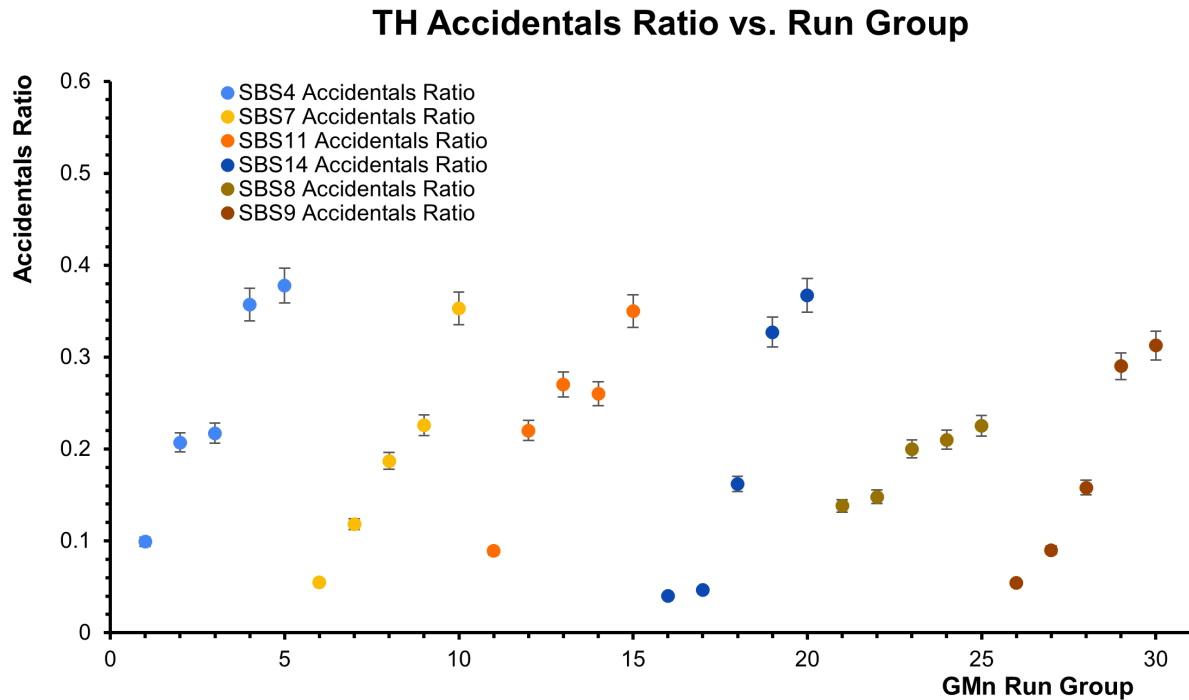


Figure 5.28: A combined plot of all accidental ratios for each of the six SBS kinematic settings during the G_M^n experiment in timeline order from left to right, separated by run group with luminosity increasing from left to right for each group of runs, which go left to right on the plot in the same order from top to bottom of Table 5.1. SBS kinematic settings 4, 7, 11, 14, and 9 show similar behavior in their upward trend such that the ratio increases with luminosity. SBS-8 shows an upward trend as well, but at a slightly lower slope caused by proximity to the beam-line.

To round-off the performance analysis for occupancy, rates, and accidentals, a study looking for potential evidence of pile-up was completed. The reason for investigating potential pile-up was predicated on the concern that the rates were too high. If the rates are too high then the FADC signals will bunch, meaning that the peak of one signal peaks in the tail of a previous signal. This would cause the baseline of the signals to increase and indicate pile-up. This study focused on the pedestal means and widths from the FADC data and an increase in these means and widths would indicate an increase in the FADC baseline. Therefore, the expectation is that as the rates increase, the means and widths would increase. Evidence of pile-up would be characterized by a noticeable systematic shift among the data points for pedestal means and widths as the rates increase. Examples plots of the FADC pedestal spectra versus PMT number for the left and right side PMTs connected to the FADC are provided in Figure 5.29. The plots in Figure 5.29 were generated from the FADC data before pedestal correction to zero, so the raw pedestal spectra could be analyzed. Interestingly, the plot of the right-side PMT pedestal spectra shows more background noise above the pedestal peak which is due to the beam-line being in closer proximity to that side of the TH detector. A Gaussian fit was applied to each pedestal distribution for each PMT similar to the commissioning analysis implemented during the study of ADC normalization. The maximum bin FADC values and root-mean-square (rms) values are extracted for the means and widths of the pedestal spectra. These data points for left and right PMTs are provided in Figures 5.30 and 5.31, respectively.

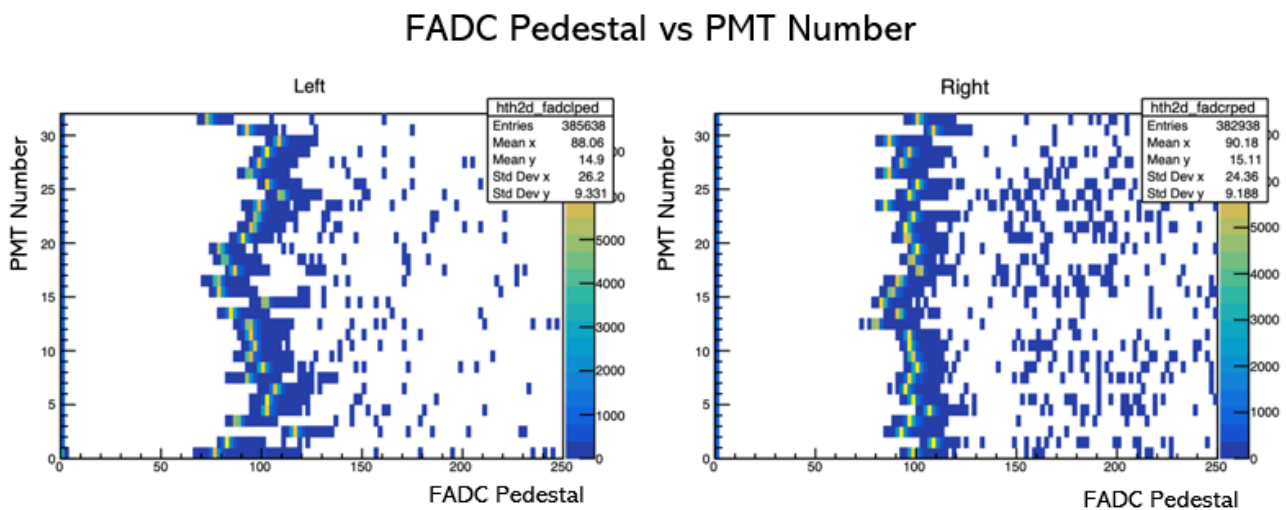


Figure 5.29: Two example plots of the FADC pedestal spectra for left (left) and right (right) PMTs versus PMT number. These plots were generated from data taken during the SBS-4 kinematic setting using an LH2 target and the BBCal trigger.

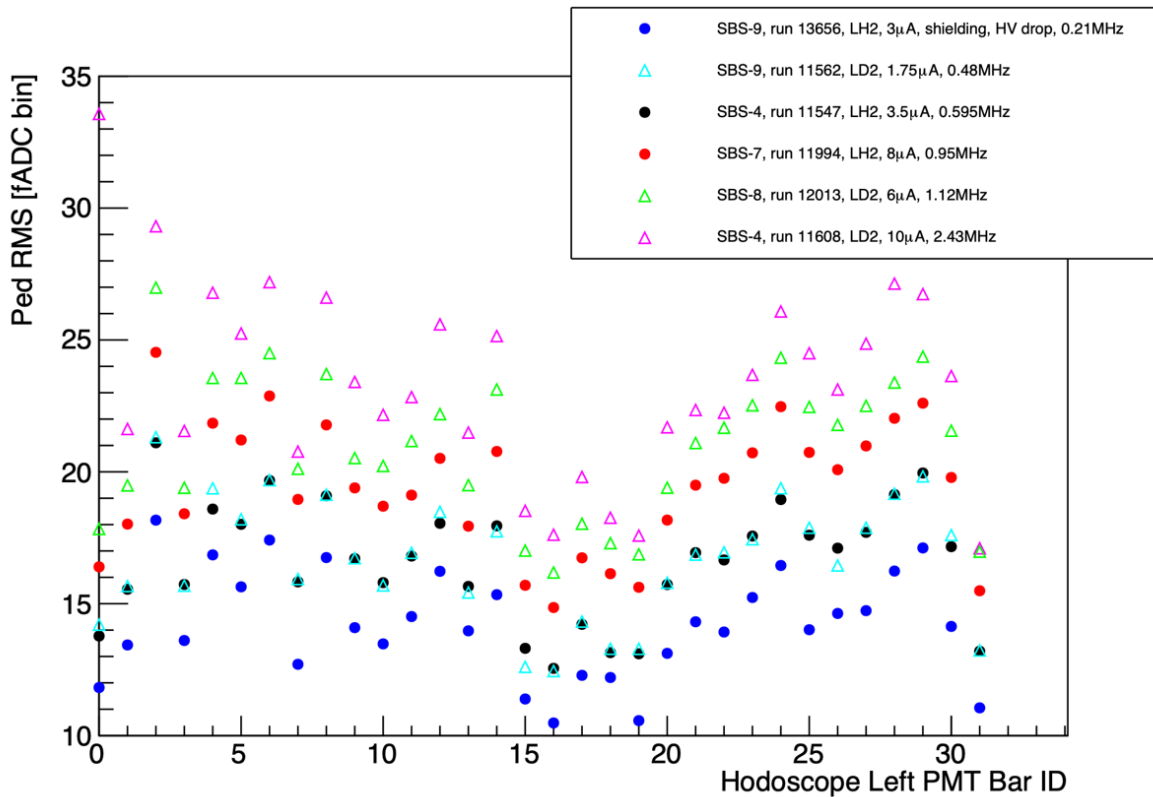
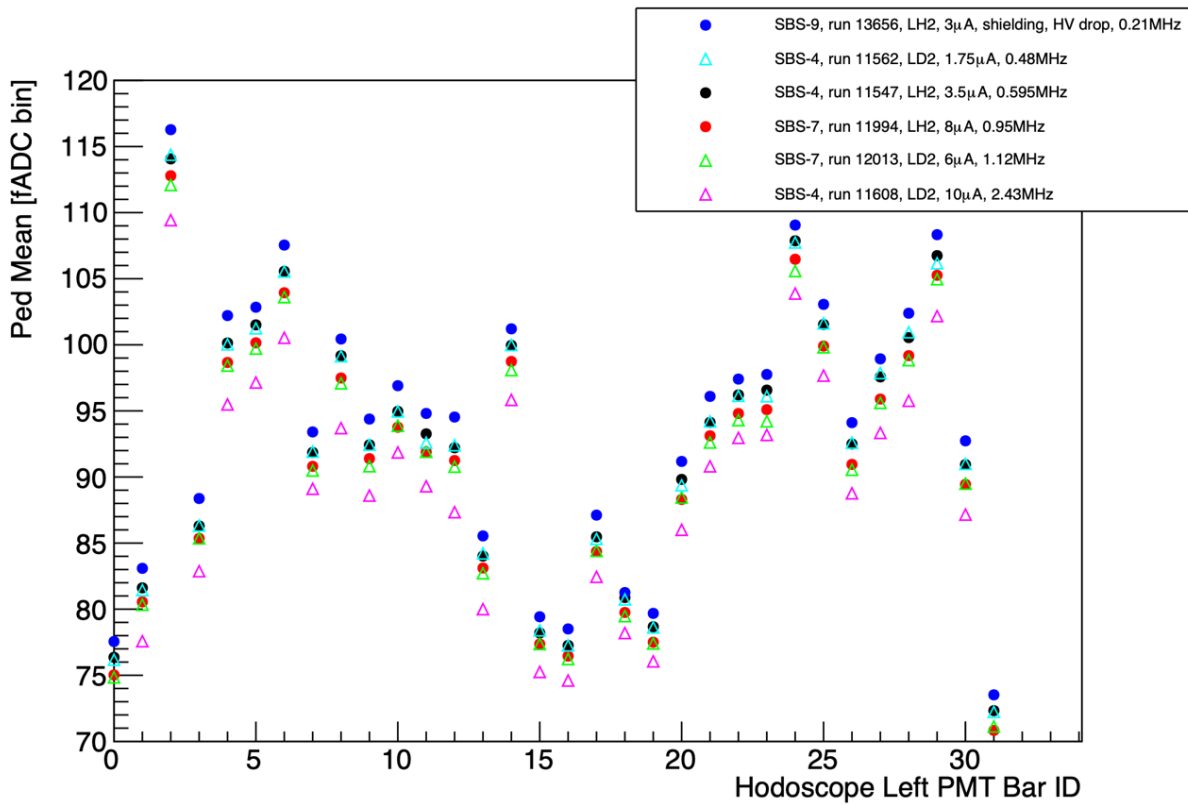


Figure 5.30: Two plots of left PMT pedestal means and rms values versus PMT number. For the PMT numbering, 0-31 on the plots corresponds to the left PMTs that were connected to the FADC readout modules during the experiment.

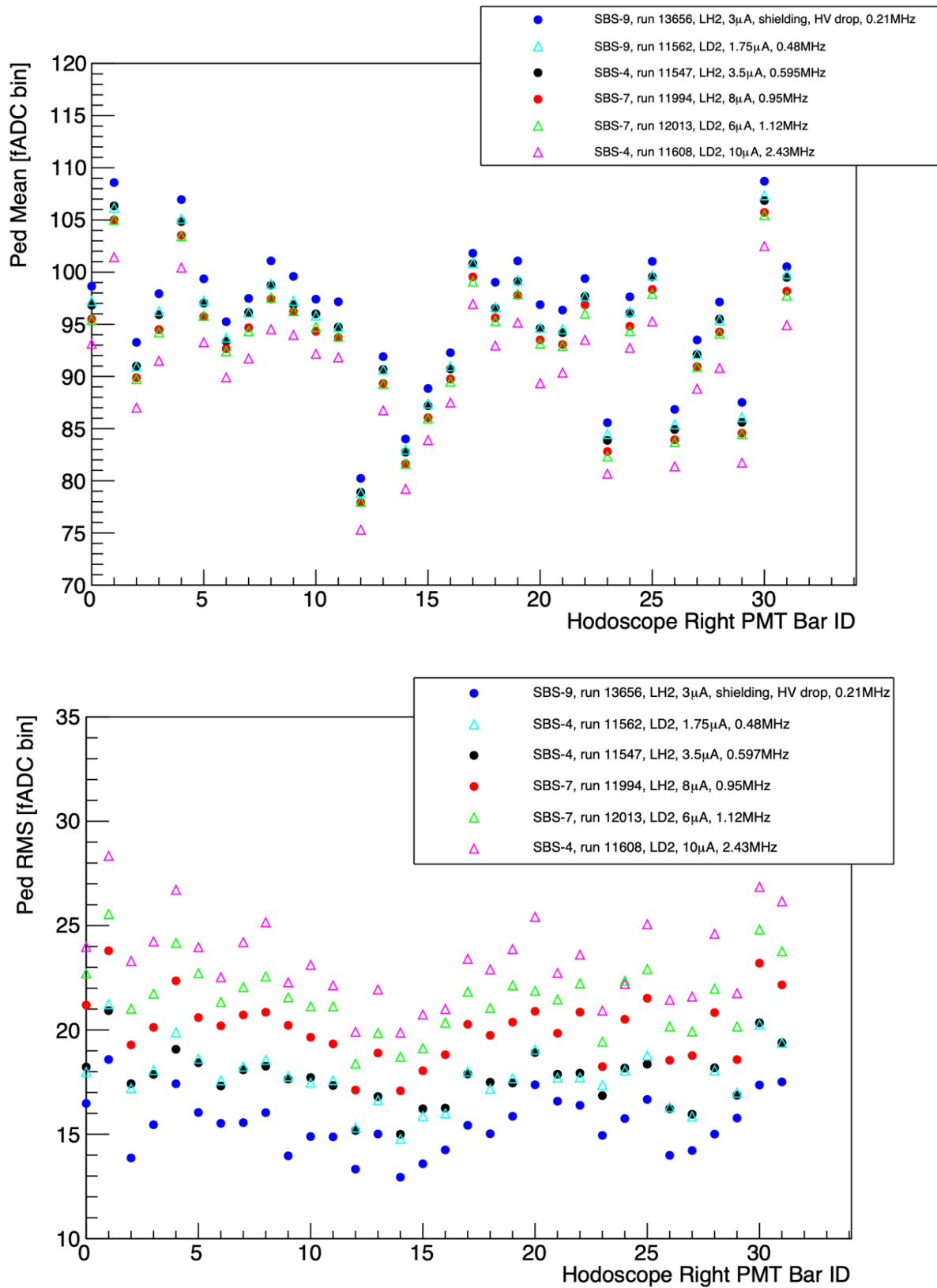


Figure 5.31: Two plots of right PMT pedestal means and rms values versus PMT number. For the PMT numbering, 0-31 on the plots corresponds to the right PMTs that were connected to the FADC readout modules during the experiment.

Based on these plots, there is no apparent pile-up occurring even in the region closest to the recommended maximum rate of TH detector. The points remain for the most part, around the same average mean value which indicates that there is little change in the magnitude of the individual values as the rates increase. Therefore it can be concluded that there is not enough evidence to cause concern over pile-up of detector signals. Therefore, the rate has little effect on how well the TH detector and its readout modules are able to record data. The pedestal means do not vary more than a few FADC bins with the change in rate across the chosen data runs used for this study, even though rates increase significantly from 0.2 MHz up to 2.4 MHz. The pedestal means tend to decrease with the rate which is the opposite of what was expected. This could in part be due to changes with the kinematic setting parameters. The pedestal widths vary slightly more than the means relative to their average rms value, but there is no evidence of the widths reaching a maxing-out limit in terms of the TH detector rates performance. This study of pile-up indicates that even at the recommended maximum limit of 2.5 MHz for the overall rate, the performance of the TH detector did not noticeably suffer in terms of its ability to record data.

5.7 Track Matching Efficiency

The track matching efficiency of the TH detector is defined on a bar by bar basis and calculated relative to the tracking data collected by the BigBite GEMs. First, the x (vertical, dispersive) and y (horizontal, non-dispersive) positions, using the transport coordinate system focal planes, of tracks in the TH detector are calculated utilizing the timing data from the left and right side PMTs for each scintillator bar by taking the mean of the x and y positions calculated for the cluster corresponding to the particle track. This value for the x and y position of the particle track is the location where the TH detector claims a particle track passed. A comparison of TH measured positions is made to where the GEMs claim projected particle tracks pass using x and y values at the TH location for that projection, given the distances between the detectors, and particle track trajectory angles. The result is four plots, two in the x focal plane and two in the y focal plane for both the TH and the GEMs, and these plots can be overlaid as in Figure 5.32. Interestingly, the number of tracks in the y focal plane increases in the direction toward the beam-line. The plots shown in Figure 5.32 were generated for all six kinematic settings using an LH2 target and the BBCal trigger with cuts applied for all-tracks, electrons, and elastic electrons.

X and Y Positions vs. Number of Tracks

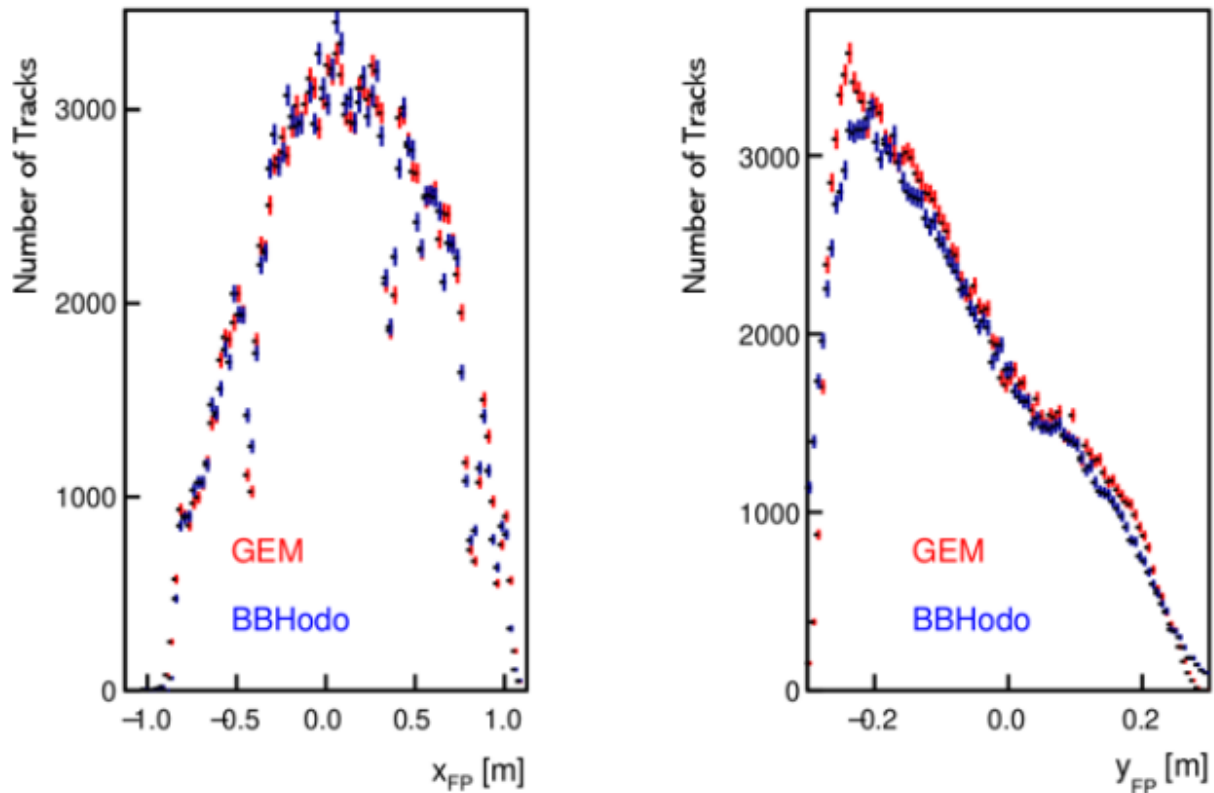


Figure 5.32: Two plots showing the comparison of particle track locations in the TH compared to where the GEMs predict the tracks should pass. These plots were generated using LH2 data and a 3.5 μA beam from the SBS-4 kinematic setting with cuts applied for only elastic electrons.

The TH data from the plots for x and y position from Figure 5.32 can be converted to weighted sums and divided by the corresponding GEM plots for x and y position which are also converted to weighted sums. This gives the efficiency values versus position in both focal planes. To observe how the efficiency varies on a bar by bar basis across the six SBS kinematic settings, it makes more sense to consider the efficiency in the dispersive x-direction focal plane rather than the y-direction non-dispersive focal plane because the TH detector is subdivided into bars vertically and not horizontally. Figure 5.33 provides an example plot of these efficiencies values versus scintillator bar number. The plots like the one shown in Figure 5.33 are generated using the bar identification data for the particle tracks to get the scintillator bar number information for each efficiency value. The efficiencies tend to be unreliable toward the upper and lower extremes of the detector due to the lower statistics. A mean of the scintillator bar efficiencies is calculated, and this process is repeated for all six SBS kinematic settings with cuts applied for all-tracks, electrons, and elastics. The mean efficiency values are plotted versus kinematic setting in Figure 5.34.

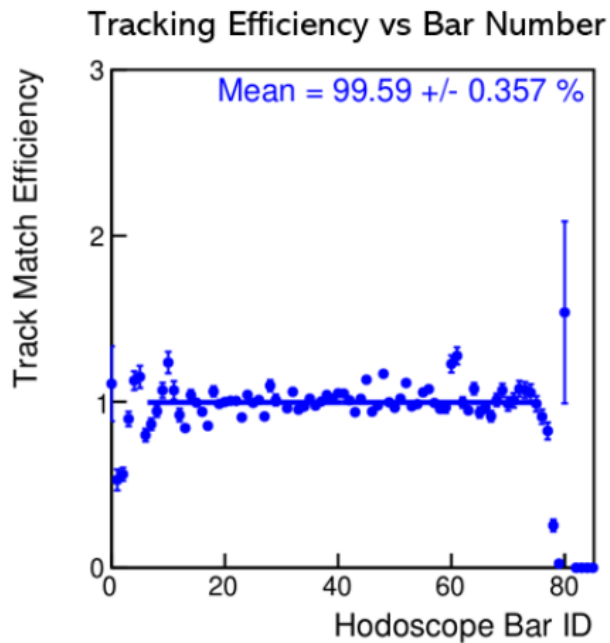


Figure 5.33: An example plot of the track matching efficiency versus bar number for data taken from the SBS-4 kinematic setting using an LH2 target, 3.5 uA beam, and the BBCal trigger. The mean is calculated by excluding a couple bars on the extremes of the TH detector at the top and bottom with efficiency values and statistics that do not allow for reliable data points.

Tracking efficiencies plotted in Figure 5.34 vary slightly between all-tracks, electrons, and elastics. A marginal trend for some, but not all of the kinematic settings shows that the efficiency decreases with the addition of more cuts, which makes sense because the higher momenta elastics created larger particle showers from the PS and therefore decreased the track matching efficiency. The all-tracks efficiencies, which are dominated by lower energy particles such as for pions, will generate less hits in the TH detector thus making it easier for the detector to identify tracks. The efficiencies show no notable variation relative to the addition of shielding during the GMn experiment run-time as provided in Table 5.1, and the 50V drop to the HV values before the start of SBS-9 does not appear to affect the efficiencies. The cosmic data uses the same ADC neighbor cuts as for charge normalization during commissioning, and the same TDC timing cuts as for the calibrations. The black all-tracks marker for SBS-8 is overlaid by the blue data marker for electron particle tracks because those two data points have close to equal track matching efficiency. The larger disparity in data points for SBS-7 was due to a higher number of unreliable bar efficiencies on the extremes at the top and bottom of the TH detector because of lower statistics in those regions for that kinematic setting, likely an effect of the BBCal trigger. Track matching efficiency >100% is due to infrequent recording of >1 hit from accidentals within narrow TDC window cuts.

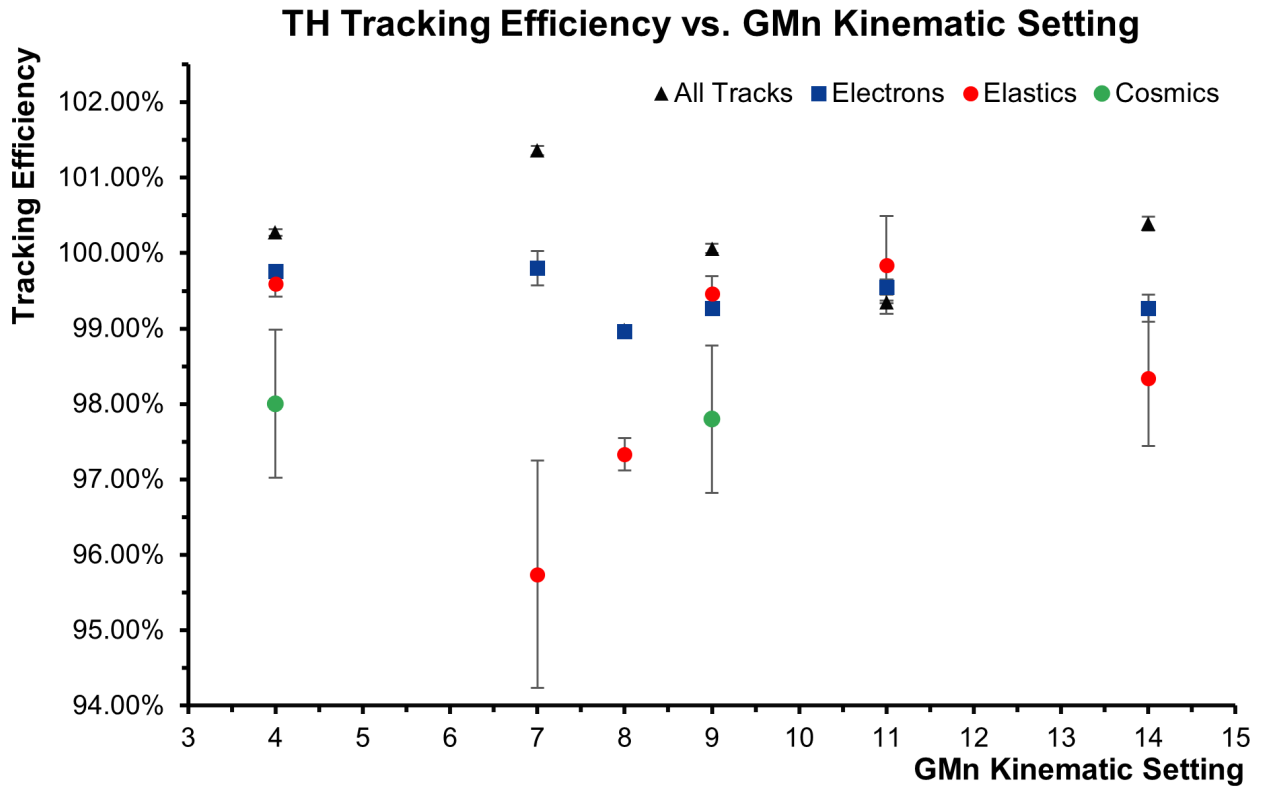


Figure 5.34: A plot of the mean track matching efficiency across all scintillator bars for the six kinematic settings with cuts applied for all-tracks, electrons, and elastics. This data was collected across several runs from each kinematic setting using an LH2 target and the BBCal trigger.

5.8 Position Resolution

To determine the position resolutions in both the horizontal and vertical directions, the same means calculated from the clusters in the x-direction and y-direction focal planes for calculating the tracking efficiency are also used for calculating the position resolutions. The difference in the calculation is that, instead of dividing the measured position calculated by the TH and the projected x and y particle track locations provided by the GEMs, the positions are subtracted to get values for the position difference of each scintillator bar such that $P_{res} = P_{TH} - P_{GEM}$. These position difference spectra for all-tracks, electrons, and elastics can then be plotted and fit with a Gaussian to get the 1-sigma standard deviation, the position resolution. A pair of 2D plots can be generated for each kinematic setting and each layer of physics cuts for the position spectra in the x-direction and y-direction versus bar number as shown in the example plots from Figure 5.35. The uniformity of these plots around zero also provides a useful visual confirmation that the calibrations are properly aligned because the calculation of the x and y particle track position for the TH detector is based on the time difference of the scintillator bars in each cluster.

Position Difference vs. Bar Number

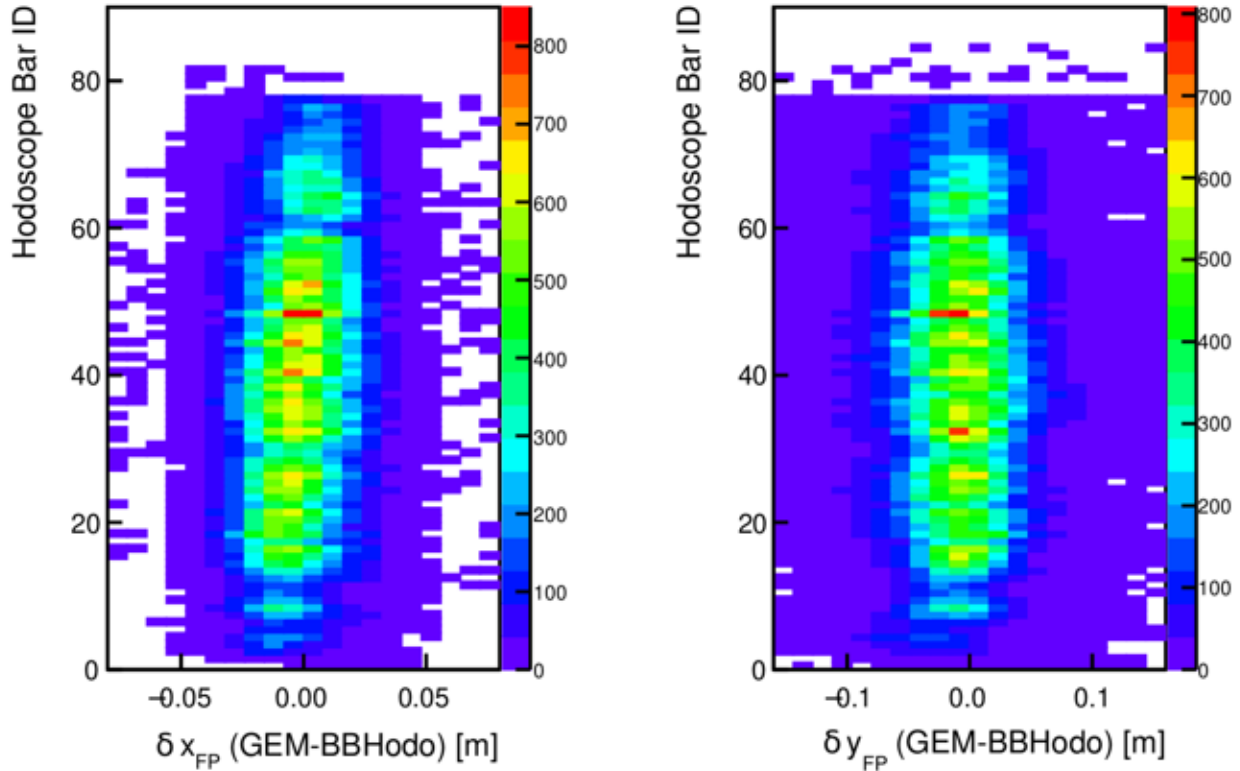


Figure 5.35: Example plots of the position difference spectra in both the x-direction and y-direction transport coordinate system focal planes versus scintillator bar number. These plots were generated with data from the SBS-4 kinematic setting with cuts applied for only elastic electrons using an LH2 target and the BBCal trigger. The same plots were generated for all six kinematic settings.

The position resolutions in both the vertical and horizontal directions can be plotted versus bar number as shown in an example from Figure 5.36. As with the tracking efficiency, the low statistics on the extremes of the TH detector are less reliable than in the center when fitting the position spectra for the 1-sigma standard deviation resolution value extracted from the Gaussian fit. A mean of the position resolutions for each scintillator bar is calculated with a linear fit to give a value for the overall position resolution of the TH detector in both the dispersive and non-dispersive focal planes. The plots shown in Figure 5.36 are generated for every SBS kinematic setting for all three layers of physics cuts. The mean position resolution in the vertical and horizontal directions is calculated using physics cuts for all-tracks, electrons, and elastics at each SBS kinematic setting, and those position resolutions are shown in Figures 5.37 and 5.38. From the plot of vertical position resolution in Figure 5.37, it is clear that the vertical position resolution varies little to none depending on the kinematic setting which makes sense because the 2.5 cm width of the scintillator bars limits this resolution. The cluster based analysis allows for the

X and Y Position Resolutions vs Bar Number

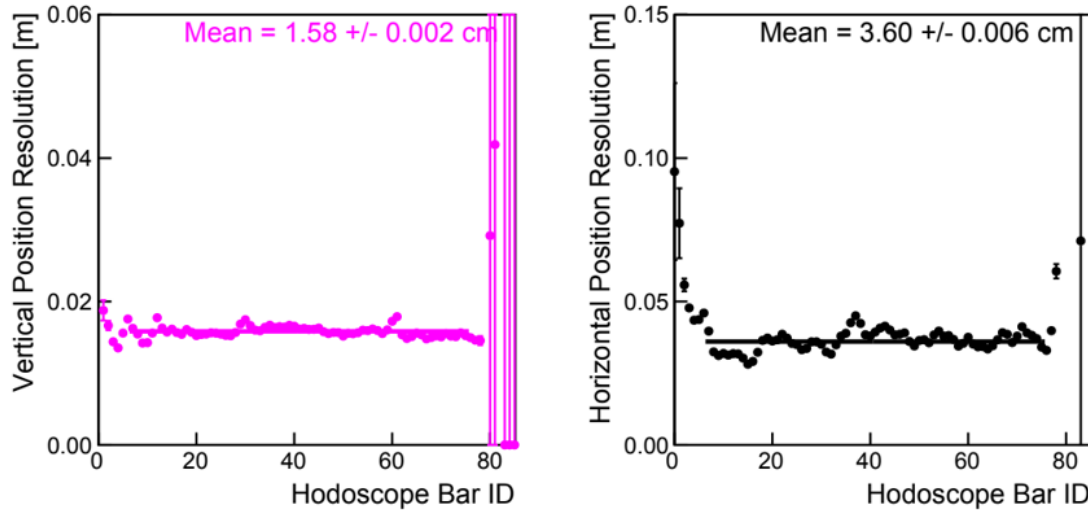


Figure 5.36: Two plots of the position resolution in both the vertical and horizontal versus bar number with a linear fit for the mean. This data was generated from the SBS-4 kinematic setting using only elastics data with an LH2 target and the BBCal trigger.

resolution to be improved slightly to within 1-2 cm. However, the vertical position resolution does have a slight variation depending on the physics cuts applied, but there does not appear to be any notable trend when comparing the all-tracks, electrons, and elastics.

The position resolution in the horizontal direction is larger than in the vertical direction because the TH detector is subdivided into bars vertically and not horizontally. This is also why the horizontal position resolution varies more depending on the kinematic than the vertical position resolution. As the GeV energy value of the incident particle track increases and decreases, the horizontal position resolution varies. A noticeable trend among the three layers of physics cuts for the horizontal position resolutions shows that generally elastic electron particles tracks have worse horizontal position resolution than electrons and all-tracks. This makes sense because the elastic electron would create a wider spread for the particle shower generated after passing through the PS detector. Compared to lower energy pions in the all-tracks data, which would create a tighter spread, the position resolution is worse on average for elastic electrons. This trend matches the simulation which shows that as the average GeV of particle tracks increase, the resolution degrades. For the position resolution data points shown in Figures 5.37 and 5.38, the horizontal values remain within a range of 3-6.5 cm and 1.25-2.25 cm for the vertical values. This horizontal position resolution is sufficient but not critical to the physics program, and improvement would only be feasible using faster tracking detectors or lower refractive index material.

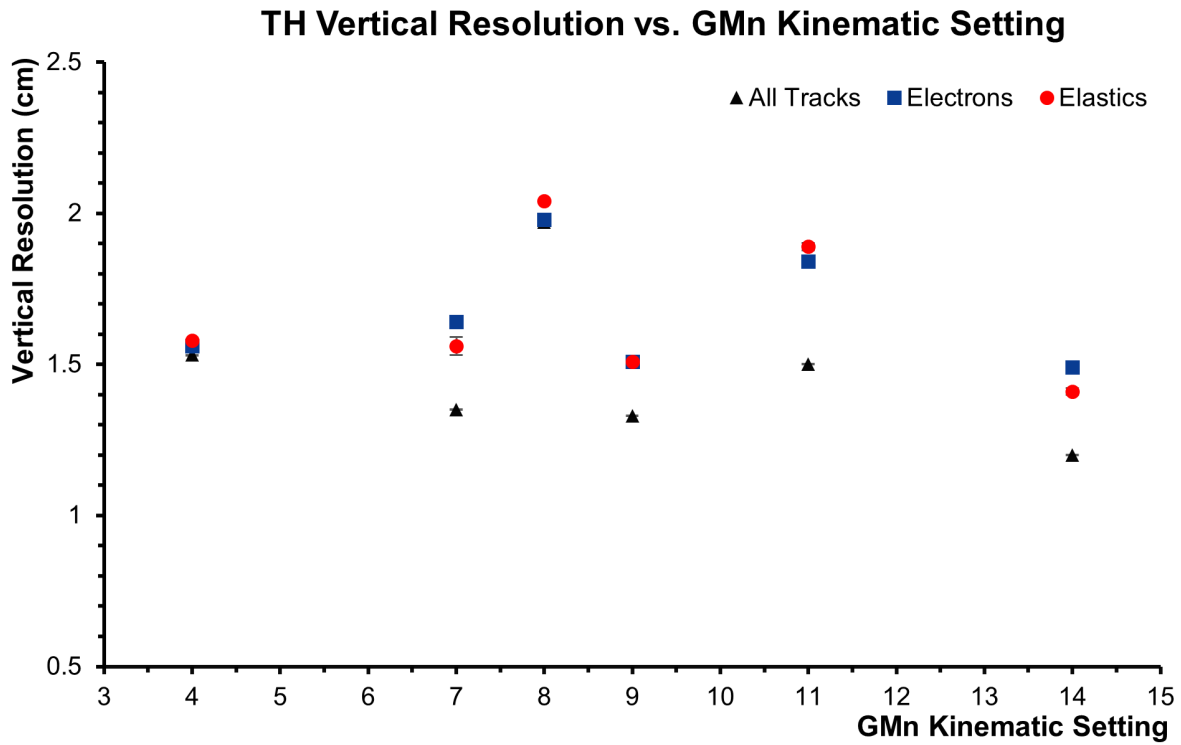


Figure 5.37: A plot of the vertical position resolution versus kinematic setting for each layer of physics cuts applied to the data using an LH2 target and BBCal trigger.

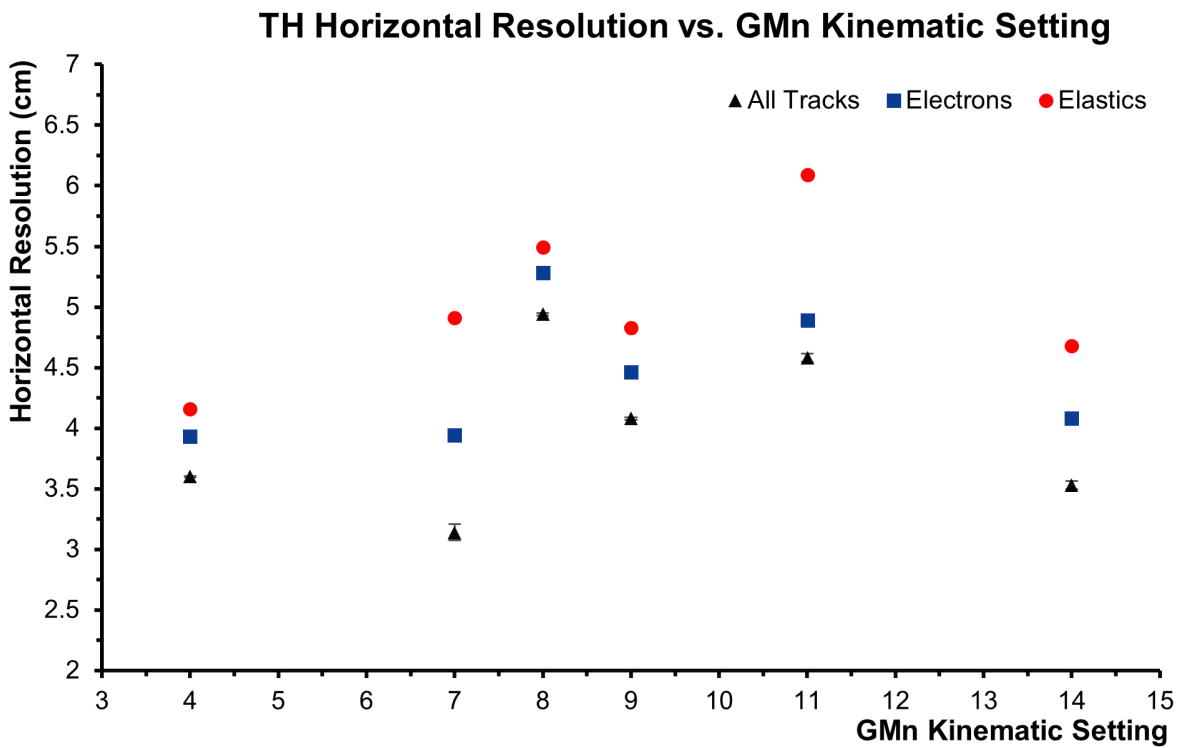


Figure 5.38: A plot of the horizontal position resolution versus kinematic setting for each layer of physics cuts applied to the data using an LH2 target and BBCal trigger.

5.9 Time Resolution

The timing resolution is calculated on a bar by bar basis by extracting the 1-sigma standard deviation in pico-seconds of the time difference distribution, which is generated by subtracting the leading edge of the calibrated TDC data between the left and right PMT of each scintillator bar. This calculation of the time difference uses a cluster-based approach similar to the calculation of the x and y locations of particle tracks for position resolution. The final time difference value for a given event is taken as an average across all scintillator bars in a cluster. The plot in Figure 5.39 provides an example for the time resolution of each scintillator bar and the mean which was measured with a linear fit to the data.

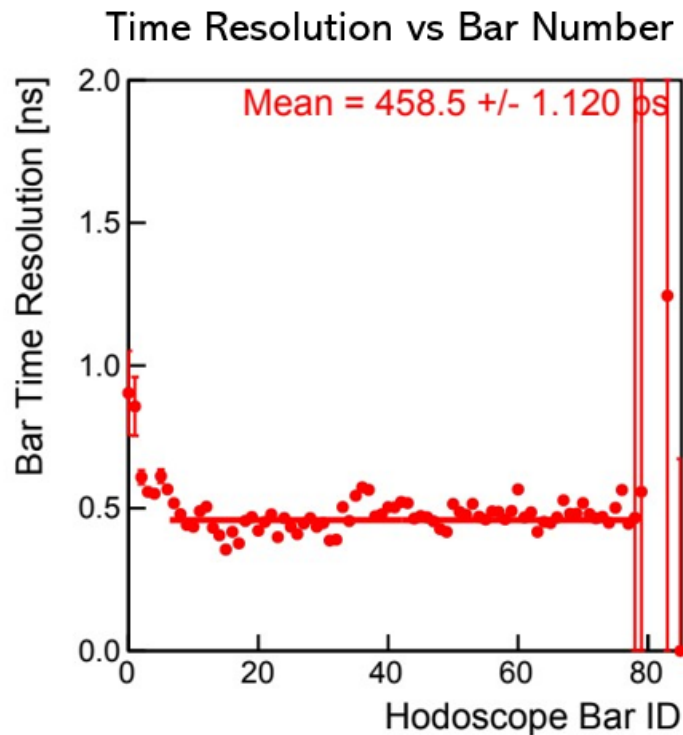


Figure 5.39: A plot of the time resolution versus scintillator bar number using a time difference and cluster-based analysis. This plot was generated using only elastics data from the SBS-4 kinematic setting with an LH2 target and the BBCal trigger.

Some of the time resolution values for scintillator bars near the top and bottom of the TH detector provided less reliable data points due to lower statistics in those regions. The time resolution analysis used to generate the plot from Figure 5.39 was repeated for all six SBS kinematic settings used in the G_M^n experiment with the three layers of physics applied for all-track, electrons, and elastic electrons.

The plot in Figure 5.40 shows the average time resolution across all scintillator bars. There is a trend in the data points shown in Figure 5.40 where the time resolution degrades with the addition of physics cuts. This trend is similar to what was observed for the horizontal position resolution which makes sense because both the time resolution and horizontal position resolution are dependent on the size of the spread from the particle shower coming from the PS detector into the TH for a given particle track. Again, the higher energy elastic electrons pass through the PS detector causing a wider spread. This leads to an increase in the 1-sigma standard deviation of the time difference distributions for each scintillator bar, therefore degrading the average time resolution measured for the whole TH detector. It can be concluded from the resolution and tracking efficiency plots in Figures 5.34, 5.37, 5.38, and 5.40, that as tracking efficiency decreases, position and time resolution worsen and vice versa. The time resolutions calculated using cosmics data in Figure 5.40 shows the intrinsic time resolution of the TH detector to be 300 ps as expected. The cosmics data uses the same ADC neighbor cuts as for charge normalization during commissioning, and the same TDC timing cuts as for the calibrations.

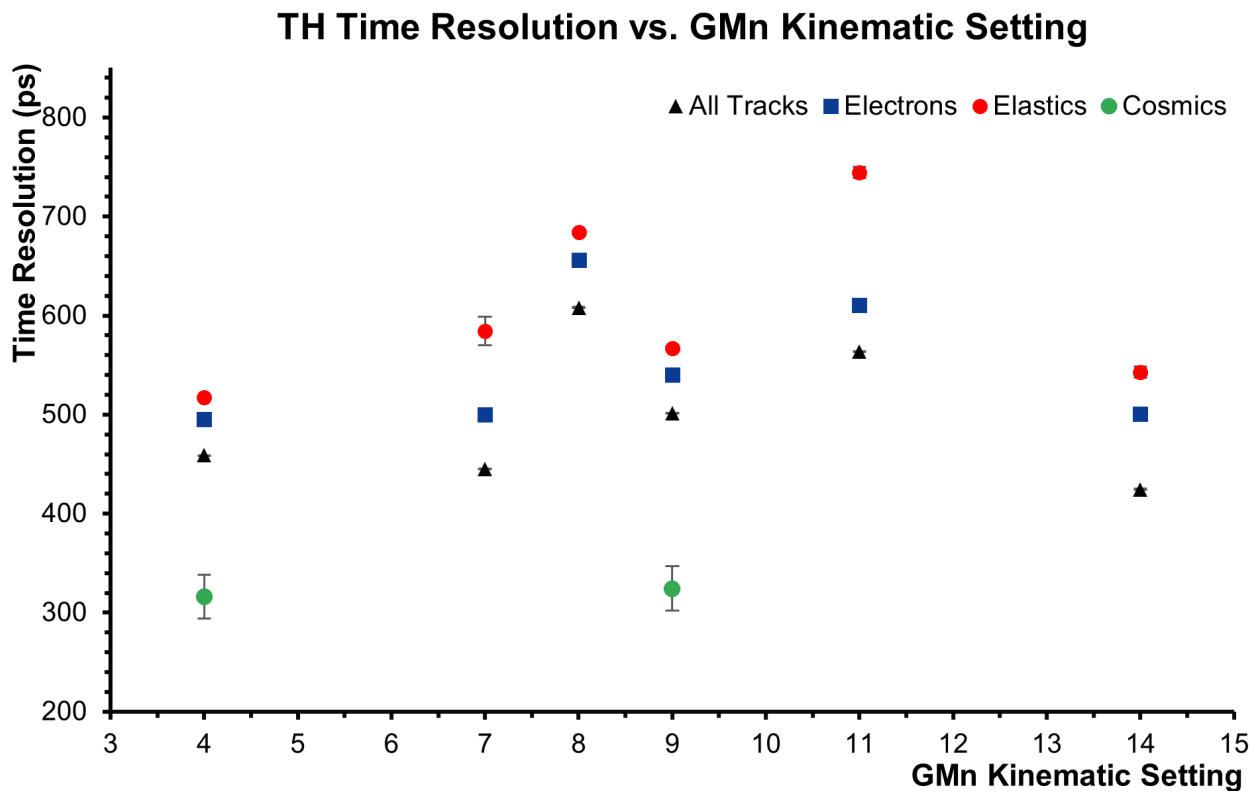


Figure 5.40: A plot of the mean time resolution versus kinematic setting for each layer of physics cuts applied to the data using an LH2 target and BBCal trigger. The cosmics data was also taken in Hall A during the GMn experiment using the BBCal trigger.

Chapter 6

Conclusion

The Super BigBite Spectrometer has been and will continue to be used in nucleon electromagnetic form factor experiments to further probe nucleon structure, QCD, and hadronic particles, which increases scientific understanding of nuclear physics into regions of higher momentum transfer that have previously been unreachable. Prediction models for the electromagnetic form factors at higher momenta diverge thus providing the scientific motivation for measurements up to ever larger values of Q^2 . This reach into higher regions of Q^2 needs to be matched by more precise resolution when measuring particle trajectories, position, energy, momentum, and timing, which is the reason for upgrading and installing the improved JLab Hall A detectors used for SBS. One of these new detectors, the Timing Hodoscope, provides precision timing data for scattered elastic electrons.

The purpose of this thesis is to provide an overview of the Timing Hodoscope construction, commissioning, installation, calibration, and performance before and during the G_M^n experiment, which was the first of five nucleon electromagnetic form factor experiments to take place as part of the SBS Hall A physics program. First, summaries of Jefferson Lab, SBS, and their associated physics background are provided before giving a detailed summary of the TH detector itself. The summary of the TH detector begins by covering its major components, data acquisition system hardware, construction, and eventual installation in Experimental Hall A. This information precedes two sections devoted to the commissioning and calibration of the TH detector. What follows is the main results of the thesis which are several data analysis studies concerning various aspects of the TH performance during the G_M^n experiment runtime. These performance studies included results for energy deposit, cluster size, rates, accidentals,

pile-up, tracking efficiency, position resolution, and time resolution across all six of the SBS kinematic settings used for the G_M^n experiment. Each of the performance studies were implemented across three layers of physics cuts for defining data sets corresponding to all particle tracks, only electrons, and only elastic electrons. In Tables 6.1-6.3, the variable E_{dep} is average mean energy deposit, C_{avg} represents the average cluster size, T_{eff} is the average track matching efficiency, H_{res} is the average horizontal position resolution, V_{res} is the average vertical position resolution, and T_{res} is the average time resolution.

Table 6.1: A table for all of the six SBS kinematic settings and their corresponding performance values for all-tracks data.

TH All-Track Performance Analysis Values						
Setting	E_{dep} (MeV)	C_{avg} (bars)	T_{eff} (%)	H_{res} (cm)	V_{res} (cm)	T_{res} (ps)
SBS-4	9.839 ± 0.003	1.996 ± 0.001	100.27 ± 0.05	3.601 ± 0.006	1.531 ± 0.001	458.5 ± 1.1
SBS-7	7.536 ± 0.006	1.594 ± 0.001	101.36 ± 0.06	3.138 ± 0.066	1.349 ± 0.001	444.9 ± 14.4
SBS-11	6.254 ± 0.005	1.342 ± 0.010	99.35 ± 0.02	4.582 ± 0.033	1.524 ± 0.001	563.9 ± 5.5
SBS-14	5.591 ± 0.006	1.443 ± 0.002	100.39 ± 0.09	3.529 ± 0.032	1.233 ± 0.001	424.3 ± 5.6
SBS-8	9.121 ± 0.003	1.664 ± 0.005	98.98 ± 0.05	4.943 ± 0.011	1.968 ± 0.001	608.0 ± 1.9
SBS-9	5.618 ± 0.002	1.493 ± 0.001	100.06 ± 0.06	4.080 ± 0.009	1.331 ± 0.001	501.4 ± 1.7

Table 6.2: A table for all of the six SBS kinematic settings and their corresponding performance values for only electrons data.

TH Electron Performance Analysis Values						
Setting	E_{dep} (MeV)	C_{avg} (bars)	T_{eff} (%)	H_{res} (cm)	V_{res} (cm)	T_{res} (ps)
SBS-4	10.802 ± 0.003	2.117 ± 0.001	99.76 ± 0.05	3.926 ± 0.002	1.560 ± 0.001	495.4 ± 0.4
SBS-7	11.978 ± 0.028	2.177 ± 0.005	99.80 ± 0.23	3.941 ± 0.009	1.644 ± 0.003	500.2 ± 1.6
SBS-11	10.072 ± 0.049	1.771 ± 0.008	99.55 ± 0.10	4.888 ± 0.005	1.837 ± 0.001	610.6 ± 0.9
SBS-14	8.272 ± 0.013	1.992 ± 0.004	99.27 ± 0.18	4.077 ± 0.007	1.486 ± 0.002	500.3 ± 1.2
SBS-8	9.711 ± 0.003	1.703 ± 0.001	98.96 ± 0.06	5.281 ± 0.003	1.980 ± 0.001	656.3 ± 0.6
SBS-9	6.946 ± 0.003	1.773 ± 0.001	99.27 ± 0.09	4.459 ± 0.004	1.511 ± 0.001	540.1 ± 0.7

Table 6.3: A table for all of the six SBS kinematic settings and their corresponding performance values for only elastic electrons data.

TH Elastic Performance Analysis Values						
Setting	E_{dep} (MeV)	C_{avg} (bars)	T_{eff} (%)	H_{res} (cm)	V_{res} (cm)	T_{res} (ps)
SBS-4	12.655 ± 0.013	2.307 ± 0.002	99.59 ± 0.17	4.161 ± 0.002	1.584 ± 0.002	517.5 ± 0.3
SBS-7	12.718 ± 0.223	2.232 ± 0.034	95.74 ± 1.50	4.907 ± 0.003	1.562 ± 0.030	584.5 ± 0.5
SBS-11	11.073 ± 0.339	1.828 ± 0.054	99.84 ± 0.65	6.086 ± 0.001	1.888 ± 0.012	744.5 ± 0.2
SBS-14	9.514 ± 0.081	2.201 ± 0.019	98.34 ± 0.90	4.679 ± 0.004	1.410 ± 0.012	542.9 ± 0.7
SBS-8	10.836 ± 0.016	1.779 ± 0.002	97.33 ± 0.22	5.493 ± 0.003	2.043 ± 0.003	684.1 ± 0.5
SBS-9	8.075 ± 0.011	1.993 ± 0.003	99.46 ± 0.24	4.834 ± 0.003	1.512 ± 0.003	566.6 ± 0.5

The summary plots of all performance analysis parameters for all three layers of physics cuts are provided throughout Chapter 5, but Tables 6.1-6.3 are tables of performance values which congregate that data together in one place allowing for an easier comparison. The average values are calculated

across all TH detector scintillator bars. These six values constitute the major parameters for the TH detector performance analysis as defined in Chapter 5.

One minor improvement to the detector hardware that was implemented after the end of the G_M^n experiment was the replacement of the HV mainframe with a newer model that has the ability to be better integrated with the EPICs HV control software. The function of the new HV mainframe is the same as the previous one, but with a slightly simpler user interface for remote operation and setting of the TH detector HV values. Two other improvements to the TH detector hardware that could be implemented involve the PMT housing assemblies and the NINO ASIC amplifier-discriminator cards. The PMT housing assemblies were originally designed to include air pumping systems, which would filter clean air throughout the PMT housing. The purpose of this would be to help mitigate degradation of the PMT itself caused by rogue helium molecules in the air originating from the cryogenic cooling systems in Hall A. Rubber tubes for this pumping system are currently installed on the PMT housing and only need to be connected to an air pumping system to be used for the original intended purpose. The final improvement to the TH detector hardware which could be implemented would be a remote control system for setting and adjusting the NINO card thresholds. A remote threshold setting system was originally designed, and the NINOs have this compatibility. Without a remote threshold system, the NINO thresholds were set manually before the start of the G_M^n experiment, but a remote connection would make it easier to set the NINO thresholds, especially for NINO cards attached at the top of the detector frame that can only be accessed using a ladder and harness.

For the commissioning process of the TH detector, one improvement would be the implementation of an absolute gain study for the PMTs. A study of relative gain was performed in lieu of an absolute gain analysis due to time constraints before the beginning of the G_M^n experiment. This absolute gain study would require the installation of LEDs pointed at the TH detector PMTs like the system of LEDs used for HCal, which allowed for a study of absolute gain for that detector. As mentioned in Chapter 4, the calibration process of the TH detector could be improved by implementing studies for radio-frequency alignment to calibrate TH timing data with that of the beam-line. Another calibration would be a time-of-flight alignment relative to HCal to further improve TH detector timing data. Discussion has taken place debating the ability of these further calibrations to improve the TH time resolution. To do so, these calibrations would need to somehow compensate for the considerable showering effect that the pre-

shower has on causing the degradation of the TH time resolution. The location of the TH detector behind the pre-shower is a major cause for the TH time resolution being on average double its intrinsic resolution, and whether or not further timing calibrations would be able to compensate for the physical location of one detector behind another remains an undetermined postulation when considering the calibration of the TH detector relative to the beam-line or to other detectors. A proposal was also made to generate calibration values for each SBS kinematic setting of the G_M^n experiment using the calibration studies already implemented. The detector calibration values for this thesis were generated using data from the SBS-4 kinematic setting because it was the first major kinematic setting of the G_M^n experiment and its, on average, lower beam current made SBS-4 one of the more stable kinematic settings for performing reliable calibration analysis. The SBS-4 calibration values were used for all six kinematic settings of the G_M^n experiment, but generating calibration values specific to each of the six kinematic settings might allow for some marginal improvements in the TH detector performance.

Despite all the improvements that could still be made to the hardware, commissioning, and calibration of the TH detector, the results of this thesis show that after application of physics cuts to ensure a data set comprised of particle tracks corresponding to elastic electrons, the data of interest for measurement of G_M^n , the Timing Hodoscope is shown on average to have a >98% tracking efficiency when compared to tracking data from the GEM detector layers. The TH has a horizontal position resolution of 4-6 cm, and this matches well with the performance simulation. In the vertical direction, the TH has a position resolution of 1.5-2 cm, which is an improvement on the 2.5 cm width of the scintillator. This is achieved through the implementation of a scintillator bar cluster-based approach to the analysis. Finally, the time resolution of the TH detector on average across all kinematic settings of the G_M^n experiment for the elastic electron data set is 500-750 ps as the data currently stands with the calibrations and analysis approach used in this thesis. These results provide a comprehensive overview of the TH detector performance during the G_M^n experiment, and give significant insight into how well the TH detector has and will continue to function, with the purpose of collecting timing information of scattered particles, for SBS Hall A nucleon electromagnetic form factor experiments.

Bibliography

- [1] B.D. Anderson, J. Arrington, S. Kowalski, R. Madey, B. Plaster, A. Yu. Semenov. *The Neutron Electric Form Factor at Q^2 up to $7 (GeV/c)^2$ from the reaction $^2H(e,e'n)$ via Recoil Polarimetry.* Jefferson Lab Experiment E12-11-009. 2012.
- [2] G. Cates, S. Riordan, B. Wojtsekhowski. *Measurement of the Neutron Electromagnetic Form Factor Ratio G_E^n/G_M^n at High 2Q ,* Jefferson Lab Experiment E12-09-016. 2012.
- [3] P. Soding, B. Wiik, G. Wolf, S.L. Wu. *The First Evidence for Three-Jet Events in $e+e-$ Collisions at PETRA - First Direct Observation of the Gluon.* Part of high-energy physics proceedings International Europhysics Conference, HEP '95, Brussels, Belgium, July 27-August 2, 1995, 3-14. Contribution to: International Europhysics Conference on High-energy Physics (HEP 95), 3-14. Report Number: DESY-96-193. September, 1996.
- [4] A. Lopes. *Four Decades of Gluons.* CERN, Accelerating Science. 18 June, 2019. Article link: <https://home.cern/news/news/physics/four-decades-gluons>.
- [5] S. B. Shea. *How did the Proton Get Its Spin?, Understanding a fundamental aspect of a fundamental particle.*, Brookhaven National Laboratory, U.S. Department of Energy. 31 March, 2017. Article link: <https://www.bnl.gov/newsroom/news.php?a=212163>.
- [6] J.R.M. Annand, B. Wojtsekhowski, B. Sawatzky, N. Piskunov, V. Bellini, M. Kohl. *Measurement of the Ratio G_E^n/G_M^n by the Double-polarized $^2H(e,e'n)$ Reaction,* Jefferson Lab Experiment PR12-17-004. 2017.
- [7] J. Lachniet. *A High Precision Measurement of the Neutron Magnetic Form Factor Using the CLAS Detector,* CLAS Collaboration, Jefferson Lab. Carnegie Mellon University. June, 2005.

- [8] F. Gross, E. Klempt, et al. *50 Years of Quantum Chromodynamics*. Cornell University, High Energy Physics - Phenomenology, arXiv:2212.11107. 26 December, 2022. Link: <https://doi.org/10.48550/arXiv.2212.11107>.
- [9] M. Ablikim, et al. *Measurements of the Electric and Magnetic Form Factors of the Neutron for Timelike Momentum Transfer*, BESIII Collaboration. Phys. Rev. Lett., 130, 151905, 14 April, 2023.
- [10] V. Sulkosky, C. Peng, et al. *Puzzle with the Precession of the Neutron Spin*. Thomas Jefferson National Research Facility. March, 2021.
- [11] J. Annand, R. Gilman, B. Quinn, B. Wojtsekhowski. *Precision Measurement of the Neutron Magnetic Form Factor at to $Q^2 = 18 (GeV/c)^2$* . Jefferson Lab experiment E12-09-019. 2008.
- [12] J. Arrington, S. Gilad, B. Moffit, B. Wojtsekhowski. *Precision Measurement of the Proton Elastic Cross Section at High Q^2* , Jefferson Lab Experiment E12-07-108. 2007.
- [13] E. Cisbani, M. Khandaker, C.F. Perdrisat, L.P. Pentchev, V. Punjabi, B. Wojtsekhowski. *Large Acceptance Proton Form Factor Ratio Measurements at 13 and 15 $(GeV/c)^2$ Using Recoil Polarization Method*, Jefferson Lab Experiment E12-07-109. 2012.
- [14] Joseph Grames, Douglas W. Higinbotham, Hugh E. Montgomery. *Thomas Jefferson National Accelerator Facility*, Nuclear Physics News, 20:3, 6-13, DOI: 10.1080/10619127.2010.506115. 2010.
- [15] *DOE Approves 12 GeV Upgrade for CEBAF*, CERN Courier, Accelerator News, Reporting on international high-energy physics. 20 October, 2008. Article link: <https://cerncourier.com/a/doe-approves-12-gev-upgrade-for-cebaf/>.
- [16] Cardman, L.S. *Physics at the Thomas Jefferson National Accelerator Facility*. Eur. Phys. J. A 28 (Suppl 1), 7–17. 2006. Link: <https://doi.org/10.1140/epja/i2006-09-002-9>.
- [17] J. Alcorn, et al. *Basic Instrumentation for Hall A at Jefferson Lab*, Nuclear Instruments and Methods in Physics Research Section A, Vol. 522, Issue 3, 294-346. Jefferson Lab. 2004. ISSN 0168-9002. Link: <https://doi.org/10.1016/j.nima.2003.11.415>.

- [18] J. O. Hansen. *Studies of Nucleon Form Factors with 12 GeV CEBAF and Super BigBite*. Jefferson Lab Experiments E12-07-109, E12-09-016 and E12-09-019; AIP Conference Proceedings, 1441 (1): 162–164. 28 September, 2012. Link: <https://doi.org/10.1063/1.3700500>.
- [19] R. D. McKeown. *The Jefferson Lab 12 GeV Upgrade*. Jefferson Lab. AIP Conference Proceedings; 1374 (1): 121–126. 24 October, 2011. Link: <https://doi.org/10.1063/1.3647109>.
- [20] D. Di. *High Momentum Transfer Nucleon Elastic Electromagnetic Form Factor Measurements Using Super BigBite Spectrometer at Jefferson Lab*. Thomas Jefferson National Research Facility, U.S. DOE Office of Science. OSTI Identifier: 1595244, Report Number(s): JLAB-PHY-19-3138; DOE/OR/23177-4911, DOE Contract Number: AC05-06OR23177 1 October, 2019. Link: <https://doi.org/10.2172/1595244>.
- [21] W. A. Oliver. *Monitoring Software and Charged Particle Identification for the CLAS12 Detector*. Thomas Jefferson National Research Facility. Virginia Commonwealth University. August, 2019. Link: <https://doi.org/10.25772/9E8A-MV09>.
- [22] H. Montgomery. *Jefferson Lab: A Long Decade of Physics*. J. Phys.: Conf. Ser. 299 011001. 2011. Link: <https://doi.org/10.1088/1742-6596/299/1/011001>.
- [23] J. Arrington, et al. *Nucleon Form Factors – A Jefferson Lab Perspective*. J. Phys.: Conf. Ser. 299 012002. 2011. Link: <https://doi.org/10.1088/1742-6596/299/1/012002>.
- [24] R. G. Sachs. *Structure of the Nucleon*. Phys. Rev. 87, 1100. 15 September, 1952. Link: <https://journals.aps.org/pr/abstract/10.1103/PhysRev.87.1100>.
- [25] J. P. Chen, et al. *Spin Structure Functions*. J. Phys.: Conf. Ser. 299 012005. 2011. Link: <https://doi.org/10.1088/1742-6596/299/1/012005>.
- [26] A. Melissinos, J. Napolitano. *Experiments in Modern Physics: Interaction of Charged Particles with Matter*. Academic Press (An imprint of Elsevier Science), Chapter 5, pp. 152–165. 1966. Link: https://cds.cern.ch/record/897801/files/0124898513_TOC.pdf.
- [27] W.S.C. Williams. *Nuclear and Particle Physics*. Clarendon Press. Department of Physics, University of Oxford and St. Edmund Hall, Oxford, UK. ISBN: 9780198520467. 1991.

- [28] A. Melissinos, J. Napolitano. *Experiments in Modern Physics: Scattering and Coincidence Experiments*. Academic Press, Chapter 9, pp. 367–422. 1966. Link: https://cds.cern.ch/record/897801/files/0124898513_TOC.pdf.
- [29] T. de Forest Jr., J.D. Walecka. *Electron scattering and nuclear structure*, *Advances in Physics*, 15:57, 1-109. 1966. Link: <https://doi.org/10.1080/00018736600101254>.
- [30] R. Hofstadter. *Electron Scattering and Nuclear Structure*, *Rev. Mod. Phys.* 28, Issue 3, 214. 1 July, 1956. Link: <https://doi.org/10.1103/RevModPhys.28.214>.
- [31] K. de Jager. *The Super BigBite Project: A Study of Nucleon Form Factors*. Jefferson Lab SBS Collaboration. Cornell University, Nuclear Experiment, arXiv:0911.3268. 17 November, 2009. Link: <https://doi.org/10.1142/S0218301310015308>.
- [32] J. Lachniet, et al. *Precise Measurement of the Neutron Magnetic Form Factor G_M^n in the Few-GeV² Region*. Jefferson Lab CLAS Collaboration, *Phys. Rev. Lett.*, 102, 192001. 12 May, 2009. Link: <https://doi.org/10.1103/PhysRevLett.102.192001>.
- [33] E. Durand. *Equations du type $F(x) = 0$: Racines d'un Polynome*. In Masson, et al. (eds.). *Solutions Numériques des Equations Algébriques*. Vol. 1. 1960.
- [34] V. Punjabi, C. F. Perdrisat, M. K. Jones, E. J. Brash, C.E. Carlson. *The Structure of the Nucleon: Elastic Electromagnetic Form Factors*. Jefferson Lab. Cornell University, Nuclear Experiment, arXiv:1503.01452. 1 June, 2015. Link: <https://doi.org/10.48550/arXiv.1503.01452>.
- [35] F. J. Ernst, R. G. Sachs, and K. C. Wali. *Electromagnetic Form Factors of the Nucleon*. *Phys. Rev.* 119, 1105, Vol. 119, Iss. 3, 1105–1114. 1 August, 1960. Link: <https://journals.aps.org/pr/abstract/10.1103/PhysRev.119.1105>.
- [36] Z. Ye, J. Arrington, R. J. Hill, G. Lee. *Proton and Neutron Electromagnetic Form Factors and Uncertainties*. *Phys. Lett. B*, Volume 777, 8-15. 2018. Link: <https://doi.org/10.1016/j.physletb.2017.11.023>.
- [37] M. Born. *Quantenmechanik der Stossvorgänge*. *Zeitschrift für Physik*, 38 (11–12): 803–827. S2CID 126244962. 1926. Link: <https://doi.org/10.1007/BF01397184>.

- [38] V. Schomaker, R. Glauber. *The Born Approximation in Electron Diffraction*. Nature 170, 290–291. 1952. Link: <https://doi.org/10.1038/170290b0>.
- [39] G. P. Gilfoyle, W. K. Brooks, K. Hafidi. *Measurement of the Neutron Magnetic Form Factor at High Q^2 Using the Ratio Method on Deuterium*. Jefferson Lab CLAS Collaboration. Jefferson Lab Experiment PHY–10–1217. February, 2011. Link: https://doi.org/10.1142/9789814329569_0028.
- [40] E. Fuchey, S. Alsalmi, B. Wojstekhowski. *Measurement of the Two-Photon Exchange Contribution to the Electron-Neutron Elastic Scattering Cross Section*. Jefferson Lab SBS Collaboration. APS Division Nuclear Physics Hawaii Meeting, ads:id.FM.005. 2020. Link: <https://ui.adsabs.harvard.edu/abs/2020APS..DNP.FM005F/abstract>.
- [41] S. Alsalmi, et al. *Measurement of the Two-Photon Exchange Contribution to the Electron-Neutron Elastic Scattering Cross Section*. Jefferson Lab Experiment PR12-20-010. 2020. Link: https://www.jlab.org/exp_prog/proposals/20/PR12-20-010_Proposal.pdf.
- [42] C. W. de Jager, et al. *The Super-Bigbite Spectrometer for Jefferson Lab Hall A*. Jefferson Lab SBS Collaboration. 20 January, 2010. Link: https://www.ge.infn.it/jlab12/files/SBS-CDR_New_Report.pdf.
- [43] F. Sauli. *GEM: A New Concept for Electron Amplification in Gas Detectors*, Nucl. Instr. & Meth. in Phys. Res., Vol. A386, 531–534. 1997. Link: https://www.physi.uni-heidelberg.de/glassel/journalclub19/gem_first.pdf.
- [44] L. Shekhtman. *Micro-pattern Gaseous Detectors*. Nucl. Instr. & Meth. in Phys. Res., Vol. A494, 128-141. 2002. Part of Proceedings, 8th International Conference on Instrumentation for colliding beam physics (INSTR02) : Novosibirsk, Russia, 128-141 February 28-March 6, 2002. Link: [https://doi.org/10.1016/S0168-9002\(02\)01456-0](https://doi.org/10.1016/S0168-9002(02)01456-0).
- [45] G. Cates, E. Cisbani, G.B. Franklin, and B. Wojtsekhowski, et al. *Measurement of the Semi-inclusive π and K Electro-production in DIS Regime from Transversely Polarized ^3He Target with the SBS and BB Spectrometers in Hall A*, Jefferson Lab Experiment E12-09-018. 15 December, 2008.

- [46] J.A. Harvey, N.W. Hill. *Scintillation Detectors for Neutron Physics Research*. Nuc. Instr. & Methods in Phys. Res., Vol. 162, 507-529. 1979. Link: [https://doi.org/10.1016/0029-554X\(79\)90730-4](https://doi.org/10.1016/0029-554X(79)90730-4).
- [47] *General Purpose EJ-200, EJ-204, EJ-208, EJ-212*. Eljen Technology, 1300 W. Broadway, Sweetwater, TX 79556. 2021. Link: <https://eljentechnology.com/products/plastic-scintillators/ej-200-ej-204-ej-208-ej-212>.
- [48] M. Moszyński, B. Bengtson. *Status of timing with plastic scintillation detectors*. Nuc. Instr. & Methods in Phys. Res., Vol. 158, 1-31. 1979. Link: [https://doi.org/10.1016/S0029-554X\(79\)90170-8](https://doi.org/10.1016/S0029-554X(79)90170-8).
- [49] B.K. Lubsandorzhev. *On the History of Photomultiplier Tube Invention*. Nuc. Instr. & Methods in Phys. Res., Section A. Vol. 567, 236-238. 2006. Link: <https://doi.org/10.1016/j.nima.2006.05.221>.
- [50] E. Hergert, S. Piatek. *The WITS Guide to Selecting a Photodetector*. Hamamatsu Photonics K.K. and affiliates, and New Jersey Institute of Technology. 9 May, 2017. Link: <https://hub.hamamatsu.com/us/en/technical-notes/detector-selection/the-wits-guide-to-selecting-a-photodetector.html>.
- [51] *29 mm (1.13") Photomultiplier 9142B Series Data Sheet*. ET Enterprises Ltd., 45 Riverside Way, Uxbridge, UB8 2YF, UK. ET Enterprises Ltd, Issue 7. 13 March, 2012. Link: <https://hallaweb.jlab.org/wiki/images/0/00/9142B.pdf>.
- [52] J. Annand, R. Montgomery. *BigBite Timing Hodoscope Electronics*. Nuclear Physics Research Group, University of Glasgow. Jefferson Lab SBS Collaboration. 17 January, 2018. Link: <https://hallaweb.jlab.org/wiki/images/e/e6/BBhodoElect.pdf>.
- [53] F. Anghinolfi, et al. *NINO: an Ultra-fast and Low-power Front-end Amplifier/Discriminator ASIC Designed for the Multigap Resistive Plate Chamber*. Nuc. Instr. & Methods in Phys. Res., Section A, Vol. 533, 183-187. 2004. Link: <https://doi.org/10.1016/j.nima.2004.07.024>.
- [54] E. Fuchey. *Introduction for BigBite Trigger Logic for SBS Form Factors Experiments*. Jefferson Lab SBS Collaboration. U.S. Department of Energy. 8 February, 2021. Link: https://hallaweb.jlab.org/wiki/images/5/57/BBtrig_introductory.pdf.

- [55] O. Hansen, B. Sawatzky, M. Jones, R. Michaels, S. Wood. *Hall A C++ Analyzer*. Jefferson Lab SBS Collaboration: GitHub, 2022. Link: <https://github.com/JeffersonLab/analyzer>.
- [56] A. Puckett, E. Fuchey, M. Jones, O. Hansen, D. Hamilton, R. Montgomery, P. King, et al. *Reconstruction and analysis code for SuperBigBite (SBS) experiments*. Jefferson Lab SBS Collaboration: GitHub, 2023. Link: <https://github.com/JeffersonLab/SBS-offline>.
- [57] E. Fuchey, A. Puckett, O. Hansen, D. Hamilton, P. King, et al. *SBS-replay*. Jefferson Lab SBS Collaboration: GitHub, 2023. Link: <https://github.com/JeffersonLab/SBS-replay>.
- [58] S. Riordan, A. Puckett, E. Fuchey, D. Flay, et al. *Super Bigbite Simulation*. Jefferson Lab SBS Collaboration: GitHub, 2023. Link: <https://github.com/JeffersonLab/g4sbs>.
- [59] A. Puckett, E. Fuchey, J. C. Cornegjo, et al. *SBS digitization library*. Jefferson Lab SBS Collaboration: GitHub, 2023. Link: <https://github.com/JeffersonLab/libbsdig>.
- [60] A. Puckett. *SBS Software and Analysis*. Jefferson Lab SBS Collaboration. University of Connecticut, Part of Proceedings, Hall A Winter Meeting, Jefferson Lab. 11 February, 2022.
- [61] S. Riordan. *SBS Software and Simulation Outline and Requirements*. Jefferson Lab SBS Collaboration. Argonne National Laboratory. 30 May, 2017. Link: https://hallaweb.jlab.org/12GeV/SuperBigBite/documents/sbs_soft_whitepaper.pdf.
- [62] R. Montgomery, et al. *Software Requirements for BigBite Timing Hodoscope*. Jefferson Lab SBS Collaboration. University of Glasgow, Part of Proceedings, SBS Collaboration Meeting, Jefferson Lab. 7 October, 2020.
- [63] J. Hu, et al. *Time Walk Measurements*. CERN. Part of Proceedings, LBL Summer Meeting, LBNL, U.S. June, 2011. Link: <https://indico.cern.ch/event/143033/contributions/>.
- [64] M. Mihovilovic, et al. *Methods for Optical Calibration of the BigBite Hadron Spectrometer*. Jefferson Lab SBS Collaboration. Cornell University, Nuclear Experiment, arXiv:1201.1442. 6 January, 2012. Link: <https://doi.org/10.48550/arXiv.1201.1442>.

- [65] S. Agostinelli et al. *GEANT4 - a simulation toolkit*. Nucl. Instr. & Meth. in Phys. Res., Section A, Vol. 506, no. 3, 250-303. 1 July, 2003. Link: [https://doi.org/10.1016/S0168-9002\(03\)01368-8](https://doi.org/10.1016/S0168-9002(03)01368-8).
- [66] P. Lecoq. *Scintillation Detectors for Charged Particles and Photons*. Particle Physics Reference Library. Springer, Cham. 2 September, 2020. Link: https://doi.org/10.1007/978-3-030-35318-6_3.
- [67] D. Montgomery, M. Schein. *Cosmic Ray Physics*. Literary Licensing, LLC. ISBN-13: 978-1258439071. Princeton University Press. 1 January, 1949.
- [68] CAEN Spa. *Mod. V1190-VX1190 A/B, 128/64 Ch Multihit TDC*. Manual Rev. 14. 29 November, 2016. Link: https://hallaweb.jlab.org/wiki/images/2/21/V1190_REV14.pdf.
- [69] CAEN Spa. *Mod. V792/V792N 32/16 channel QDC*. Manual Rev. 18. 4 November, 2010. Link: https://twiki.cern.ch/twiki/pub/DREAM/CaenDoc/v792_rev18.pdf.
- [70] H. Dong, C. Cuevas, D. Curry, E. Jastrzembski, F. Barbosa, J. Wilson, M. Taylor. *VXS Switch Card for High Density Data Acquisition System*, IEEE Southeast Con. 2007, Richmond, VA. 22-25 March, 2007. Link: <https://www.jlab.org/Hall-B/ftof/manuals/FADC250UsersManual.pdf>.

Appendices

Appendix A

List of Abbreviations

Table A.1: A list of abbreviations used throughout this thesis with their corresponding definitions, and the page numbers of their first use.

List of Abbreviations		
Abbreviation	Definition	First Use (Page No.)
2H	Deuterium	3
3He	Helium-3	9
ADC(s)	Analogue-to-Digital Converter(s)	iii
BBCal	BigBite Calorimeter	32
CDet	Coordinate Detector	30
CEBAF	Continuous Electron Beam Accelerator Facility	6
DAQ	Data Acquisition	iii
DC	Direct Current	50
ECL	Emitter-Coupled Logic	54
EM	Electromagnetic	26
EMFF(s)	Electromagnetic Form Factor(s)	3
EPICs	Experimental Industrial Control System	62
FADC(s)	Flash Analogue-to-Digital Converter(s)	58
FF(s)	Form Factor(s)	25

Abbreviation	Definition	First Use (Page No.)
FoM	Figures of Merit	25
GEM(s)	Gas Electron Multiplier(s)	11
G_E^n	Neutron Sachs Electric Form Factor	3
GEn	GEn Experiment	25
GEn-Recoil	GEn Recoil Experiment	25
G_E^p	Proton Sachs Electric Form Factor	3
GEp-Recoil	GEp Recoil Experiment	25
GeV	Giga-Electronvolt	3
G_M^n	Neutron Sachs Magnetic Form Factor	3
GMn	GMn Experiment	6
G_M^p	Proton Sachs Magnetic Form Factor	3
GPD(s)	Generalized Parton Distribution(s)	6
GUI(s)	Graphic User Interface(s)	62
HCal	Hadron Calorimeter	26
HRS	High Resolution Spectrometer	9
HV	High Voltage	51
JLab	Jefferson Lab	7
LD2	Liquid Deuterium	26
LH2	Liquid Hydrogen	28
LHRS	Left High Resolution Spectrometer	9
LINAC(s)	Linear Accelerator(s)	8
LTR	Level Translator-Repeater	54
LV	Low Voltage	50
LVDS	Low Voltage Differential Signal	54
MeV	Mega-Electronvolt	10
NIM	Nuclear Instrument Module	58
NINO(s)	NINO ASIC Amplifier-Discriminator Card(s)	47

Abbreviation	Definition	First Use (Page No.)
NPol	Neutron Polarimeter	30
nTPE	Neutron Two-Photon Exchange Experiment	25
PMT(s)	Photo-multiplier Tube(s)	40
pQCD	Perturbative Quantum Chromodynamics	6
PS	Pre-shower	35
PV(s)	Process Variable(s)	62
Q^2	Squared Four-Momentum Transfer	2
QCD	Quantum Chromodynamics	2
QED	Quantum Electrodynamics	15
RF	Radio-Frequency	9
RHRS	Right High Resolution Spectrometer	9
ROB	Readout Board	34
SBS	Super BigBite Spectrometer	3
SH	Shower	35
SVC	Scintillator Velocity Correction	189
TAO	TDC Alignment Offset	189
TDC(s)	Time-to-Digital Converter(s)	iii
TDO	Time Difference Offset	189
TH	Timing Hodoscope	6
TOT	Time over Threshold	59
TPE	Two-Photon Exchange	26
TWI	Time-walk Intercept	189
TWS	Time-walk Slope	189

Appendix B

NINO ASIC Amplifier-Discriminator Card Circuit Diagrams

Listed in this appendix are circuit diagrams of NINO ASIC amplifier-discriminator chips, and these schematics are provided on request from the Nuclear Physics Research Group, University of Glasgow.

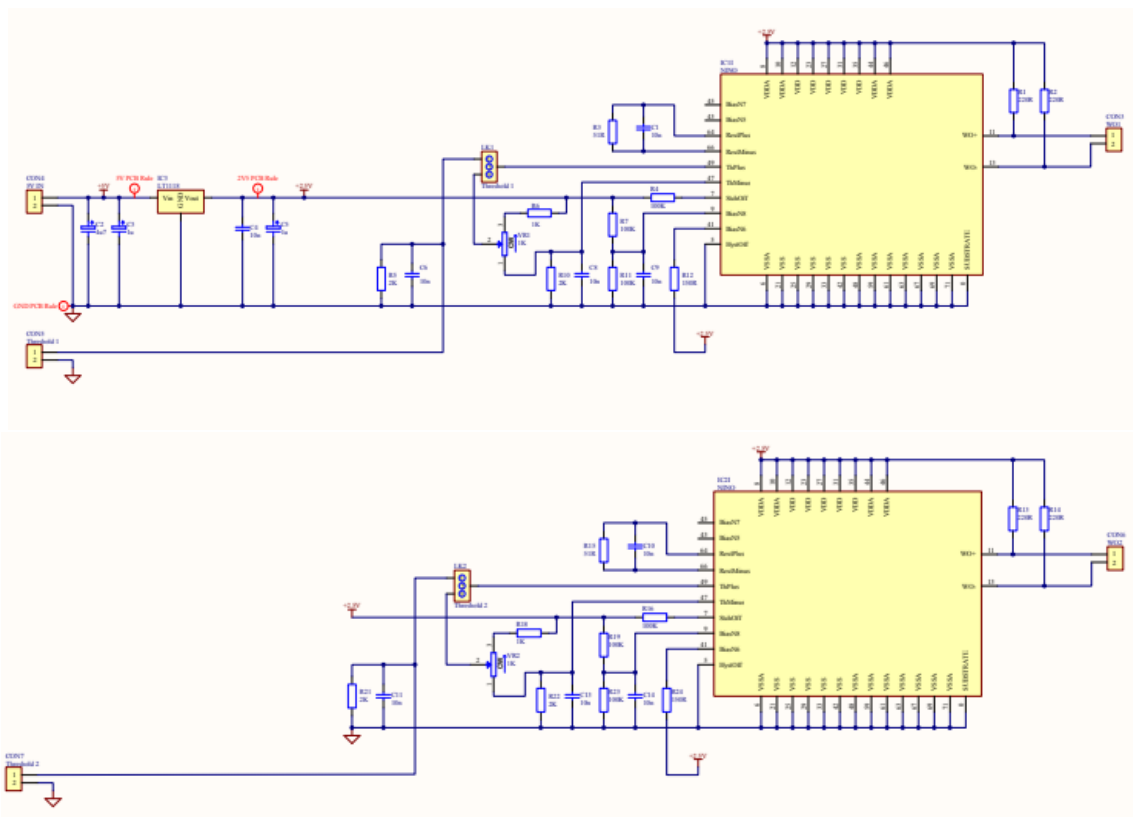


Figure B.1: Schematics of the circuit diagrams for two slightly different versions of the NINO ASIC chip used for the TH detector. Diagram by J. Annand.

Appendix C

High and Low Voltage Mapping Tables

Listed in this appendix are two tables of the cable mapping for the LV and HV systems used to power the NINO cards, and PMTs, respectively.

Table C.1: Table of the mapping for the labelling scheme used corresponding between the front-end NINO ASIC amplifier-discriminator cards and the LV power cables to the TH detector frame at the LV distribution box.

NINO	Power Cable
H-NINO-R5	H-NINO-LV-R5
H-NINO-R4	H-NINO-LV-R4
H-NINO-R3	H-NINO-LV-R3
H-NINO-R2	H-NINO-LV-R2
H-NINO-R1	H-NINO-LV-R1
H-NINO-R0	H-NINO-LV-R0
H-NINO-L5	H-NINO-LV-L5
H-NINO-L4	H-NINO-LV-L4
H-NINO-L3	H-NINO-LV-L3
H-NINO-L2	H-NINO-LV-L2
H-NINO-L1	H-NINO-LV-L1
H-NINO-L0	H-NINO-LV-L0

A single power cable runs from the LV power supply in the electronics bunker to the LV distribution box on the TH detector frame. Another grounding cable is connected to the BigBite package detector frame, which itself is grounded to a common ground in Experimental Hall A such that all detectors in the SBS electron arm are properly grounded.

Table C.2: Mapping of the labels for the entire TH detector HV system from the PMT bases to HV patch panels on the TH frame to the HV channel names for the HV mainframe. During the experiment run time, this mainframe is controlled remotely from outside Experimental Hall A.

Bars $\xrightarrow{HV\text{cables}}$ HV Patch Panels						
Frame		HV Distribution Panels			CAEN Channels	
Bar	HV Cable	Panel	Chan.	Multiway	Name	No.
1-L	H-HV-L0	H-HV-PP-L0	0-0	H-HV-MW-L0	hodo_L0	2.0001
1-R	H-HV-R0	H-HV-PP-R0	0-0	H-HV-MW-R0	hodo_R0	0.0001
2-L	H-HV-L1	H-HV-PP-L0	0-1	H-HV-MW-L0	hodo_L1	2.0002
2-R	H-HV-R1	H-HV-PP-R0	0-1	H-HV-MW-R0	hodo_R1	0.0002
3-L	H-HV-L2	H-HV-PP-L0	0-2	H-HV-MW-L0	hodo_L2	2.0003
3-R	H-HV-R2	H-HV-PP-R0	0-2	H-HV-MW-R0	hodo_R2	0.0003
4-L	H-HV-L3	H-HV-PP-L0	0-3	H-HV-MW-L0	hodo_L3	2.0004
4-R	H-HV-R3	H-HV-PP-R0	0-3	H-HV-MW-R0	hodo_R3	0.0004
5-L	H-HV-L4	H-HV-PP-L0	0-4	H-HV-MW-L0	hodo_L4	2.0005
5-R	H-HV-R4	H-HV-PP-R0	0-4	H-HV-MW-R0	hodo_R4	0.0005
6-L	H-HV-L5	H-HV-PP-L0	0-5	H-HV-MW-L0	hodo_L5	2.0006
6-R	H-HV-R5	H-HV-PP-R0	0-5	H-HV-MW-R0	hodo_R5	0.0006
7-L	H-HV-L6	H-HV-PP-L0	0-6	H-HV-MW-L0	hodo_L6	2.0007
7-R	H-HV-R6	H-HV-PP-R0	0-6	H-HV-MW-R0	hodo_R6	0.0007
8-L	H-HV-L7	H-HV-PP-L0	0-7	H-HV-MW-L0	hodo_L7	2.0008
8-R	H-HV-R7	H-HV-PP-R0	0-7	H-HV-MW-R0	hodo_R7	0.0008
9-L	H-HV-L8	H-HV-PP-L0	0-8	H-HV-MW-L0	hodo_L8	2.0009
9-R	H-HV-R8	H-HV-PP-R0	0-8	H-HV-MW-R0	hodo_R8	0.0009
10-L	H-HV-L9	H-HV-PP-L0	0-9	H-HV-MW-L0	hodo_L9	2.0010
10-R	H-HV-R9	H-HV-PP-R0	0-9	H-HV-MW-R0	hodo_R9	0.0010
11-L	H-HV-L10	H-HV-PP-L0	0-10	H-HV-MW-L0	hodo_L10	2.0011
11-R	H-HV-R10	H-HV-PP-R0	0-10	H-HV-MW-R0	hodo_R10	0.0011

Bar	HV Cable	Panel	Chan.	Multiway	Name	No.
12-L	H-HV-L11	H-HV-PP-L0	0-11	H-HV-MW-L0	hodo_L11	2.0012
12-R	H-HV-R11	H-HV-PP-R0	0-11	H-HV-MW-R0	hodo_R11	0.0012
13-L	H-HV-L12	H-HV-PP-L0	0-12	H-HV-MW-L0	hodo_L12	2.0013
13-R	H-HV-R12	H-HV-PP-R0	0-12	H-HV-MW-R0	hodo_R12	0.0013
14-L	H-HV-L13	H-HV-PP-L0	0-13	H-HV-MW-L0	hodo_L13	2.0014
14-R	H-HV-R13	H-HV-PP-R0	0-13	H-HV-MW-R0	hodo_R13	0.0014
15-L	H-HV-L14	H-HV-PP-L0	0-14	H-HV-MW-L0	hodo_L14	2.0015
15-R	H-HV-R14	H-HV-PP-R0	0-14	H-HV-MW-R0	hodo_R14	0.0015
16-L	H-HV-L15	H-HV-PP-L0	0-15	H-HV-MW-L0	hodo_L15	2.0016
16-R	H-HV-R15	H-HV-PP-R0	0-15	H-HV-MW-R0	hodo_R15	0.0016
17-L	H-HV-L16	H-HV-PP-L0	1-0	H-HV-MW-L0	hodo_L16	2.0017
17-R	H-HV-R16	H-HV-PP-R0	1-0	H-HV-MW-R0	hodo_R16	0.0017
18-L	H-HV-L17	H-HV-PP-L0	1-1	H-HV-MW-L0	hodo_L17	2.0018
18-R	H-HV-R17	H-HV-PP-R0	1-1	H-HV-MW-R0	hodo_R17	0.0018
19-L	H-HV-L18	H-HV-PP-L0	1-2	H-HV-MW-L0	hodo_L18	2.0019
19-R	H-HV-R18	H-HV-PP-R0	1-2	H-HV-MW-R0	hodo_R18	0.0019
20-L	H-HV-L19	H-HV-PP-L0	1-3	H-HV-MW-L0	hodo_L19	2.0020
20-R	H-HV-R19	H-HV-PP-R0	1-3	H-HV-MW-R0	hodo_R19	0.0020
21-L	H-HV-L20	H-HV-PP-L0	1-4	H-HV-MW-L0	hodo_L20	2.0021
21-R	H-HV-R20	H-HV-PP-R0	1-4	H-HV-MW-R0	hodo_R20	0.0021
22-L	H-HV-L21	H-HV-PP-L0	1-5	H-HV-MW-L0	hodo_L21	2.0022
22-R	H-HV-R21	H-HV-PP-R0	1-5	H-HV-MW-R0	hodo_R21	0.0022
23-L	H-HV-L22	H-HV-PP-L0	1-6	H-HV-MW-L0	hodo_L22	2.0023
23-R	H-HV-R22	H-HV-PP-R0	1-6	H-HV-MW-R0	hodo_R22	0.0023
24-L	H-HV-L23	H-HV-PP-L0	1-7	H-HV-MW-L0	hodo_L23	2.0024
24-R	H-HV-R23	H-HV-PP-R0	1-7	H-HV-MW-R0	hodo_R23	0.0024
25-L	H-HV-L24	H-HV-PP-L0	1-8	H-HV-MW-L0	hodo_L24	2.0025

Bar	HV Cable	Panel	Chan.	Multiway	Name	No.
25-R	H-HV-R24	H-HV-PP-R0	1-8	H-HV-MW-R0	hodo_R24	0.0025
26-L	H-HV-L25	H-HV-PP-L0	1-9	H-HV-MW-L0	hodo_L25	2.0026
26-R	H-HV-R25	H-HV-PP-R0	1-9	H-HV-MW-R0	hodo_R25	0.0026
27-L	H-HV-L26	H-HV-PP-L0	1-10	H-HV-MW-L0	hodo_L26	2.0027
27-R	H-HV-R26	H-HV-PP-R0	1-10	H-HV-MW-R0	hodo_R26	0.0027
28-L	H-HV-L27	H-HV-PP-L0	1-11	H-HV-MW-L0	hodo_L27	2.0028
28-R	H-HV-R27	H-HV-PP-R0	1-11	H-HV-MW-R0	hodo_R27	0.0028
29-L	H-HV-L28	H-HV-PP-L0	1-12	H-HV-MW-L0	hodo_L28	2.0029
29-R	H-HV-R28	H-HV-PP-R0	1-12	H-HV-MW-R0	hodo_R28	0.0029
30-L	H-HV-L29	H-HV-PP-L0	1-13	H-HV-MW-L0	hodo_L29	2.0030
30-R	H-HV-R29	H-HV-PP-R0	1-13	H-HV-MW-R0	hodo_R29	0.0030
31-L	H-HV-L30	H-HV-PP-L0	1-14	H-HV-MW-L0	hodo_L30	2.0031
31-R	H-HV-R30	H-HV-PP-R0	1-14	H-HV-MW-R0	hodo_R30	0.0031
32-L	H-HV-L31	H-HV-PP-L0	1-15	H-HV-MW-L0	hodo_L31	2.0032
32-R	H-HV-R31	H-HV-PP-R0	1-15	H-HV-MW-R0	hodo_R31	0.0032
33-L	H-HV-L32	H-HV-PP-L0	2-0	H-HV-MW-L0	hodo_L32	2.0033
33-R	H-HV-R32	H-HV-PP-R0	2-0	H-HV-MW-R0	hodo_R32	0.0033
34-L	H-HV-L33	H-HV-PP-L0	2-1	H-HV-MW-L0	hodo_L33	2.0034
34-R	H-HV-R33	H-HV-PP-R0	2-1	H-HV-MW-R0	hodo_R33	0.0034
35-L	H-HV-L34	H-HV-PP-L0	2-2	H-HV-MW-L0	hodo_L34	2.0035
35-R	H-HV-R34	H-HV-PP-R0	2-2	H-HV-MW-R0	hodo_R34	0.0035
36-L	H-HV-L35	H-HV-PP-L0	2-3	H-HV-MW-L0	hodo_L35	2.0036
36-R	H-HV-R35	H-HV-PP-R0	2-3	H-HV-MW-R0	hodo_R35	0.0036
37-L	H-HV-L36	H-HV-PP-L0	2-4	H-HV-MW-L0	hodo_L36	2.0037
37-R	H-HV-R36	H-HV-PP-R0	2-4	H-HV-MW-R0	hodo_R36	0.0037
38-L	H-HV-L37	H-HV-PP-L0	2-5	H-HV-MW-L0	hodo_L37	2.0038
38-R	H-HV-R37	H-HV-PP-R0	2-5	H-HV-MW-R0	hodo_R37	0.0038

Bar	HV Cable	Panel	Chan.	Multiway	Name	No.
39-L	H-HV-L38	H-HV-PP-L0	2-6	H-HV-MW-L0	hodo_L38	2.0039
39-R	H-HV-R38	H-HV-PP-R0	2-6	H-HV-MW-R0	hodo_R38	0.0039
40-L	H-HV-L39	H-HV-PP-L0	2-7	H-HV-MW-L0	hodo_L39	2.0040
40-R	H-HV-R39	H-HV-PP-R0	2-7	H-HV-MW-R0	hodo_R39	0.0040
41-L	H-HV-L40	H-HV-PP-L0	2-8	H-HV-MW-L0	hodo_L40	2.0041
41-R	H-HV-R40	H-HV-PP-R0	2-8	H-HV-MW-R0	hodo_R40	0.0041
42-L	H-HV-L41	H-HV-PP-L0	2-9	H-HV-MW-L0	hodo_L41	2.0042
42-R	H-HV-R41	H-HV-PP-R0	2-9	H-HV-MW-R0	hodo_R41	0.0042
43-L	H-HV-L42	H-HV-PP-L0	2-10	H-HV-MW-L0	hodo_L42	2.0043
43-R	H-HV-R42	H-HV-PP-R0	2-10	H-HV-MW-R0	hodo_R42	0.0043
44-L	H-HV-L43	H-HV-PP-L0	2-11	H-HV-MW-L0	hodo_L43	2.0044
44-R	H-HV-R43	H-HV-PP-R0	2-11	H-HV-MW-R0	hodo_R43	0.0044
45-L	H-HV-L44	H-HV-PP-L0	2-12	H-HV-MW-L0	hodo_L44	2.0045
45-R	H-HV-R44	H-HV-PP-R0	2-12	H-HV-MW-R0	hodo_R44	0.0045
46-L	H-HV-L45	H-HV-PP-L0	2-13	H-HV-MW-L0	hodo_L45	2.0046
46-R	H-HV-R45	H-HV-PP-R0	2-13	H-HV-MW-R0	hodo_R45	0.0046
47-L	H-HV-L46	H-HV-PP-L0	2-14	H-HV-MW-L0	hodo_L46	2.0047
47-R	H-HV-R46	H-HV-PP-R0	2-14	H-HV-MW-R0	hodo_R46	0.0047
48-L	H-HV-L47	H-HV-PP-L0	2-15	H-HV-MW-L0	hodo_L47	2.0048
48-R	H-HV-R47	H-HV-PP-R0	2-15	H-HV-MW-R0	hodo_R47	0.0048
49-L	H-HV-L48	H-HV-PP-L1	2-15	H-HV-MW-L1	hodo_L48	6.0001
49-R	H-HV-R48	H-HV-PP-R1	0-0	H-HV-MW-R1	hodo_R48	4.0001
50-L	H-HV-L49	H-HV-PP-L1	2-14	H-HV-MW-L1	hodo_L49	6.0002
50-R	H-HV-R49	H-HV-PP-R1	0-1	H-HV-MW-R1	hodo_R49	4.0002
51-L	H-HV-L50	H-HV-PP-L1	2-13	H-HV-MW-L1	hodo_L50	6.0003
51-R	H-HV-R50	H-HV-PP-R1	0-2	H-HV-MW-R1	hodo_R50	4.0003
52-L	H-HV-L51	H-HV-PP-L1	2-12	H-HV-MW-L1	hodo_L51	6.0004

Bar	HV Cable	Panel	Chan.	Multiway	Name	No.
52-R	H-HV-R51	H-HV-PP-R1	0-3	H-HV-MW-R1	hodo_R51	4.0004
53-L	H-HV-L52	H-HV-PP-L1	2-11	H-HV-MW-L1	hodo_L52	6.0005
53-R	H-HV-R52	H-HV-PP-R1	0-4	H-HV-MW-R1	hodo_R52	4.0005
54-L	H-HV-L53	H-HV-PP-L1	2-10	H-HV-MW-L1	hodo_L53	6.0006
54-R	H-HV-R53	H-HV-PP-R1	0-5	H-HV-MW-R1	hodo_R53	4.0006
55-L	H-HV-L54	H-HV-PP-L1	2-9	H-HV-MW-L1	hodo_L54	6.0007
55-R	H-HV-R54	H-HV-PP-R1	0-6	H-HV-MW-R1	hodo_R54	4.0007
56-L	H-HV-L55	H-HV-PP-L1	2-8	H-HV-MW-L1	hodo_L55	6.0008
56-R	H-HV-R55	H-HV-PP-R1	0-7	H-HV-MW-R1	hodo_R55	4.0008
57-L	H-HV-L56	H-HV-PP-L1	2-7	H-HV-MW-L1	hodo_L56	6.0009
57-R	H-HV-R56	H-HV-PP-R1	0-8	H-HV-MW-R1	hodo_R56	4.0009
58-L	H-HV-L57	H-HV-PP-L1	2-6	H-HV-MW-L1	hodo_L57	6.0010
58-R	H-HV-R57	H-HV-PP-R1	0-9	H-HV-MW-R1	hodo_R57	4.0010
59-L	H-HV-L58	H-HV-PP-L1	2-5	H-HV-MW-L1	hodo_L58	6.0011
59-R	H-HV-R58	H-HV-PP-R1	0-10	H-HV-MW-R1	hodo_R58	4.0011
60-L	H-HV-L59	H-HV-PP-L1	2-4	H-HV-MW-L1	hodo_L59	6.0012
60-R	H-HV-R59	H-HV-PP-R1	0-11	H-HV-MW-R1	hodo_R59	4.012
61-L	H-HV-L60	H-HV-PP-L1	2-3	H-HV-MW-L1	hodo_L60	6.0013
61-R	H-HV-R60	H-HV-PP-R1	0-12	H-HV-MW-R1	hodo_R60	4.0013
62-L	H-HV-L61	H-HV-PP-L1	2-2	H-HV-MW-L1	hodo_L61	6.0014
62-R	H-HV-R61	H-HV-PP-R1	0-13	H-HV-MW-R1	hodo_R61	4.0014
63-L	H-HV-L62	H-HV-PP-L1	2-1	H-HV-MW-L1	hodo_L62	6.0015
63-R	H-HV-R62	H-HV-PP-R1	0-14	H-HV-MW-R1	hodo_R62	4.0015
64-L	H-HV-L63	H-HV-PP-L1	2-0	H-HV-MW-L1	hodo_L63	6.0016
64-R	H-HV-R63	H-HV-PP-R1	0-15	H-HV-MW-R1	hodo_R63	4.0016
65-L	H-HV-L64	H-HV-PP-L1	1-15	H-HV-MW-L1	hodo_L64	6.0017
65-R	H-HV-R64	H-HV-PP-R1	1-0	H-HV-MW-R1	hodo_R64	4.0017

Bar	HV Cable	Panel	Chan.	Multiway	Name	No.
66-L	H-HV-L65	H-HV-PP-L1	1-14	H-HV-MW-L1	hodo_L65	6.0018
66-R	H-HV-R65	H-HV-PP-R1	1-1	H-HV-MW-R1	hodo_R65	4.0018
67-L	H-HV-L66	H-HV-PP-L1	1-13	H-HV-MW-L1	hodo_L66	6.0019
67-R	H-HV-R66	H-HV-PP-R1	1-2	H-HV-MW-R1	hodo_R66	4.0019
68-L	H-HV-L67	H-HV-PP-L1	1-12	H-HV-MW-L1	hodo_L67	6.0020
68-R	H-HV-R67	H-HV-PP-R1	1-3	H-HV-MW-R1	hodo_R67	4.0020
69-L	H-HV-L68	H-HV-PP-L1	1-11	H-HV-MW-L1	hodo_L68	6.0021
69-R	H-HV-R68	H-HV-PP-R1	1-4	H-HV-MW-R1	hodo_R68	4.0021
70-L	H-HV-L69	H-HV-PP-L1	1-10	H-HV-MW-L1	hodo_L69	6.0022
70-R	H-HV-R69	H-HV-PP-R1	1-5	H-HV-MW-R1	hodo_R69	4.0022
71-L	H-HV-L70	H-HV-PP-L1	1-9	H-HV-MW-L1	hodo_L70	6.0023
71-R	H-HV-R70	H-HV-PP-R1	1-6	H-HV-MW-R1	hodo_R70	4.0023
72-L	H-HV-L71	H-HV-PP-L1	1-8	H-HV-MW-L1	hodo_L71	6.0024
72-R	H-HV-R71	H-HV-PP-R1	1-7	H-HV-MW-R1	hodo_R71	4.0024
73-L	H-HV-L72	H-HV-PP-L1	1-7	H-HV-MW-L1	hodo_L72	6.0025
73-R	H-HV-R72	H-HV-PP-R1	1-8	H-HV-MW-R1	hodo_R72	4.0025
74-L	H-HV-L73	H-HV-PP-L1	1-6	H-HV-MW-L1	hodo_L73	6.0026
74-R	H-HV-R73	H-HV-PP-R1	1-9	H-HV-MW-R1	hodo_R73	4.0026
75-L	H-HV-L74	H-HV-PP-L1	1-5	H-HV-MW-L1	hodo_L74	6.0027
75-R	H-HV-R74	H-HV-PP-R1	1-10	H-HV-MW-R1	hodo_R74	4.0027
76-L	H-HV-L75	H-HV-PP-L1	1-4	H-HV-MW-L1	hodo_L75	6.0028
76-R	H-HV-R75	H-HV-PP-R1	1-11	H-HV-MW-R1	hodo_R75	4.0028
77-L	H-HV-L76	H-HV-PP-L1	1-3	H-HV-MW-L1	hodo_L76	6.0029
77-R	H-HV-R76	H-HV-PP-R1	1-12	H-HV-MW-R1	hodo_R76	4.0029
78-L	H-HV-L77	H-HV-PP-L1	1-2	H-HV-MW-L1	hodo_L77	6.0030
78-R	H-HV-R77	H-HV-PP-R1	1-13	H-HV-MW-R1	hodo_R77	4.0030
79-L	H-HV-L78	H-HV-PP-L1	1-1	H-HV-MW-L1	hodo_L78	6.0031

Bar	HV Cable	Panel	Chan.	Multiway	Name	No.
79-R	H-HV-R78	H-HV-PP-R1	1-14	H-HV-MW-R1	hodo_R78	4.0031
80-L	H-HV-L79	H-HV-PP-L1	1-0	H-HV-MW-L1	hodo_L79	6.0032
80-R	H-HV-R79	H-HV-PP-R1	1-15	H-HV-MW-R1	hodo_R79	4.0032
81-L	H-HV-L80	H-HV-PP-L1	0-15	H-HV-MW-L1	hodo_L80	6.0033
81-R	H-HV-R80	H-HV-PP-R1	2-0	H-HV-MW-R1	hodo_R80	4.0033
82-L	H-HV-L81	H-HV-PP-L1	0-14	H-HV-MW-L1	hodo_L81	6.0034
82-R	H-HV-R81	H-HV-PP-R1	2-1	H-HV-MW-R1	hodo_R81	4.0034
83-L	H-HV-L82	H-HV-PP-L1	0-13	H-HV-MW-L1	hodo_L82	6.0035
83-R	H-HV-R82	H-HV-PP-R1	2-2	H-HV-MW-R1	hodo_R82	4.0035
84-L	H-HV-L83	H-HV-PP-L1	0-12	H-HV-MW-L1	hodo_L83	6.0036
84-R	H-HV-R83	H-HV-PP-R1	2-3	H-HV-MW-R1	hodo_R83	4.0036
85-L	H-HV-L84	H-HV-PP-L1	0-11	H-HV-MW-L1	hodo_L84	6.0037
85-R	H-HV-R84	H-HV-PP-R1	2-4	H-HV-MW-R1	hodo_R84	4.0037
86-L	H-HV-L85	H-HV-PP-L1	0-10	H-HV-MW-L1	hodo_L85	6.00038
86-R	H-HV-R85	H-HV-PP-R1	2-5	H-HV-MW-R1	hodo_R85	4.0038
87-L	H-HV-L86	H-HV-PP-L1	0-9	H-HV-MW-L1	hodo_L86	6.0039
87-R	H-HV-R86	H-HV-PP-R1	2-6	H-HV-MW-R1	hodo_R86	4.0039
88-L	H-HV-L87	H-HV-PP-L1	0-8	H-HV-MW-L1	hodo_L87	6.0040
88-R	H-HV-R87	H-HV-PP-R1	2-7	H-HV-MW-R1	hodo_R87	4.0040
89-L	H-HV-L88	H-HV-PP-L1	0-7	H-HV-MW-L1	hodo_L88	6.0041
89-R	H-HV-R88	H-HV-PP-R1	2-8	H-HV-MW-R1	hodo_R88	4.0041
90-L	H-HV-L89	H-HV-PP-L1	0-6	H-HV-MW-L1	hodo_L89	6.0042
90-R	H-HV-R89	H-HV-PP-R1	2-9	H-HV-MW-R1	hodo_R89	4.0042

Appendix D

List of Cables and Electronics Hardware

Listed below is a complete inventory of the electronics hardware going from the TH detector frame to the Hall A electronics bunker used for the TH detector data acquisition system.

1. **12** NINO ASIC amplifier discriminator cards, 6 on each side of the TH detector frame. They are labelled H-NINO-## where the first # is either L or R for left and right side and the second # goes from 0 to 5 corresponding to the physical NINO card location from bottom (0) to top (5) on the detector frame. The physical location of these cards can be seen in the photos from Figure 3.10 and a photo of two mounted NINOs with cables is shown in Figure 3.12.
2. **4** HV distribution boxes, 2 on each side of the TH detector frame. They are labelled H-HV-PP-## where the first # is either L or R and the second # goes from 0 to 1 as shown in Figure 3.8 and Figure 3.10. The cable mapping for each HV distribution box is detailed in Table 3.8 and the labeling of the connections on the HV distribution boxes is in the form H-HV-##-# where the first # is L or R, the second # is 0 or 1, and the third # goes from 0-95. Three photos of the four HV distribution boxes are provided in Figure 3.11.
3. **1** LV distribution box on bottom right side of the TH detector frame. It is labelled H-LV-DISTRIB and a photo of the LV distribution box is in Figure 3.12. NINO power cable mapping to each LV distribution box channel can be found in Table 3.7.
4. **2** patch panels for collecting digital and analogue signals from NINO cards. Both are located on the upper right side of the TH detector frame as seen in Figure 3.8. They are labelled TH LOGIC and

TH ANALOG corresponding to the connected TDC and ADC cables respectively. The ADC patch panel takes in four 34-pin 17-pair ribbon cables and outputs 64 individual BNC connector ADC coax cables. The TDC patch panel takes in and outputs 12 34-pin 17-pair TDC ribbon cables. A photo of both patch panels is provided in Figure 3.13 and their cable mapping is provided in Table 3.4, 3.5, and 3.6.

5. **1** LVDS to ECL level translator repeater (LTR), which is attached to a separate electronics rack along with its own LV power supply. In Hall A the LTR is housed in the electronics bunker racks shown in Figure 3.25. The LTR is labelled LVDS2ECL1 and a photo is provided in Figure 3.13. Input TDC ribbon cables coming from the TH LOGIC patch panel begin by connecting to the LTR on the left most slot when looking from the front of the rack, and move sequentially across. The LTR mapping is detailed in Table 3.6 and a color-coded map is in Figure 3.15.
6. **1** patch panel for the ECL TDC signals from the LTR located in the electronics bunker racks shown in Figure 3.25. A photo is provided in Figure 3.13. The patch panel mapping is identical to the level translator, and is also detailed in Table 3.6 and a color coded map is in Figure 3.15. This patch panel is exactly the same as the TDC patch panel at the TH detector frame.
7. **1** patch panel for collecting ADC analogue signals located in the electronics bunker racks as shown in Figure 3.14. The patch panel is a straight through junction which takes in 64 BNC connector ADC coax cables in the back and outputs the same from the front which split into individual LEMO connections that go directly to the FADC readout modules.

Listed below is a complete inventory of the cables going from the TH detector frame to the Hall A electronics bunker used for the TH detector data acquisition system.

- **180** co-axial signal cables which are connected to the PMT bases. They connect to the inputs of 12 total NINO cards. There are 90 cables and 6 cards on each side of the BB frame. These cables have a length of 1.5m and consist of RG174 type co-axial and have MCX connectors on each end. These gold pin cables can be seen connected to the tops of the NINO cards in Figure 3.12.
- **180** HV co-axial cables (90 per side) with a length of 4m connected from the base of each PMT. They connect to the HV distribution panels on the BB frame. The HV cables have a custom

connector at the PMT base end of the type BaBar DIRC PMT HV connector and a Cage 50541 type D01 3-pin connector which goes to the HV distribution box. These HV cables can be seen connected to the HV distribution boxes shown in Figure 3.11.

- **4** braided 48-channel multi-way cables of length 60m. They are connected to one of four HV distribution panels on the BB frame, going to the HV mainframe power supply in the electronics bunker.
- **12** LV shielded pair 20 AWG power cables of length 5m going from the NINO cards to the LV distribution panel on the BB frame. The cables have a Molex LLC 0050579402 connector at the NINO card, and are soldered directly to the LV distribution box. There is one cable for each card, i.e. 6 per side of the frame. These braided LV cable can be seen connected to the LV distribution box in Figure 3.12.
- **2** 8-AWG cables of length 60m going from the LV distribution box on the detector frame to the LV power supply unit in the electronics bunker.
- **12** 34-way twisted ribbon cables of length 2m for TDC signals going from the NINO cards to the TDC patch panel on the right hand side of the frame. These cables can be seen attached to the NINO card in Figure 3.12.
- **24** 34-way twisted ribbon cables twelve of which have a length of 30m for TDC signals which reach from the patch panels on the BB frame to the electronics via a level translator located in a separated electronics holding rack. 12 cables run from the TDC frame patch panel to the level translator. The remaining 12 of length 10m reach from the level translator to the TDC signal patch panel in the electronics bunker. These cables can be seen coming from the detector frame TDC patch panel in Figure 3.12 and in both photos from Figure 3.13. Another set of 12 10m long TDC extension cables of the same type were added to reach the LTR in the electronics bunker.
- **12** 34-way twisted ribbon cables of length 1m which reach from the TDC digital signal patch panel in the electronics bunker to the input of the CAEN VME v1190 TDC readout modules in the DAQ crate. These again are the same type of cables shown in Figure 3.13.

- **8** 34-way twisted ribbon cable of length 2m (4 on each side), soldered to 16 way co-axial ribbon cable, from the NINO analogue output going to the detector frame ADC patch panel. These cables are shown coming from the NINO in Figure 3.12.
- **64** individual signal co-axial cables of length 100m with BNC connectors on each end. These are connected coming from the detector frame ADC patch panel going to the ADC patch panel in the electronics bunker. These co-axial signal cables are shown coming out of the ADC patch panel on the detector frame in Figure 3.12.
- **64** individual signal co-axial cables of length 5m which reach from the ADC analogue signal patch panel in the electronics bunker going to the inputs of the four FADC FASTBUS readout modules. These cables have BNC connectors at the ADC patch panel and LEMO connectors going into the FADC readout modules.

Appendix E

DAQ Mapping Tables

Listed below are several tables showing the mapping of cables and electronics hardware used for the TH detector data acquisition system.

Table E.1: Map for the labelling of components from the scintillator bars to the NINO card inputs.

Scintillator bars → NINO cards							
Left Side				Right Side			
Bar	Cable	NINO	Input	Bar	Cable	NINO	Input
1-L	H-Signal-L0	H-NINO-L0	0	1-R	H-Signal-R0	H-NINO-R0	0
2-L	H-Signal-L1	H-NINO-L0	1	2-R	H-Signal-R1	H-NINO-R0	1
3-L	H-Signal-L2	H-NINO-L0	2	3-R	H-Signal-R2	H-NINO-R0	2
4-L	H-Signal-L3	H-NINO-L0	3	4-R	H-Signal-R3	H-NINO-R0	3
5-L	H-Signal-L4	H-NINO-L0	4	5-R	H-Signal-R4	H-NINO-R0	4
6-L	H-Signal-L5	H-NINO-L0	5	6-R	H-Signal-R5	H-NINO-R0	5
7-L	H-Signal-L6	H-NINO-L0	6	7-R	H-Signal-R6	H-NINO-R0	6
8-L	H-Signal-L7	H-NINO-L0	7	8-R	H-Signal-R7	H-NINO-R0	7
9-L	H-Signal-L8	H-NINO-L0	8	9-R	H-Signal-R8	H-NINO-R0	8
10-L	H-Signal-L9	H-NINO-L0	9	10-R	H-Signal-R9	H-NINO-R0	9
11-L	H-Signal-L10	H-NINO-L0	10	11-R	H-Signal-R10	H-NINO-R0	10

Bar	Cable	NINO	Input	Bar	Cable	NINO	Input
12-L	H-Signal-L11	H-NINO-L0	11	12-R	H-Signal-R11	H-NINO-R0	11
13-L	H-Signal-L12	H-NINO-L0	12	13-R	H-Signal-R12	H-NINO-R0	12
14-L	H-Signal-L13	H-NINO-L0	13	14-R	H-Signal-R13	H-NINO-R0	13
15-L	H-Signal-L14	H-NINO-L0	14	15-R	H-Signal-R14	H-NINO-R0	14
16-L	H-Signal-L15	H-NINO-L0	15	16-R	H-Signal-R15	H-NINO-R0	15
17-L	H-Signal-L16	H-NINO-L1	0	17-R	H-Signal-R16	H-NINO-R1	0
18-L	H-Signal-L17	H-NINO-L1	1	18-R	H-Signal-R17	H-NINO-R1	1
19-L	H-Signal-L18	H-NINO-L1	2	19-R	H-Signal-R18	H-NINO-R1	2
20-L	H-Signal-L19	H-NINO-L1	3	20-R	H-Signal-R19	H-NINO-R1	3
21-L	H-Signal-L20	H-NINO-L1	4	21-R	H-Signal-R20	H-NINO-R1	4
22-L	H-Signal-L21	H-NINO-L1	5	22-R	H-Signal-R21	H-NINO-R1	5
23-L	H-Signal-L22	H-NINO-L1	6	23-R	H-Signal-R22	H-NINO-R1	6
24-L	H-Signal-L23	H-NINO-L1	7	24-R	H-Signal-R23	H-NINO-R1	7
25-L	H-Signal-L24	H-NINO-L1	8	25-R	H-Signal-R24	H-NINO-R1	8
26-L	H-Signal-L25	H-NINO-L1	9	26-R	H-Signal-R25	H-NINO-R1	9
27-L	H-Signal-L26	H-NINO-L1	10	27-R	H-Signal-R26	H-NINO-R1	10
28-L	H-Signal-L27	H-NINO-L1	11	28-R	H-Signal-R27	H-NINO-R1	11
29-L	H-Signal-L28	H-NINO-L1	12	29-R	H-Signal-R28	H-NINO-R1	12
30-L	H-Signal-L29	H-NINO-L1	13	30-R	H-Signal-R29	H-NINO-R1	13
31-L	H-Signal-L30	H-NINO-L1	14	31-R	H-Signal-R30	H-NINO-R1	14
32-L	H-Signal-L31	H-NINO-L1	15	32-R	H-Signal-R31	H-NINO-R1	15
33-L	H-Signal-L32	H-NINO-L2	0	33-R	H-Signal-R32	H-NINO-R2	0
34-L	H-Signal-L33	H-NINO-L2	1	34-R	H-Signal-R33	H-NINO-R2	1
35-L	H-Signal-L34	H-NINO-L2	2	35-R	H-Signal-R34	H-NINO-R2	2
36-L	H-Signal-L35	H-NINO-L2	3	36-R	H-Signal-R35	H-NINO-R2	3
37-L	H-Signal-L36	H-NINO-L2	4	37-R	H-Signal-R36	H-NINO-R2	4
38-L	H-Signal-L37	H-NINO-L2	5	38-R	H-Signal-R37	H-NINO-R2	5
39-L	H-Signal-L38	H-NINO-L2	6	39-R	H-Signal-R38	H-NINO-R2	6

Bar	Cable	NINO	Input	Bar	Cable	NINO	Input
40-L	H-Signal-L39	H-NINO-L2	7	40-R	H-Signal-R39	H-NINO-R2	7
41-L	H-Signal-L40	H-NINO-L2	8	41-R	H-Signal-R40	H-NINO-R2	8
42-L	H-Signal-L41	H-NINO-L2	9	42-R	H-Signal-R41	H-NINO-R2	9
43-L	H-Signal-L42	H-NINO-L2	10	43-R	H-Signal-R42	H-NINO-R2	10
44-L	H-Signal-L43	H-NINO-L2	11	44-R	H-Signal-R43	H-NINO-R2	11
45-L	H-Signal-L44	H-NINO-L2	12	45-R	H-Signal-R44	H-NINO-R2	12
46-L	H-Signal-L45	H-NINO-L2	13	46-R	H-Signal-R45	H-NINO-R2	13
47-L	H-Signal-L46	H-NINO-L2	14	47-R	H-Signal-R46	H-NINO-R2	14
48-L	H-Signal-L47	H-NINO-L2	15	48-R	H-Signal-R47	H-NINO-R2	15
49-L	H-Signal-L48	H-NINO-L3	0	49-R	H-Signal-R48	H-NINO-R3	0
50-L	H-Signal-L49	H-NINO-L3	1	50-R	H-Signal-R49	H-NINO-R3	1
51-L	H-Signal-L50	H-NINO-L3	2	51-R	H-Signal-R50	H-NINO-R3	2
52-L	H-Signal-L51	H-NINO-L3	3	52-R	H-Signal-R51	H-NINO-R3	3
53-L	H-Signal-L52	H-NINO-L3	4	53-R	H-Signal-R52	H-NINO-R3	4
54-L	H-Signal-L53	H-NINO-L3	5	54-R	H-Signal-R53	H-NINO-R3	5
55-L	H-Signal-L54	H-NINO-L3	6	55-R	H-Signal-R54	H-NINO-R3	6
56-L	H-Signal-L55	H-NINO-L3	7	56-R	H-Signal-R55	H-NINO-R3	7
57-L	H-Signal-L56	H-NINO-L3	8	57-R	H-Signal-R56	H-NINO-R3	8
58-L	H-Signal-L57	H-NINO-L3	9	58-R	H-Signal-R57	H-NINO-R3	9
59-L	H-Signal-L58	H-NINO-L3	10	59-R	H-Signal-R58	H-NINO-R3	10
60-L	H-Signal-L59	H-NINO-L3	11	60-R	H-Signal-R59	H-NINO-R3	11
61-L	H-Signal-L60	H-NINO-L3	12	61-R	H-Signal-R60	H-NINO-R3	12
62-L	H-Signal-L61	H-NINO-L3	13	62-R	H-Signal-R61	H-NINO-R3	13
63-L	H-Signal-L62	H-NINO-L3	14	63-R	H-Signal-R62	H-NINO-R3	14
64-L	H-Signal-L63	H-NINO-L3	15	64-R	H-Signal-R63	H-NINO-R3	15
65-L	H-Signal-L64	H-NINO-L4	0	65-R	H-Signal-R64	H-NINO-R0	0
66-L	H-Signal-L65	H-NINO-L4	1	66-R	H-Signal-R65	H-NINO-R4	1
67-L	H-Signal-L66	H-NINO-L4	2	67-R	H-Signal-R66	H-NINO-R4	2

Bar	Cable	NINO	Input	Bar	Cable	NINO	Input
68-L	H-Signal-L67	H-NINO-L4	3	68-R	H-Signal-R67	H-NINO-R4	3
69-L	H-Signal-L68	H-NINO-L4	4	69-R	H-Signal-R68	H-NINO-R4	4
70-L	H-Signal-L69	H-NINO-L4	5	70-R	H-Signal-R69	H-NINO-R4	5
71-L	H-Signal-L70	H-NINO-L4	6	71-R	H-Signal-R70	H-NINO-R4	6
72-L	H-Signal-L71	H-NINO-L4	7	72-R	H-Signal-R71	H-NINO-R4	7
73-L	H-Signal-L72	H-NINO-L4	8	73-R	H-Signal-R72	H-NINO-R4	8
74-L	H-Signal-L73	H-NINO-L4	9	74-R	H-Signal-R73	H-NINO-R4	9
75-L	H-Signal-L74	H-NINO-L4	10	75-R	H-Signal-R74	H-NINO-R4	10
76-L	H-Signal-L75	H-NINO-L4	11	76-R	H-Signal-R75	H-NINO-R4	11
77-L	H-Signal-L76	H-NINO-L4	12	77-R	H-Signal-R76	H-NINO-R4	12
78-L	H-Signal-L77	H-NINO-L4	13	78-R	H-Signal-R77	H-NINO-R4	13
79-L	H-Signal-L78	H-NINO-L4	14	79-R	H-Signal-R78	H-NINO-R4	14
80-L	H-Signal-L79	H-NINO-L4	15	80-R	H-Signal-R79	H-NINO-R4	15
81-L	H-Signal-L80	H-NINO-L5	0	81-R	H-Signal-R80	H-NINO-R5	0
82-L	H-Signal-L81	H-NINO-L5	1	82-R	H-Signal-R81	H-NINO-R5	1
83-L	H-Signal-L82	H-NINO-L5	2	83-R	H-Signal-R82	H-NINO-R5	2
84-L	H-Signal-L83	H-NINO-L5	3	84-R	H-Signal-R83	H-NINO-R5	3
85-L	H-Signal-L84	H-NINO-L5	4	85-R	H-Signal-R84	H-NINO-R5	4
86-L	H-Signal-L85	H-NINO-L5	5	86-R	H-Signal-R85	H-NINO-R5	5
87-L	H-Signal-L86	H-NINO-L5	6	87-R	H-Signal-R86	H-NINO-R5	6
88-L	H-Signal-L87	H-NINO-L5	7	88-R	H-Signal-R87	H-NINO-R5	7
89-L	H-Signal-L88	H-NINO-L5	8	89-R	H-Signal-R88	H-NINO-R5	8

Table E.2: Table of mapping for the labelling scheme used for the TH detector frame TDC patch panel (TH LOGIC) and ADC patch panel (TH ANALOG).

Frame Patch Panels				
TH LOGIC	TH ANALOG			
81-90R	37-25	37-26	37-27	37-28
65-80R	37-29	37-30	37-31	37-32
49-64R	35-17	35-18	35-19	35-20
33-48R	35-21	35-22	35-23	35-24
17-32R	35-25	35-26	35-27	35-28
1-16R	35-29	35-30	35-31	35-32
81-90L	38-25	38-26	38-27	38-28
65-80L	38-29	38-30	38-31	38-32
49-64L	38-17	38-18	38-19	38-20
33-48L	38-21	38-22	38-23	38-24
17-32L	33-25	33-26	33-27	33-28
1-16L	33-29	33-30	33-31	33-32
NOT USED	36-17	36-18	36-19	36-20
NOT USED	36-21	36-22	36-23	36-24
NOT USED	36-25	36-26	36-27	36-28
NOT USED	36-29	36-30	36-31	36-32

Table E.3: Table of mapping for the labelling scheme corresponding between the components going from the front-end NINO ASIC amplifier-discriminator cards on the TH detector frame to the FADC readout modules in the DAQ crate located inside the Hall A SBS electronics bunker.

NINO	ADC Ribbon Cable	TH ANALOG Frame
H-NINO-R0	8	35-24 - 37-25
H-NINO-R1	7	38-24 - 35-25
H-NINO-L0	4	33-32 - 38-17
H-NINO-L1	3	36-32 - 36-17
TH ANALOG Bunker	Coaxial Cable	ADC Slot
35-24 - 37-25	35-24 - 37-25	16
38-24 - 35-25	38-24 - 35-25	17
33-32 - 38-17	33-32 - 38-17	14
36-32 - 36-17	36-32 - 36-17	15

Table E.4: The TDC slot labels are slightly different from the ADC as they have an additional letter. This letter corresponds with which set of pins (L-left, R-right) the Nugent cables connectors attach to on the TDC v1190 readout modules. The TDC slot number corresponds to the v1190's position in the DAQ crate, same as the FADCs.

NINO	TH LOGIC Ribbon Cable	LVDS2ECL1 Ribbon Cable
H-NINO-R5	81-90R	81-90R
H-NINO-R4	65-80R	65-80R
H-NINO-R3	49-64R	49-64R
H-NINO-R2	33-48R	33-48R
H-NINO-R1	17-32R	17-32R
H-NINO-R0	1-16R	1-16R
H-NINO-L5	81-90L	81-90L
H-NINO-L4	65-80L	65-80L
H-NINO-L3	49-64L	49-64L
H-NINO-L2	33-48L	33-48L
H-NINO-L1	17-32L	17-32L
H-NINO-L0	1-16L	1-16L
TH LOGIC Bunker Cable	Cable to TDC	TDC Slot
81-90R	81-90R	3C
65-80R	65-80R	3C
49-64R	49-64R	3B
33-48R	33-48R	3B
17-32R	17-32R	3A
1-16R	1-16R	3A
81-90L	81-90L	2C
65-80L	65-80L	2C
49-64L	49-64L	2B
33-48L	33-48L	2B
17-32L	17-32L	2A
1-16L	1-16L	2A

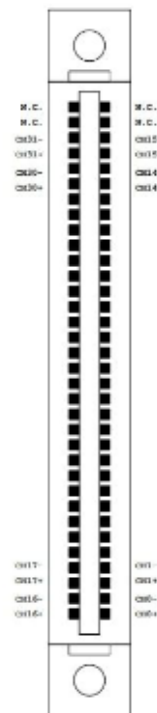
Appendix F

Readout Module Diagrams

Listed below are several diagrams pertaining to the ADC and TDC readout modules used for the TH detector data acquisition system.



(a) Front view of TDC v1190.



(b) Input connector pin.

Figure F.1: Caen v1190 TDC diagrams from manual. Inputs A, B, C, and D for the v1190 (a) are labelled under their respective locations. The diagram of the input connector (b) for the v1190 shows the locations of the pin assignments. Images from [68].

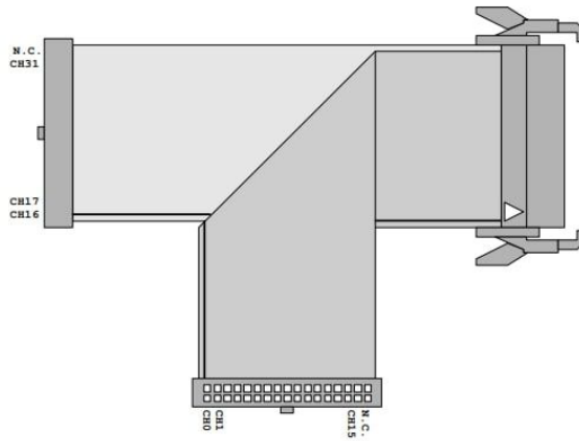


Figure F.2: Input Connector (Mod. A967 Cable Adapter) takes in two TDC ribbon cables (two sets of 16 channels each) and delivers their signals to the v1190s. Image from [52].

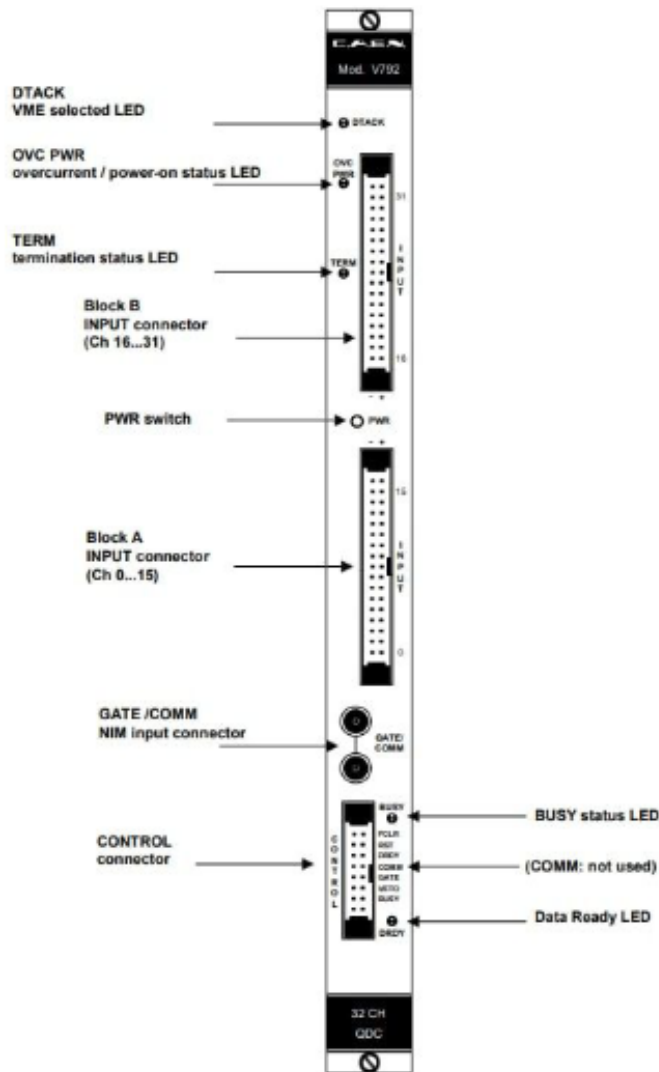


Figure F.3: Front view of the CAEN v792 ADC readout module. These were replaced by the FADCs and were mostly used initially simply to confirm all ADC data coming from the PMT signals through the NINO analogue output looked as expected. Image from [69].

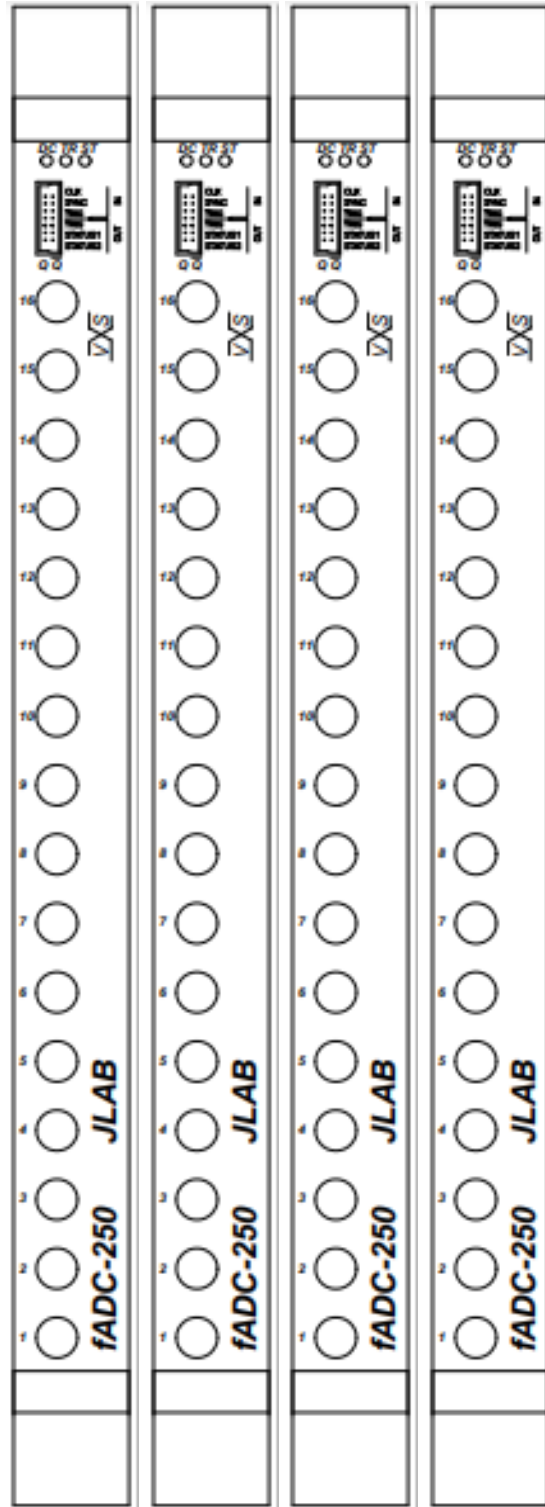


Figure F.4: Front view of the FADC readout modules. Four FADCs were installed to replace the two v792s. Their channels are labelled 1 to 16 from bottom to top. This picture shows four FADCs together as they are in slots 14-17 of the DAQ crate. The two FADCs on the left read in 32 channels from the left side of 32 scintillator bar PMT assemblies in the TH detector, and the same corresponding scintillator bar PMT assemblies channels for the two FADCs on the right to the right side of the TH detector. Image from [70].

Appendix G

Table of Charge Normalization HV Values

Table G.1: List of HV value settings from the ADC charge normalization study which were used for the G_M^n Experiment. These values are from after the 50V drop across all channels which occurred before the SBS-9 kinematic setting run period.

HV values used for G_M^n Experiment							
PMT No.	HV (-)	PMT No.	HV (-)	PMT No.	HV (-)	PMT No.	HV (-)
1-L	918	1-R	729	2-L	944	2-R	877
3-L	717	3-R	899	4-L	817	4-R	829
5-L	792	5-R	996	6-L	805	6-R	930
7-L	1067	7-R	946	8-L	983	8-R	767
9-L	909	9-R	853	10-L	884	10-R	792
11-L	757	11-R	873	12-L	925	12-R	716
13-L	833	13-R	856	14-L	953	14-R	871
15-L	890	15-R	901	16-L	953	16-R	863
17-L	953	17-R	833	18-L	808	18-R	824
19-L	805	19-R	836	20-L	862	20-R	847
21-L	696	21-R	832	22-L	818	22-R	771
23-L	968	23-R	890	24-L	899	24-R	889
25-L	909	25-R	923	26-L	847	26-R	898
27-L	692	27-R	820	28-L	813	28-R	866

PMT No.	HV (-)						
29-L	768	29-R	906	30-L	864	30-R	877
31-L	942	31-R	847	32-L	955	32-R	912
33-L	776	33-R	934	34-L	860	34-R	804
35-L	777	35-R	774	36-L	826	36-R	808
37-L	904	37-R	784	38-L	827	38-R	877
39-L	809	39-R	787	40-L	1021	40-R	855
41-L	834	41-R	864	42-L	831	42-R	956
43-L	885	43-R	853	44-L	890	44-R	921
45-L	811	45-R	817	46-L	900	46-R	930
47-L	926	47-R	909	48-L	1084	48-R	937
49-L	694	49-R	994	50-L	768	50-R	728
51-L	1065	51-R	883	52-L	863	52-R	911
53-L	740	53-R	806	54-L	835	54-R	957
55-L	926	55-R	813	56-L	813	56-R	818
57-L	762	57-R	895	58-L	841	58-R	875
59-L	826	59-R	823	60-L	761	60-R	907
61-L	928	61-R	862	62-L	864	62-R	769
63-L	864	63-R	860	64-L	833	64-R	873
65-L	866	65-R	961	66-L	832	66-R	993
67-L	850	67-R	965	68-L	961	68-R	920
69-L	958	69-R	786	70-L	957	70-R	972
71-L	873	71-R	952	72-L	853	72-R	873
73-L	837	73-R	950	74-L	901	74-R	807
75-L	824	75-R	883	76-L	915	76-R	885
77-L	953	77-R	699	78-L	947	78-R	971
79-L	778	75-R	877	80-L	893	80-R	839
81-L	794	81-R	888	82-L	794	82-R	780

PMT No.	HV (-)						
83-L	797	83-R	804	84-L	927	84-R	862
85-L	956	85-R	1053	86-L	930	86-R	983
87-L	757	87-R	791	88-L	890	88-R	934
89-L	919	89-R	804	90-L	0	90-R	0

Appendix H

Table of Relative Gain FADC Values

Table H.1: List of FADC mV values for each HV setting, from 700V to 100V in one hundred volt increments, used during the study of PMT relative gain for the TH detector. The mV values listed below were generated in Hall A using cosmic ray data with the BBCal trigger. The average error across all PMTs for mV values at 700, 800, 900, and 1000 V are ± 0.3 , ± 0.5 , ± 0.7 , and ± 2.1 mV, respectively.

FADC (mV) values for each HV setting									
PMT No.	700 V	800 V	900 V	1000 V	PMT No.	700 V	800 V	900 V	1000 V
33-L	1.3	16.7	70.2	144.8	33-R	0.1	0.3	2.4	19.7
34-L	2.8	4.7	21.1	49.1	34-R	0.4	3.9	26.1	92.5
35-L	2.1	24.4	81.3	153.9	35-R	1.9	23.0	57.7	141.8
36-L	0.3	2.8	26.0	68.5	36-R	0.6	1.8	12.7	38.9
37-L	1.6	4.4	15.1	38.0	37-R	4.9	13.4	62.8	150.6
38-L	6.0	14.2	47.8	84.5	38-R	0.5	0.7	12.6	42.1
39-L	6.6	20.9	44.9	104.4	39-R	1.4	16.8	65.6	151.0
40-L	0.1	0.2	2.5	22.1	40-R	1.9	1.7	16.4	49.9
41-L	3.7	8.4	23.0	32.1	41-R	0.5	2.1	23.8	61.4
42-L	5.9	8.8	34.0	85.4	42-R	0.1	0.2	1.2	9.1
43-L	1.2	1.4	13.9	37.0	43-R	0.3	1.7	34.5	63.8
44-L	0.5	1.0	19.3	53.6	44-R	0.3	0.8	3.0	22.4
45-L	1.1	13.7	62.8	138.2	45-R	1.8	6.3	34.2	86.4

PMT No.	700 V	800 V	900 V	1000 V	PMT No.	700 V	800 V	900 V	1000 V
46-L	0.9	1.3	16.9	45.0	46-R	0.1	0.3	3.5	20.0
47-L	0.9	1.6	9.8	24.5	47-R	0.3	0.5	3.6	24.7
48-L	0.5	0.6	1.1	8.5	48-R	0.1	0.2	1.8	23.8
49-L	2.6	49.0	153.0	329.3	49-R	0.3	0.3	1.6	9.0
50-L	2.6	12.7	59.9	154.0	50-R	1.4	23.8	98.4	206.7
51-L	0.5	0.5	1.5	12.3	51-R	1.0	1.2	10.2	35.7
52-L	0.4	1.2	9.9	31.3	52-R	0.1	0.29	3.5	31.1
53-L	1.6	23.7	107.2	185.6	53-R	0.5	14.2	50.5	134.0
54-L	2.1	2.3	19.7	66.6	54-R	0.1	0.1	1.6	17.8
55-L	0.2	0.6	6.2	19.3	55-R	6.9	14.8	30.2	88.9
56-L	1.0	15.6	36.1	148.3	56-R	4.4	9.6	34.5	88.9
57-L	1.5	16.1	61.7	160.9	57-R	0.2	0.5	8.8	27.8
58-L	0.7	2.2	15.3	51.1	58-R	0.4	1.0	10.5	47.8
59-L	3.9	5.46	42.1	87.5	59-R	0.6	3.2	30.2	84.0
60-L	1.2	15.4	80.4	149.5	60-R	0.1	0.3	8.2	22.7
61-L	0.5	1.4	7.4	25.2	61-R	0.1	0.1	2.5	34.3
62-L	0.1	0.4	23.6	75.6	62-R	6.4	43.7	101.1	201.5
63-L	3.6	13.9	24.3	45.8	63-R	0.2	0.6	14.0	42.2
64-L	5.5	5.9	35.7	57.2	64-R	3.1	3.2	16.2	53.3

Appendix I

Table of Calibration Values

Table I.1: A table of calibration values for every scintillator bar in the TH detector: bar number, TDC alignment offset (TAO) in nanoseconds (ns), Time-walk slope (TWS), Time-walk intercept (TWI) in ns, TDC time difference offset (TDO) in ns, and scintillation velocity correction (SVC).

TH Calibration Values								
Bar No.	TAO (L)	TAO (R)	TWS (L)	TWS (R)	TWI (L)	TWI (R)	TDO	SVC
1	-963.53	-957.10	-0.27	-0.45	2.35	5.54	-2.65	0.18
2	-913.80	-909.29	-0.16	-0.33	0.60	2.83	-0.68	0.18
3	-922.10	-967.00	-0.13	-0.29	0.27	3.07	-2.66	0.18
4	-926.80	-948.40	-0.09	-0.27	-0.99	1.92	-2.86	0.17
5	-919.10	-948.20	-0.07	-0.23	0.02	2.02	-2.40	0.16
6	-947.01	-996.50	-0.19	-0.30	1.64	3.38	-1.70	0.18
7	-951.75	-957.60	-0.14	-0.21	1.59	3.18	-1.26	0.17
8	-972.50	-977.40	-0.04	-0.13	0.55	3.11	-1.17	0.15
9	-948.60	-955.07	-0.10	-0.14	2.32	3.33	-1.05	0.15
10	-943.80	-945.50	-0.12	-0.20	3.88	4.67	-1.28	0.16
11	-921.68	-941.50	-0.14	-0.20	3.19	3.14	-1.47	0.16
12	-939.30	-920.81	-0.11	-0.17	2.58	3.68	-1.43	0.15
13	-937.67	-947.85	-0.10	-0.18	2.14	3.40	-1.66	0.14
14	-971.20	-975.50	-0.11	-0.15	1.30	2.09	-1.38	0.16

Bar No.	TAO (L)	TAO (R)	TWS (L)	TWS (R)	TWI (L)	TWI (R)	TDO	SVC
15	-934.28	-943.70	-0.13	-0.14	1.68	1.6	-1.36	0.15
16	-936.07	-924.77	-0.20	-0.20	2.50	2.3	-1.30	0.16
17	-926.60	-953.23	-0.33	-0.27	4.86	3.63	-0.88	0.18
18	-855.90	-884.47	-0.37	-0.33	4.89	4.78	-0.90	0.19
19	-882.14	-927.45	-0.33	-0.34	4.3	4.11	-1.01	0.19
20	-914.35	-918.23	-0.37	-0.36	4.05	3.94	-1.07	0.19
21	-858.40	-919.76	-0.37	-0.37	3.89	4.10	-1.17	0.19
22	-886.60	-937.98	-0.32	-0.38	3.1	4.27	-1.17	0.19
23	-905.56	-945.30	-0.34	-0.35	4.11	4.47	-1.11	0.20
24	-941.20	-971.20	-0.31	-0.33	4.24	4.24	-1.06	0.18
25	-908.72	-960.70	-0.27	-0.28	3.66	4.00	-1.25	0.17
26	-903.17	-950.50	-0.27	-0.28	4.07	3.73	-1.19	0.17
27	-880.26	-953.30	-0.29	-0.29	4.31	4.52	-1.05	0.17
28	-886.90	-954.77	-0.3	-0.30	4.26	5.01	-0.92	0.18
29	-887.57	-969.60	-0.32	-0.30	4.60	4.92	-0.75	0.18
30	-931.13	-988.20	-0.33	-0.31	5.39	5.59	-0.93	0.18
31	-898.90	-942.20	-0.30	-0.29	4.59	4.53	-1.17	0.18
32	-889.19	-946.07	-0.24	-0.25	3.79	4.41	-1.48	0.17
33	-889.99	-1003.10	-0.27	-0.23	3.90	2.55	-1.37	0.17
34	-820.38	-890.70	-0.31	-0.26	3.89	2.57	-1.04	0.18
35	-846.15	-920.06	-0.28	-0.22	4.2	2.87	-0.83	0.17
36	-870.48	-958.28	-0.32	-0.20	4.75	2.70	-0.55	0.16
37	-867.60	-929.60	-0.30	-0.19	5.37	3.47	-0.41	0.16
38	-840.30	-924.30	-0.33	-0.24	4.62	3.96	0.01	0.17
39	-848.70	-931.60	-0.29	-0.25	4.54	4.77	-0.03	0.17
40	-916.46	-979.80	-0.31	-0.25	4.84	5.76	0.01	0.17
41	-855.40	-947.02	-0.26	-0.25	4.11	4.37	-0.20	0.17

Bar No.	TAO (L)	TAO (R)	TWS (L)	TWS (R)	TWI (L)	TWI (R)	TDO	SVC
42	-860.26	-967.30	-0.27	-0.26	3.79	4.50	-0.21	0.18
43	-866.47	-938.37	-0.35	-0.28	4.36	4.28	-0.17	0.18
44	-851.77	-933.00	-0.32	-0.28	4.38	4.77	-0.15	0.18
45	-856.76	-936.40	-0.28	-0.28	3.96	4.69	-0.38	0.18
46	-903.30	-973.52	-0.31	-0.35	4.10	5.64	-0.54	0.19
47	-848.45	-929.36	-0.32	-0.38	3.81	6.16	-0.56	0.19
48	-851.59	-921.76	-0.32	-0.38	4.43	6.99	-0.53	0.19
49	-864.01	-980.40	-0.36	-0.33	5.70	6.43	-0.16	0.18
50	-793.70	-876.70	-0.30	-0.27	3.73	4.61	-0.31	0.17
51	-864.30	-951.30	-0.25	-0.19	3.36	3.71	-0.36	0.16
52	-866.40	-958.50	-0.21	-0.15	3.20	2.66	-0.64	0.16
53	-828.60	-919.90	-0.22	-0.18	2.73	3.06	-0.74	0.16
54	-858.62	-972.10	-0.33	-0.30	5.02	5.49	-0.48	0.18
55	-862.30	-933.45	-0.37	-0.37	6.32	7.10	-0.73	0.19
56	-873.50	-960.50	-0.35	-0.38	5.54	7.07	-0.66	0.19
57	-839.80	-958.92	-0.26	-0.28	4.59	5.74	-0.67	0.17
58	-850.30	-943.56	-0.16	-0.16	2.51	3.47	-0.66	0.16
59	-839.60	-929.90	-0.16	-0.14	2.50	2.87	-0.63	0.16
60	-822.26	-930.35	-0.18	-0.20	3.25	4.66	-0.79	0.16
61	-867.25	-946.60	-0.20	-0.26	3.91	6.43	-1.02	0.16
62	-895.52	-965.30	-0.17	-0.25	4.47	6.88	-1.06	0.16
63	-849.80	-932.16	-0.17	-0.25	4.63	6.73	-1.10	0.16
64	-837.20	-939.47	-0.22	-0.24	6.30	7.98	-1.0	0.17
65	-893.25	-1015.40	-0.22	-0.22	5.70	6.47	-0.78	0.17
66	-809.30	-955.60	-0.24	-0.17	5.87	5.39	-0.62	0.17
67	-856.80	-1008.50	-0.33	-0.27	7.24	7.19	-0.41	0.18
68	-870.20	-1000.60	-0.36	-0.30	7.00	7.17	-0.38	0.18

Bar No.	TAO (L)	TAO (R)	TWS (L)	TWS (R)	TWI (L)	TWI (R)	TDO	SVC
69	-868.77	-973.50	-0.29	-0.23	5.50	5.60	-0.45	0.17
70	-891.59	-1041.80	-0.25	-0.22	5.29	5.93	-0.41	0.16
71	-867.04	-1017.50	-0.30	-0.31	5.51	6.76	-0.73	0.19
72	-889.80	-1050.50	-0.37	-0.42	6.54	9.01	-0.87	0.20
73	-876.04	-1042.30	-0.34	-0.41	6.37	8.79	-0.72	0.19
74	-892.70	-1029.30	-0.33	-0.35	7.58	8.72	-0.79	0.18
75	-881.36	-1028.40	-0.23	-0.23	5.53	5.28	-0.82	0.17
76	-880.90	-1026.38	-0.16	-0.10	4.48	3.67	-0.76	0.15
77	-892.20	-995.80	-0.16	-0.12	4.14	3.26	-1.10	0.14
78	-902.60	-1071.20	-0.13	-0.05	3.37	2.05	-0.77	0.15
79	-859.98	-1010.98	-0.30	-0.30	4.40	10.80	2.06	0.15
80	-873.60	-1004.10	-0.25	-0.14	4.11	8.30	1.49	0.14
81	-956.04	-1121.05	-0.50	-0.36	7.69	5.00	-0.36	0.20
82	-886.50	-1057.90	-0.81	-0.69	12.20	10.50	-0.21	0.18
83	-908.43	-1094.70	-0.82	-0.62	12.96	8.16	-0.68	0.17
84	-973.10	-1141.90	-0.54	-0.41	9.24	5.89	-0.36	0.20
85	-937.20	-1127.30	-0.44	-0.44	6.58	6.40	-0.95	0.15
86	-937.36	-1141.46	-0.54	-0.43	7.10	7.14	-0.68	0.17
87	-917.70	-1112.96	-0.28	-0.27	4.27	4.99	-0.68	0.17
88	-973.30	-1161.10	-0.29	-0.57	14.70	25.69	-0.68	0.17
89	-936.40	-1110.45	-0.37	-0.43	14.50	17.39	-0.68	0.17
90	24.20	24.20	0.00	0.00	0.00	0.00	-0.68	0.17